AD-A280 424

||||||||||||

THREE FLIGHTS INTO THUNDERSTORMS WITH THE REVISED ROCKET ELECTRIC FIELD SOUNDING (REFS) PAYLOAD

J. C. Willett
D. C. Curtis
G. Y. Jumper
W. F. Thorn

DTIC QUALITY INSPECTED

DTIC
ELECTE
JUN 2 1994
S
G
D

10 August 1993

94-18955

||||||||||||||||||||

PHILLIPS LABORATORY
Directorate of Geophysics
AIR FORCE MATERIEL COMMAND
HANSCOM AIR FORCE BASE, MA 01731-3010

94 6 20 022

This report has been reviewed by the ESC Public Affairs Office (PA) and is releasable to the National Technical Information Service (NTIS).

"This technical report has been reviewed and is approved for publication"

FOR THE COMMANDER

DONALD D. GRANTHAM, Chief
Atmospheric Structure Branch

ROBERT A. McCLATCHEY, Director
Atmospheric Sciences Division

REPORT DOCUMENTATION PAGE

Public reporting burden for this collection of information is estimated to average 1 hour per response, including the time for reviewing instructions, searching existing data sources, gathering and maintaining the data needed, and completing and reviewing the collection of information. Send comments regarding this burden estimate or any other aspect of this collection of information, including suggestions for reducing this burden, to Washington Headquarters Services, Directorate for Information Operations and Reports, 1215 Jefferson Davis Highway, Suite 1204, Arlington, VA 22202-4302, and to the Office of Management and Budget, Paperwork Reduction Project (0704-0188), Washington, DC 20503.

1. AGENCY USE ONLY (Leave blank)	2. REPORT DATE 10 August 1993	3. REPORT TYPE AND DATES COVERED Scientific Oct 91 -- Jul 93

4. TITLE AND SUBTITLE

Three Flights Into Thunderstorms With The Revised Rocket Electric Field Sounding (REFS) Payload

6. AUTHOR(S)

J. C. Willett   G. Y. Jumper
D. C. Curtis   W. F. Thorn

5. FUNDING NUMBERS

PE 61102F

2310CP06

PE 62101F

6670GX12

7. PERFORMING ORGANIZATION NAME(S) AND ADDRESS(ES)

Phillips Laboratory, GPAA
29 Randolph Rd.
Hanscom AFB, MA 01731-3010

8. PERFORMING ORGANIZATION REPORT NUMBER

PL-TR-93-2182

IP, No. 347

9. SPONSORING/MONITORING AGENCY NAME(S) AND ADDRESS(ES)

10. SPONSORING/MONITORING AGENCY REPORT NUMBER

11. SUPPLEMENTARY NOTES

12a. DISTRIBUTION/AVAILABILITY STATEMENT

Approved for public release; distribution unlimited

12b. DISTRIBUTION CODE

13. ABSTRACT (Maximum 200 words)

Three sounding rockets were launched into thunderstorms from the Langmuir Laboratory in New Mexico during July, 1992, to measure profiles of the ambient vector electrostatic field. The eight individual, shutter field mills on each of these rockets had a nominal full-scale range of +/-900 kV/m and sensitivity of 225 V/m. The electric-field soundings passed several self-consistency tests and were corroborated by measurements from the surface and from both tethered and free balloons. Mill noise levels of less than 450 V/m, as well as other error sources, yielded a relative uncertainty of the measured ambient field components less than 1 kV/m in flight. Absolute calibrations of both the longitudinal and the transverse field components (relative to the rocket axis of symmetry) were accurate to +/-10% or better. Field magnitudes greater than 80 kV/m and electrostatic potential magnitudes over 120 MV were encountered inside the storms. The average field driving one natural cloud-to-ground lightning flash was estimated at 30 kV/m or less. Grounded triggering rockets were launched immediately after each sounding rocket, but no lightning was triggered, suggesting that ambient fields of 10 kV/m over the lowest 500 m were not sufficient to trigger lightning with the rocket-and-wire technique.

14. SUBJECT TERMS

Lightning, Field mills, Triggered lightning, Rocket, Electric fields

15. NUMBER OF PAGES
150

16. PRICE CODE

17. SECURITY CLASSIFICATION OF REPORT	18. SECURITY CLASSIFICATION OF THIS PAGE	19. SECURITY CLASSIFICATION OF ABSTRACT	20. LIMITATION OF ABSTRACT
Unclassified	Unclassified	Unclassified	SAR

Contents

Illustrations

Tables

Preface

The authors recognize the invaluable participation of SSgt. Jim Andersen of PL/SXAD, both during the assembly and testing of the payloads and throughout the field experiment, as a major ingredient in the success of the 1992 program. Sincere thanks are also due to Professors Bill Winn, Bill Rison, and Charlie Moore and to students Debbie Prell, Mary Walsh, and Clay Smith of NMIMT for supplying essential equipment, providing field support, launching triggering rockets, and generally contributing to the productivity and enjoyment of our stay at Langmuir Laboratory. Tom Marshall of U. Miss., Dave Rust of NOAA/NSSL, and Oklahoma University students Maribeth Stolzenburg, Tom Shepherd, Megan Maddox, and Ken Eack provided the tethered- and free-balloon measurements for comparison with the rocket soundings. Gene Laycock, of Phillips Laboratory Field Operations, arranged helicopter airlift of equipment (when the alternative was muleback). Finally, a major contribution to the morale of the group was made by the expert cooking and moral support of Kara Naber. This work was supported, in part, by AFOSR under 6.1 Work Unit 2310CP06.

Three Flights Into Thunderstorms With The Revised Rocket Electric Field Sounding (REFS) Payload

1. INTRODUCTION

This report is the sequel to Willett et al.,[1] which described the original design and initial testing of a rocket payload to measure profiles of the ambient vector electrostatic field below and inside thunderstorms. The principal purpose of the Rocket Electric-Field Sounding (REFS) payload is to quantify the conditions for triggered lightning, in conjunction with rocket-triggering experiments. A secondary research goal is to obtain snapshots of the vertical electrical structure of thunderstorms that cannot be acquired by either balloons or aircraft. A potential practical application is the operational measurement of fields aloft in support of space launches.

The REFS payload carries eight shutter-type field mills arranged symmetrically in opposing pairs, a high-voltage self-charging system, and several other sensors to help determine the position, orientation, and proper functioning of the vehicle during flight (see Table 1). REFS is intended to fly on a 2.75 in. Folding-Fin Aircraft Rocket (FFAR) motor to an altitude of roughly 15,000 ft AGL. A novel feature of the design due to W.P. Winn, W. Rison, and J.J. Jones of the New Mexico Institute of Mining and Technology (NMIMT) is the use of a single rotating shell, covering most of the payload, as the shutter for all of the mill stators (see Figure 1).

The design was engineered so that it could provide the maximum information for identifying and correcting invalid measurements. In spite of the inherent redundancy of eight mills and the self check provided by the charging system, it was thought that onboard, synchronous rectification might obscure several possible malfunctions. Thus, the raw waveform from the charge amplifier of each mill was digitized at over 2300 samples per second and telemetered to the ground along with shutter-position information.

The prototype payload was flight tested in fair weather at the NASA Wallops Flight Facility on 5 November, 1990, as described by Willett et al.[1] As a result, several design problems were identified and corrected. The revisions to the original design are detailed in Section 2 below. After

Table 1. REFS Data Channels in the Order They Appear in the Telemetry Stream

Channel	Description
0	Analog Zero
1	Battery Voltage
2	Optical Detector with 1 Pulse per Revolution
3	Optical Detector with 16 Pulse per Revolution
4	Atmospheric Pressure
5	Longitudinal Acceleration
6	Voltage on Corona Assembly
7	Transverse Magnetic Field (single-component)
8	Top-Right Field Mill
9	Top-Left Field Mill
10	Middle-Right Field Mill
11	Middle-Left Field Mill
12	Bottom-Right Field Mill
13	Bottom-Left Field Mill
14	Middle-Bottom Field Mill
15	Middle-Top Field Mill

an abortive attempt at the NASA Kennedy Space Center during August, 1991, three revised payloads were successfully launched into thunderstorms from the Langmuir Laboratory (operated by NMIMT in the Magdalena mountains of south-central New Mexico) during July 1992. The remainder of this report discusses the data obtained during these flights.

2. DESIGN REVISIONS

Several changes in payload design were made following the first test flight described by Willett et al.[1] The most significant such changes involved the high-voltage charging system.

2.1 High-Voltage System

The original design called for both positive and negative 10 kV supplies alternately connected to the corona assembly through high-voltage relays. It was found that the relays caused trouble and that dual polarity was not required. Measurements on the modular high-voltage supplies in use indicated a 0-90 percent turn-on time of only 20-25 ms and a 100-10 percent turn-off time of 100-200 ms when loaded with 250 MΩ, making relays unnecessary. Therefore, the system was simplified as shown in Figure 2. The output of a negative high-voltage supply was connected directly to the re-designed corona assembly described by Willett et al.[1] (Section 8). (The 500 MΩ

ROCKET ELECTRIC FIELD SOUNDER (REFS)

ROTATING SHELL
(SHUTTER)

SHUTTER WINDOWS
(IN OPPOSING PAIRS)
FOR 8 FIELD MILLS

S-BAND TRANSMITTER
AND ANTENNA

"MIGHTY MOUSE"
ROCKET MOTOR

CORONA WIRE
FOR CHARGING
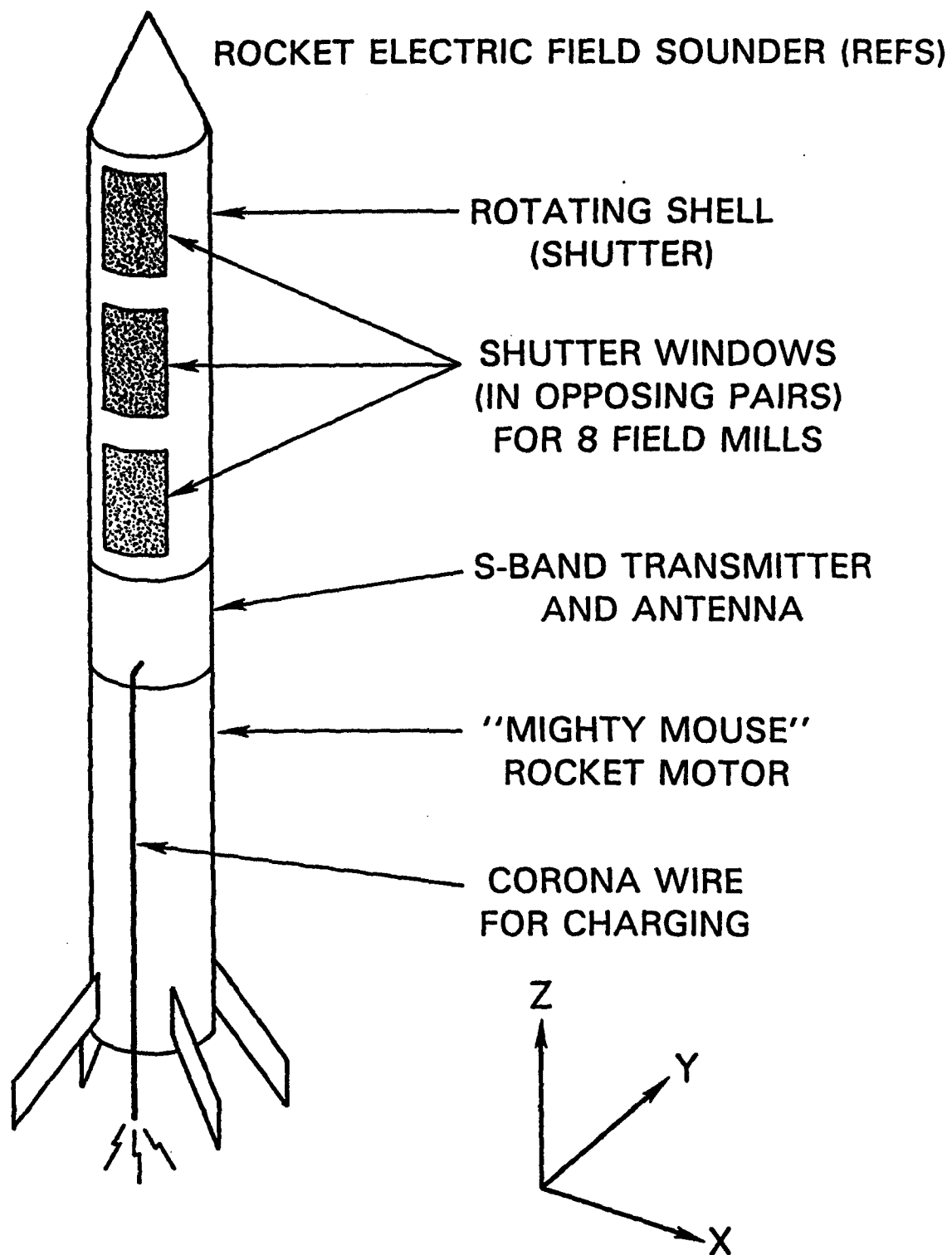
Figure 1. Schematic illustration of the REFS payload mounted on its rocket motor (not to scale). The outer, rotating shell (shutter), with its six cut-outs (three shown), periodically exposes eight "stator" electrodes, mounted on the payload body, to the external field. The coordinate system defined in Section 3, with the z-axis pointing forward along the longitudinal axis of the rocket, the x-axis in the direction of the middle-top stator, and the y-axis in the direction of the top-, middle-, and bottom-right stators, is also shown

3
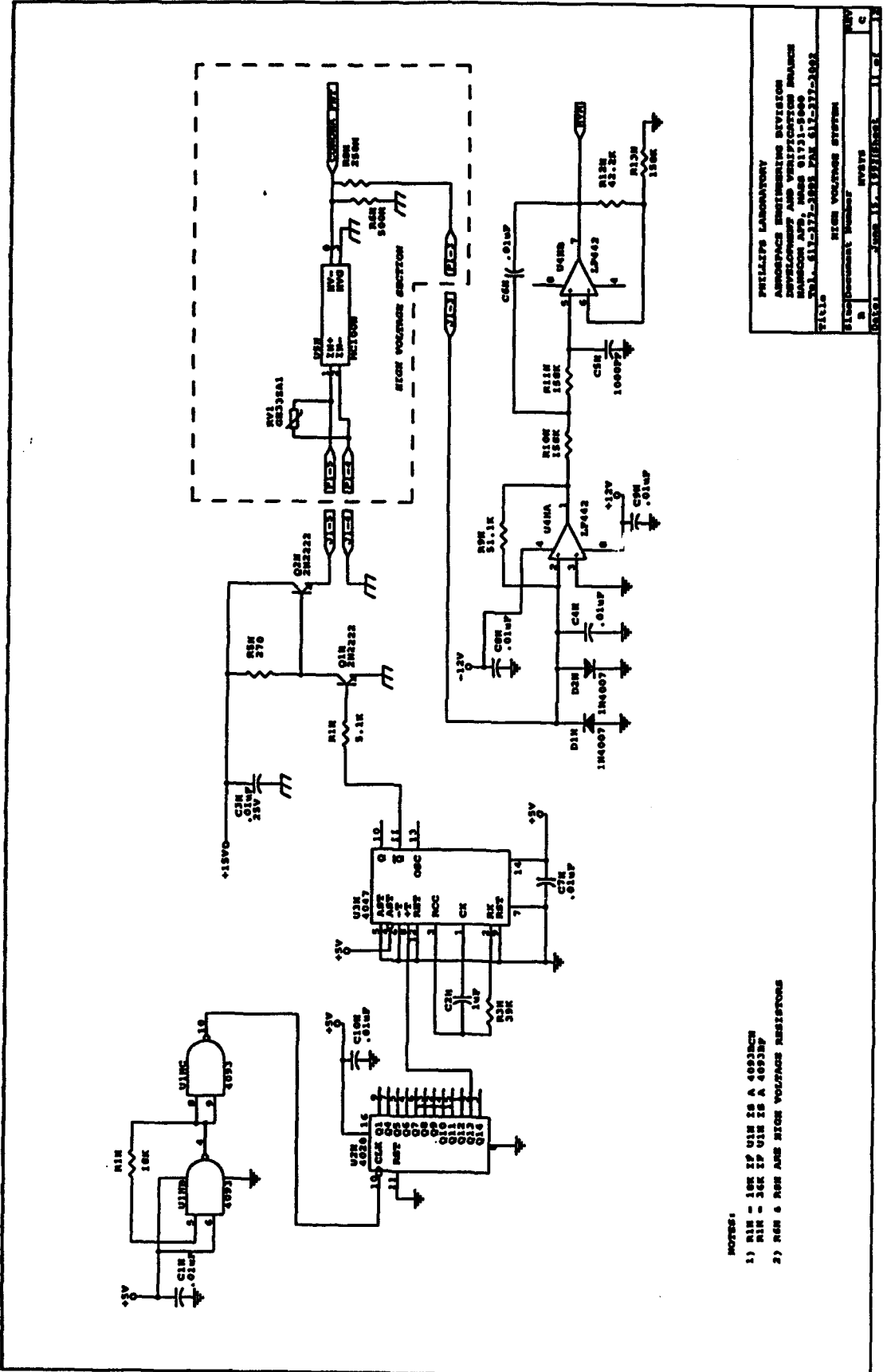
Figure 2. Schematic diagram of the modified high-voltage system for the 1992 flights

resistor to ground is vestigial). The duty cycle chosen was to energize the supply for 100 ms every 1.5 s.

Bench tests of this system indicated two anomalies that may be important for interpreting flight performance. First, it was noted that the corona assembly was no longer energized when the entire payload was electrified to a negative potential larger than about -25 kV relative to its environment. The control circuitry still cycled power to the modular high-voltage supply, but the supply produced no output. Similar behavior could be induced in a grounded payload by bringing a positively charged electrode close to one of the corona emitters. A gro   ᵓd or negatively charged electrode, however, did not cause this failure.

It was concluded that, although loading the modular high-voltage supply after it was energized did not cause it to fail, it was unable to turn on while negative current was being drawn from its output because of a choice made in its design. This failure mode might have been correctable by installation of a high-voltage diode to ground on the output of the supply, but such a diode was not readily available to us. In flight, the consequence of such a failure would be that a payload that was being strongly negatively charged by natural processes could not actively discharge itself. On the other hand, the periodic bursts of positive charging by the high-voltage system during normal operation ought to discourage the build-up of strong negative charge on the payload, and in any case, the first test flight had shown that the payload would discharge rapidly after any charging current terminated. Therefore, this problem was not judged to be severe and was not corrected.

The second anomaly was an indication by the high-voltage monitor of continuous negative voltage on the corona assembly when an electrode at a high negative potential approached one of the corona emitters on a grounded payload. This behavior was explained by the very high internal impedance inherent in the negative high-voltage supply to negative voltage on its output, even when the supply was not energized. Thus, the effective resistance of the corona assembly under these conditions was set at 167 MΩ by the two parallel resistors to ground. Steady current due to positive corona from the emitter was dropped across this resistance, raising the system to high negative potentials. In flight, natural positive charging of the payload would be expected to induce the same behavior. This was not judged to be a problem of system operation, but only one of interpretation of the resulting, slowly varying, negative potential (with respect to the payload) on the corona assembly.

2.2 Field-Mill Sensitivity

The nominal full-scale sensitivity of the field mills on the original payload, incorrectly described by Willett et al.[1] (Section 3.1) as +/-1 MV/m, was actually +/-2 MV/m for constant or slowly varying fields. This error, which does not affect any of the calibrations in this or the previous report, resulted from neglecting the 330 ms time constant of the charge amplifiers. Such a relatively short time constant rapidly removes any DC level from the output of a field-mill circuit. (The polarity of the measured field is preserved in the phase of the remaining AC signal.) Thus, although the sudden application of a field of +2 MV/m would have briefly saturated the

5

original mills, after several tenths of a second they would have drifted on scale with an AC amplitude near full scale.

The main reason that the field mills were originally designed for such low sensitivity was concern over possible large vehicle charging. As a result of the rapid decay of vehicle charge observed in the 5 November 91 flight, the size of the feedback capacitor was decreased by about a factor of 2, thereby yielding a nominal full-scale sensitivity to slowly varying fields of about 900 kV/m for the payloads described herein. To keep the time constant of the charge amplifier approximately constant, the feedback resistor was increased by a comparable factor. The nominal values of these two components for the 1992 flights were 4700 pF and 62 MΩ.

2.3 Magnetic Field Circuitry

This circuit was intended to measure rotation of the payload by sensing the component of Earth's magnetic field transverse to the rocket axis. Accurate measurement of the magnetic field was not the goal. The magnetic-field sensor used was a Hall-effect device. It had extreme temperature sensitivity that could not easily be fully compensated. An attempt was made to stabilize the circuit with a thermistor, as shown in Figure 3. This helped, and made the Hall device useful, but there was still substantial drift with temperature. The thermistor and bias resistors were selected to keep the output within bounds for the expected temperature range. Nevertheless, on one occasion the launch had to be delayed until the payload warmed up sufficiently to bring the magnetic-field signal on scale.

2.4 Mechanical-Design Changes

Since the REFS rocket is launched from a tube, special provisions had to be made to incorporate the high-voltage corona-discharge wire that runs along the length of the rocket motor. The original design had the corona wire taped to the side of the rocket motor and the end of the wire, with the insulation removed, terminated between the fins near the nozzle exit plane. Since the wire was attached to the exterior of the rocket motor, provisions were made to center the motor in a launch tube of sufficient diameter to clear the corona wire. A series of small teflon bumpers were glued to the fore and aft ends of the motor, centering the rocket in the tube and allowing for sufficient clearance between the corona wire and the tube walls, as described by Willett et al.[1] (Sections 4.1 and 4.4).

This arrangement was unsatisfactory (see Willett et al., Sections 7.3.1 and 7.3.2.4),[1] and a method was sought to improve the corona-discharge system. The new arrangement consisted of a corona-point assembly and a new forward spacer. The corona assembly (Willett et al., Figure 53)[1] consisted of a cylindrical, fiber-glass (G-10) housing around which spring-steel corona "fingers" were attached. This assembly was glued in place surrounding the aft end of the rocket motor. The housing served a second purpose as a spacer to center the aft end of rocket in the launch tube. The rocket was loaded into the launch tube with the corona "fingers" compressed. Immediately upon clearing the tube, the fingers extended into the air stream, providing a significant improvement in corona charging compared with the original method (see Section 4.3.4,

Figure 3. Schematic diagram of the modified magnetic field sensor for the 1992 flights

7

below). The forward spacer was also constructed from G-10 in the form of a ring glued around the forward end of the rocket motor.

While the new corona-assembly/motor-spacer arrangement worked well electrically and mechanically, it probably caused a major increase in aerodynamic drag, as discussed in Section 4.2, below. It appears that this design must be further modified for future flights.

The launcher used for the 1992 flights also differed significantly from that used at Wallops Island in 1990 (see Willett et al., Section 4.4).[1] The Wallops Island launcher consisted of a 4 ft long aluminum tube. This launch tube was approximately the same length as the rocket motor, affording no protection for the payload. The new launch tube was 8 ft. long, enclosing the entire vehicle to protect it from the elements, and was constructed of fiber-glass (G-10), allowing the telemetry signal to radiate through it. (After the rocket was loaded, a plastic bag was fastened over the business end of the launcher to keep rain out.) The 8 ft. launcher also constrained the orientation of the vehicle longer during liftoff, decreasing the uncertainty in effective launch azimuth and elevation.

Several slots were cut in the launch tube for access to the umbilical connector and for illumination of the optical sensors, as shown in Fig. 4. The umbilical cutout was approximately 2.5 in. long and 0.5 in. wide. After the rocket was loaded into the launch tube, the umbilical was inserted through the cutout and into the payload. The umbilical wire was then secured to the launcher immediately below the opening. When the rocket launched, it pulled the umbilical, which fell through the cutout to remain harmlessly outside the launcher. The cutouts for the optical sensors consisted of a series of radial slots in the launch tube at the same longitudinal location as the photo-diodes. This allowed enough light to reach these sensors to verify proper function while the rocket was inside the launch tube.

The rocket motors used for the REFS program are military surplus 2.75 inch Folding Fin Aircraft Rockets (FFAR). The fins remain in a "folded" condition while in the launch tube. Immediately after ignition, chamber pressure forces a plunger out between the fins, deploying them. Intended for launch from aircraft, the motors were modified by Wallops Flight Facility for ground-based launchers. The motors were originally designed with a case-ground ignitor, where the motor case acts as the negative lead for the ignitor circuit. The ignitors were modified to a two-wire system by Wallops Flight Facility. This offered a higher degree of safety for the launch crew, as the ignitor could remain shorted throughout the entire loading and arming operations.

3. LABORATORY CALIBRATIONS

Two pieces of background information will be useful in understanding the payload calibrations. First, the nominal sensitivity of the on-board, 12-bit, A/D converter is 1.465 mV per digital unit (DU), as before. This value will be used to convert from volts to DU for those sensors that were not calibrated "end-to-end" through the telemetry system. Second, the matrix notation and symmetry assumptions for the ambient-field calculation developed by Willett et al. (Section 6.1)[1] will be used throughout this report and are repeated here:

8
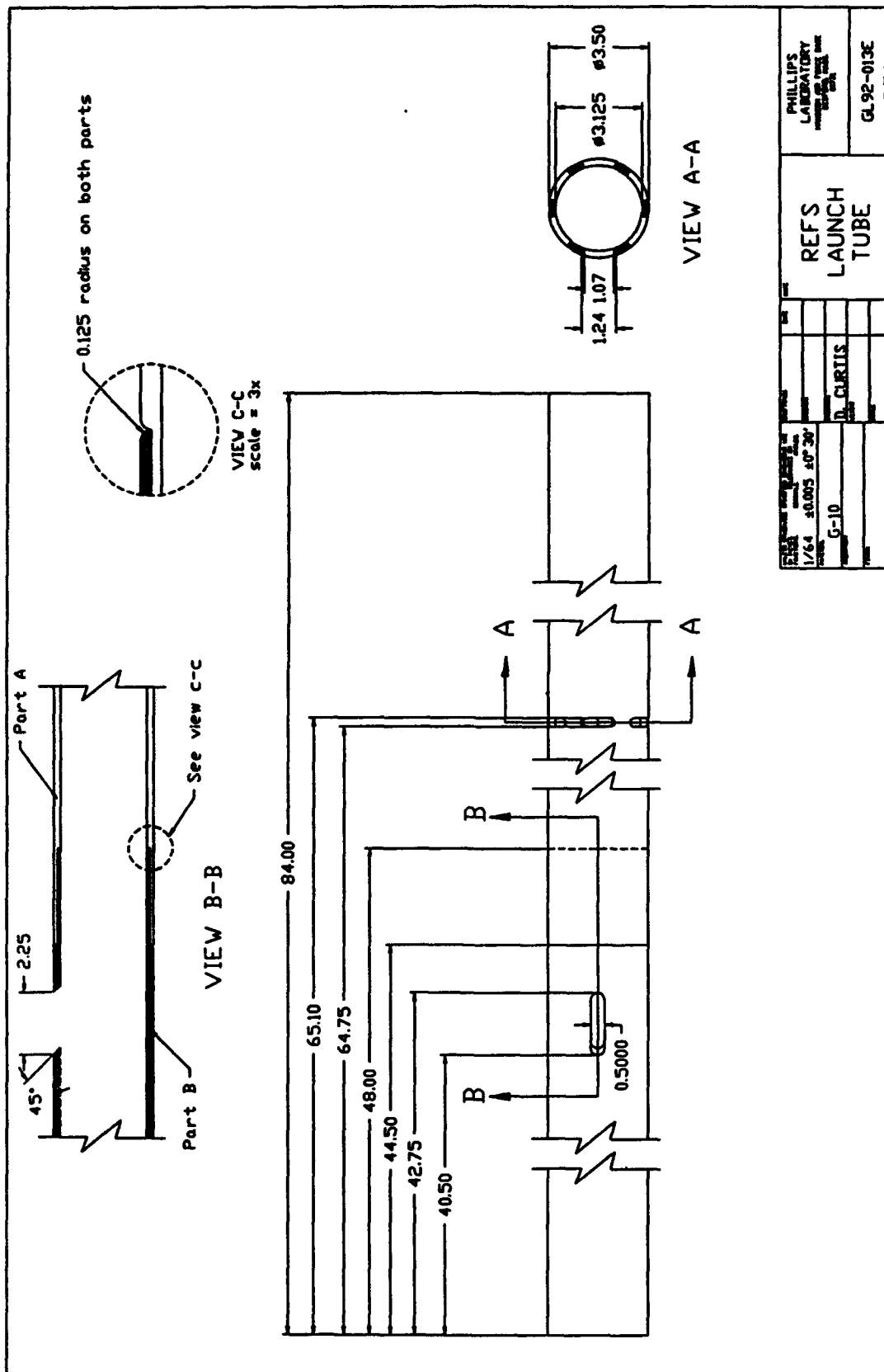
Figure 4. Design drawing of the new launch tube for the 1992 flights

9

$$
\begin{pmatrix} F_{tr} \\ F_{tl} \\ F_{mr} \\ F_{ml} \\ F_{br} \\ F_{bl} \\ F_{mb} \\ F_{mt} \end{pmatrix}
=
\begin{pmatrix}
0 & a_{ty} & a_{tz} & a_{tv} \\
0 & -a_{ty} & a_{tz} & a_{tv} \\
0 & a_{my} & a_{mz} & a_{mv} \\
0 & -a_{my} & a_{my} & a_{mv} \\
0 & a_{by} & a_{bz} & a_{bv} \\
0 & -a_{by} & a_{bz} & a_{bv} \\
-a_{my} & 0 & a_{mz} & a_{mv} \\
a_{my} & 0 & a_{mz} & a_{mv}
\end{pmatrix}
\begin{pmatrix} E_x \\ E_y \\ E_z \\ V \end{pmatrix}
\qquad (1)
$$

F_{ij} represents the normal fields at the surfaces of the various mills, where i denotes longitudinal position along the payload (top, middle, or bottom) and j indicates azimuthal position around the circumference (right, bottom, left, or top, reading clockwise while looking forward along the payload axis). On the other hand, in the coefficients, a_{ijk}, and ambient field, E_k, k denotes either the components of a right-handed, Cartesian coordinate system (x, y, z, oriented so that the positive z-axis is forward along the payload symmetry axis and the positive y-axis is in the direction that the "right" mills are facing), or vehicle potential (v). The field coefficients, a_{ijk} (k≠v), are dimensionless, but the potential coefficients, a_{ijv}, have dimensions of m^{-1} since they convert from potential to field.

3.1 Accelerometers

A single-axis, longitudinal accelerometer was included in the design primarily to determine the times of motor ignition and burnout. Each of the accelerometers flown in 1992 was calibrated at PL/SXA so that its data could be used to aid in the trajectory analysis, as discussed in Section 4.2.2, below. To accomplish this, each accelerometer integrated circuit (IC) was mounted to a right-angle bracket located on the outer rim of a spin table, as shown in Figure 5. Electrical connections to the IC were passed through a slip-ring system in the center of the table to a stationary breadboard of supporting electronics (see Willett et al., Figure 9),[1] and the output voltage was read with a digital voltmeter.

The table was spun at a predetermined set of rates and voltages from the accelerometer were recorded. By measuring the distance from the center of the spin table to the accelerometer and knowing the angular velocity of the table (as measured by its control system) the centripetal acceleration was determined. The data so obtained are presented in Table 2. (Here, as elsewhere in this report, the instruments are identified by their launch dates.) The data in this table are also plotted in Figure 6, which shows reasonably consistent and linear performance of these accelerometers.

Figure 5. Spin-table apparatus for calibration of the accelerometers
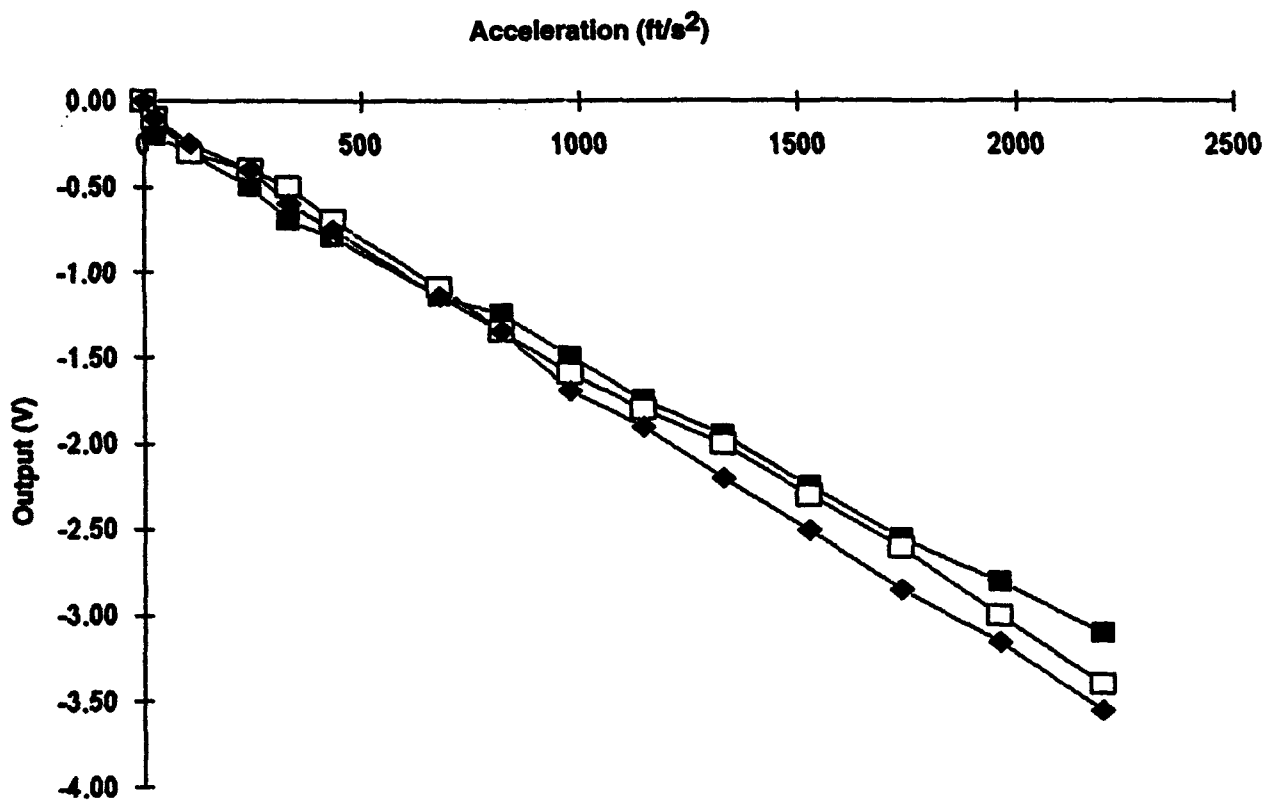
Figure 6. Calibration data for the three accelerometers are plotted as output voltage versus applied acceleration for 8 July 92 (solid squares), 17 July 92 (open squares), and 19 July 92 (solid diamonds)

Table 2. Accelerometer Calibrations for Each Flight

Acceleration	Accelerometer Output Voltage (V)		
(ft/s²)	8-Jul-92	17-Jul-92	19-Jul-92
2198	-3.10	-3.40	-3.55
1960	-2.80	-3.00	-3.15
1737	-2.55	-2.60	-2.85
1526	-2.25	-2.30	-2.50
1329	-1.95	-2.00	-2.20
1146	-1.75	-1.80	-1.90
977	-1.50	-1.60	-1.70
821	-1.25	-1.35	-1.35
678	-1.15	-1.10	-1.15
434	-0.70	-0.50	-0.60
244	-0.50	-0.40	-0.40
108	-0.30	-0.30	-0.25
27	-0.20	-0.10	-0.10
0	0	0	0

3.2 Pressure Sensors

A pressure sensor was included in the design to determine the time and altitude of apogee. Each sensor was calibrated in the pressure chamber located at Phillips Lab/Aerospace Engineering Branch. (This chamber was calibrated and read in *altitude*, according to the US Standard Atmosphere, 1962.) To accomplish the calibration, both electronics boards (digital and analog) from each payload were inserted into the bell jar. Electrical wires were connected from the output of the pressure circuit on the analog board (see Willett et al., Figure 7)[1] to a digital voltmeter external to the bell jar, as shown in Figure 7. The jar was slowly evacuated to predetermined altitudes, and voltage readings from the pressure sensor were recorded. Data from these calibrations are presented in Table 3 and plotted in Figure 8.

Note that, at the altitudes relevant to REFS, the 1962 and 1976 US Standard Atmospheres are identical. Thus, the altitudes in the table can be readily converted to pressures. If a temperature profile is available for the flight, these pressures can then be converted back to actual flight altitudes. For the purposes of this report, however, the output of the pressure sensors during the flights, interpreted as altitude according the US Standard Atmosphere via Table 3, was simply offset to make the measured altitude just before launch agree with the known launcher altitude of 10,400 ft MSL. This procedure also has the effect of removing slowly varying offsets in the sensors themselves.

Table 3. Pressure-Sensor Calibrations for Each Flight

Altitude (kft.)	Pressure-Sensor Output Voltage (V)		
	8-Jul-92	17-Jul-92	19-Jul-92
0.0	-1.930	-1.930	-1.980
0.5	-1.878	-1.882	-1.961
1.0	-1.846	-1.850	-1.929
2.0	-1.785	-1.791	-1.868
3.0	-1.730	-1.732	-1.808
4.0	-1.667	-1.673	-1.750
5.0	-1.612	-1.617	-1.694
6.0	-1.556	-1.563	-1.638
7.0	-1.502	-1.509	-1.583
8.0	-1.451	-1.458	-1.533
9.0	-1.400	-1.407	-1.482
10.0	-1.351	-1.359	-1.435
11.0	-1.304	-1.312	-1.387
12.0	-1.258	-1.266	-1.342
13.0	-1.214	-1.223	-1.298
14.0	-1.171	-1.180	-1.254
15.0	-1.130	-1.139	-1.213
16.0	-1.089	-1.100	-1.173
17.0	-1.050	-1.061	-1.133
18.0	-1.013	-1.024	-1.096
19.0	-0.976	-0.988	-1.059
20.0	-0.941	-0.952	-1.024
22.0	-0.877	-0.886	-0.958
24.0	-0.812	-0.824	-0.895
26.0	-0.755	-0.768	-0.838
28.0	-0.700	-0.714	-0.783
30.0	-0.650	-0.663	-0.733
32.0	-0.604	-0.617	-0.687
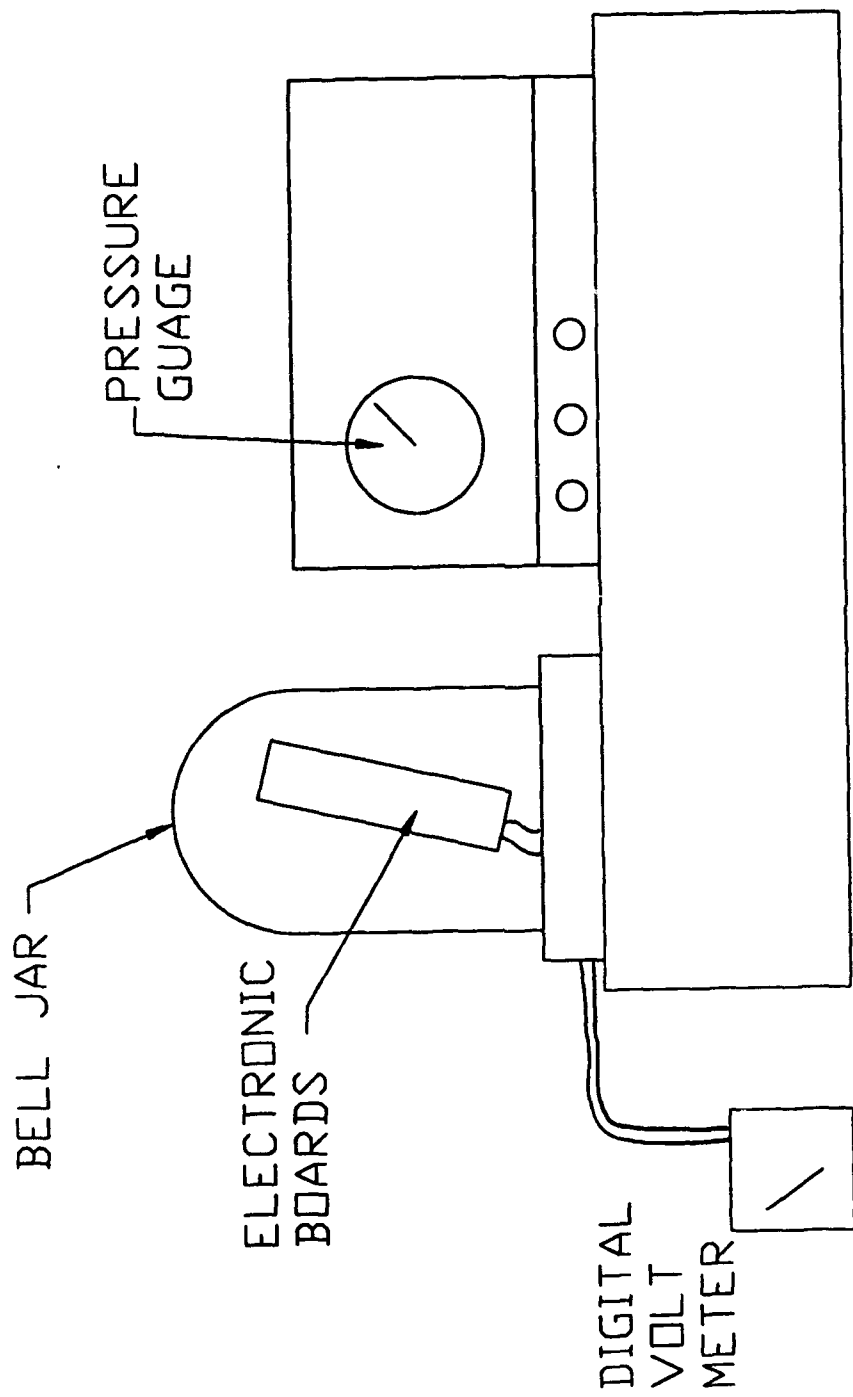
PRESSURE CHAMBER SETUP

Figure 7. Pressure-chamber apparatus for calibration of the pressure sensors

15
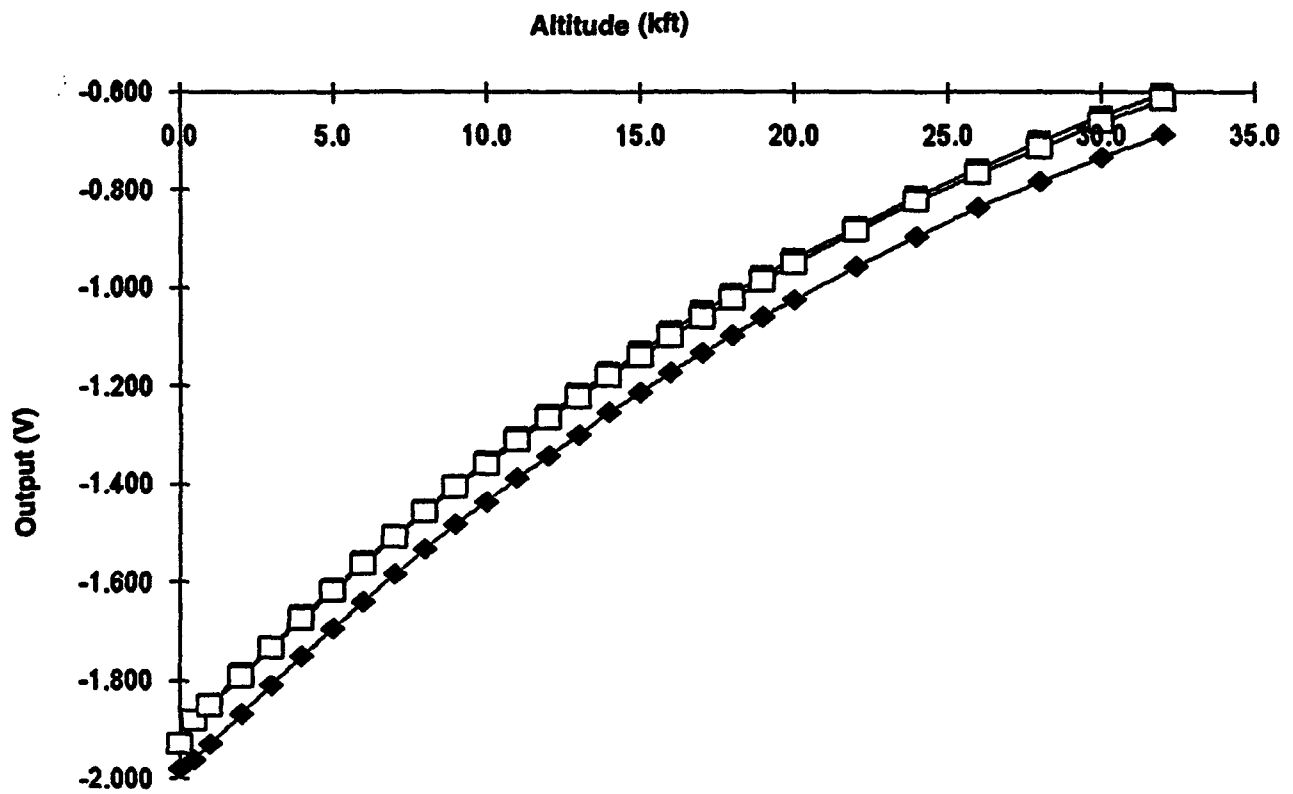
Figure 8.   Calibration data for the pressure sensors are plotted as output voltage versus altitude (US Standard
           Atmosphere, 1962) for 8 July 92 (solid squares), 17 July 92 (open squares), and 19 July 92 (solid diamonds)

3.3 Field-Mill Electronics -- "De-Droop" Algorithm

The calibration of our field mills is strongly affected by the sensitivity of the charge amplifiers and associated electronics. This sensitivity was measured as described by Willett et al. (Section 6.2.1)[1] using a rise-time-limited square wave of 15.100 Vpp amplitude applied through a capacitor of 744 pf, resulting in a charge of 11 234 pC deposited on the stators.

An improvement over the previous report is the incorporation of a "de-droop" algorithm into all analysis of data from the field mills. This is desirable because the charge amplifiers have a time constant that is not always long compared to the mechanical period of the mills. Thus, after the shutter opens or closes, the amplifier output "droops" slightly toward zero, as illustrated in Figure 9.

Simple circuit analysis yields the following equation for the voltage, v, at the output in terms of the current, i, into the input of the charge amplifier, where R and C are the feedback resistance and capacitance that determine the time constant $\tau = RC$:

$$\frac{dv}{dt} + \frac{1}{RC} v = - \frac{i}{C} \tag{2}$$

Since the field measured by a mill is given by $F = Q/A\varepsilon_0$, where the charge on the stator, Q, is the integral of -i, and A is the effective area of the mill, we can integrate Eq.(2) to obtain

$$F = \frac{C}{A\varepsilon_0} [v + \frac{1}{\tau} \int_0^t v \, dt \,]. \tag{3}$$

As noted in Section 2 above, the sensitivity of the mills was increased for the 1992 flights by decreasing the feedback capacitor to 0.0047 µf. The feedback resistor was correspondingly increased to 62 MΩ, yielding a time constant of 291 ms, similar to the previous value.

The expression in brackets above can be non-dimensionalized and applied directly to the digital output of the field-mill channels as follows:

$$(DU)' = (DU) + \frac{1}{N} \int_0^n (DU) \, dn', \tag{4}$$

where (DU) represents the telemetry output in "digital units" [- 2048, +2047], N = 675 is the number of samples in one time constant, determined by the frame rate of 2314.8 per second, and n is the sample number. Equation (4) has been applied to the raw field-mill data throughout the remainder of this report, so that all future references to field-mill output imply (DU)', not (DU). (The integral in (4) was implemented in software by the trapezoid rule.) For example, the raw data in Figure 9, becomes that shown in Figure 10 after "de-drooping".

The results of the calibration are presented in Table 4 in terms of the charge on each stator per digital unit of output from the telemetry system. As before, each mill is designated by two letters, the first denoting its longitudinal position (Top, Middle, or Bottom) and the second indicating its azimuthal location (Right, Bottom, Left, or Top). The magnitude of these calibration factors is about half those for the 1990 launch, as expected.

17
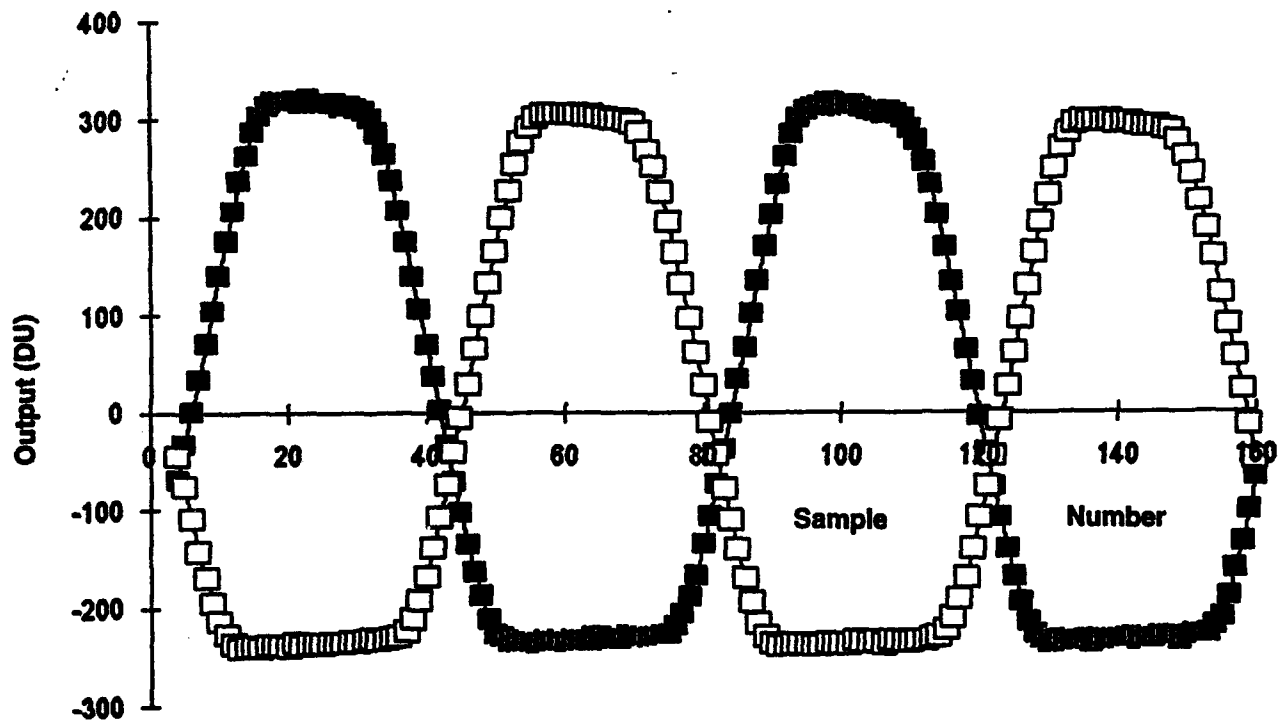
Figure 9. Raw waveform from the middle-right (solid squares) and middle-bottom (open squares -- 180 degrees out of phase) mills while a potential of -30 kV was applied to the payload. The output of the mill channels in digital units (DU) is plotted against sample number in the telemetry stream. Since there are 2314.8 samples per second, about 69 ms of data are shown

18
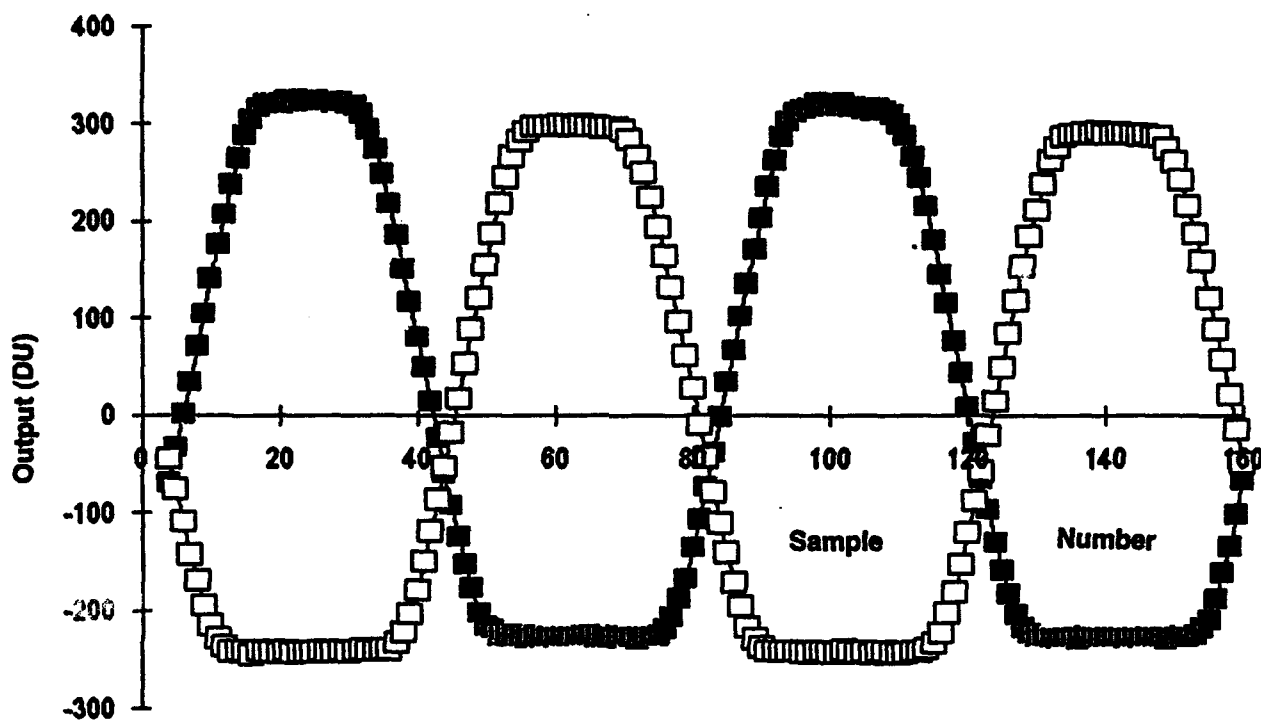
Figure10. Similar to Figure 9 but showing the same data after "de-drooping". Notice the flatter tops and bottoms of the truncated-triangle waveforms compared with Figure 9

Table 4. Calibration of Field-Mill Electronics (pC/DU)

Flight	Stator							
	TR	TL	MR	ML	BR	BL	MB	MT
8-Jul-92	-5.404	-5.431	-5.445	-5.395	-5.414	-5.381	-5.458	-5.413
17-Jul-92	-5.398	-5.493	-5.385	-5.433	-5.428	-5.432	-5.420	-5.372
19-Jul-92	-5.437	-5.451	-5.401	-5.380	-5.446	-5.437	-5.436	-5.478

3.4 Vehicle Potential Calibration

The potential coefficients, a_{iv} (i = t, m, or b), of the mills were determined as described by Willett et al. (Section 6.2.1).[1] Each payload was suspended in the laboratory and elevated to a potential of -30 kV. The de-drooped mill signals were synchronously rectified to produce two field estimates, in digital units, for each revolution of the rotating shell. Averages and standard deviations of 26-40 such estimates, from which the potential calibrations are calculated in pC/V using the stator calibrations in Table 4, are quoted in Table 5. We have no explanation for the larger standard deviations on 17 July 92.

Table 5. Potential Calibrations

Flight	Mill							
	TR	TL	MR	ML	BR	BL	MB	MT
8-Jul-92								
Ave. (DU)	578.7	590.1	533.2	543.4	519.3	520.9	544.6	522.0
Std. (DU)	1.4	1.4	2.0	1.5	2.5	3.1	1.9	1.5
(pC/V)	0.1043	0.1068	0.0968	0.0977	0.0937	0.0934	0.0991	0.0942
17-Jul-92								
Ave. (DU)	600.6	589.2	539.4	525.2	514.4	503.6	528.8	542.1
Std. (DU)	5.3	5.6	6.3	6.4	7.1	7.0	5.9	6.6
(pC/V)	0.1081	0.1079	0.0968	0.0951	0.0931	0.0912	0.0955	0.0971
19-Jul-92								
Ave. (DU)	592.6	576.3	547.6	538.9	528.7	515.0	545.8	530.5
Std. (DU)	0.8	0.7	1.5	1.5	0.9	1.1	1.4	1.7
(pC/V)	0.1074	0.1047	0.0986	0.0966	0.0960	0.0933	0.0989	0.0969

The potential calibrations at each longitudinal position in Table 5 are averaged, first for each payload and then among all three payloads, in Table 6. The average calibrations (pC/V) are then converted to potential coefficients (m^{-1}) using the nominal effective area of the mills, A = 0.00274 m^2. Similar results for the 1990 payload are reproduced for comparison. The calibrations for the two years are similar, but not identical. Notably, the difference between longitudinal positions is considerably greater in the 1992 data. The present values should be better because the raw fields on which they are based are larger by about a factor of 6 (twice the sensitivity times three times

the applied potential). On the other hand, the larger potential used in 1992 might have caused errors due to space-charge effects. The ratios of potential coefficients at different longitudinal positions can be measured in flight, as discussed in Section 4.3.4.

Table 6. Overall Potential Coefficients

	top	middle	bottom
8-Jul-92			
ave. (pC/V)	0.1055	0.0969	0.0936
17-Jul-92			
ave. (pC/V)	0.1080	0.0961	0.0921
19-Jul-92			
ave. (pC/V)	0.1061	0.0977	0.0947
overall 1992			
ave. (pC/V)	0.1065	0.0969	0.0934
std. (pC/V)	0.0016	0.0015	0.0015
a_{iv} (m^{-1})	4.393	3.998	3.854
1990 unit			
ave. (pC/V)	0.1062	0.1000	0.0988
a_{iv} (m^{-1})	4.38	4.12	4.08

3.5 Vehicle Transverse-Field Calibration

Tom Marshall (U. Mississippi) and Dave Rust (NOAA/NSSL) set up a large, parallel-plate field chamber in the Balloon Hangar at Langmuir Laboratory to calibrate their balloon-borne field mill. In addition to a calibrated, high-voltage power supply driving the upper, horizontal, 3 m square plate, this apparatus was equipped with a calibrated, flush-mounted field mill in the center of the lower plate, which consisted of sheet metal lying on the dirt floor of the hangar. Thus, the average field computed from the voltage difference and separation of the plates could be compared with the surface field measured at the grounded plate to check for perturbations caused either by corona or electrode-effect space charge or by net or induced charge on the instrument being calibrated.

We used this chamber to determine the transverse-field coefficients of the rocket-borne mills. The payload that was later launched on 19 July, 1992, was mated to a dummy rocket motor and suspended horizontally so that it was centered in the chamber, as illustrated in Figure 11. The rocket was oriented with the positive y-axis pointing downward, so that the "left" stators were facing the upper plate. The plate separation of 1.43 m was large compared to the 7 cm payload diameter. The 4.2 m diagonal of the upper (smaller) plate, along which the rocket's symmetry axis was oriented, was significantly greater than the 1.1 m payload length. Since the ratio of plate separation to shortest plate dimension was less than 1/2, we expect the actual transverse field applied to the payload to be given by the ratio of plate voltage to plate separation with an accuracy better than 10 percent -- adequate for our purposes.

21

Figure 11. Photograph of the setup for the transverse-field calibration. The rocket is suspended with nylon cord midway between the large high-voltage electrode (top, with rolled edges to minimize corona) and sheets of aluminum on the floor of the Balloon Hangar. The surface field mill mounted in one of these sheets is visible beneath the rocket

The potential applied to the upper plate during these measurements ranged over [-200, +200] kV. Throughout this range, the field at the surface of the lower plate varied linearly with the average field, the two independent calibrations agreeing within 10 percent. Thus, there is no evidence that either space charge or charge on the rocket distorted the ambient field in the chamber.

Table 7 shows the results for one of man, applied voltages on the upper plate. The first two rows give the raw data -- averages and standard deviations of 114 individual field readings (in digital units) from each mill. The average values have been converted to pC using the actual stator calibrations (from Table 4) in the next row. Since the potential on the upper plate was positive in this case, negative charge was induced on the "left" (upper) mills and positive charge on the "right" mills. The sums and differences of opposing mills, proportional to net charge on the rocket (assuming that there is no longitudinal field) and transverse ambient field, respectively, are listed in the next two rows. Finally, these sums and differences have been expressed in proportion to the applied transverse field, -28.0 kV/m (downward) in this case, in the sixth and seventh rows, respectively. To get "V/E_y", we used the potential calibrations for this payload from Table 6. To get the transverse-field coefficients (a_{iy}) themselves, we used the nominal mill-surface area, A = 0.00274 m^2. Note that we have defined DIFF/2 = (left - right)/2 in the first three columns, opposite the usual polarity of E_y, to account for the fact that the payload y-axis points downward in this experiment. Further, note that the lower right entry in the table (which we will call $a_{m'y}$ for lack of any better notation) is not really a measure of the sensitivity of the MB and MT mills to E_y, which should be zero by symmetry. This entry should be viewed simply as an indication that the payload was indeed oriented with its x-axis approximately horizontal.

Table 7. Transverse-Field Calibration of Payload 19-Jul-92 with +40 kV on the Upper Plate.

	Mill							
	TR	TL	MR	ML	BR	BL	MB	BT
Ave. (DU)	-121.9	140.8	-119.6	139.2	-117.3	138.5	13.8	5.6
Std. (DU)	1.3	1.4	1.2	1.3	1.1	1.3	1.7	1.6
Ave. (pC)	662.9	-767.4	646.2	-749.0	638.7	-752.7	-75.1	-30.9
SUM/2 (pC)	-52.3		-51.4		-57.0		-53.0	
DIFF/2 (pC)	-715.2		-697.6		-695.7		22.1	
"V/E_y" (V/kV/m)	17.6				21.5		19.4	
a_{iy}	1.053		1.027		1.025		-0.033	

The mill fields due to net charge (SUM/2) are much smaller than those due to transverse field (DIFF/2) in the first three columns of Table 7, indicating that the payload is properly isolated.
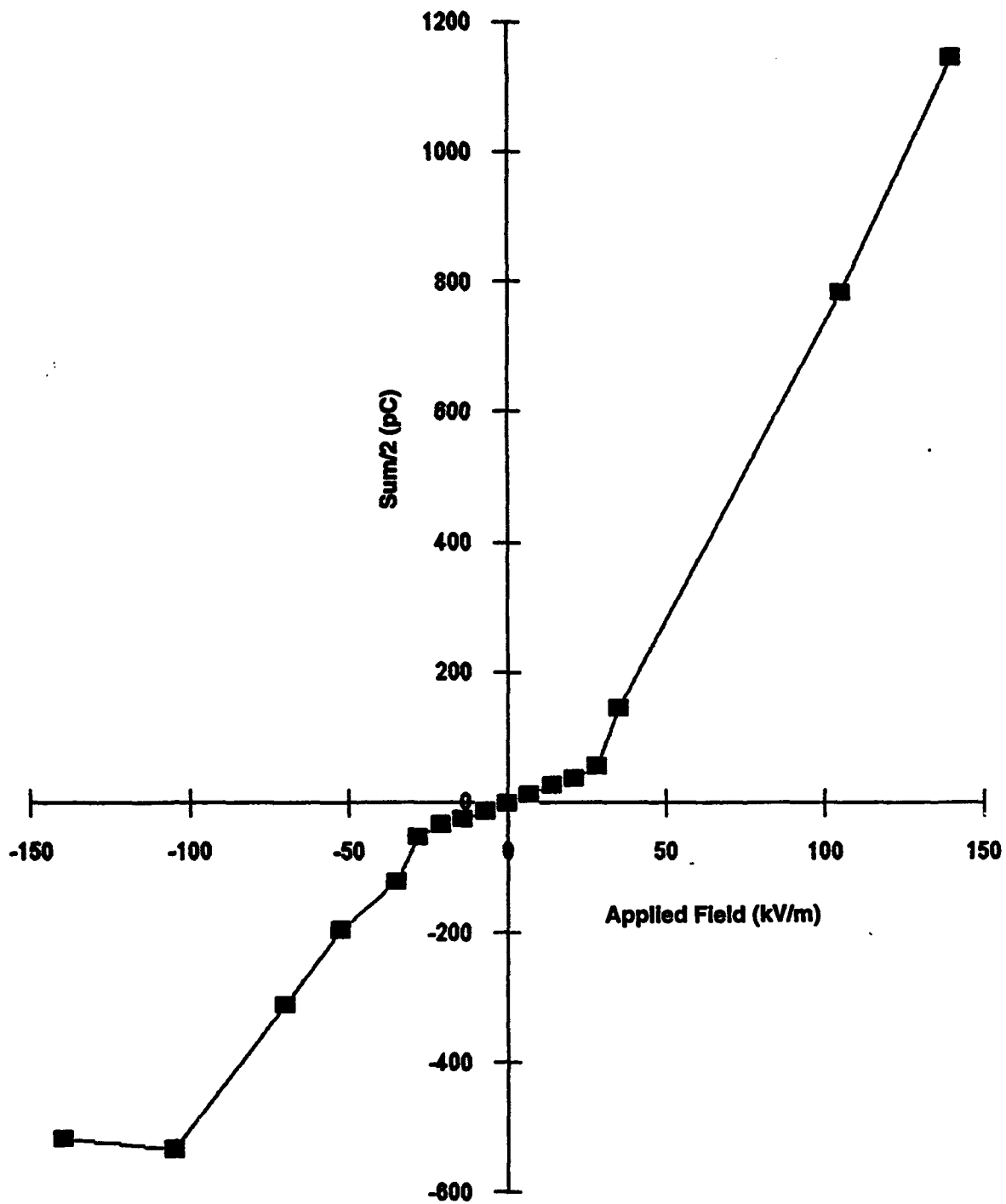
Figure 12. Average of SUM/2 (proportional to net charge on the rocket, assuming that there is no longitudinal field) over all four pairs of mills versus applied transverse field (E_y) in the calibration chamber

This does not remain true at higher applied voltages, however, where the rocket charges strongly in the polarity opposite that of the potential applied to the upper plate. SUM/2 becomes almost 1/3 of DIFF/2 at -200 kV. Figure 12 illustrates this effect, suggesting corona onset somewhere in the apparatus at ambient field magnitudes near 30 kV/m. Nevertheless, Figure 13 indicates that this payload charging has little effect on the measurement of transverse field, since DIFF/2 increases linearly with ambient field throughout the range of applied potentials.

Table 8 summarizes the values of "V/E_y" (listed as (V/kV/m)) and a_{ty} for many values of the potential applied to the upper plate. The last two rows present averages of these values over the limited set of the cases (applied fields of +-28.0, +-21.0, and +-14.0 kV/m) for which payload charging is minimal and over all the cases. The limited averages will be used hereafter in this report.

Table 8. Summary of Transverse-Field Calibrations of Payload 19-Jul-92.

E_y (kV/m)	Top (V/kV/m)	a_{ty}	Middle-R&L (V/kV/m)	a_{my}	Bottom (V/kV/m)	a_{by}	Middle-T&B (V/kV/m)	a_{my}
-139.9	38.1	1.052	36.4	1.016	37.6	1.011	37.4	-0.034
-104.9	51.4	1.044	50.7	1.012	51.9	1.007	51.6	-0.036
-69.9	45.4	1.050	44.1	1.017	45.5	1.012	45.1	-0.035
-52.4	37.5	1.053	37.1	1.022	38.6	1.017	38.1	-0.036
-35.0	36.1	1.060	34.4	1.024	36.2	1.019	34.9	-0.036
-28.0	17.6	1.053	18.8	1.027	21.5	1.025	19.4	-0.033
-21.0	14.5	1.050	16.8	1.029	20.3	1.027	16.9	-0.031
-14.0	13.9	1.070	18.4	1.054	23.8	1.053	18.6	-0.034
-7.0	13.1	1.006	20.0	1.005	28.9	1.009	19.7	-0.029
0.0	--	--	--	--	--	--	--	--
7.0	8.8	1.037	19.2	1.038	20.6	1.040	22.0	0.054
14.0	11.2	1.037	19.6	1.038	21.9	1.038	20.8	0.055
21.0	11.2	1.028	18.6	1.027	21.1	1.025	20.0	0.053
28.0	13.1	1.034	20.8	1.030	23.2	1.029	21.7	0.061
35.0	34.8	1.054	42.9	1.049	45.5	1.047	43.9	0.072
104.9	68.5	1.024	76.5	1.021	79.5	1.019	77.6	0.067
139.9	75.6	1.016	83.8	1.012	87.1	1.010	85.0	0.058
Lim. Ave.:	13.6	1.045	18.8	1.034	22.0	1.033	19.6	--
All. Ave.:	--	1.042	--	1.026	--	1.024	--	--
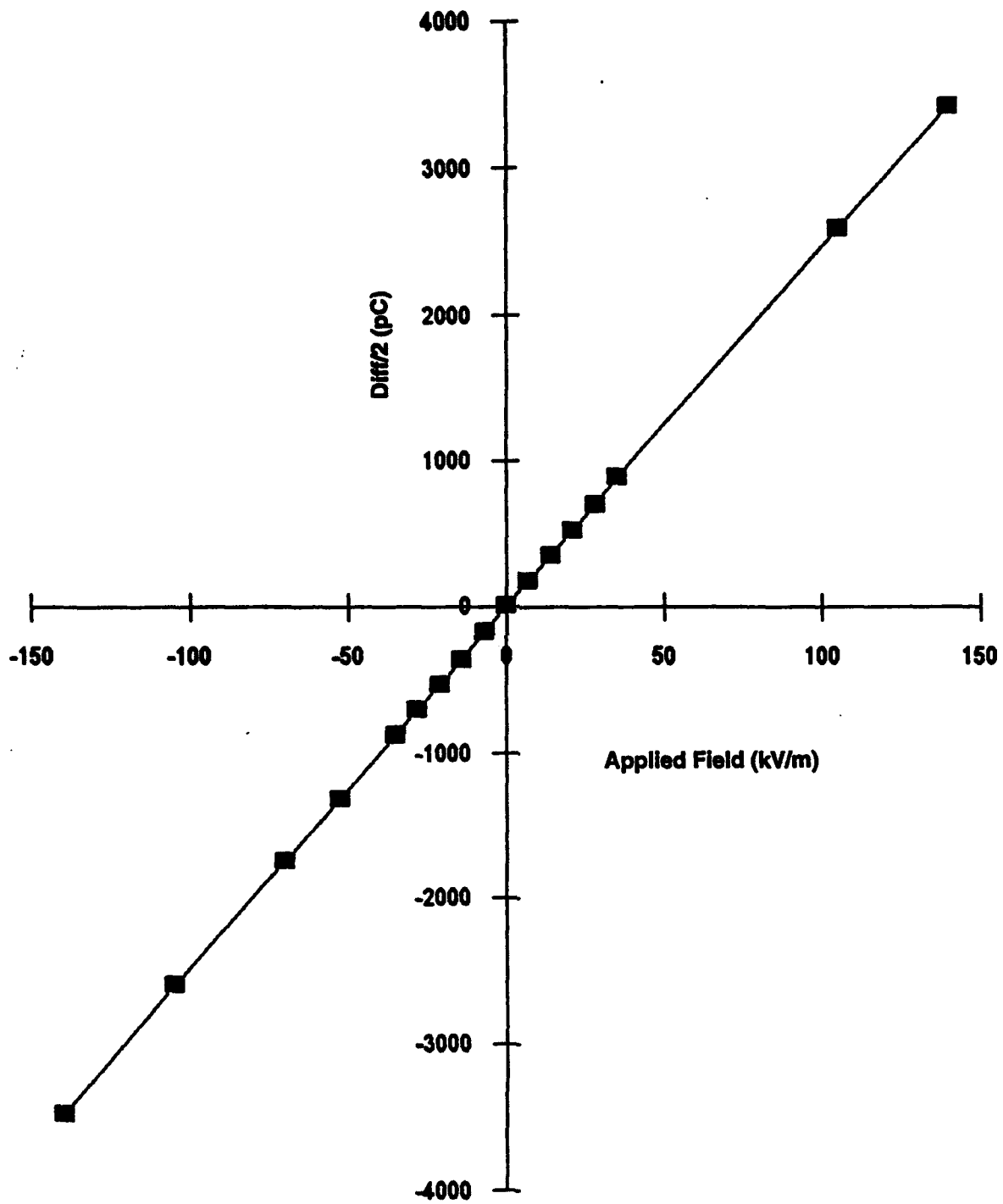
Figure 13. Average of DIFF/2 (proportional to transverse field) over all four pairs of mills versus applied transverse
field (E_y) in the calibration chamber

Notice that the normalized potential estimates (V/kV/m) from different stator pairs, while generally within a factor of 2, do not agree (except between the two "middle" pairs), suggesting that there may be a small longitudinal field in the chamber. The cause of such a longitudinal field is not clear, but as long as the net charge sensed by each pair of mills remains negligible, this should not affect our calibration. Notice also that the transverse-field coefficients (a_{iy}) are only slightly greater than unity, although the theoretical value for an infinite cylinder is exactly 2. The present values can presumably be explained by the facts that the nominal effective area used for our mills is certainly an over-estimate and that each mill averages the field over nearly 1/8 of the payload circumference. In any case, the same value of effective area has been used for the longitudinal-field coefficients (a_{iz}) as well. Thus, any error in this value affects only our estimates of the local fields at the mills and factors out of the calculation for ambient field. Finally, it seems clear that the transverse-field coefficients get slightly larger toward the nose of the rocket, which seems reasonable. This effect is unlikely to be due to fringing of the applied field in the chamber. Nevertheless, this may be stretching the accuracy of the data.

3.6 Summary of Calibration Matrix

Equation (5) summarizes the calibration coefficients, as best we know them from laboratory measurements (see also Equation (1)). The transverse-field coefficients in the first two columns of the calibration matrix are the "limited" averages found in Table 8, above. The third column contains averages of the longitudinal-field coefficients measured at each longitudinal position, from Willett et al.[1] (Section 6.2.2, Table 8 -- "payload protrusion" of 41 in). The fourth column repeats the overall average potential coefficients from Table 6, above.

$$
\begin{pmatrix} F_{tr} \\ F_{tl} \\ F_{mr} \\ F_{ml} \\ F_{br} \\ F_{bl} \\ F_{mb} \\ F_{mt} \end{pmatrix} = \begin{pmatrix} 0 & 1.045 & 3.84 & 4.393 \\ 0 & -1.045 & 3.84 & 4.393 \\ 0 & 1.034 & 2.39 & 3.998 \\ 0 & -1.034 & 2.39 & 3.998 \\ 0 & 1.033 & 1.41 & 3.854 \\ 0 & -1.033 & 1.41 & 3.854 \\ -1.034 & 0 & 2.39 & 3.998 \\ 1.034 & 0 & 2.39 & 3.998 \end{pmatrix} \begin{pmatrix} E_x \\ E_y \\ E_z \\ V \end{pmatrix} \tag{5}
$$

These values constitute our best estimate of the rocket calibration at the time of writing. Their self-consistency and absolute accuracy are evaluated during analysis of the flight data in Section 5.3.

4. TEST FLIGHTS INTO THUNDERSTORMS

The three REFS payloads described above were launched into thunderstorms from the West Knoll (elevation 10,400 ft MSL) at Langmuir Laboratory during July, 1992. Figure 14 shows the lay of the land The launch site was chosen so that the rockets could land inside the controlled area to the south and south-east of Langmuir, outlined in Figure 15, without overflying any occupied buildings. The fire-control, telemetry-receiving, and data-recording facilities were located

27

Figure 14. Topographical map of Langmuir Laboratory, showing the launcher (solid triangle) on West Knoll, the telemetry trailer (solid square) near the Comet Observatory, and the balloon winch (solid circle) near the balloon hangar
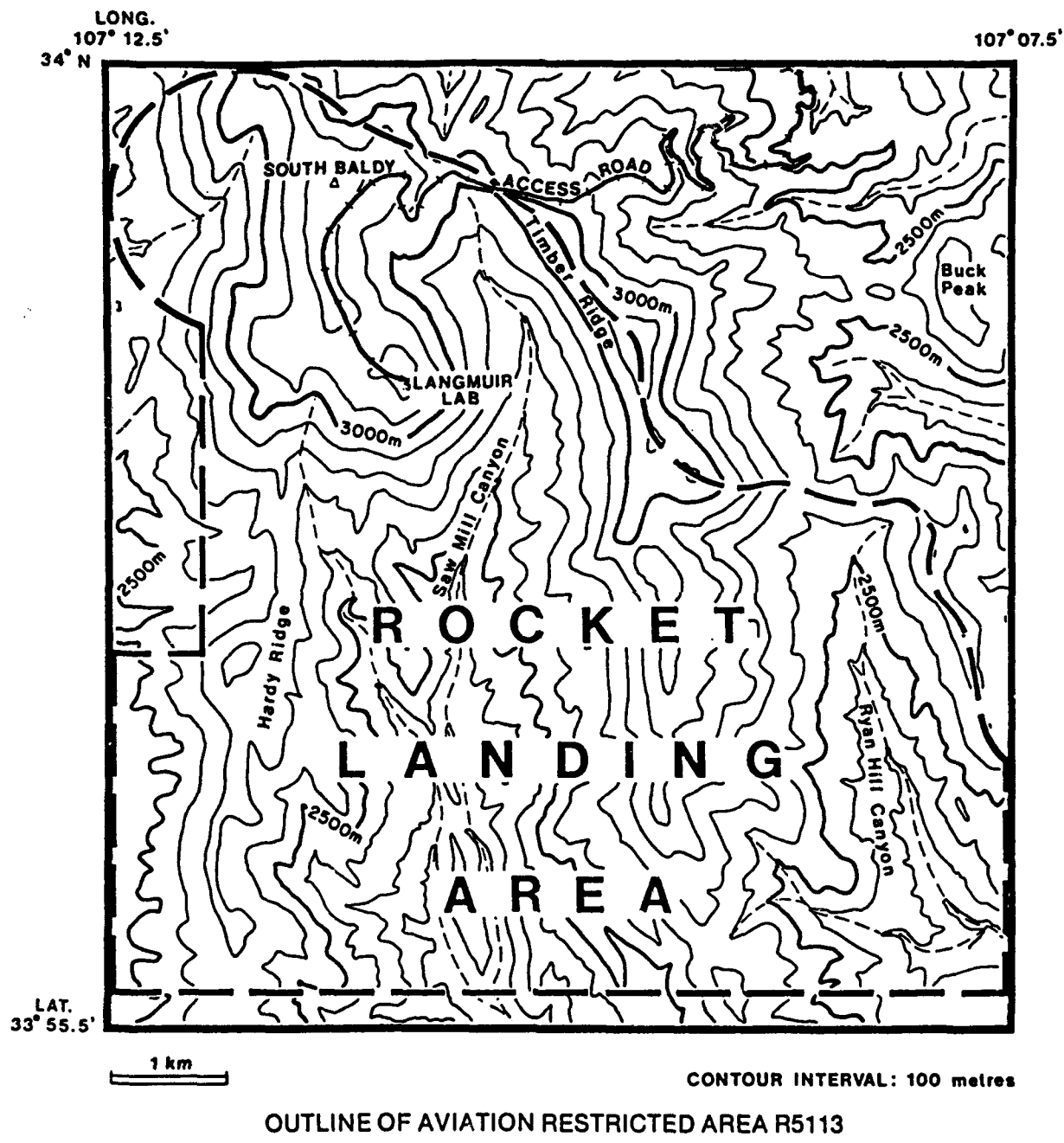
Figure 15. Topographical map of the Langmuir Lab rocket-landing area (heavy dashed line)

in a trailer on the ridge just south of the Comet Observatory, about 3000 ft NNE of the launcher. This location was chosen to be close to the plane of the trajectory, so that the tracking antenna would have to slew rapidly in only one axis, and to be far enough from the launcher that the slew rate would not be excessive. A discussion of the telemetry system and its performance can be found in Section 4.3.1 below. The payload was controlled and the rocket fired by a fiber-optic link between control trailer and launcher.

The launcher was elevated 80 degrees above the horizontal and aimed at azimuth 175 degrees true. Table 9 summarizes the flight times and apogee altitudes for the three flights. Notice that the first flight was shorter (60.8 s) and did not go as high as the second and third flights (66.5 and 66.8 s, respectively). This difference is believed to have been caused primarily by the differing cant angles of the fins mounted on the rocket motors. A discussion of the rocket trajectories and the effects of the canted fins can be found in Section 4.2 below.

Table 9. Basic Data on the July, 1992, Flights

Date	Ignition	Burnout*	Apogee		Impact**
(M/DD)	(MST)	(MST)	(MST)	(ft AGL)	(MST)
7/08	16:11:48.039	16:11:49.72	16:12:14.2	12,670	16:12:49.37
7/17	14:28:08.781	14:28:10.41	14:28:37.7	15,260	14:29:15.70
7/19	14:56:17.867	14:56:19.54	14:56:47.1	15,680	14:57:25.47

* Burnout is reckoned as the time of maximum deceleration.

** Impact is the time of signal loss, estimated at 10,400 ft MSL

The primary supporting data for these flights came from three ground-based field mills, the closest located on West Knoll a few tens of meters from the rocket launcher, and from tethered or free balloons carrying field meters of the type described by Winn et al. (Appendix)[2]. There is relatively little meteorological information available on the storms into which the rockets were launched, mainly because the Langmuir radar was not operational during July. These supporting data will be discussed in this report only to the extent that they bear on the validity of the rocket measurements (see Sections 5.3.3 and 5.3.4).

4.1 Payload Mechanical Performance

The modified motors shipped from Wallops Flight Facility to New Mexico for our use arrived with a different fin arrangement than expected. The fins on these motors were significantly smaller than those used for our previous tests, and concern arose about the smaller fin area reducing the stability of the REFS rocket. It was decided to change all the motors back to the standard-length fin. In addition to cannibalizing one pair of standard straight fins from a dummy motor, we were able to obtain from NMIMT some otherwise identical fins whose mounting surfaces had been machined to apply small amounts of angle of attack, or cant. These fins were available in two versions, canted nominally 1.0 or 1.5 degrees, and were intended to apply aerodynamic torque after motor burnout, maintaining rocket rotation throughout the flight. (The

exhaust nozzles of the standard 2.75 FFAR motor are "scarfed," or angled, to spin-stabilize the rocket during the burn phase.)

Table 10 compares several important properties of the rocket flights that were conducted at Langmuir Laboratory in 1992 to those of the Wallops Island flight in 1990. There were two flights with dummy payloads containing only telemetry transmitters on 3 and 6 July. The second of these showed that the flight was stable, although shorter in duration, with the 1.5 degree fins (actually measured to be canted 1.68 degrees). Based on this result, it was decided to fly the first REFS payload with these fins. The flight on 8 July showed that this fin cant caused the vehicle to spin too fast, so the remaining flights were made with 1.0 degree fins (actually measured to be canted 0.87 degree).

Table 10. Flight Data Summary

Launch Date	Cant (deg.)	Accel. Max (G's)	Burn Time (s)	Flt. Time (s)	Super- sonic (T+s)	Sub- sonic (T+s)	Alt. Max (ft AGL)	Rotation Rate Max (RPS)
5/11/90	0	?	1.5	61	0.85	4.45	12936	17
3/7/92	0	N/A	N/A	70	N/A	N/A	N/A	N/A
6/7/92	1.68	N/A	N/A	59	N/A	N/A	N/A	N/A
8/7/92	1.68	39	1.65	61.0	0.8	4.40	12670	28.5
17/7/92	0.87	41	1.60	66.6	0.8	5.68	15260	20.0
19/7/92	0.87	45	1.67	67.1	0.8	5.52	15680	18.2

An interesting aspect of these flights is the amount of rotation imparted to the rockets by the canted fins. Figures 16, 17, and 18 compare rotation rates among all four REFS flights. As could be expected, the rockets with more fin cant had higher rotation rates throughout their flights. The 17 and 19 July launches used the same fins and showed nearly the same rotation rates, while the 8 July flight spun fastest, and the original Wallops Island flight -- with straight fins -- nearly stopped rotating and may even have reversed direction in mid-flight.

The outer shell, or rotor, of the REFS payload acts as a shutter for the electric-field mills. This shell is driven by an electric motor geared to achieve a no-load rotation speed of about 15 RPS. The shell's rotation is in the same sense as the rocket's during flight. It was therefore expected to see a reduction in speed of the shell during the burn phase of the flight, while the scarfed nozzles were applying torque. Figures 19, 20, 21, and 22 graphically depict the shell's response during the four flights. A rapid loss of rotational speed occurred during the burn phase. Immediately after motor burnout, the shell regained much of its initial rotation rate. Various fluctuations in the rotation rate during the remainder of the flights are still unexplained. These variations might be due to changes in the vehicles' angle of attack or to temperature changes with altitude.

Rocket Rotation Comparison
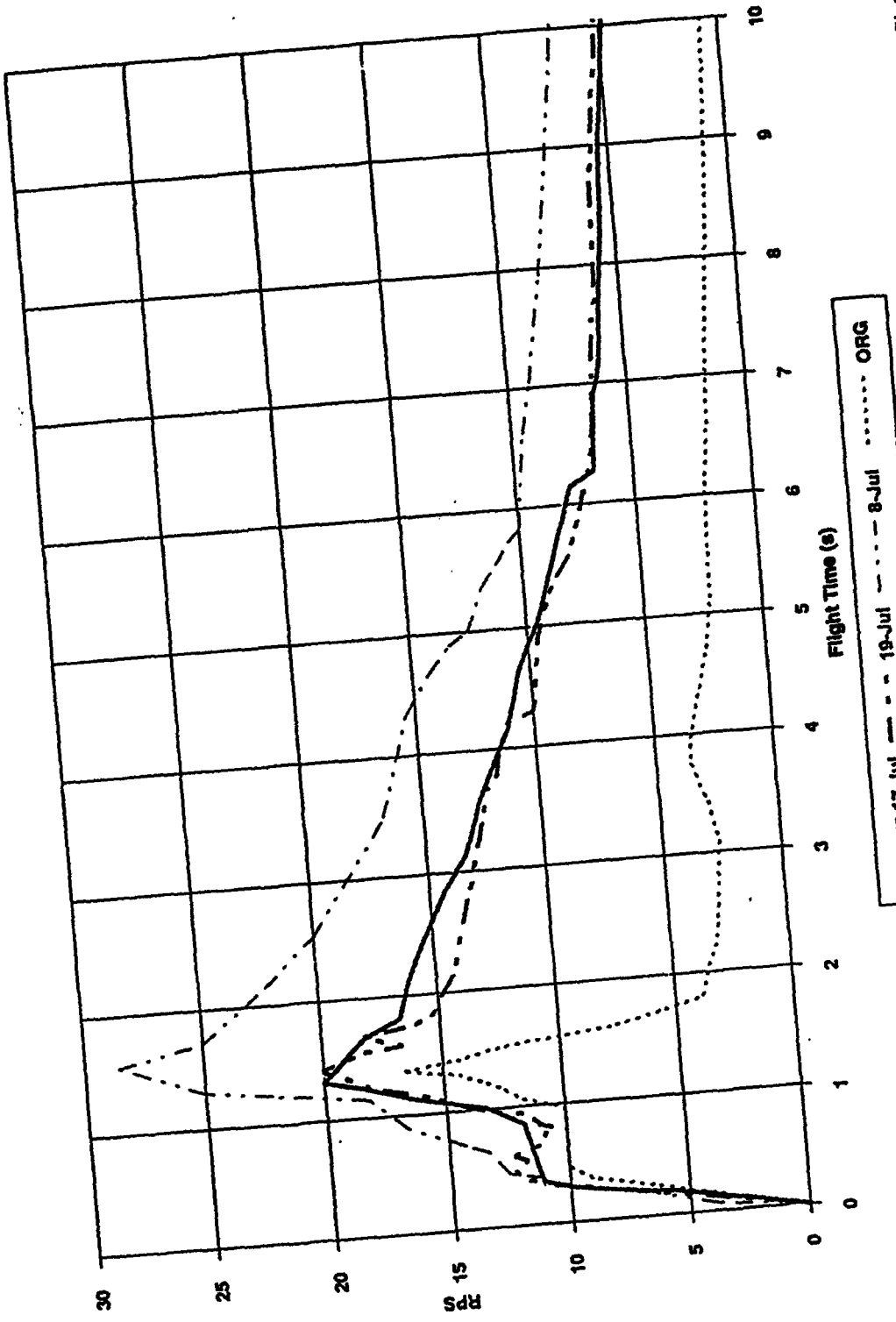
Figure 16. Rocket-rotation rate in revolutions per second, obtained from the magnetic-field sensors, versus time for the first 10 s of each REFS flight. The thin dot-dashed curve is for the 8 July flight at Langmuir Laboratory with nominal 1.5 degree fin cant. The thick solid and dot-dashed curves apply to the 17 and 19 July flights, respectively, with nominal 1.0 degree fin cant

32

Rocket Rotation Comparison
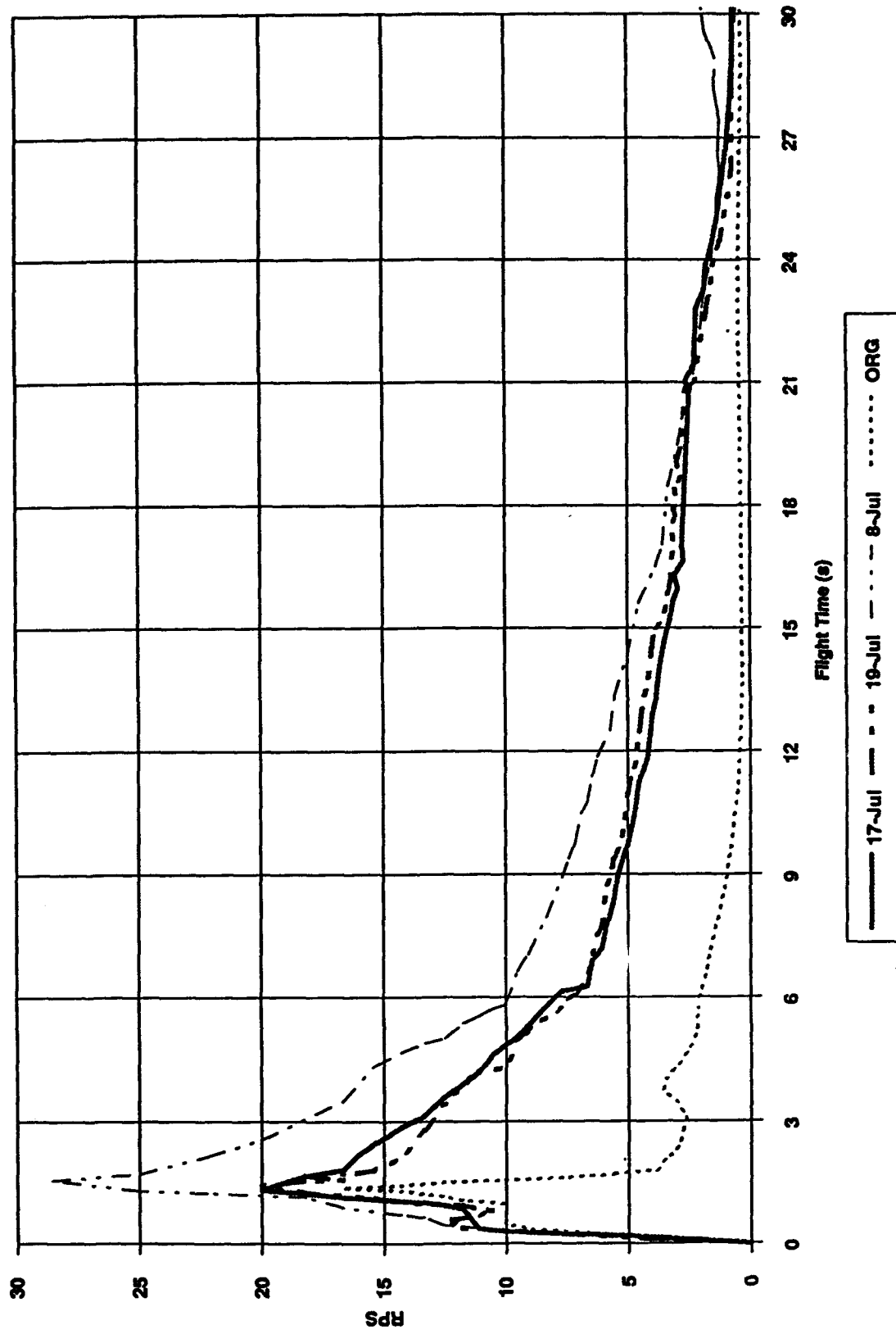
Figure 17. Similar to Figure 16 for the first half of each flight

33

Rocket Rotation Comparison
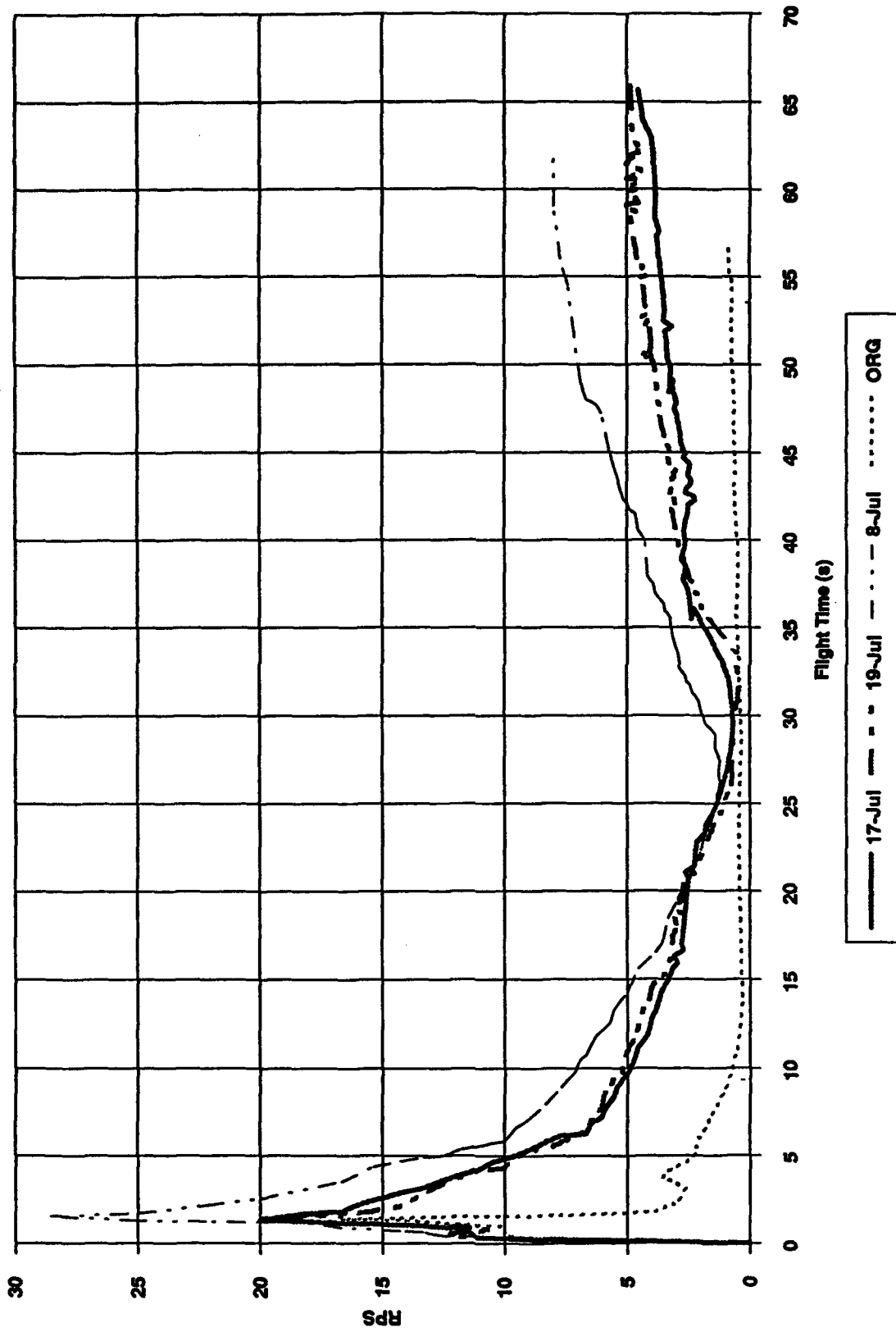
Figure 18. Similar to Figure 16 for the entire flights

34

Shell Rotation Comparison
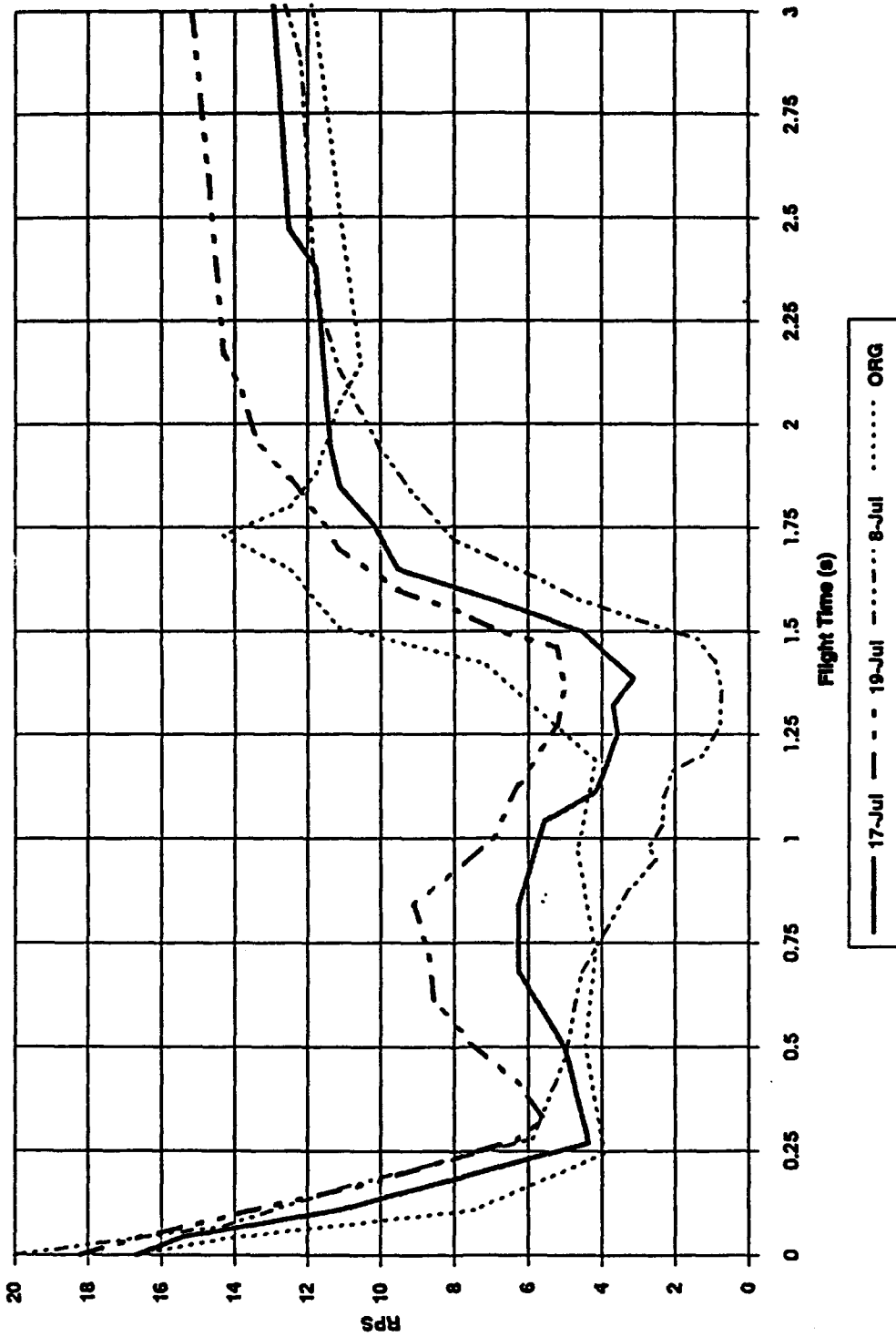
Figure 19. Shell rotation rate in revolutions per second, obtained from the optical detectors, versus time for the first 3 s of each REFS flight. Otherwise similar to Figure 16

35

Shell Rotation Comparison
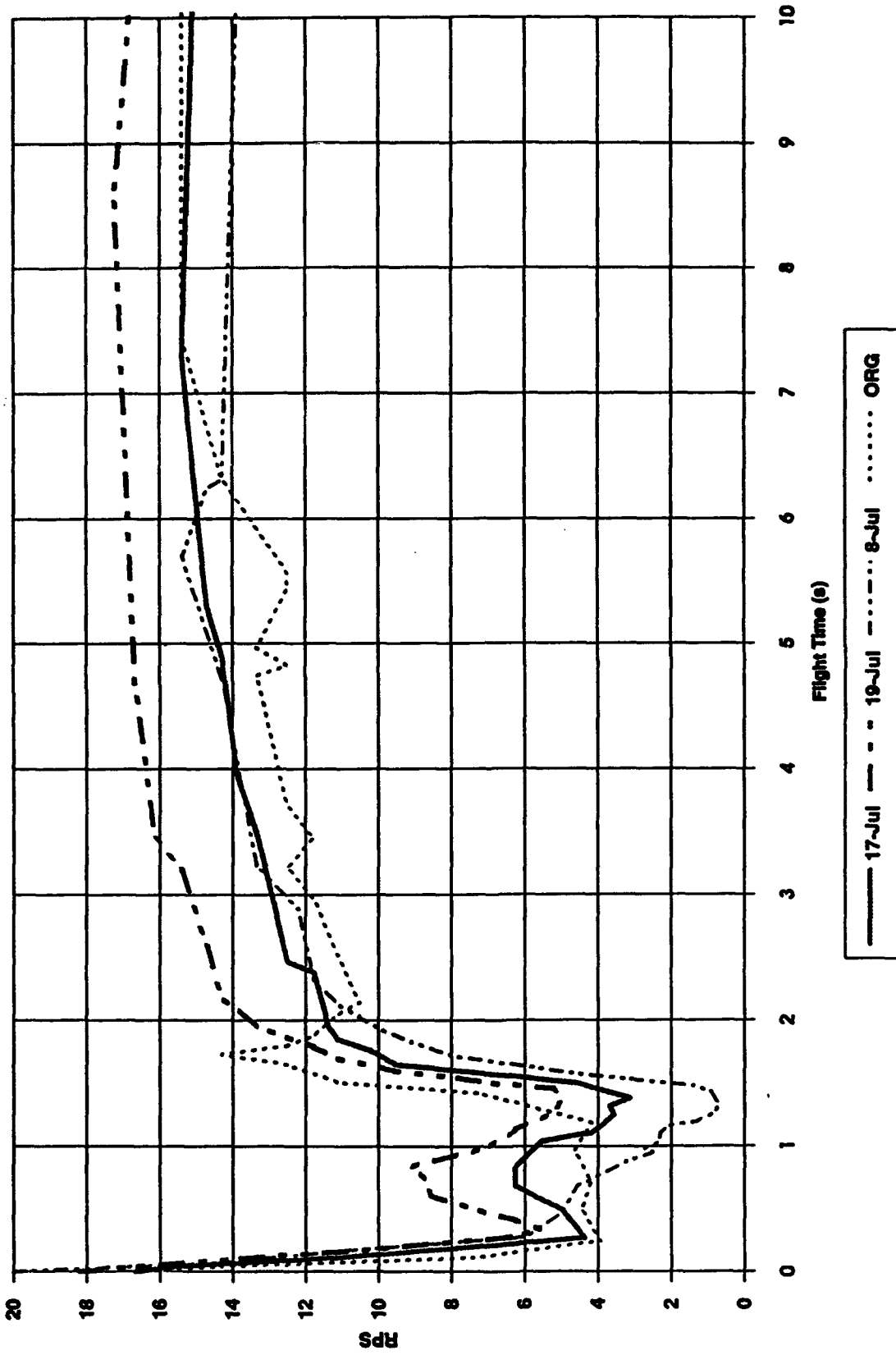
Figure 20. Similar to Figure 19 for the first 10 s of the flights

36

Shell Rotation Comparison
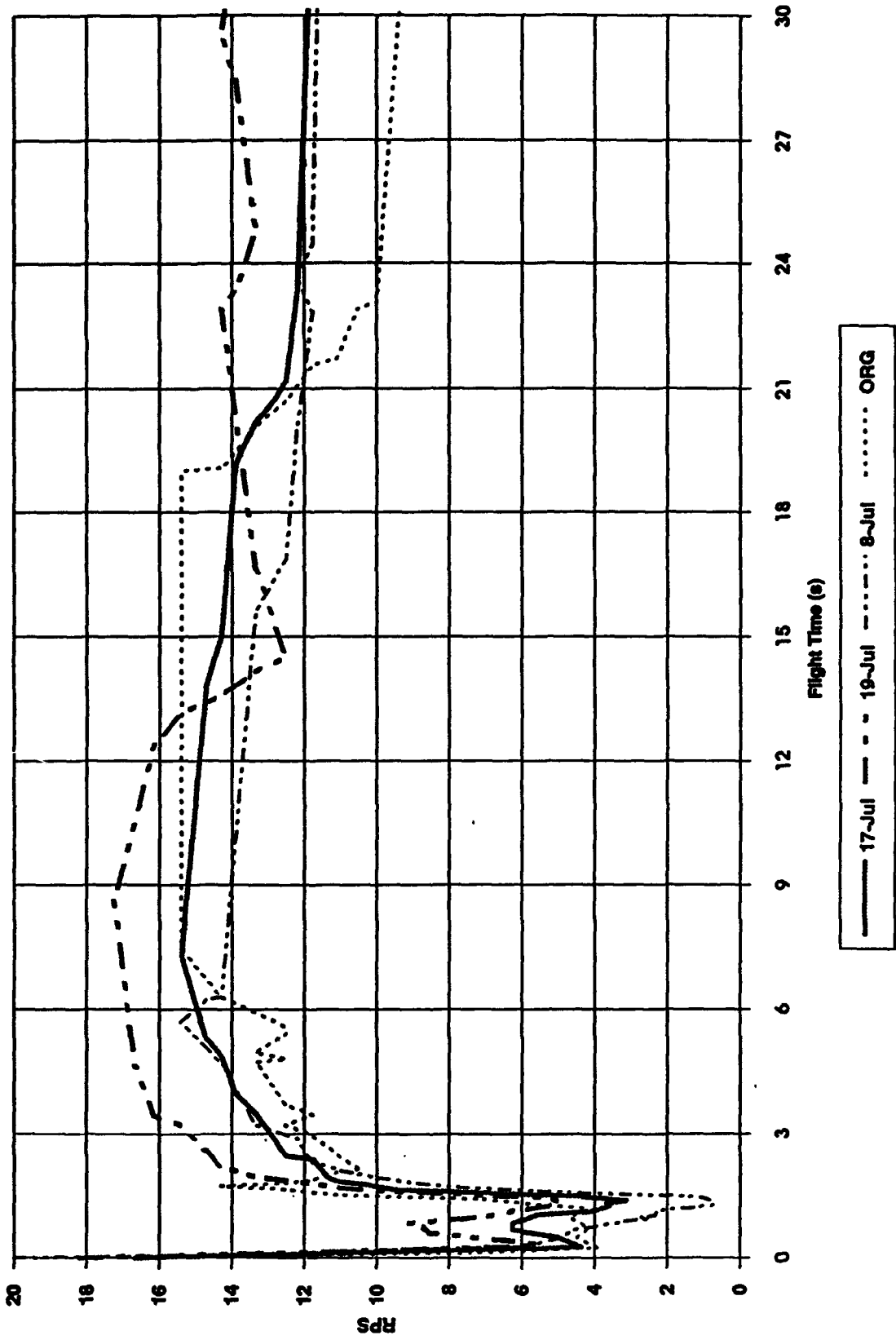
Figure 21. Similar to Figure 19 for the first half of each flight

Shell Rotation Comparison
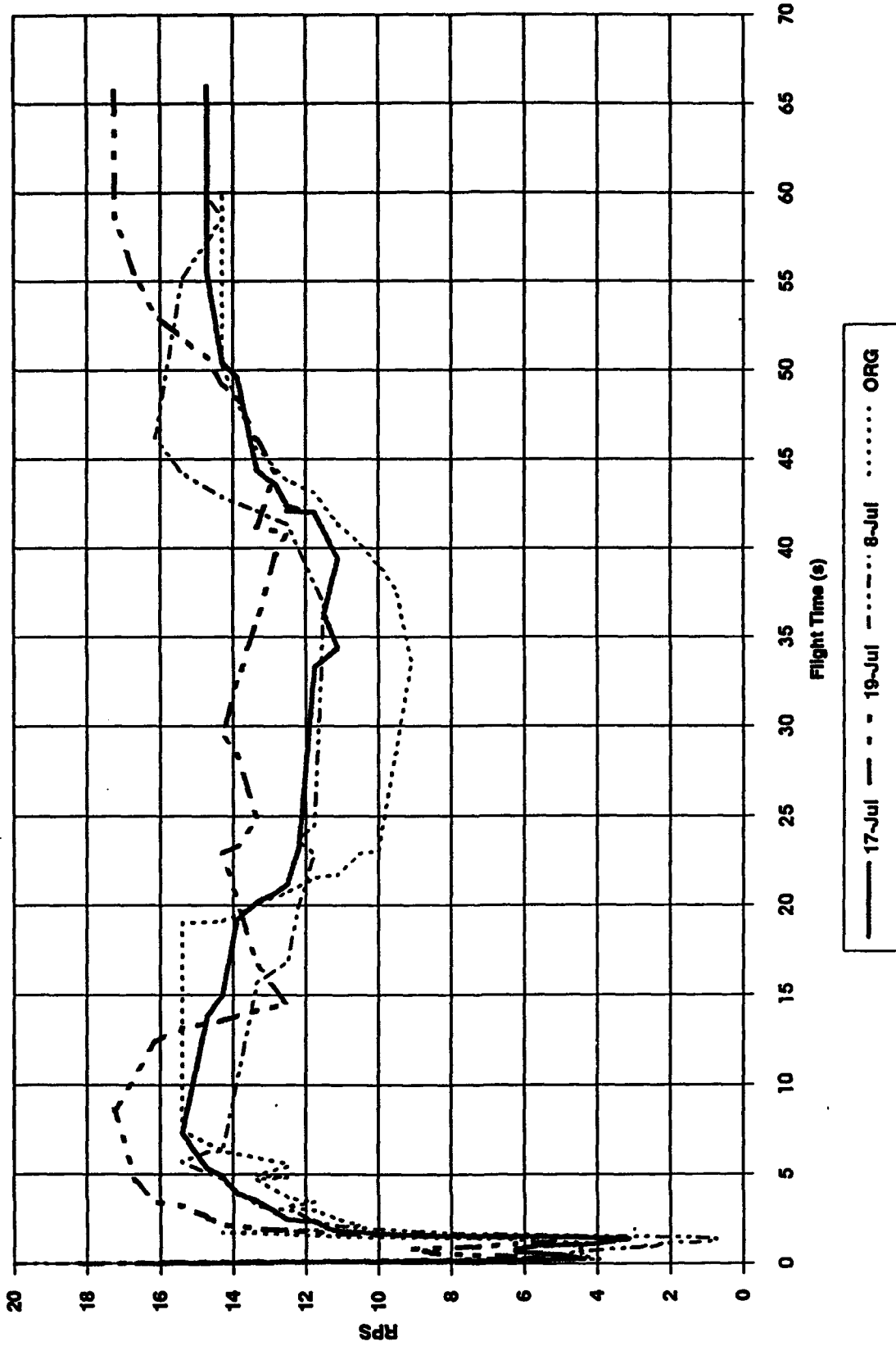
Figure 22. Similar to Figure 19 for the entire flights

4.2 Trajectory Analysis

The utility of an electric field measurement is closely tied to the correct identification of the position of the measurement. It was, therefore, discouraging that the original REFS trajectory was not very close to preflight predictions[1]. In the period prior to, during, and after the Langmuir Laboratory launch series, attempts were made to improve the aerodynamic model, as described in Section 4.2.3 below. In spite of those attempts, the improvement was not sufficient for accurate position determination. There was also an unsuccessful attempt to estimate position from the on-board accelerometers, as described in Section 4.2.2 below. To provide a timely, yet reasonably accurate, approximation of the trajectories, a scheme was developed to scale the output of a simple trajectory model to the known flight data. That model is described in the next section.

4.2.1 APPROXIMATE MODEL

Since site observations indicated that the trajectories remained essentially planar, a two-dimensional coordinate system known as the "wind axes coordinates" was used to describe the motion (Hankey).[3] This model incorporates the assumption that all forces are in-plane. It was further assumed that the rocket remained aligned with the velocity vector, which resulted in the alignment of the thrust vector with velocity and the absence of lift. This model, then, ignores known periods when the angle of attack is non-zero. However, to the best of our knowledge, the only significant angle of attack is induced by cross wind over the launch tube, and this is predicted to damp out within 2 seconds. The missile is very stable in pitch and yaw and is predicted to respond to an angle of attack by spiraling into alignment with moderately damped oscillations.[4] Gusts and wind shear associated with the thunderstorm environment could initiate later periods of oscillation, but these should also damp out rapidly.

An existing computer program implemented the wind-axis model, a standard-atmosphere table, and all of the other physics required to correctly model two-dimensional flight around a spherical Earth. Admittedly, this is overkill for the REFS missile, but it was available and easy to use. The coordinate system shown in Figure 23 remains attached to the velocity vector, which rotates about an inertial coordinate system at a rate equal to the rotation of the vehicle about the center of Earth plus the rotation of the vector about the local horizon. This is the algebraic difference of the change to the angles γ and θ shown in Figure 23. When Newton's Law is correctly applied to this coordinate system, the following equations result:

$$\frac{dV}{dt} = \frac{T}{m} - \frac{D}{m} - \frac{\mu}{r^2} \sin \gamma \qquad (6)$$

$$\frac{d\gamma}{dt} = -\frac{\mu}{r^2} \cos \gamma + \frac{V}{r} \cos \gamma \qquad (7)$$

where: V = Magnitude of velocity

T = Thrust

D = Drag

39
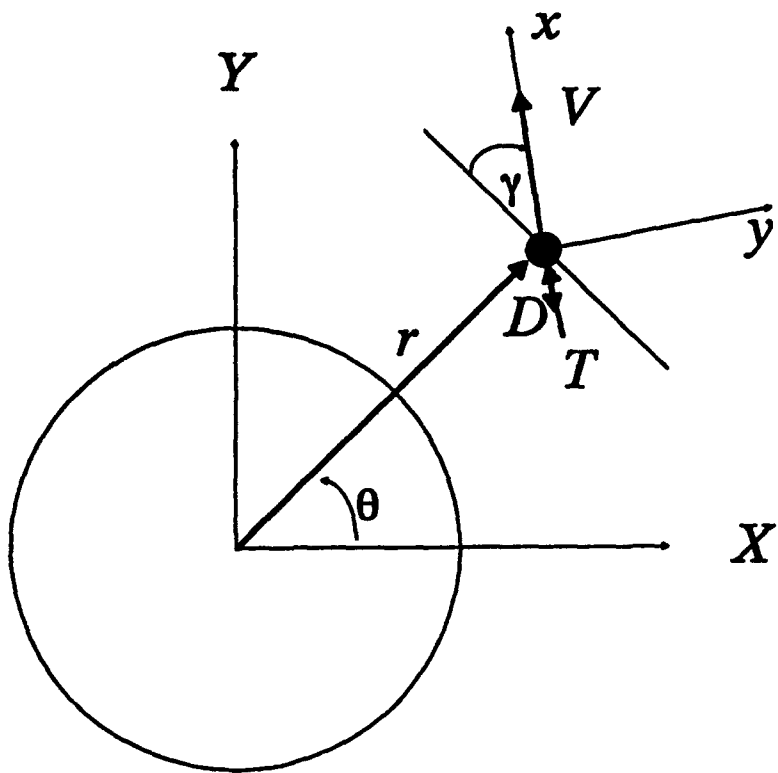
Figure 23. Wind-axis coordinate system. The x-axis of the lower-case (non-inertial) coordinate system remains aligned with the velocity vector, V. the flight-path, γ, is the angle relative to the local horizon. The angle θ is measured relative to the X-axis of the upper-case (inertial) coordinate system, whose origin is at the center of Earth

m = Mass

r = radius from center of Earth

t = time

μ = universal gravitational constant

Altitude and range are computed with the additional equations:

$$\frac{dr}{dt} = V \sin \gamma \qquad (8)$$

$$r \frac{d\theta}{dt} = V \cos \gamma \qquad (9)$$

The altitude is the magnitude of the radius vector minus the magnitude of the radius at the surface. If changes to r are not large compared to the radius of the Earth, which is especially true for the REFS missile, then r(dθ/dt) is the down-range velocity, which is integrated to provide range.

The system of equations was solved using the software applications package, Advanced Continuous Simulation Language (ACSL), produced by Mitchell & Gauthier Associates of Concord, Massachusetts. This package solves ordinary differential equations in a manner that requires only a modest knowledge of numerical analysis. The equations and parameters that model the system are expressed using FORTRAN-like statements and solved using one of several integration options. Tabular and graphical output are easily produced.

A copy of the REFS ACSL model is listed in Appendix A. The parameters and tables in this model reflect the best preflight estimates for the REFS system. For no-wind, fully-nominal launch conditions the results are identical to those of the more complex, six-degree-of-freedom model used by Willett et al.[1] As before, the drag tables were obtained from the program "The USAF Automated Missile DATCOM * Rev 7/89" for a missile configuration that actually did not match the "as flown" REFS configuration very well. Conspicuously absent were the fiber-glass rings associated with the corona-point assembly (see Section 2.4) and the canted fins (see Section 4.1).

The technique used to predict a reasonably accurate trajectory was to scale the nominal trajectory to match two of the known experimental results, apogee altitude (determined from the pressure sensor) and apogee time (determined from both pressure and acceleration measurements) for each flight. The procedure was to increase the drag in the model (using a drag-multiplication factor, CdFac, applied to the entire drag table) until the maximum altitude of the flight was correct. This invariably resulted in a predicted flight time that was shorter than observed. To some extent, the dual agreement could be improved by adjusting the initial flight-path angle (launch elevation) along with the drag multiplier; however this was not done. Instead, a trajectory with the correct apogee was arbitrarily "stretched" along the time axis until predicted and actual apogee times coincided. Since this also resulted in a nearly correct time of impact, the scheme was deemed usable.

A drag-multiplication factor of 1.65 and time-stretching factors of 1.062 and 1.074 yielded a good match for the flights with a fin cant of 0.87 deg. (17 and 19 July, respectively). Drag- and

41

time-multiplication factors of 2.25 and 1.078, respectively, yielded a good match to the flight with 1.68 deg. fin cant (8 July). The effect of these drag-multiplication factors is shown in Figure 24. The predicted altitudes, ranges, and times (before time stretching) for the nominal and drag-multiplied predictions are compared with the observed data in Table 11.

Table 11. Comparison of Predicted and Observed Trajectories

Trajectory	Apogee (MSL)			Impact	
	Time (s)	Range (ft)	Alt. (ft)	Time (s)	Range (ft)
Nominal:					
Predicted	32.0	7,054	30,213	70.5	12,800
0.87 deg. cant:					
Predicted	27.2	5,160	25,530	62.1	9,005
17 Jul 92	28.9	--	25,664	66.9	--
19 Jul 92	29.2	--	26,084	67.6	--
1.68 deg. cant:					
Predicted	24.3	4,190	23,080	57.2	7,130
08 Jul 92	26.2	--	23,071	61.3	--

4.2.2 ACCELEROMETER DATA ANALYSIS

The aforementioned simplified trajectory model forms the basis for the determination of a trajectory from the single-axis accelerometer data collected during the flights. An accelerometer, depicted as an instrumented spring in Figure 25, measures the force response of a test mass to gravity and acceleration:

$$m \frac{dV}{dt} = \mathbf{F}_a + \mathbf{W} + \mathbf{F}_s \tag{10}$$

where $\mathbf{F}_a$ is the force applied by the spring (and measured by the accelerometer), $\mathbf{W}$ is the weight of the mass, m, and $\mathbf{F}_s$ is the (irrelevant) side force that constrains the mass. This equation applies to the velocity relative to an inertial frame, so the equation must be corrected for the rotation of the rocket in the same manner that was used to generate Eqs. 6 and 7. Since $\mathbf{F}_a$ is entirely in the x-direction and perpendicular to $\mathbf{F}_s$, we can write the x-component of Eq. (10), with reference to Figure 25, as follows:

$$m \frac{dV}{dt} = F_a - W \sin \gamma \tag{11}$$

42
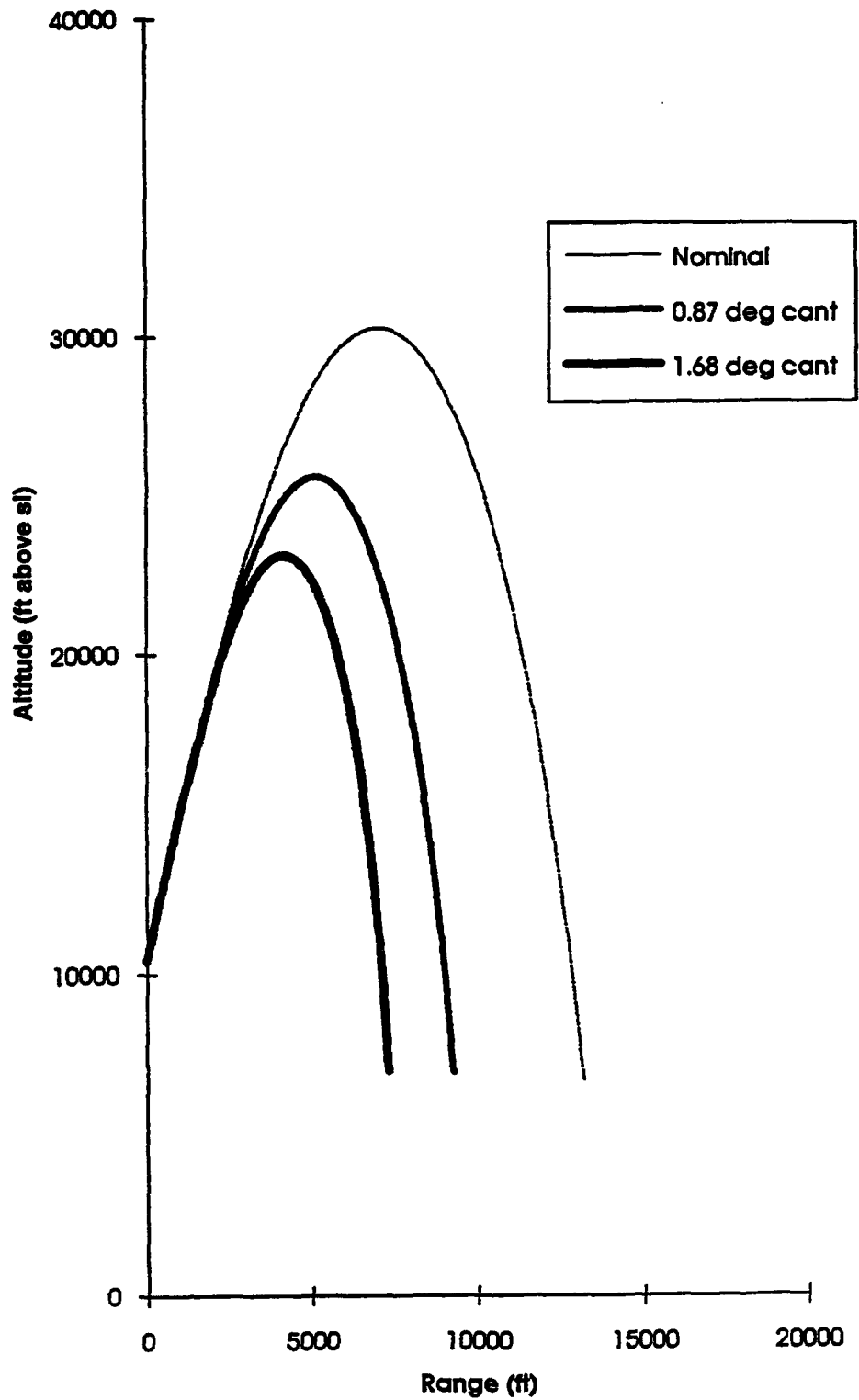
Figure 24. The nominal trajectory is compared to the two trajectories computed with drag increased to match the apogees achieved by rockets with fin-cant angles of 0.87 and 1.68 degrees. The "1.68 deg. cant" trajectory represents our best estimate of the actual trajectory followed by the sounding on 8 July, whereas the "0.87 deg. cant" trajectory represents our best estimate of those on 17 and 19 July

43
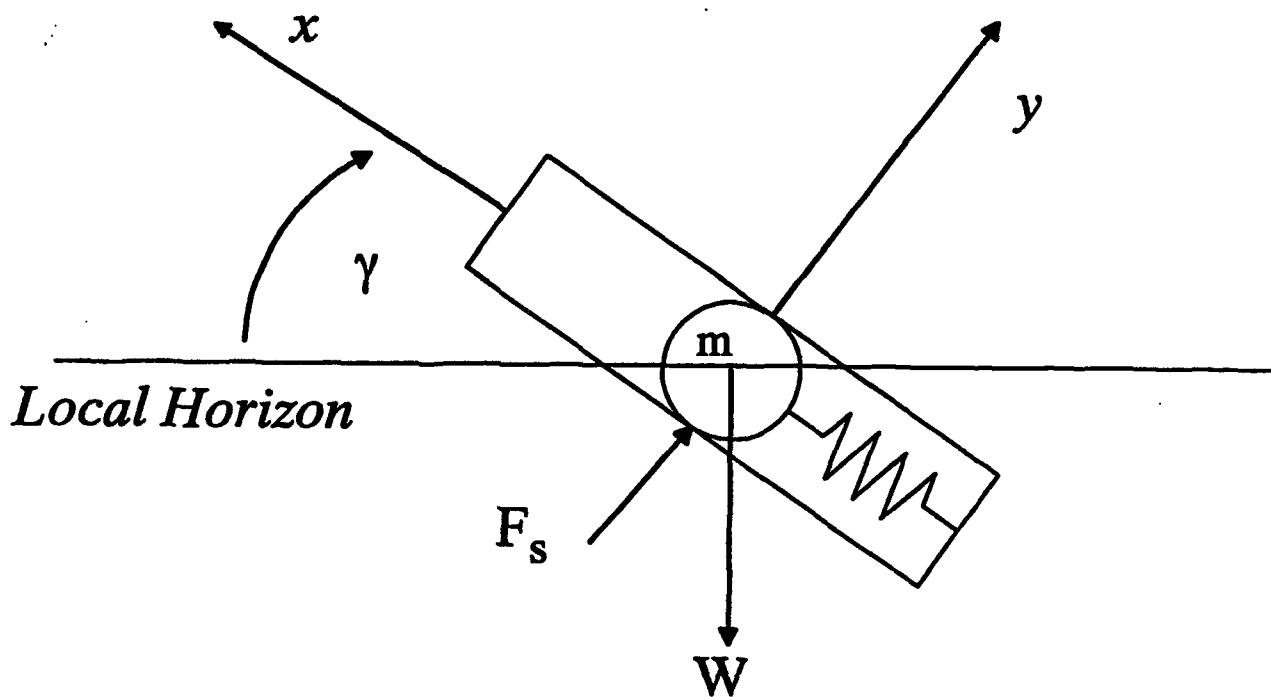
Figure 25. Schematic of an accelerometer in wind-axis coordinates. Weight, W, and side force F_s are shown. Not shown is the axial force, F_a, exerted by the spring on the test mass, m. The coordinate axes and angles correspond to those in Figure 23

Assuming the output of the meter is proportional to F_a/m, and substituting mass times gravitational acceleration, g, we have the equation which is used to decouple acceleration from the accelerometer output:

$$\frac{dV}{dt} = \frac{F_a}{m} - g \sin \gamma \tag{12}$$

The above equation is also used to calibrate the accelerometer. By using several orientations with respect to horizontal and by varying the acceleration environment, calibration curves are generated.

Presumably the acceleration of the rocket is the same as that of the test mass, so velocity can be determined using the relationship:

$$V(t) - V_0 = \int_{t_0}^{t} \frac{dV}{dt} \cdot dt' \tag{13}$$

Since the flight-path angle must be available on a continuous basis for Eq. (12), Eqs. (7), (8), and (9) must be integrated simultaneously with Eq. (13) to predict the trajectory.

When this procedure was applied to the REFS accelerometer data from the flight of 17 July, the result was the distorted trajectory shown in Figure 26. The distortion was caused, in part, by the fact that the accelerometers did not have the proper sensitivity for this calculation. They had a maximum range of 200g's. The rockets had a maximum acceleration of only 40g's and spent most of the flight between plus and minus 1g; therefore, for most of the flight, the signal was lost in the noise of the instrument. In future REFS designs, it would be desirable to have an accelerometer that is robust enough for the 40g launch, yet sensitive enough for the rest of the flight. A second possible reason for the distortion is that the actual trajectory was too complex for the planar, wind-axis coordinate system.

4.2.3. AERODYNAMIC-MODEL IMPROVEMENTS

As evident in Table 11, preflight analysis seriously over-predicted the maximum altitude. In subsequent analysis it was discovered that the fiberglass rings associated with the corona-discharge assembly were not included in the original analysis. These rings were added without consultation with the aerodynamic staff. Step increases and decreases in cross sectional area are a direct violation of "area rule" conventions, resulting in very high wave drag in the transonic and supersonic portions of the flight. Such step changes are never used in aeronautical design, and violate the assumptions implicit in the available drag-prediction programs. The drag on REFS in the transonic/supersonic regime must have been at least double the earlier prediction. Changes have already been incorporated into the REFS design to eliminate this problem in future fabrication.

Inspection of Table 10 in Section 4.1 reveals that increasing fin-cant angle had a systematic effect on the flight characteristics, also increasing the drag over that used in the pre-flight analysis. In addition to the three REFS launches, there were two launches with dummy payloads,

45

Altitude vs Range
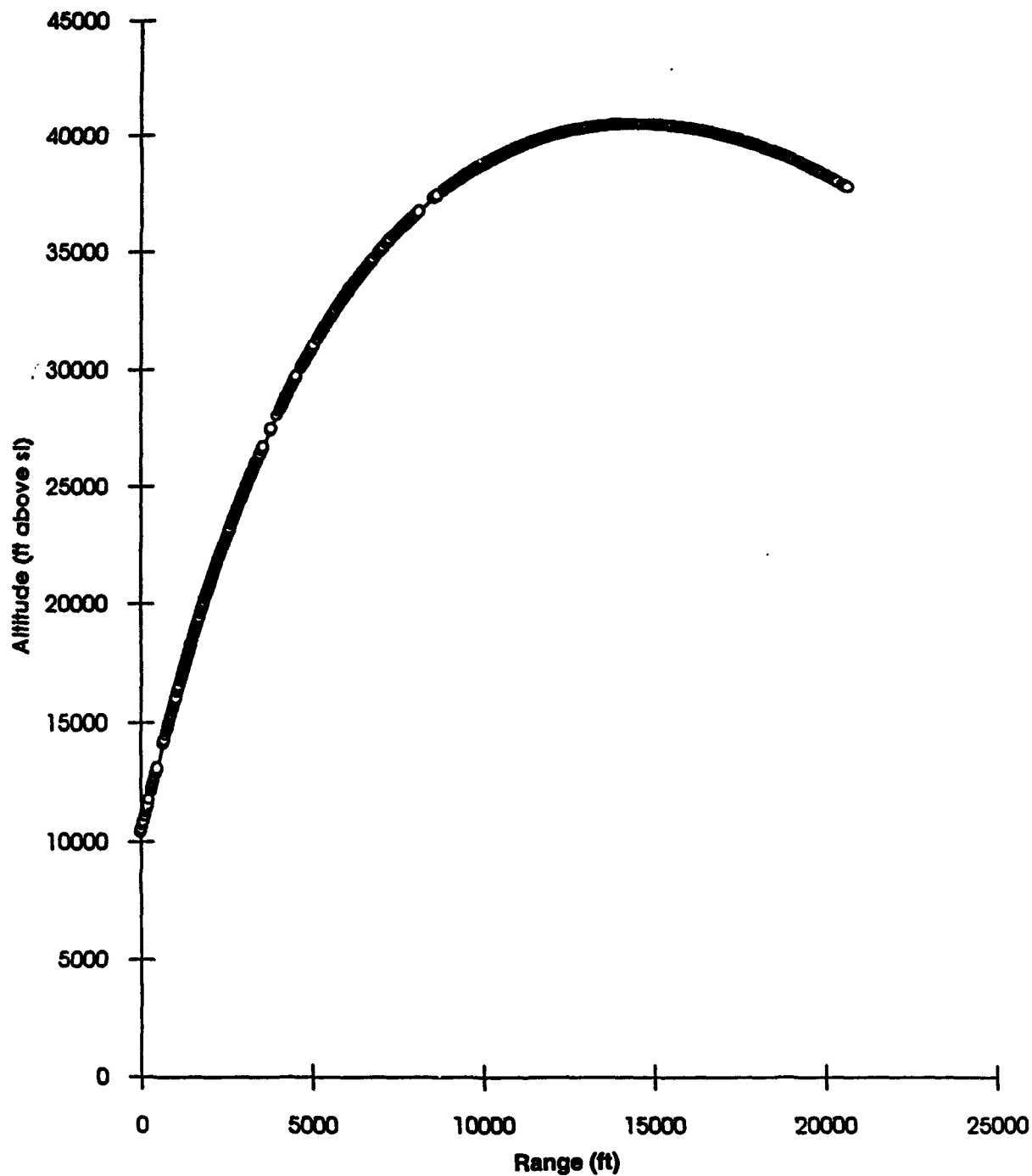
Figure 26. Trajectory deduced from the accelerometer output alone for the flight of 17 Jul 92. The calculation takes the rocket so high that it is still at a very high altitude at the time of impact. Possible reasons for this discrepancy are inaccuracy in the accelerometer output and failure of the wind-axis model to properly account for out-of-plane motion

46

which matched the REFS payload in weight and center of gravity and contained transmitters to verify telemetry reception, at Langmuir Laboratory in 1992. The dummy rocket with straight fins launched on 3 July had the longest flight time. The payload launches of 17 and 19 July, with intermediate fin-cant angle, had reduced flight time. The payload launch on 8 July and the dummy with the same high fin-cant angle that was launched on 5 July had the shortest flight times. The measured maximum altitudes of the REFS flights on 8, 17, and 19 July show that the longer flights also had higher maximum altitudes, confirming the presumed relationship between drag and fin cant. This is consistent with expectations based on induced drag and transonic effects, which are discussed briefly below. The original REFS missile launched at NASA/Wallops Flight Facility in November, 1990, had no fin cant, but it was launched at sea level, so it cannot be directly compared to the Langmuir Laboratory data.

Figure 16, in Section 4.1, shows the rotation of the original REFS rocket, and that of the launches of 8, 17, and 19 July, 1992, during the first 10 seconds of flight. If the fin cant of the original was actually zero, then its rotation should have reversed direction eventually, due to the negative torque from the rotating shell. The rockets launched on 17 and 19 July had enough fin cant to overcome the shell torque and maintain a positive spin throughout the flight. The fin torque also added to the rocket-motor torque during burn to produce a higher maximum spin rate than the original as well as a higher spin rate throughout the flight. The rocket launched on 8 July had an even higher maximum and sustained spin rates, as expected. Note also the interruption of the increase in spin rate from around t + 0.5 s to about t + 1 s. This period coincides with the transonic region of the flight, when the wave drag dramatically increases total drag.

In an attempt to quantify the increased drag due to the canted fins, more complex models were formulated that included induced drag over the spinning fins, especially when the fins were in critical (transonic) flight regimes. The total flow velocity over the fins is the vector sum of the free-stream velocity and the tangential velocity due to spin. Therefore, the faster the spin, the sooner the fins enter transonic flight and increase the wave drag. Except for the initial spin-up and decay, the fins are probably at a slightly positive average angle of attack to counter the reverse torque of the shell rotation and skin friction. For this period there is additional drag induced by the lift of the fins. The higher the spin rate, the higher the skin-friction resistance, requiring higher angle of attack and induced drag.

Any improved analysis of the fin effects is complicated by the fact that the fins can swing freely on their pivots, so that the sweep angle after exiting the launch tube can vary from near 0 degrees to a maximum of about 45 degrees, depending on the interaction of the centripetal acceleration and the drag on the fins. Suffice it to say that, after several attempts, a more accurate model of the system could not be accomplished in time for this report. In fact, it was concluded that manufacturing tolerances and aerodynamic uncertainties were such that the preflight trajectory predictions may never be accurate enough to use for electrostatic-field location. Future efforts should consider the acquisition of accurate position data along with electric- and magnetic-field information.

4.3 Payload Electrical Performance

4.3.1 TELEMETRY SYSTEM -- DROP-OUTS

The prime receiving system was an OSU Mini Tracker, a transportable system designed and fabricated by Oklahoma State University. It consisted of a free-standing pedestal with a 4 foot dish. The dish has 190 deg of elevation and +/- 360 deg of azimuth swing. The tracker is capable of 30 deg/s motion and 100 deg/s^2 acceleration. The antenna has a monopulse converter feed with an internal preamplifier. The dish provides a 3 dB beam width of about 7 degrees. The monopulse converter is an array of 4 dipole antennas located slightly off center. These antennas are scanned in sequence. As they are scanned, the converter output becomes amplitude modulated. This modulation provides the basic error signal necessary for tracking. A single coaxial cable brings the signal to a Scientific Atlanta receiver. The AM output of the receiver is demodulated to provide error signals to drive the tracker. The system can be operated in a manual or an auto-track mode. A TV camera was mounted to the edge of the dish. The camera was bore-sighted to the antenna pattern, providing a visual indication of tracking performance.

A second antenna, a horn, was also used. It had a 3 dB beam width of about 45 degrees in each axis. This was a fixed-position antenna aimed to cover the lower part of the expected trajectory, where the risk of losing track with the Mini Tracker was greatest. The output of a preamplifier at the horn was fed to a Microdyne receiver.

Data from the two receivers were recorded on direct (as opposed to FM) channels of a Honeywell 101 instrumentation tape recorder. This recorder had 7 tracks. Each receiver output was fed to a "bit sync," an instrument designed to clean up the noisy signal from a telemetry receiver and produce a digital PCM output. The raw data as well as the bit-sync data from each receiver were recorded. The other 3 tracks were used to record time code (on an FM channel) and two ground-based instruments. The field mill at West Knoll was successfully recorded on a second FM channel. The remaining direct channel was allocated to an unsuccessful attempt to measure "fast field changes" associated with upward leaders in rocket-triggered lightning.

There were several telemetry problems unique to this rocket series. When launching from a mountain ridge, one has limited locations to put things. The grounds of Langmuir Laboratory have several high points, as illustrated in Figure 14. The main laboratory building is on one. The launch site was located on another -- West Knoll. The telemetry site was on a third, close to the Comet Observatory, lying near the plane of the planned rocket trajectory. There was a canyon between the telemetry site and the launch site. The telemetry site was about 250 feet above and 3000 feet away from the launch site. The antenna pedestal was set up with a 3 degree tilt toward the launch site. This was necessary to be able to point down at the launch site with travel to spare.

Problems were encountered with multipath -- reflections off the ground on both sides of the canyon. The dish antenna was moved to a location that provided a minimum opportunity for reflection at the receiving end. There was not much that could be done about reflections near the launcher.

Probably the most important problem was that the small rockets used for these measurements have very high accelerations. Because of the short launcher-tracker separation forced on us by the terrain, the calculated angular acceleration and velocities during the first few seconds were at the advertised limits of the tracker. This, coupled with the multipath also caused by the terrain, suggested that the tracker might have difficulty following the vehicle off of the launch pad.

Because of the marginal situation, two test launches were made with dummy transmitters as the only instrumentation. The tracker was unable to track the first launch from an initial orientation pointing at the launcher. A manual repointing of the antenna was able to establish auto track after about 15 seconds, however, and tracking was maintained for the remainder of the flight.

This failure led to the development of a new strategy. For the second test flight, and for all the data flights, the tracker was initially aimed up at 45 degrees on the expected azimuth. Normally, this pointing allowed a barely usable signal from the tracker when the rocket was in the launcher -- not a major concern since the horn antenna was expected to provided the primary data for the first few seconds of the flight. As the rocket flew through the antenna's main beam, auto track was initiated, and the tracker followed the rest of the flight. This procedure worked well on 3 of the 4 remaining flights. On 19 July, however, auto track was lost for unknown reasons 15-25 s into the flight. Tracking was re-established manually some 15 s later, after the intermittent loss of several seconds of data, and auto track worked for the remainder of the flight.

A link analysis was done for the REFS flight. Table 12 summarizes the calculations for the two receive paths. The transmitter output is only 200 mW. While this is low compared to typical rocket flights, it is sufficient for the short slant ranges involved with this experiment. The slant range for the tracker includes the entire flight. The slant range for the horn is for the initial conditions -- to the launch pad and first few seconds of the trajectory. The transmit-antenna gain varies with the direction from the payload. There is a gain of -8dB or more for 98 percent of the antenna coverage. The nose and tail of the rocket have small cones with gains of less than -20 dB. Cable losses are estimated based on cable type, length and number of connectors. The polarization loss of 3dB arises from the fact that the payload transmits circular polarization, whereas the receive antennas are linearly polarized. Sky noise for the tracker is based on looking above the earth. Sky noise for the horn is based on looking at the hillside. The minimum signal-to-noise ratio that will normally give a bit error rate of 1 in 10^6 bits is 16 dB. The signal-to-noise margins of 14.5 and 6 dB are the amount in excess of this minimum. Since the noise is statistical, there will be times when the signal is overwhelmed. The margin is an indication of how often this will happen.

There were significant RF signal dropouts at both receivers during all three data flights. Of most interest are those of the tracker. The first flight on 8 July into a weak storm experienced only minor dropouts during the 2-1/2 s beginning about 15 s into the flight. The other two flights penetrated heavier precipitation and suffered more serious dropouts. On 17 July there were two short periods of severe dropouts -- 2 s starting about 18 s into the flight and 4 s starting around t + 35 s. The 19 July flight showed severe dropouts between t + 20 s and t + 37 s, the worst

Table 12. Signal/Noise Calculation for REFS Flights

ITEM	TRACKER		HORN	
	VALUE	UNITS	VALUE	UNITS
TRANSMITTER POWER	0.2	Watts	0.2	Watts
CABLE LOSS TO ANTENNA	3	dB	3	dB
TRANSMIT ANTENNA GAIN	-8	dB	-8	dB
SLANT RANGE	6	km	2	km
FREQUENCY	2235.5	MHz	2235.5	MHz
POLARIZATION LOSS	3	dB	3	dB
• SIGNAL @ RECEIVE ANT	-106	dBm	-96.4	dBm
SKY NOISE TEMP	150	deg K	270	deg K
RECEIVE ANTENNA GAIN	24	dB	7	dB
CABLE LOSS - ANT/PREAMP	1	dB	1	dB
PREAMP GAIN (NO AMP=0)	30	dB	32	dB
PREAMP NOISE FIGURE (NO AMP=1)	1.4		1.4	
CABLE LOSS - PREAMP/RECEIVER	10	dB	10	dB
RECEIVER NOISE FIGURE	11		11	
BAND WIDTH	1	MHz	1	MHz
• SYSTEM NOISE @ ANTENNA	-112.5	dBm	-111.5	dBm
• SIGNAL TO NOISE RATIO	30.5	dB	22	dB
MINIMUM S/N RATIO	16	dB	16	dB
• S/N MARGIN AT RECEIVER	14.5	dB	6	dB
DISH ANTENNA DATA				
DIAMETER	4	FEET		
• GAIN	25.1	dB		
• BEAM WIDTH	8	DEG		

occurring during the first 3 s and last 7 s of this period. Dropouts in the last flight coincide with the period during which auto track was lost, but those in the other flights remain unexplained.

The dropouts from the horn antenna were more predictable because of its relatively low gain and poor coverage of the upper part of the rocket trajectory. In every case the horn gave good coverage of the first few seconds of the flight, where it was needed to cover for the tracker during the lock-on sequence. On 8 July the only significant dropouts occurred between t + 9 s and t + 23

s. On 17 July, however, the data was unusable from t + 5 s through t + 29 s. 19 July was the worst case, with the only usable data received during the first 5 s and the last 10 s of the flight.

The transmit antenna used on the rocket was a wrap-around design that had deep nulls at the nose and tail. If either of these areas of the antenna pattern were pointed at a receive antenna, a dropout would be expected. This phenomenon might explain the first period of dropouts experienced by the tracker, although it occurred at somewhat different times on the three flights. Looked at in detail, however, individ·ial dropouts from the two antennas did not generally coincide, in spite of the fact that the line of sight to the rocket was nearly the same for both. Several theories for this behavior have been advanced, though none provides a good explanation of the results. Having the antenna track across the sun would cause an increase in noise but not loss of track. Noise associated with a lighting discharge should not be of long enough duration to cause loss of track and should appear simultaneously in both receivers. It is recommended that the AGC outputs of all receivers be recorded in future experiments to aid in the diagnosis of telemetry problems.

In data analysis, the existence of different dropouts on the two independent telemetry receivers was handled in the following manner. A program was written to compile the most continuous merged record possible by switching between the two available telemetry streams as necessary. Starting with the signal from the horn antenna, whenever a gap was detected in the data from the current source, the other source was checked. If it could provide data at the required time, it became the current source and remained so until a gap was detected in its stream. When simultaneous dropouts occurred in both sources, the merged record was padded with dummy frames to maintain a continuous frame count. The resulting merged data stream was much easier to analyze and was used throughout this report.

4.3.2 FAULTY DIGITIZATION ON 8 JULY

The only electronic "glitch" that was noticed in these flights was a relatively minor digital problem with the payload launched on 8 July. The nature of this problem is illustrated in Figure 27. Evidently the output shows a preference for certain levels, as though a few of the lowest-order bits of the A/D converter had a preference for one state. Analysis of the digital levels shows, however, that the problem is subtle. There are no missing bit patterns, but there is a higher-than-normal frequency of occurrence of the hexadecimal digits 4 and F in the least significant four bits of the twelve-bit data words. This "noise" occurs from time to time on all data channels during this flight. Fortunately, the errors introduced are small enough to be ignored, being about twice the noise level in most cases. Further, no such problems were observed on the other two flights.

4.3.3 FIELD MILLS -- ANOMALOUS BEHAVIOR

Generally, the field mills behaved very well, as we shall see in Section 5. Nevertheless, there was one significant problem with the system, and several other puzzling phenomena were observed that deserve comment.

51
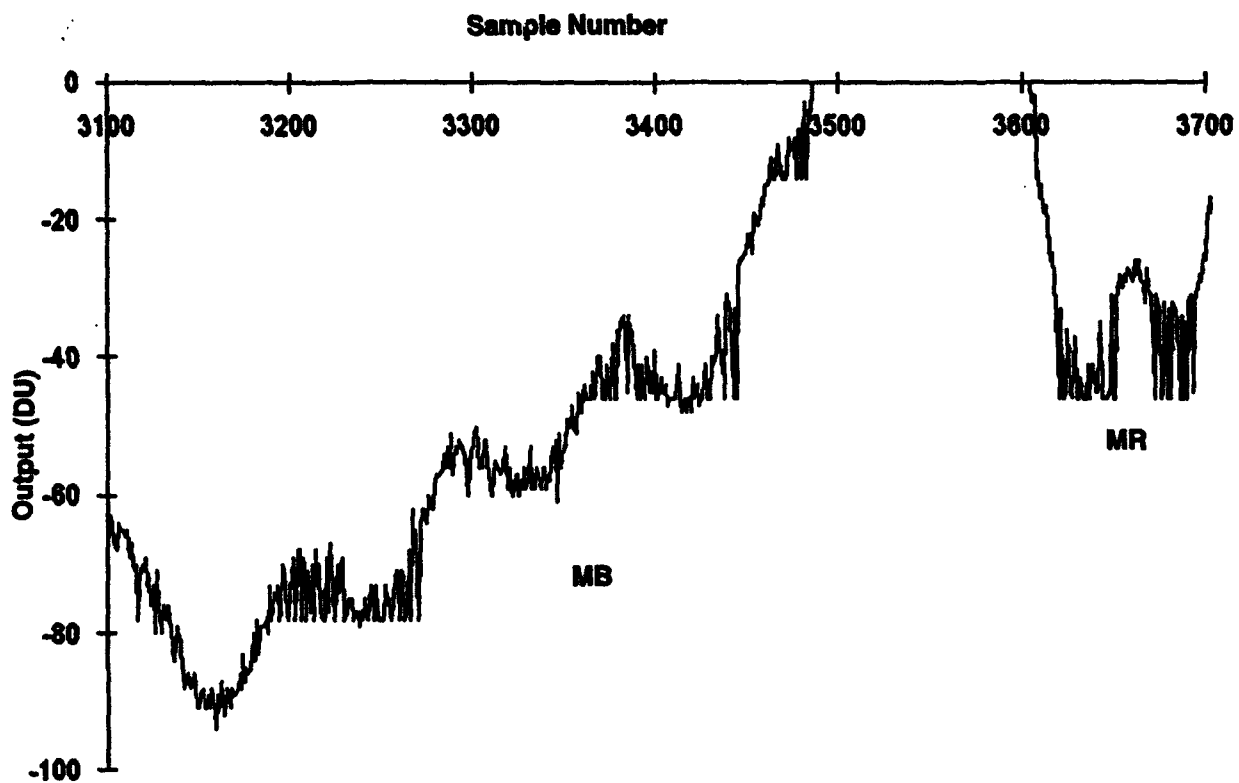
Figure 27. A sample of the digital "noise" occurring on all data channels during the 8 July flight. Shown here is a greatly expanded section of raw data (prior to de-dropping) from the Middle-Bottom (MB -- left trace) and MR (right trace) field mills during the last part of the motor burn. The horizontal axis is sample number (2314.8 samples/s) starting at an arbitrary origin, and the vertical axis is digital units

The system problem was that the rotating shell slowed significantly during rocket-motor burn, as described in Section 4.1 above. Although this complicated the analysis of the field data on all three flights, the problem was particularly severe on 8 July. In that case the shell slowed to a minimum of 0.72 RPS just before burnout. Figure 28 shows the output of the two optical detectors and the accelerometer during the last two rotation periods in the burn phase. The longest full revolution took 0.48 s.

The most annoying aspects of this problem were the rapid changes in repetition rate and shape of the optical pulses illustrated in the figure. Considerable effort was expended on tuning the peak-finding algorithm in the synchronous-rectifier software so that it could follow the shell rotation accurately during motor burn. We were ultimately successful in calculating fields for every mill period comprising valid data.

Another aspect of this problem is illustrated in Figure 29, which shows the output of four of the eight field mills during the same time period plotted in Figure 28. Even after the de- drooping algorithm has been applied, there is an appreciable drift in these data over one mill period. The significance of this secular trend will be discussed below. The present concern is that the mill period has become so long that synchronous rectification can no longer fully remove the drift. The effect of secular trends has been minimized in the rectification algorithm by calculating the difference between the average of each "uncovered" interval and that of the two "covered" intervals on either side of it.

The first puzzling phenomenon to be discussed here is the noise observed on all the field mills during motor burn in the flight of 17 July, illustrated in Figure 30. Notice that the noise pulses are nearly identical and simultaneous on all mills and occur only while the stators are uncovered. Thus, this noise appears to be the result of abrupt spikes in the vehicle potential. This type of noise was not evident later on this flight, nor was it detected during either of the other flights. Its cause is not known.

A second puzzle is already evident in Figures 29 and 30, during motor burn, but is further illustrated by Figure 31, about 57 s after burnout on 19 July. All of these de-drooped field-mill plots show secular trends that result from zero offsets in the raw data. The nature of the charge amplifiers connected to the stators is to produce such offsets in response to steady currents at their inputs.

Closer examination of these three figures indicates, however, that the nature of the secular trends in Figures 29 and 30 is not the same as that in Figure 31. The trends illustrated in the first two figures appear to continue through both the covered (upper) and the uncovered (lower) portions of the mill period. This behavior was observed primarily during motor burn and is hard to explain in terms of real currents to the stators. Figure 31, on the other hand, shows a trend (clearly indicated by the downward march of the covered -- lower -- portions of the waveforms over several periods) that is apparently due almost entirely to net stator current during the uncovered -- upper -- portions (as indicated by the near-zero slopes of the covered portions). This latter behavior was observed a few times after burnout on the flights of 17 and 19 July and might be due to ionic conduction currents to the stators while they are uncovered.
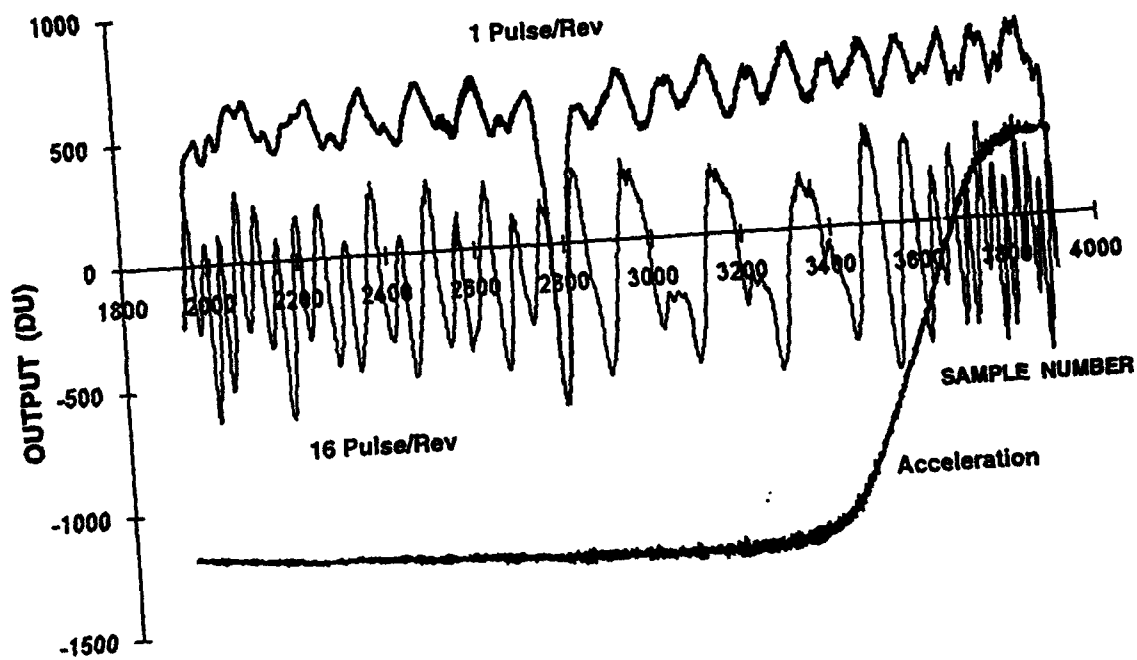
Figure 28. The last two shell rotations during motor burn on the flight of 8 July. Raw data from the optical detectors giving one pulse per shell revolution (upper thick trace) and 16 pulses per revolution (thin trace) are shown together with that of the accelerometer (lower thick trace) on scales similar to those in Figure 27
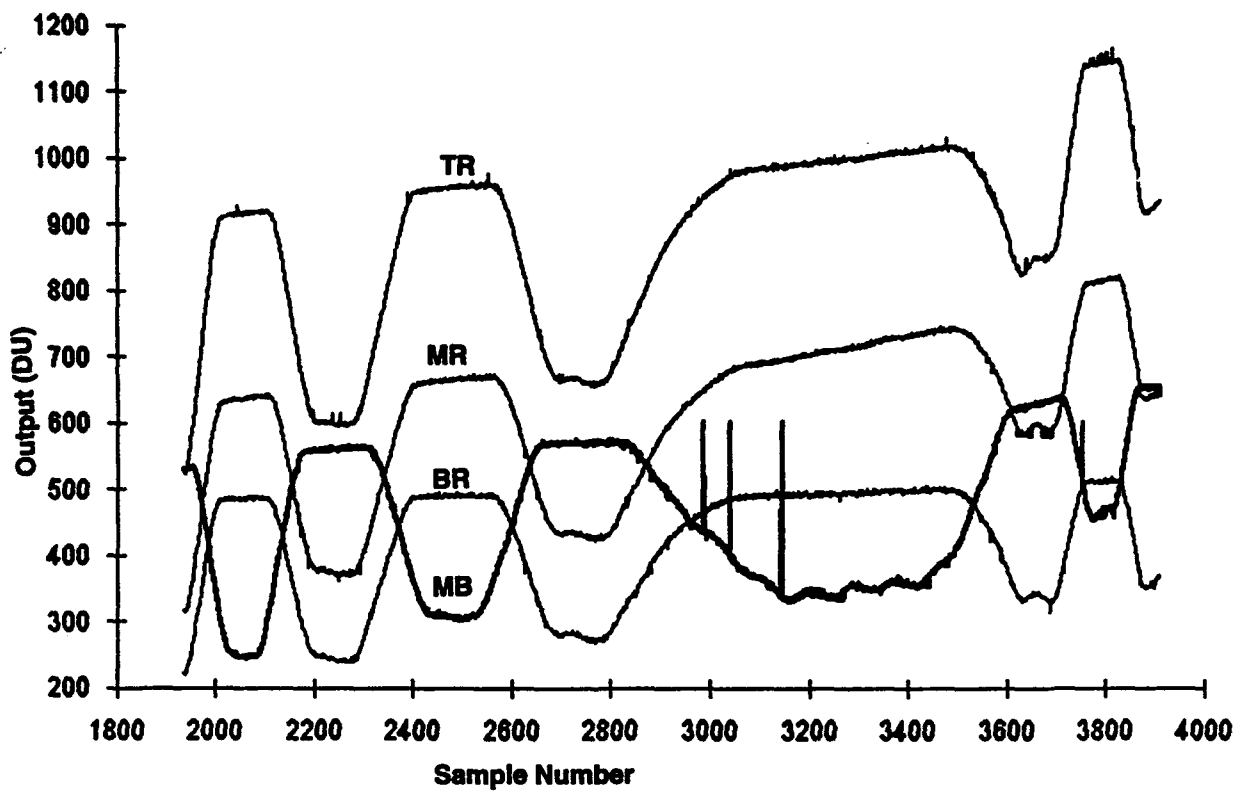
Figure 29. The de-drooped output of field mills TR (top trace), MR (middle thin trace), BR (bottom thin trace) and MB (thick trace) during the same time period and with the same scales as in Figure 28. The four glitches to 600 DU are caused by data dropouts
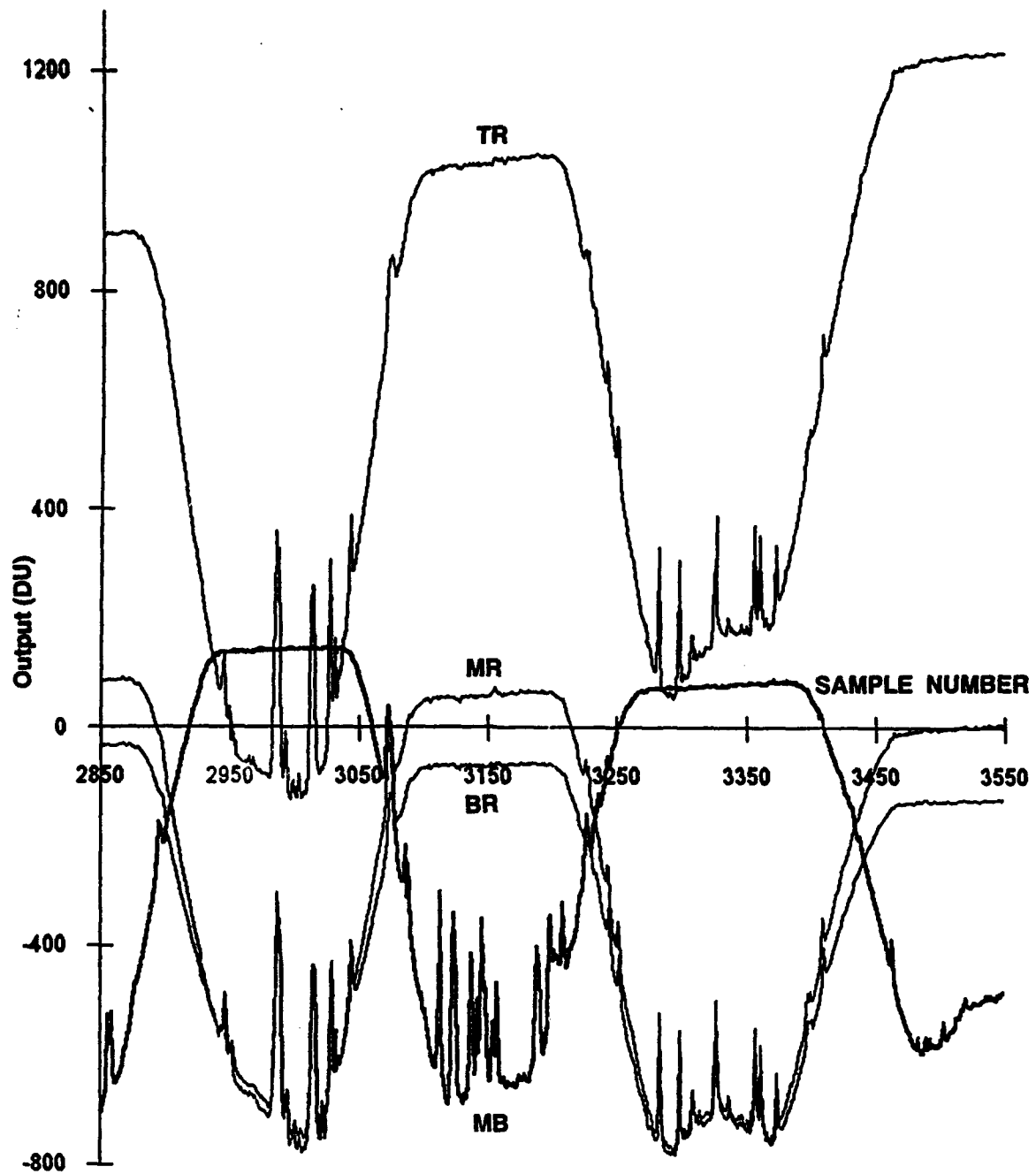
Figure 30. De-drooped traces during motor burn on 17 July of the same four field mills on similar scales to those in Figure 29, showing a type of noise common to all field channels
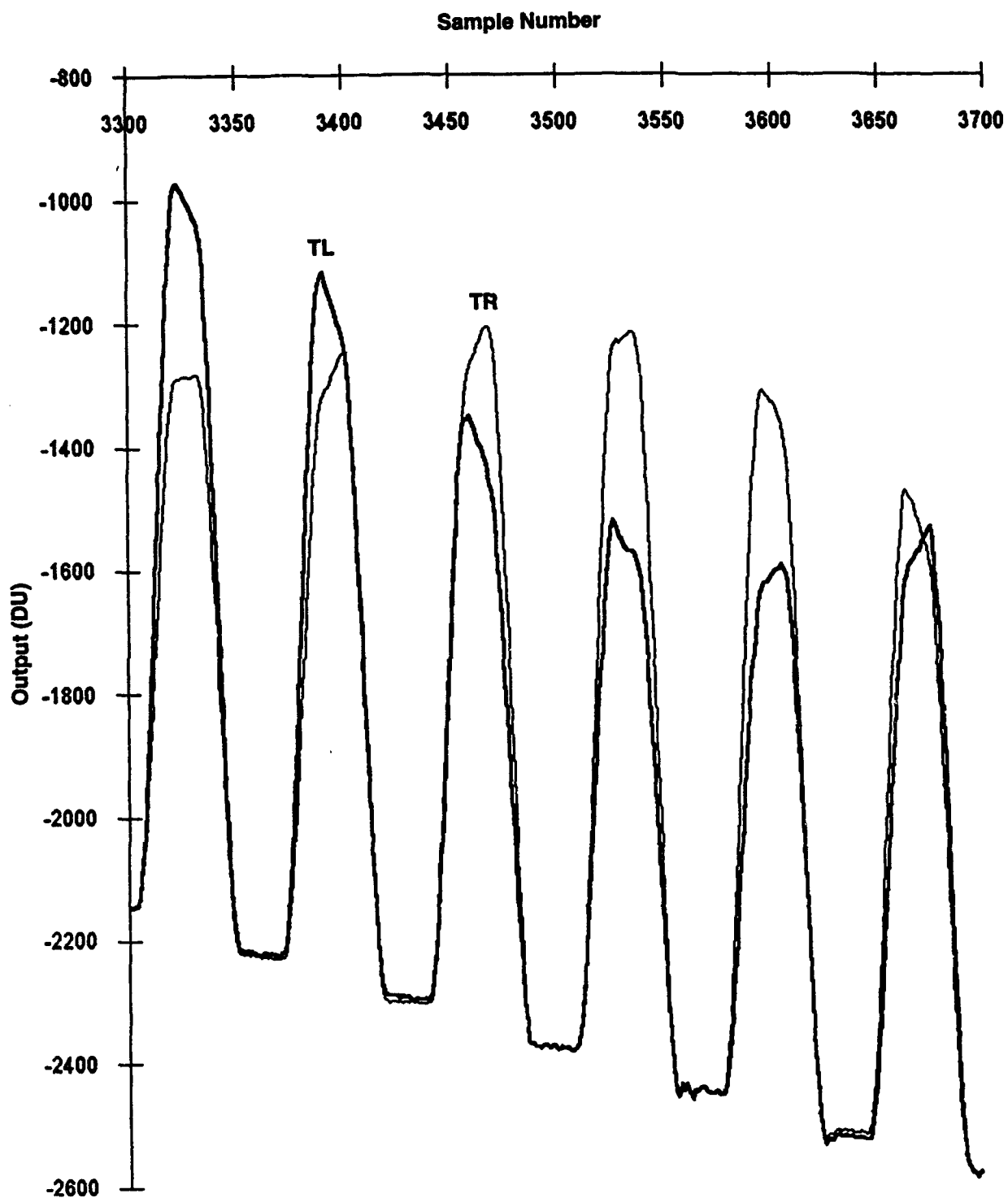
Figure 31. An example of secular drift on the field mills. De-drooped traces of field mills TR (thin line) and TL (thick line) from the middle of the flight on 19 July are shown here. The scales are again similar to those of Figure 27

57

The polarity of the net charge transfer implied by the trend in Figure 31 is such as to decrease the charge induced on the stators by the external field, as would be expected of a conduction current, but what about its magnitude? The field-induced charge, Q_E, can be compared with the presumed conductive charge transfer, Q_λ, during one effective uncovered interval, T, to deduce the electrical relaxation time due to the polarity of ion supposed to be carrying the current.

$$Q_E = \varepsilon_0 AE \tag{14}$$

$$Q_\lambda = -\lambda AET \tag{15}$$

where $\varepsilon_0 = 8.85 \times 10^{-12}$ is the dielectric permittivity of air, λ is its effective conductivity, and A is the stator effective area, giving the desired relaxation time as

$$\varepsilon_0 /\lambda = T(Q_E/-Q_\lambda). \tag{16}$$

Estimating values of T and the charge ratio from the figure gives a relaxation time less than 0.28 s, which is some three orders of magnitude shorter than that in ambient air at Langmuir Laboratory!

Evidently, none of these trends can be considered to have been fully explained. The best that can be said is that they are usually slow enough to be well removed by synchronous rectification and therefore should not compromise the integrity of the field measurements.

The final puzzling phenomenon to be discussed is a class of impulsive events recorded by the field mills on two of the three flights. There was one period of about 5 s in the latter part of the 17 July flight, and there were two shorter periods -- one early and one late -- in the 19 July flight, during which a series of impulsive steps drove one or more of the mills to saturation. Figure 32 illustrates three events in such a series from 17 July. The first of these is shown in more detail in Figure 33. Notice that the impulses may occur when the stators are either covered or uncovered, that they appear simultaneously on all eight field channels, and that an individual mill may or may not suffer an offset as a result. Events of this kind did not appear during the 8 July flight. Their cause is unknown.

4.3.4 CHARGING SYSTEM -- IN-FLIGHT POTENTIAL CALIBRATION

The revised on-board charging system performed well in flight. It was most effective at modulating the vehicle charge on 8 July, when the ambient fields were relatively small (magnitudes < 20 kV/m -- see Section 5.2 for the measured fields). In this flight there was, however, one period of about 9 s during descent when the peak voltage on the corona assembly was reduced from its normal level of about -9 kV to near zero for a few charging cycles. There was no apparent reason for this behavior, since the ambient field and charge on the vehicle were both passing through zero at the time.

Figure 34 shows the voltage on the corona assembly for all three flights. On 17 July there was a period of about 6 s early in the flight when the high-voltage system indicated continuous negative voltages as large as -2.8 kV, corresponding to steady currents as large as 17 μ A flowing
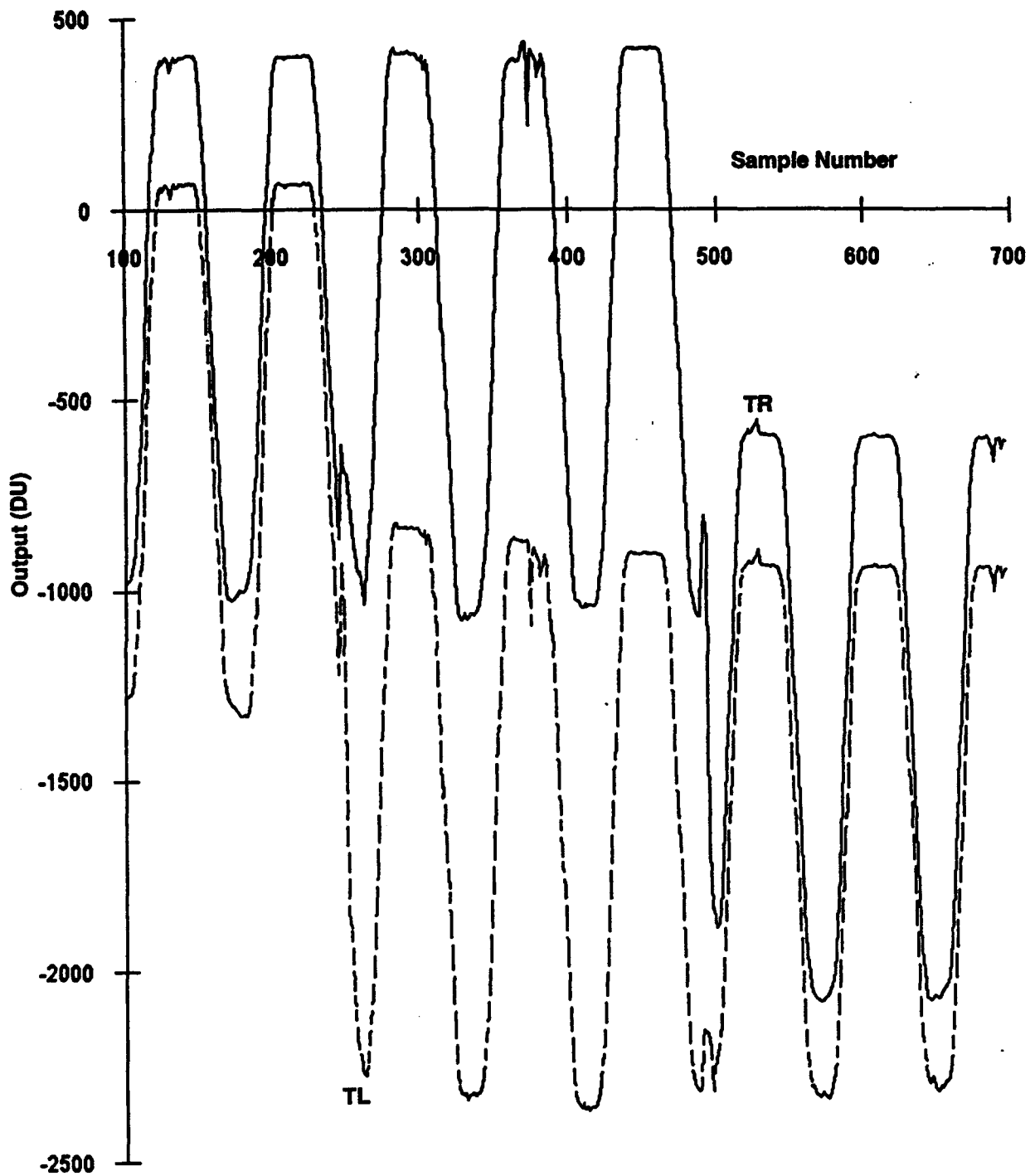
Figure 32. De-drooped traces of field mills TR (solid line) and TL (dashed line) showing three impulsive events late in the flight on 17 July. The scales are again similar to those of Figure 27
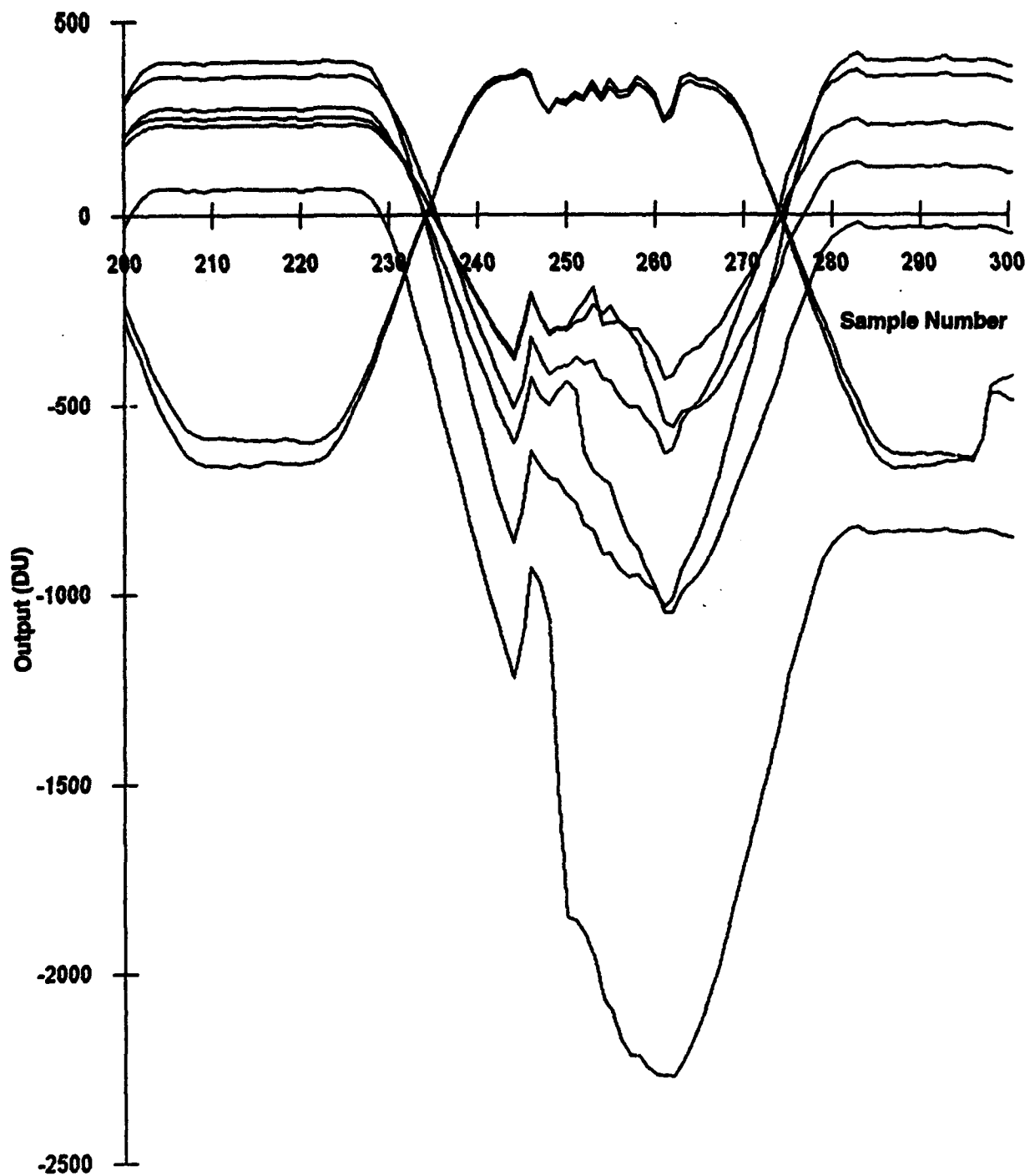
Figure 33. An expansion of the first impulsive event in Figure 32, showing traces from all eight field mills. The scales are identical to those in the previous figure
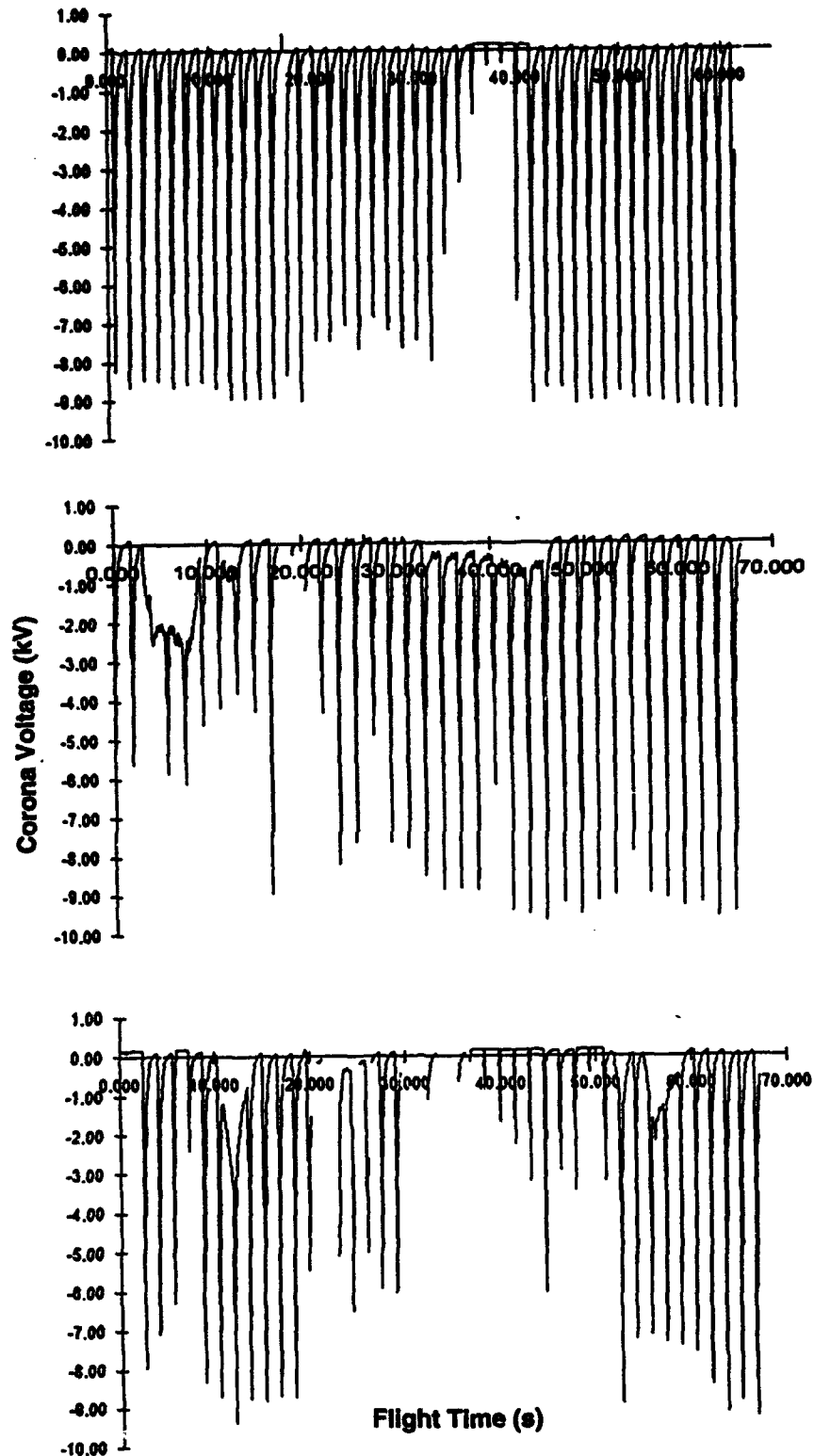
Figure 34. Voltage measured on the corona assembly of the high-voltage system as a function of time during the 8 July (top panel), 17 July (middle panel), and 19 July 92 (bottom panel) flights. Gaps in the records are caused by telemetry drop-outs. (Only gaps longer than 250 ms have been shown as breaks in the traces.) See Figures 40, 41, and 42 for corresponding plots of computed ambient field and vehicle potential

from the corona assembly as discussed in Section 2.1, upon which the usual charging peaks were superimposed. This behavior coincided with a very strong negative longitudinal field that should have drawn a positive current from the corona assembly on the tail of the rocket. Similar behavior was also observed for some 15 s in the middle of the same flight and during three brief periods on 19 July. In addition, there were extended periods of reduced charging voltage on both 17 and 19 July. The other anomaly noted in the laboratory, failure of the high-voltage supply to turn on when the payload was negatively charged (or in a strong positive longitudinal field), was not observed in flight.

The large and rapidly changing vehicle potentials experienced on 17 and 19 July prevented easy recognition of, and in many cases entirely eliminated, any response to the on-board charging system. Presumably the natural vehicle charging easily overwhelmed the artificial. Thus, it was only 8 July that offered a good opportunity to measure ratios of the potential coefficients in flight. The potential variation during the best section of this flight is plotted in Figure 35 (although the derivation of vehicle potential is not explained until Section 5.1 and, in any case, is not needed to perform this calibration).

The theory of in-flight potential calibration can be simply explained using the definition of F_{ip} in Equation (18), below. The field changes measured simultaneously by the right and left mills were added at each longitudinal position:

$$\Delta F_{ip} = (\Delta F_{ir} + \Delta F_{il}) /2 = a_{iz} \Delta E_z + a_{iv} \Delta V, \quad i = t, m, b \tag{17}$$

Since all field changes used here were keyed to the appearance of high voltage on the corona assembly and occurred over time intervals of 145 ms or less, it can be assumed that $\Delta E_z = 0$ in Eq. (17). Thus, ratios of the ΔF_{ip}'s are equal to corresponding ratios of the potential coefficients. Such ratios were computed of sums at the top and middle positions to the sum at the bottom position. This was done separately for each of the 11 largest potential changes shown in Figure 35, and weighted means of these ratios were derived using ΔF_{bp} as the weighting factor. Table 13 shows the resulting mean ratios and their estimated uncertainties in its first two rows. Based on an assumed value of 3.854 for a_{bv}, from Section 3.4, we can compute the other potential coefficients from the mean ratios as in the third row of the table. The mean laboratory values of these coefficients are repeated from Table 6 for comparison. The agreement is seen to be excellent.

Table 13. Comparison of In-Flight and Laboratory Potential Coefficients

Quantity	Top	Middle	Bottom
Mean Ratio to Bottom	1.122	1.037	--
Uncertainty of Mean	0.006	0.007	--
Implied a_{iv} (m^{-1})	4.322	3.995	(3.854)
Laboratory a_{iv} (m^{-1})	4.393	3.998	3.854

62
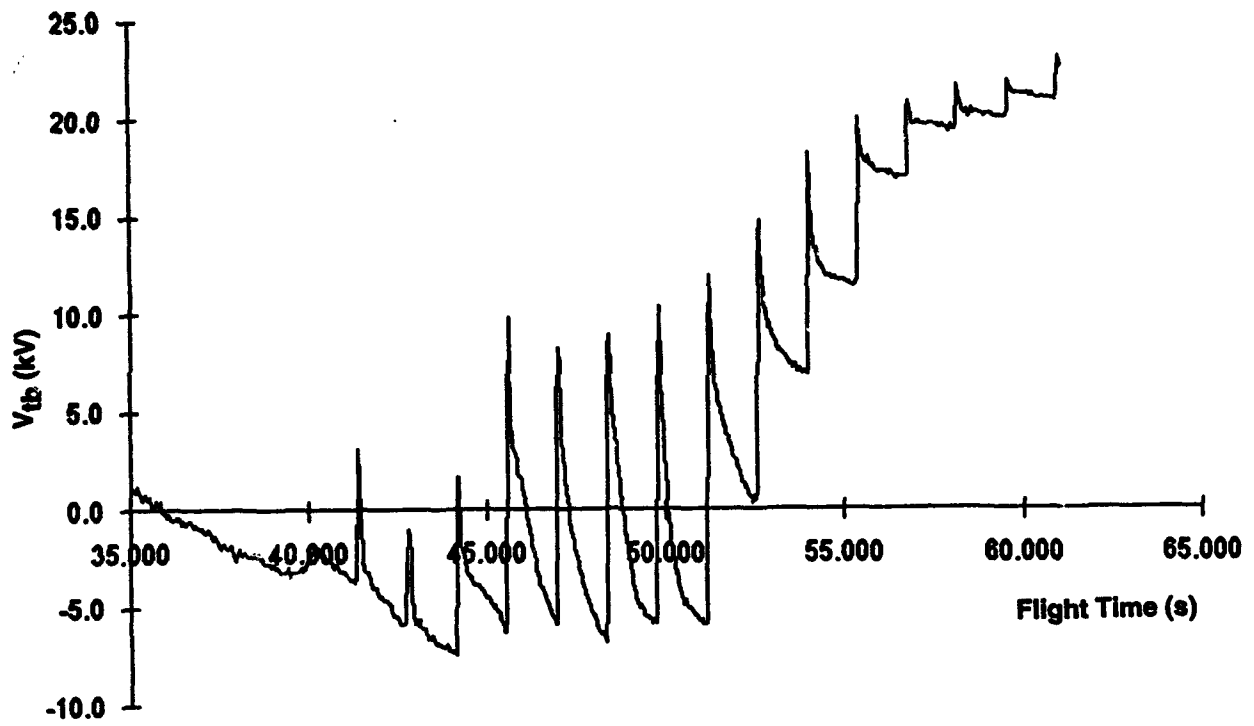
Figure 35. Computed vehicle potential versus time after launch during the last 27 s of the 8 July flight. Note the clear signature of the on-board charging system during most of this period

4.3.5 MAGNETIC-FIELD SENSOR

In spite of the design modification of the magnetic-field sensor described in Section 2.3, difficulties remained with temperature drift. In fact, one launch opportunity was missed on 10 July because the magnetometer saturated after the rocket was loaded into the launcher. The payload in question was modified in the field to adjust the zero offset in its magnetic-field circuitry and was eventually launched successfully on 19 July.

Other anomalies that appeared on all three flights were a brief burst of high-frequency ringing just after ignition and higher-frequency, continuous noise from about t + 1/2 s through roughly t + 15 s. These anomalies are illustrated in Figure 36, which shows raw magnetic-field data for the first 0.8 s of the flight on 17 July. Figure 37 is a blow-up of the ringing induced by motor ignition, which has a definite period of about 2.6 ms. Figure 38 is a similar blow-up of the continuous noise at about t + 1 s, after the velocity became super-sonic but before motor burnout. The cause of this latter noise is unknown but is apparently not related to supersonic flight, which begins at about t + 0.8 s and ends about t + 4.5 s.

It is presumed that the mu-metal flux concentrators vibrated as a result of both motor ignition and some other mechanical forcing to produce these signatures. It is recommended that these flux concentrators be stiffened and more firmly anchored to the circuit boards in future payloads. In spite of these problems, however, it was possible to interpret the magnetic- field data in terms of rocket rotation throughout all three flights. The resulting rotation rates have already been discussed in Section 4.1.

4.3.6 OPTICAL DETECTORS

Both optical detectors performed well on all three flights. The data from these detectors was used to determine the rate of shell rotation, as discussed in Section 4.1, above, and to provide the reference for synchronous rectification of the electric-field signals, as described by Willett et al.[1] (Sections 3.5 and 6.1). Here we illustrate the third function of the optical detectors -- as a cloud-penetration sensor.

The intensity of visible light is nearly isotropic inside clouds but is rarely so in clear air. Therefore, the peak output from the optical detectors (when exposed by the holes in the rotating shell) should fluctuate as the rocket rotates when the payload is below cloud base (or above cloud top), but these fluctuations should disappear inside clouds. This effect is shown in Figure 39 for the flight on 8 July. The times of cloud penetration and the resulting cloud-base heights estimated from the rockets' optical detectors are listed in Table 14. There was no evidence that any of these rockets came out the cloud tops. In several cases the cloud boundaries were fuzzy, as indicated by the letter "F" in the table.
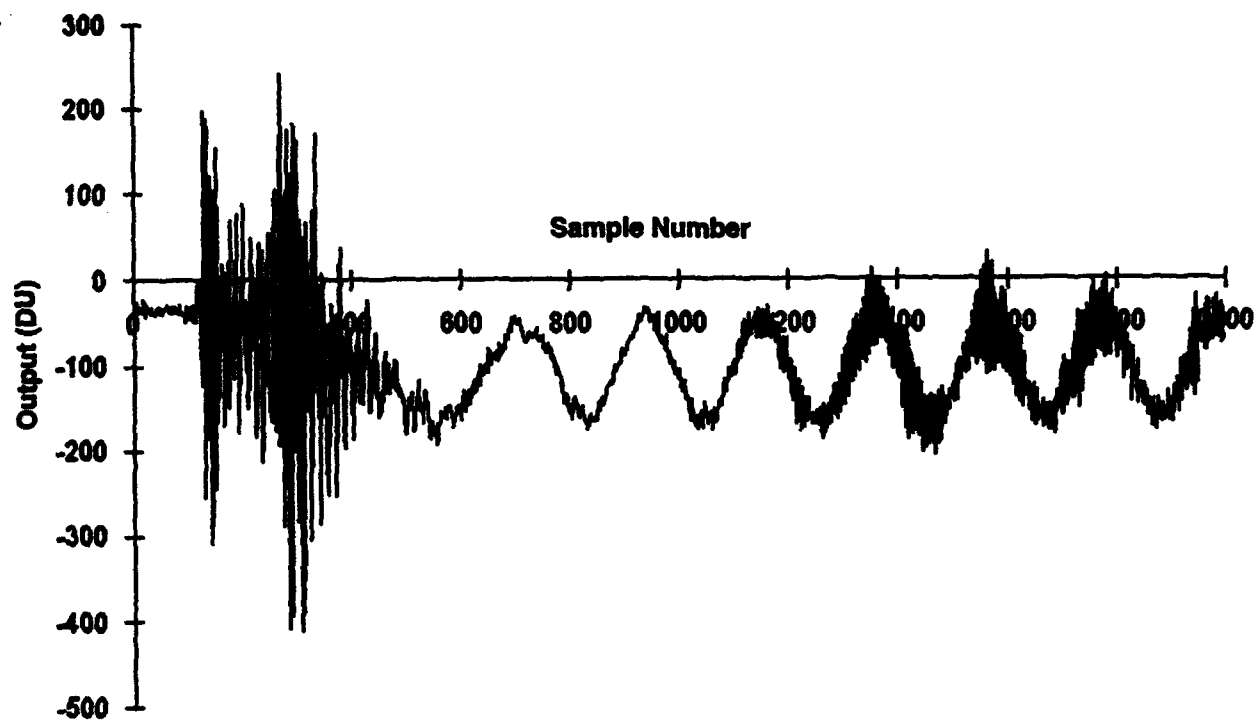
Figure 36. Raw magnetometer output during the beginning of the 17 July flight. About 0.86 s of data are shown. Motor ignition occurred at sample 115, where the burst of ringing begins. Continuous noise starts around sample 1200, near the beginning of the first transonic-sonic portion of the flight
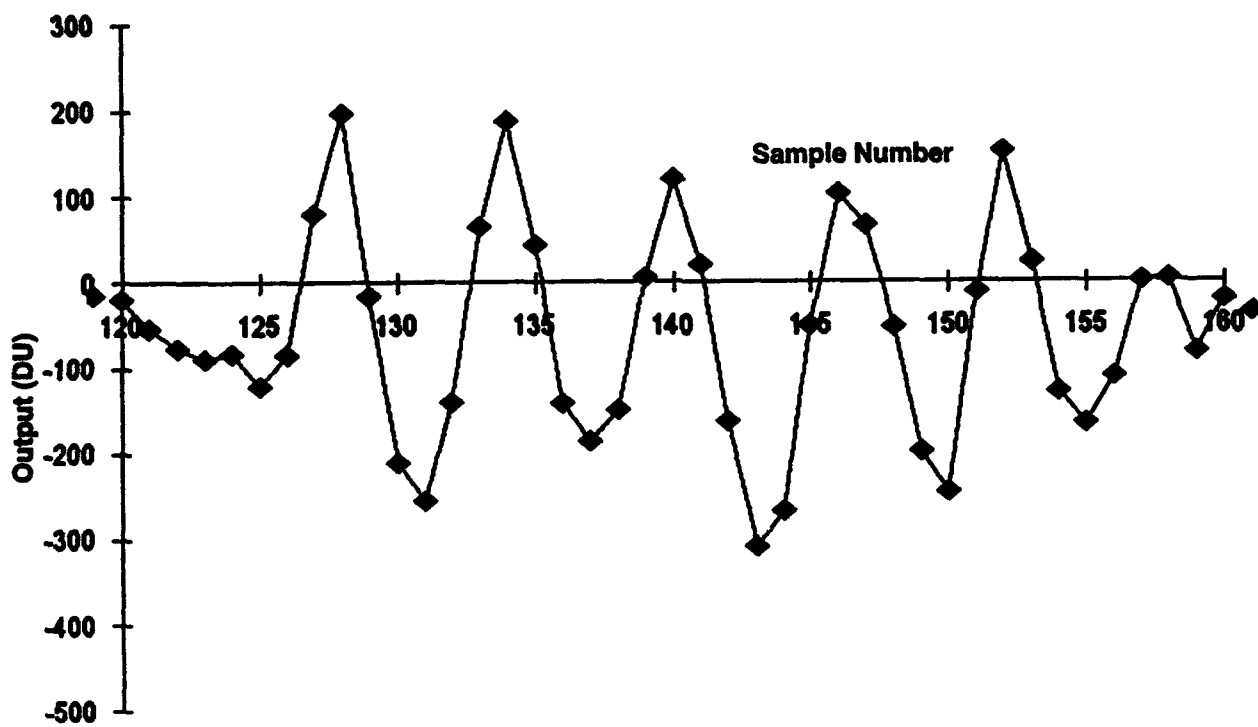
Figure 37. A blow-up of about 17 ms at the beginning of the ignition-induced ringing shown in Figure 36. Individual samples from the magnetometer are plotted as solid diamonds connected by line segments

66
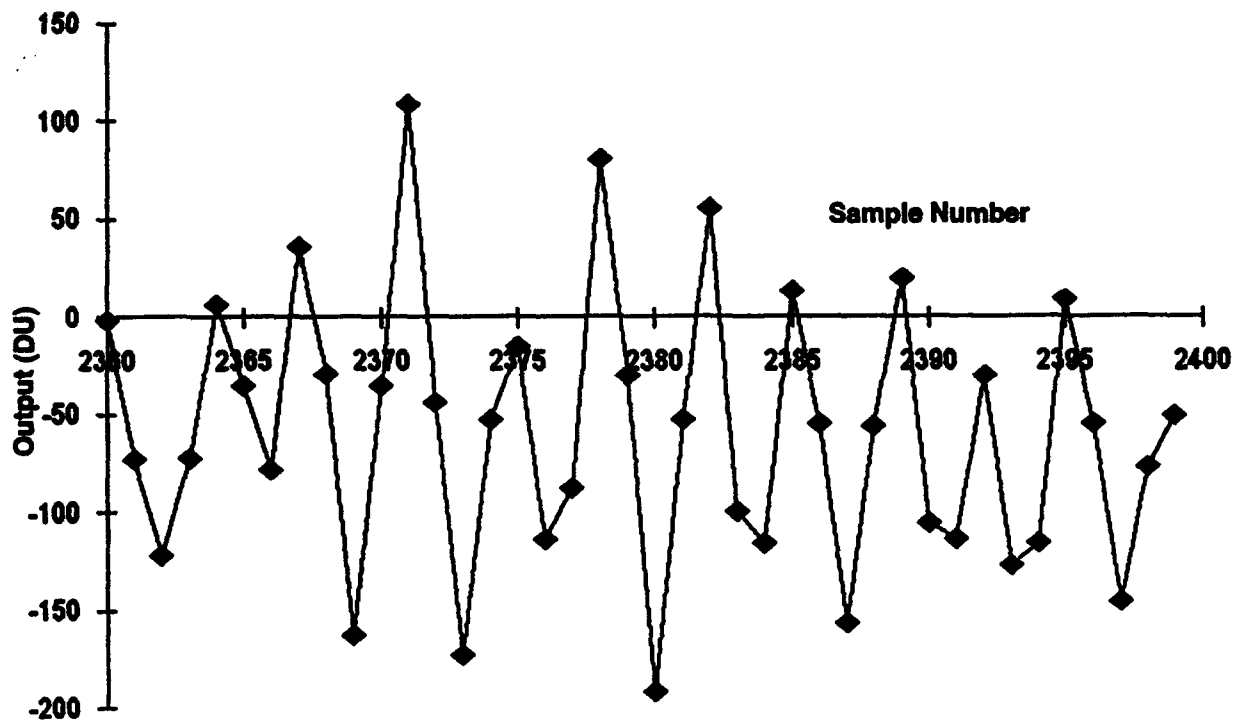
Figure 38. A blow-up of a section of the continuous noise that occurred shortly after the end of Figure 36. Otherwise similar to Figure 37
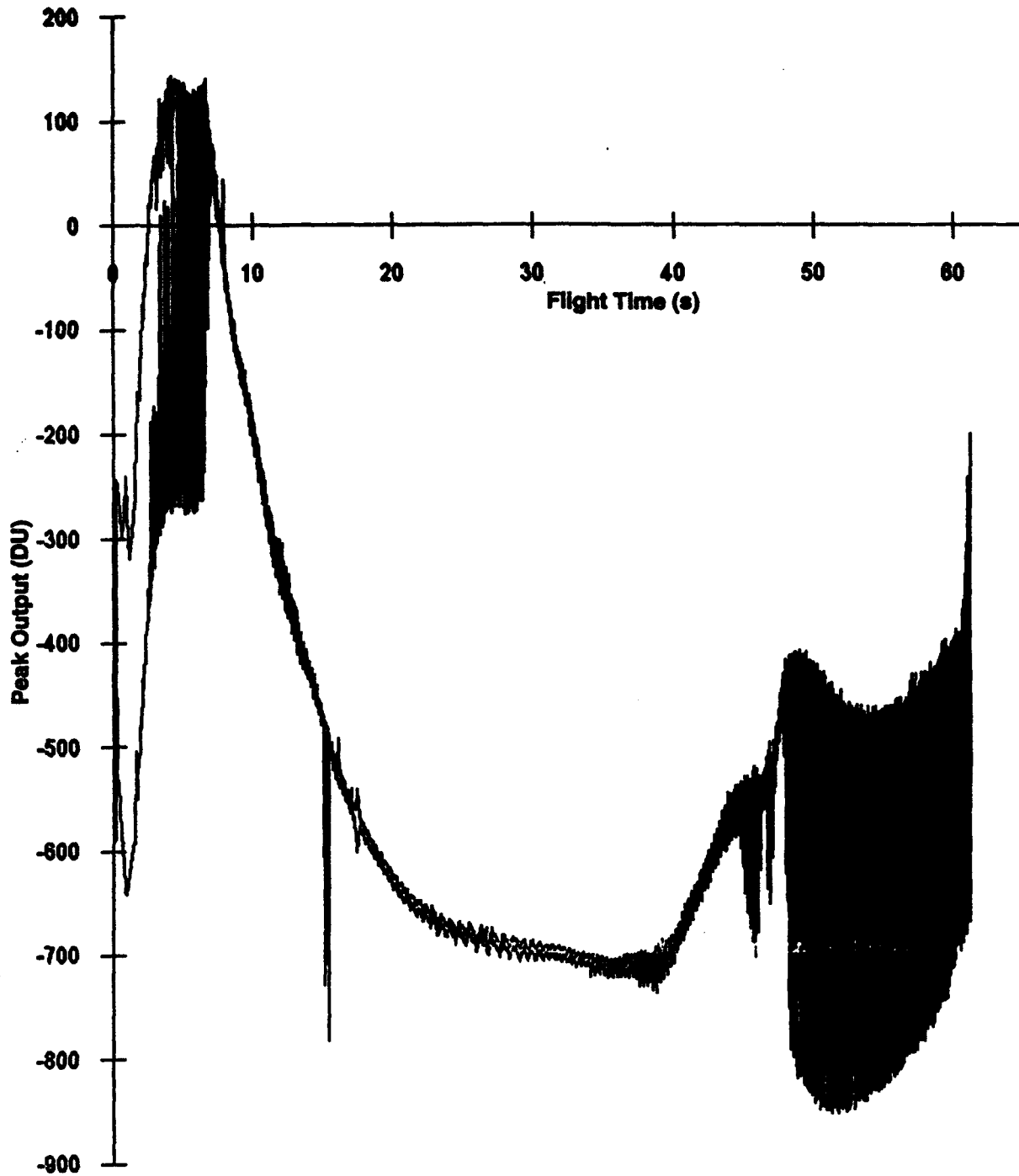
Figure 39. The envelope of peak output from the 16-pulse-per-revolution optical detector, versus time during the flight on 8 July. Increasing light intensity drives the output more negative. To produce this plot, the peaks that occurred each time a hole in the rotating shell passed over the photodiode -- about every ten frames except during motor burn -- were recorded. Then the maxima (upper curve) and minima (lower curve) of seven consecutive peaks were plotted. Where the rocket rotation is very rapid, during the first few seconds of the flight, the maximum and minimum curves are slowly varying and distinct

Table 14. Times and Heights the Rockets Penetrated Cloud Base

Flight	Direction	Time (s after launch)	Height (m AGL)
08 July	Upward	6.71	1980
	Downward	48.09	2120
17 July	Upward	3.0 F	1020
	Downward	60.92	980
19 July	Upward	4.7 F	1600
	Downward	60.0 F	1260

5. AMBIENT-FIELD DETERMINATION

This section describes the direct method used in this report to calculate the vector ambient field (in the rocket's coordinate system defined in Figure 1, Section 1) and the vehicle potential as functions of time during each flight. This calculation assumes that the laboratory calibration coefficients given at the end of Section 3 are correct. No attempt is made here to use either the magnetic-field data described in Section 4.3.5 or the trajectories derived in Section 4.2 to transform the vector field from the rocket's coordinate system into one fixed to Earth. The trajectories indicate, however, that the vehicle is oriented with its longitudinal axis nearly parallel to the vertical during most of each flight. Therefore, the longitudinal field (E_z) can be taken as a good approximation to the vertical field except near apogee. A future publication will describe efforts to refine the laboratory calibrations based on the behavior of the field vector in a coordinate system attached to Earth. Here we will use simpler means to assess the reliability of our computed fields by using the redundancy inherent in the data, as well as by comparison with ground-based and balloon-borne mills.

5.1 Theory

Because of the symmetry designed into the REFS payload, it is easy to compute the ambient field and vehicle potential from the local fields measured by the eight mills. Starting with Eq. (1) (beginning of Section 3), we define differences (F_{im}) and sums (F_{ip}) of the right and left mills at each longitudinal position $(i = t, m, b)$, as well as a similar difference (F_{mn}) and sum (F_{mq}) of the middle-top and middle-bottom mills, as follows:

$$\left.\begin{array}{l} F_{im} = (F_{ir} - F_{il})/2 = a_{iy}E_y \\ F_{ip} = (F_{ir} + F_{il})/2 = a_{iz}E_z + a_{iv}V \end{array}\right\} \; i = t, m, b$$

(18)

$$F_{mn} = (F_{mt} - F_{mb})/2 = a_{my}E_x$$

$$F_{mq} = (F_{mt} + F_{mb})/2 = a_{mz}E_z + a_{mv}V$$

69

These equations can then be solved directly for Ex, Ey, Ez, and V.

$$E_x = F_{mn}/a_{my}$$

$$E_{yi} = F_{im}/a_{iy}, \quad i = t, m, b$$

$$
\left.
\begin{aligned}
E_{zij} &= \frac{a_{jv}F_{ip} - a_{iv}F_{jp}}{a_{jv}a_{iz} - a_{iv}a_{jz}} \\[2mm]
V_{ij} &= \frac{a_{iz}F_{jp} - a_{jz}F_{ip}}{a_{jv}a_{iz} - a_{iv}a_{jz}}
\end{aligned}
\right\} \quad ij = tm, tb, mb
$$

(19)

Notice that there are three independent ways to solve for E_y, three ways to calculate E_z and V by inverting 2×2 matrices (only two of which are independent) and one way to find E_x. Where ambiguity exists, the solutions are identified with the additional subscripts tm, tb, or mb to indicate the longitudinal positions from which data were used. We will consider only the solutions derived from the tm and tb combinations from here on, since there is no evidence that the top mills are unreliable. Notice further that F_{mq} has not been used to obtain a third independent solution for E_z and V because F_{mt} and F_{mb} were not measured simultaneously with the other differences and sums.

A few other comments are in order about Eqs. (19). From the calibration coefficients summarized in Eq. (5), we know (as was already evident from the geometry of the vehicle) that all the a_{iv} are approximately equal to $a_v = 4 \ m^{-1}$, whereas the (dimensionless) a_{iz} are quite different at different longitudinal positions. (These coefficients are summarized in Table 15 below for convenience.)

Table 15. Summary of Calibration Coefficients a_{ij} from Section 3

Longitudinal Position, i	Field Component, j		
	x,y	z	v (m⁻¹)
t	1.045	3.84	4.393
m	1.034	2.39	3.998
b	1.033	1.41	3.854

Therefore, the determinant appearing in the denominators of the third and fourth equations in (19) is approximately equal to $a_v(a_{iz} - a_{jz})$, which cannot approach zero. Furthermore an approximate value of E_{zij} is given by $(F_{ip} - F_{jp})/(a_{iz} - a_{jz})$, which is seen to be directly proportional to the difference $F_{ip} - F_{jp}$ between the sums of pairs of mills at different longitudinal positions.

5.2 Raw Electrical Time Series

Time series of E_{ztb}, E_h, and V_{tb} for each of the three flights are plotted in Figures 40, 41, and 42, as computed from Eqs. (19). The versions of E_z and V derived from the top and bottom mills were chosen for display because the difference $F_{tp} - F_{bp}$ was larger than the other two options, permitting the most accurate deduction of E_z, and because a_{tz} and a_{bz} are more different than the other two pairs of longitudinal-field coefficients, suggesting a smaller error due to these laboratory calibrations in the determination of both E_z and V. E_h represents an estimate of the net magnitude of the two ambient-field components transverse to the rocket axis, as derived from the the middle mills via F_{mn} and F_{mm}:

$$E_h = (E_x{}^2 + E_{ym}{}^2)^{-1/2} \tag{20}$$

E_{ym} was chosen over the other two possibilities because this choice introduced only one calibration coefficient (a_{my}) into Eq. (20).

E_h is a rather crude estimate of the transverse field because F_{mn} and F_{mm} were not sampled at exactly the same time. The principal error that is introduced by this lack of simultaneity is due to the rocket rotation, especially early and late in the flight when this rotation, driven by the scarfed nozzles and canted fins on the rocket motor, is most rapid. The origin of this sampling error is illustrated in Figure 43 and partially explains the oscillations in E_h, which are usually smallest (and slowest) near apogee. Knowledge of the rotational orientation of the rocket as a function of time, to be derived from the magnetic-field sensor, will be required to obtain an accurate estimate of the transverse field, or to resolve it into components. Until this is done, it will not be possible to project the ambient field vector from the rocket's coordinate system onto one attached to Earth.

It is evident from Figures 40, 41, and 42 that the vehicle potential tends to follow the longitudinal field. This probably happens because the rocket's tail fins easily go into corona, tending to equalize rocket potential to the ambient at their location. Thus, for example, a positive (forward directed) longitudinal field causes negative charge to be emitted from the tail of an uncharged or negatively charged rocket, leaving it with a net positive charge. This mechanism does not constitute a problem for the measurement of ambient field.

There is, however, a short period early in the flight on 17 July when the data are suspect. Notice the behavior of the computed longitudinal field between about t + 3 and t + 8 s in Figure 41. This field component decreases rapidly from a zero crossing to a plateau around -80 kV/m, where it stays for 3 - 4 s before increasing rapidly toward zero. At the same time the potential, which has been following E_z as usual, suddenly reverses its downward trend, increasing rapidly to a relatively steady level near -10 kV. Then as E_z leaves its plateau, V abruptly decreases, after which it reverses its trend again and resumes following E_z.

This peculiar behavior of E_z was not repeated at other times or on other flights. A possible explanation for it is that, near -80 kV/m, the ambient longitudinal field had become strong enough to cause corona at the nose of the rocket as well as at the tail. Corona from the nose would emit charge of opposite polarity to that from the tail, tending to discharge the vehicle and

71
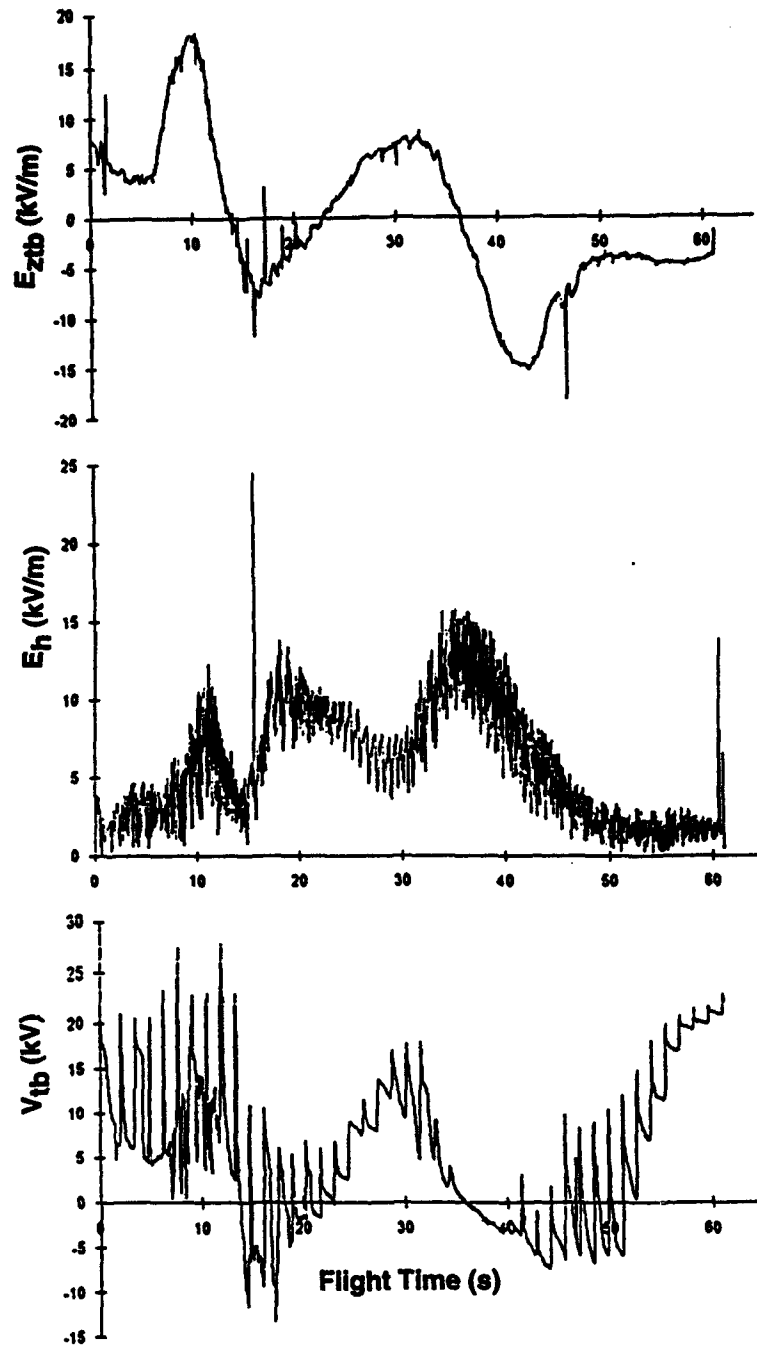
Figure 40. Raw electrical time series for the flight on 8 July 92. Apogee occurred at t + 26.2 s in this case. The top panel shows the component of the ambient field along the rocket axis (E_{ztb}); the middle panel shows an estimate (E_h) of the magnitude of the field components perpendicular to the rocket axis; and the bottom panel shows the vehicle potential (V_{tb}). Simultaneous gaps in all three records are caused by telemetry drop-outs, by the saturation of one or more field mills, or by failure of the synchronous-rectification algorithm to correctly determine the rotational position of the shell (usually caused by a brief telemetry dropout). Only gaps longer than 250 ms have been shown as breaks in the traces. Note the regular transients in V_{tb} caused by the on-board corona-charging system. Some of the other spikes in the data are spurious and will be removed by further processing
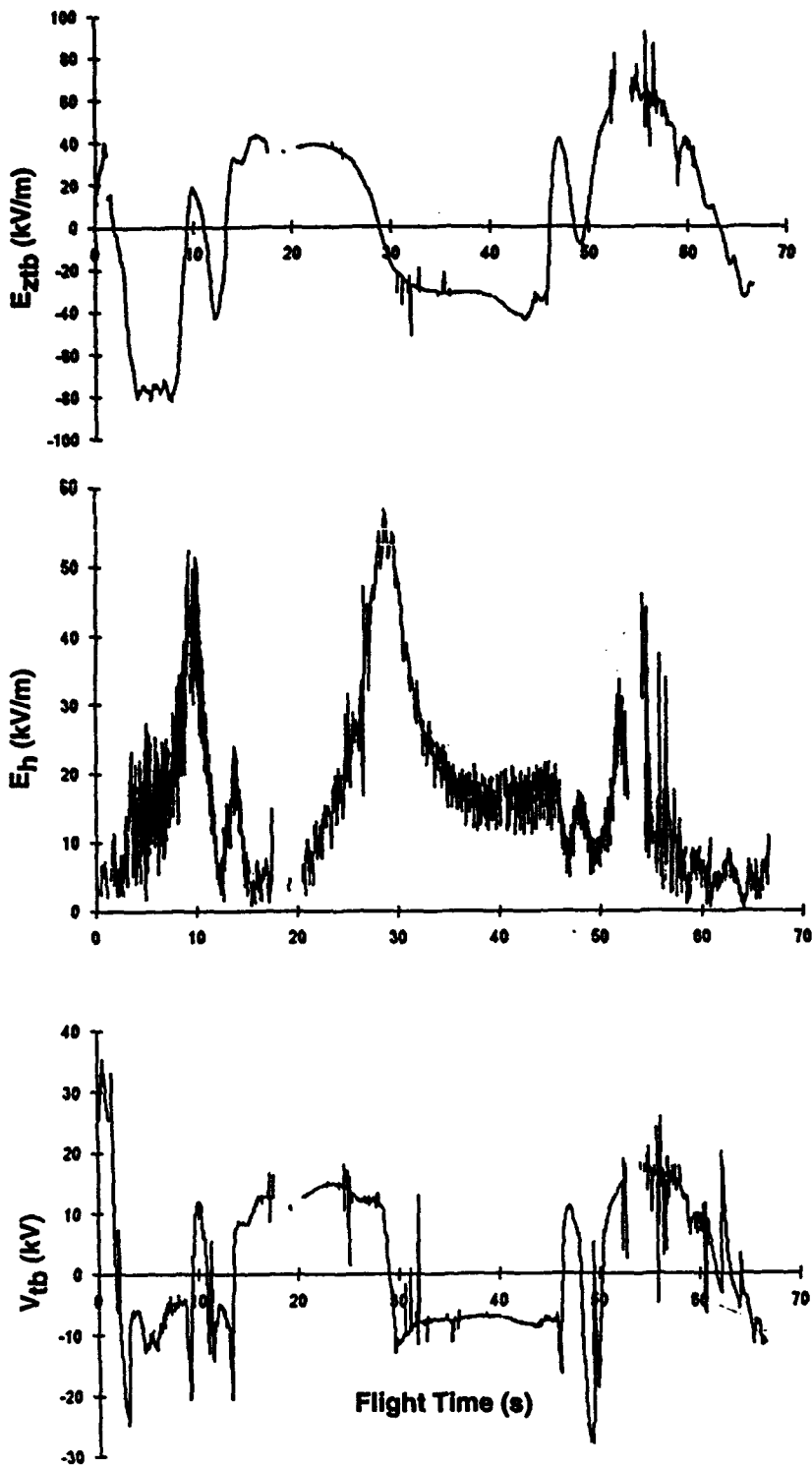
Figure 41. Raw electrical time series for the flight on 17 July 92. Apogee occurred at t + 28.9 s in this case. See caption of Figure 40 for details
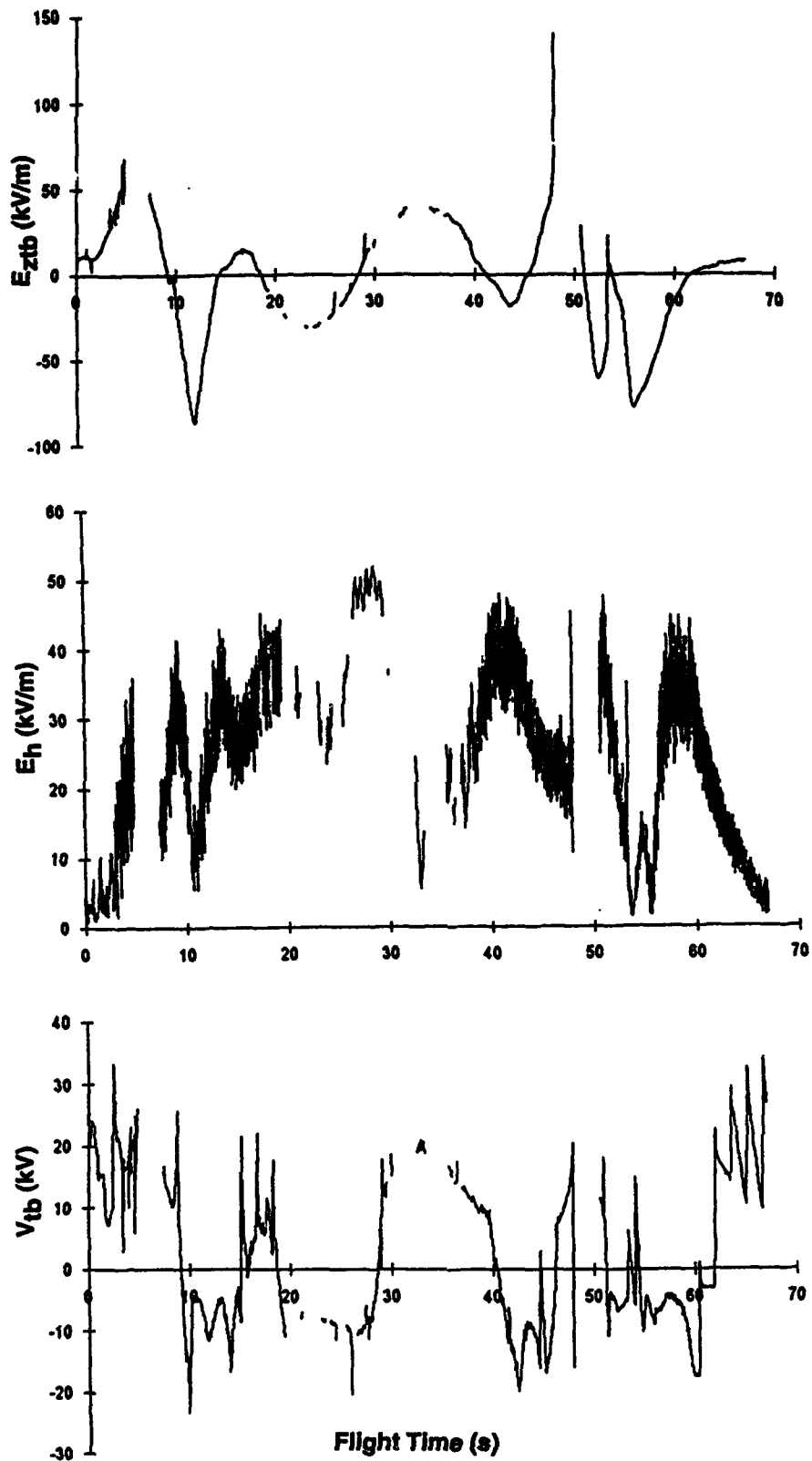
Figure 42. Raw electrical time series for the flight on 19 July 92. Apogee occurred at t + 29.2 s in this case. See caption of Figure 40 for details

74
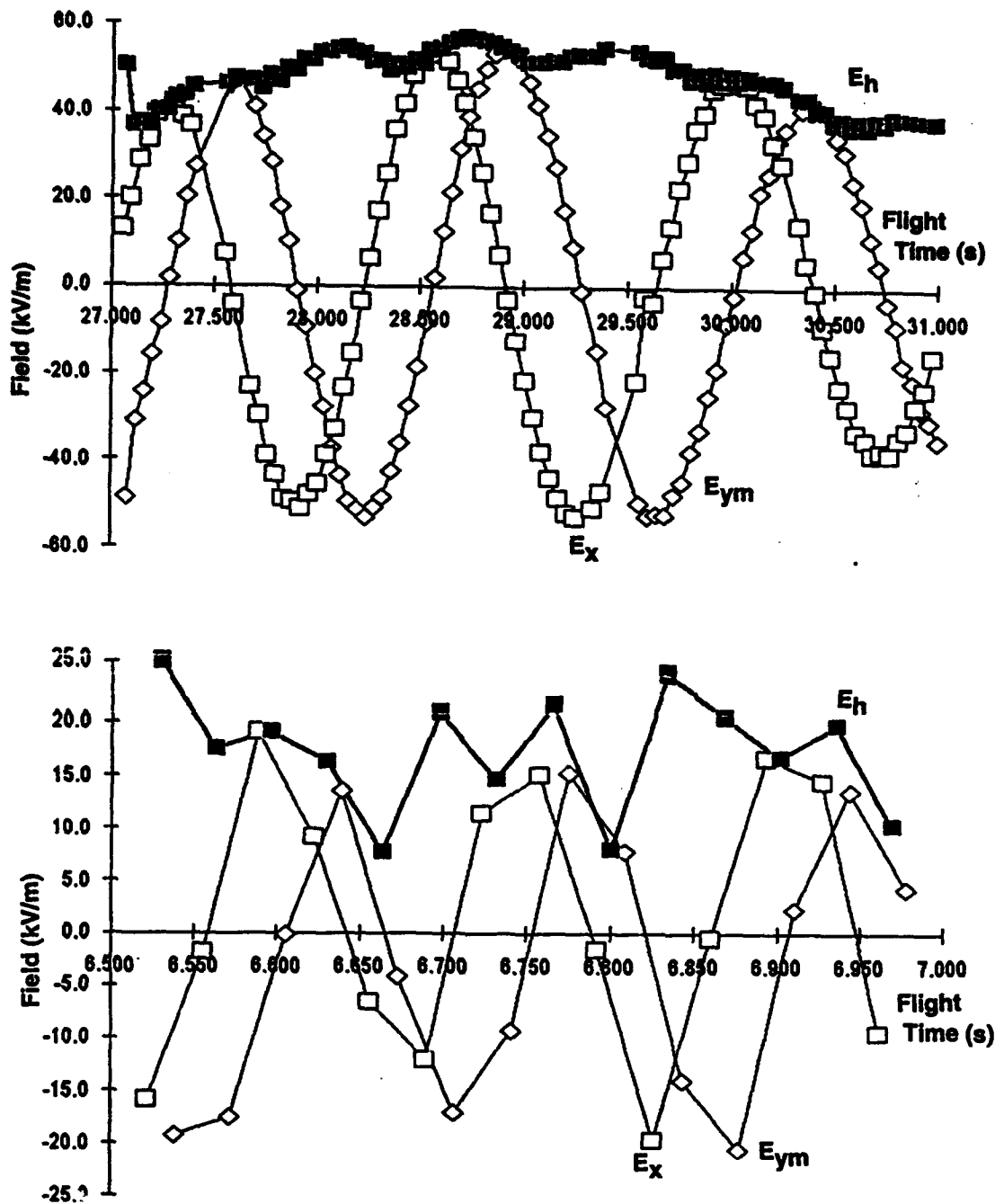
Figure 43. Raw time series of E_x (open squares), E_{ym} (open diamonds), and E_h (solid squares) during 2-1/2 rocket-rotation periods in 4 s at apogee (upper panel) and in less than 0.5 s early in the flight (lower panel) on 17 July. Notice that the two transverse-field components have similar amplitude but are about 90 deg. out of phase in both cases, as expected. The more rapid rotation in the latter case, however, causes significant differences in sampling phase (because the shell-rotation period is no longer short compared to the rocket-rotation period), producing rapid fluctuations in E_h (which has been plotted at times midway between those at which its inputs were sampled)

thus explaining the observed reversal in the trend of its potential. Such a situation might be expected to interfere with the measurement of ambient field, since bipolar corona would not be limited by the capacitance of the rocket. The resulting space charge, emitted from the nose and carried past the payload in the air stream, could become large and might explain the observed plateau in E_z, which would then be spurious. (If this explanation is correct, such spurious data could be obviated in future flights, or at least postponed to higher longitudinal fields, by increasing the radius of curvature of the nose cone.)

Closer examination reveals problems with the above explanation, however. There were several other times during the 17 and 19 July flights when trend reversals in V occurred without the large magnitude or apparent saturation of E_z described above. One such example is shown in Figure 44, where the longitudinal field reached only -43 kV/m. The V reversals were generally observed to coincide with the appearance of continuous negative voltages on the corona assembly (discussed in Section 4.3.4 above), suggesting that there might have been continuous corona from the rocket during all of these periods of reduced V magnitude. In the case shown here, the trend reversal and continuous high-voltage indication both appear to have begun when E_z decreased below about -16 kV/m. This is typical of the phenomenon, which began at E_z between -8 and -20 kV/m in the other cases of this kind.

It is tempting to ascribe all of these sudden trend reversals in V to the onset of corona from the nose of the rocket. Unfortunately, it is then difficult to explain the apparent saturation of E_z at -80 kV/m near the beginning of the 17 July flight, shown in more detail in Figure 45. If the potential and corona-voltage anomalies that began at E_z = -22 kV/m in this case are ascribed to negative-corona onset at the nose, as before, this leaves no explanation for the sudden plateau in E_z that was encountered about one second later. A further paradox is that similar trend reversals in V never occurred when the longitudinal-field polarity was positive. It is hard to believe that the onset conditions for positive corona at the nose were never exceeded during these flights.

We can estimate the onset conditions for corona at the nose of the rocket due to either ambient longitudinal field or net charge on the vehicle. Using the prolate spheroidal formulas from Willett et al.[1] (Section 6.3, Equations 8 and 13), where z = c refers to the tip of the spheroid, we choose the semi-major axis, c = 1.05 m, to match the length of the rocket and the semi-minor axis, b = 0.071 m, to match the tip radius of curvature (b^2/c = 0.00475 m). This gives the longitudinal-field and potential coefficients as 92.0 (dimensionless) and 61.9 m^{-1}, respectively. If the breakdown field in air at atmospheric density is taken as 2.7 MV/m, the nose of the vehicle should go into corona when the longitudinal field exceeds 29 kV/m (in the absence of corona from the tail) or when the vehicle potential exceeds 44 kV (in the absence of ambient field). Reduced air density at higher altitude will yield proportionally smaller values.

Now suppose that corona from the sharp tail of the rocket is so efficient that it equalizes the vehicle to the ambient potential at that level (or, equivalently, charges the rocket to a voltage such that the field at its tail vanishes). Corona onset at the nose can then be estimated in two ways. First, suppose that the (forward-directed) field at the tail of our spheroid due to vehicle potential, -61.9 V, cancels that due to ambient field, 92.0 E_z. The vehicle potential is seen to be proportional to the longitudinal field (V = 1.5 E_z), and the longitudinal-field coefficient at the nose is doubled, reducing the corona-onset field to 15 kV/m. Alternatively, suppose that corona-
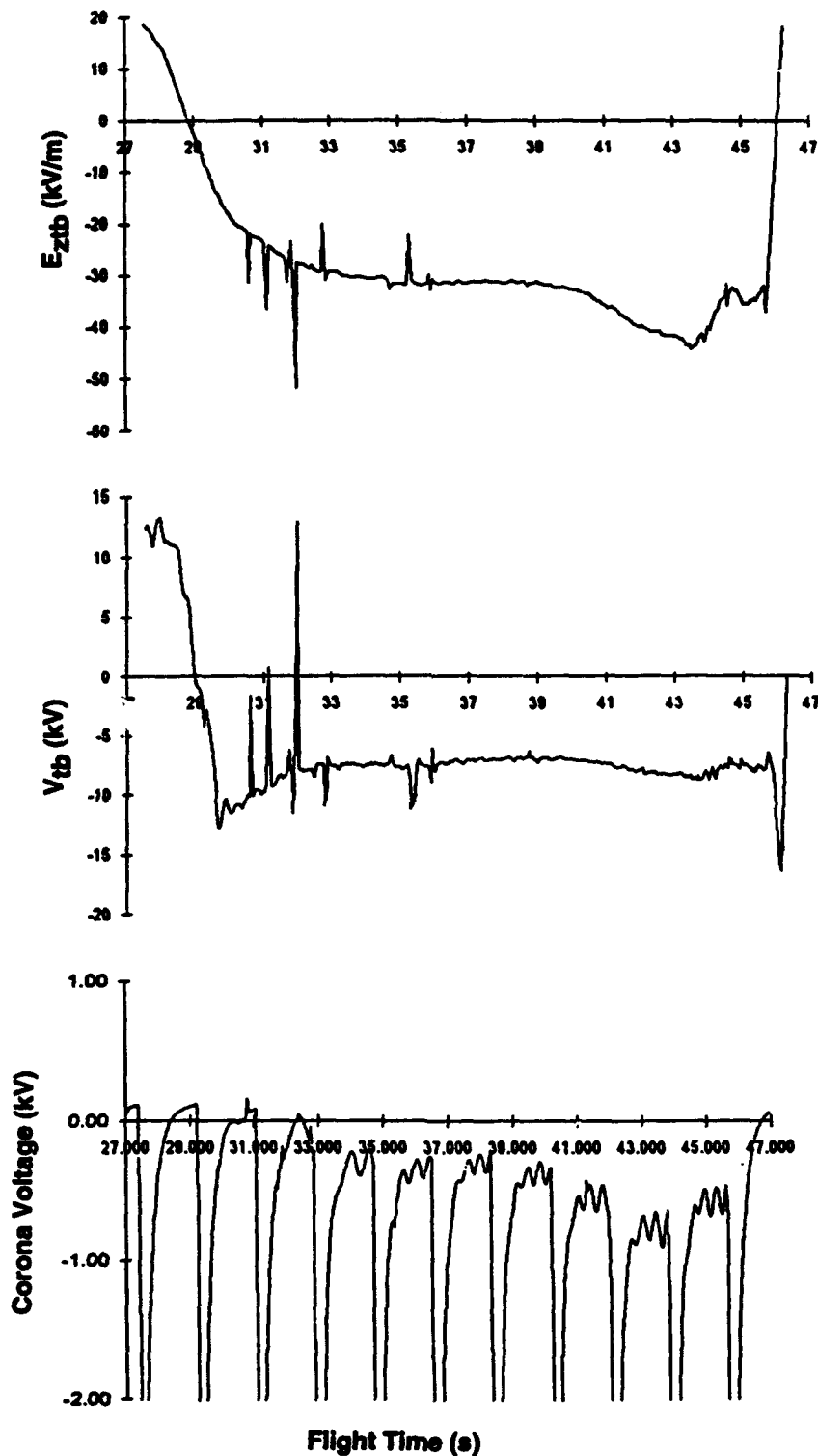
Figure 4c. Magnification of the raw time series from the 17 July flight, showing E_{ztb} (top panel), V_{tb} (middle panel), and voltage on the corona assembly (bottom panel) for ten seconds during descent. Notice the trend reversal in V_{tb} as E_{ztb} falls below -16 kV/m and the continuous negative voltage on the corona assembly during the entire duration of reduced V_{tb} magnitude

77
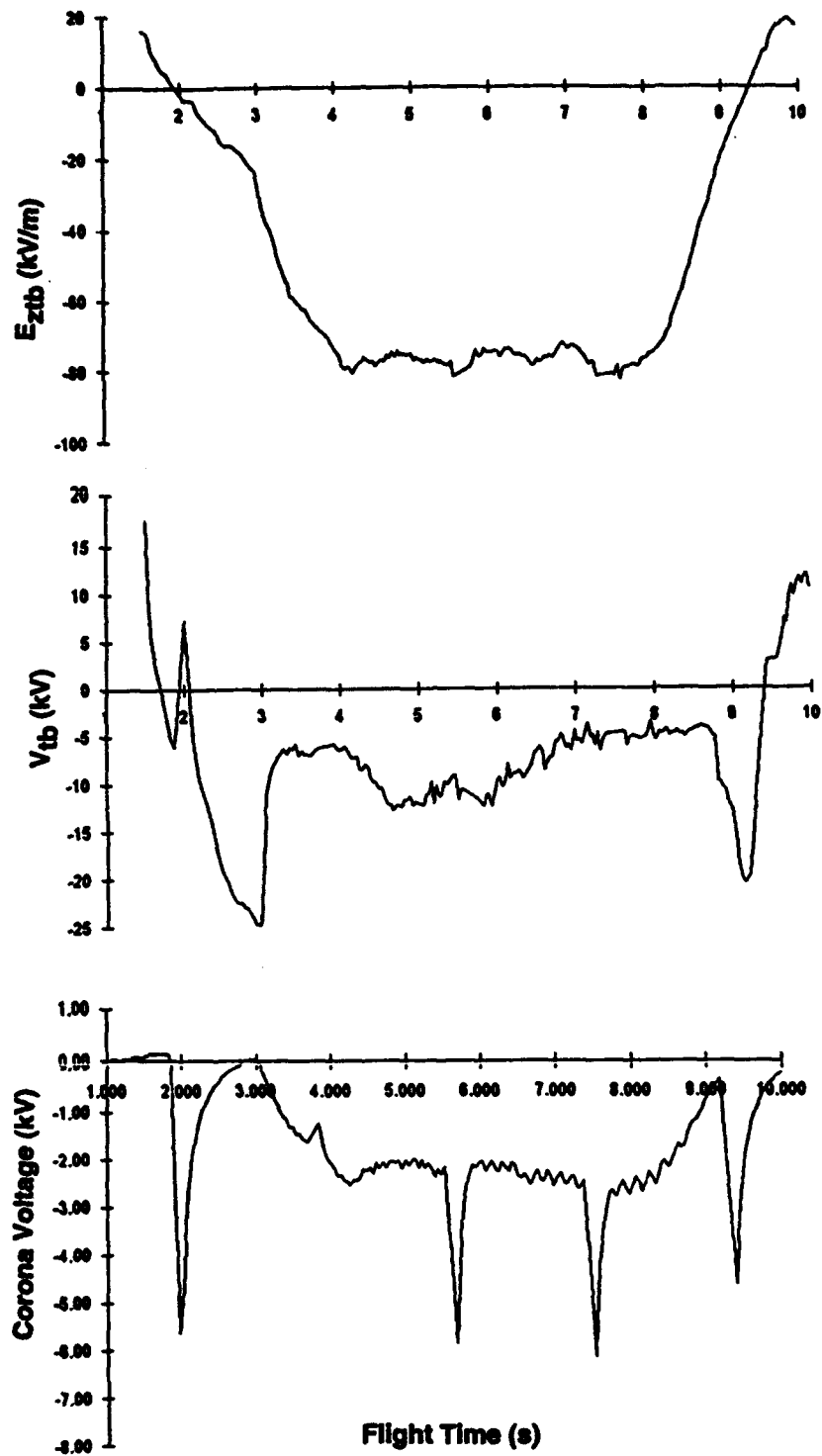
Figure 45. Magnification of the raw time series for nine seconds early in the 17 July flight, similar to Figure 44. Notice that the trend reversal in V_{tb} and the continuous negative voltage on the corona assembly begin together as E_{ztb} falls below -22 kV/m, fully one second before it reaches the plateau at -80 kV/m. The anomalies end as E_{ztb} rises through -18 kV/m, about one second after leaving its plateau

equalization of the tail is equivalent to an uncharged vehicle of twice the length in an ambient field. The semi-axes of the corresponding spheroid become $c = 2.11$ m and $b = 0.100$ m (preserving the nose curvature), giving a longitudinal-field coefficient of 161 and a corona-onset condition of 17 kV/m, in good agreement with the first method. (Note that the maximum possible radius of curvature of the nose, a hemispherical nose cap of radius 0.0349 m, yields $b = 0.271$ m, a field coefficient of 33.7, and a corona-onset field of 80 kV/m by the second method.)

This calculation appears to be in reasonable agreement with our observations for negative longitudinal fields, where the trend reversal in V, presumed to be caused by negative-corona onset at the nose, occurred between -8 and -22 kV/m. Unfortunately, positive corona from the nose should then have occurred both on 19 July and on 17 July, when E_z was computed to exceed +60 kV/m. The fact that no trend reversals were observed for positive E_z can only be rationalized by assuming that positive corona from the nose is much less "efficient" than negative corona from the tail, so that the vehicle potential remains anchored to the ambient potential near the tail.

Our calculation fails to give the observed proportionality between V and E_z, however. Simultaneous values of these variables during the three flights, excluding periods of negative E_z on 17 and 19 July, imply the approximate relation, $V = 0.3E_z$. This suggests that corona from the tail of the rocket is doing a relatively poor job of anchoring the potential of the vehicle in either field polarity, seeming to contradict the conclusion of the previous paragraph.

It appears that we really do not understand either the trend reversal in V or the plateau in E_z discussed in this section. We may, nevertheless, be able to detect a difference between the data in the plateau and other data at smaller negative values of E_z. Figure 46 shows the stator signals from all eight mills during the period while $E_{ztb} = -80$ kV/m. Notice that the noise is relatively large and highly correlated on all channels, even though two of the stators are covered. This is in contrast to a period of $E_{ztb} = -40$ kV/m, shown in Figure 47, where there is also significant noise but it is not highly correlated and only appears on uncovered stators. Further remarks about the validity of this E_z plateau may be found in Section 5.4.

5.3 Validation of Measurements

Figure 48 illustrates just how robust these rocket data are. All the differences and sums of opposing mills that were defined in Eqs. (18) are plotted during the four seconds around apogee on 17 July. Notice that the sums from the two pairs of middle mills (F_{mp} and F_{mq}), are almost indistinguishable, even though not measured simultaneously as discussed above, whereas there is a large and consistent difference between these and both the upper (F_{tp}) and lower (F_{bp}) sums. All of these sums converge to a low value (implying zero longitudinal field and little charge on the vehicle) near apogee (t + 28.9 s). These observations lend considerable credibility to the calculated longitudinal field, which depends primarily on $F_{ip} - F_{jp}$ as pointed out above. Even in the presence of large vehicle charge, as indicated by the large positive and negative offsets of all the sums at the beginning and end of this figure, respectively, the longitudinal field is still clearly distinguishable.

Notice further that the differences of the top, middle (right and left) and bottom mill pairs (F_{lm}) are essentially the same, whereas F_{mn} is 90 deg. out of phase, as expected. Clearly, the
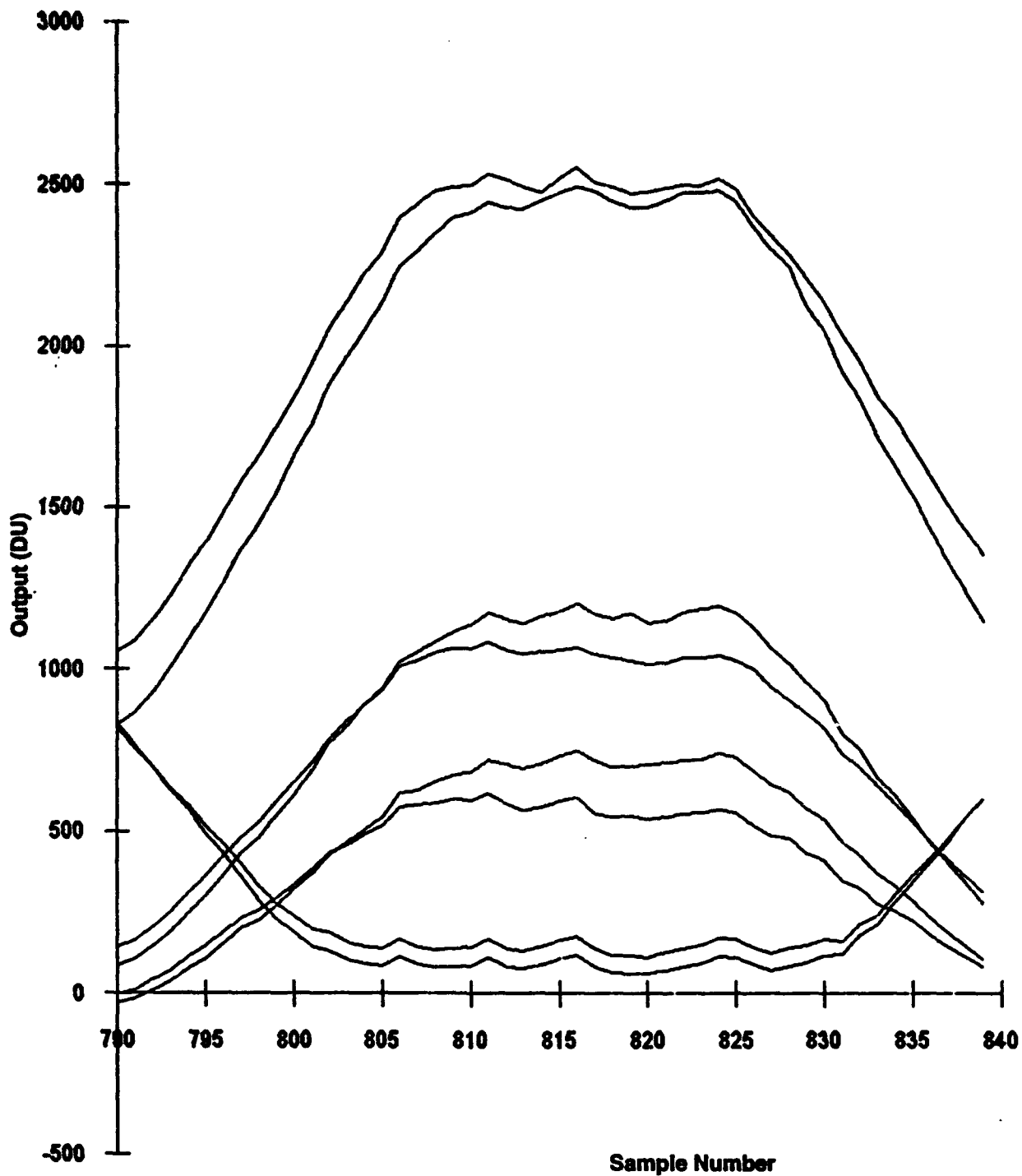
Figure 46. Telemetry output from all eight stator channels for roughly half a mill period during the -80 kV/m "plateau" in E_z early on the 17 July flight. All the stators except MB and MT, the lowest pair of traces, are uncovered during most of this interval

80
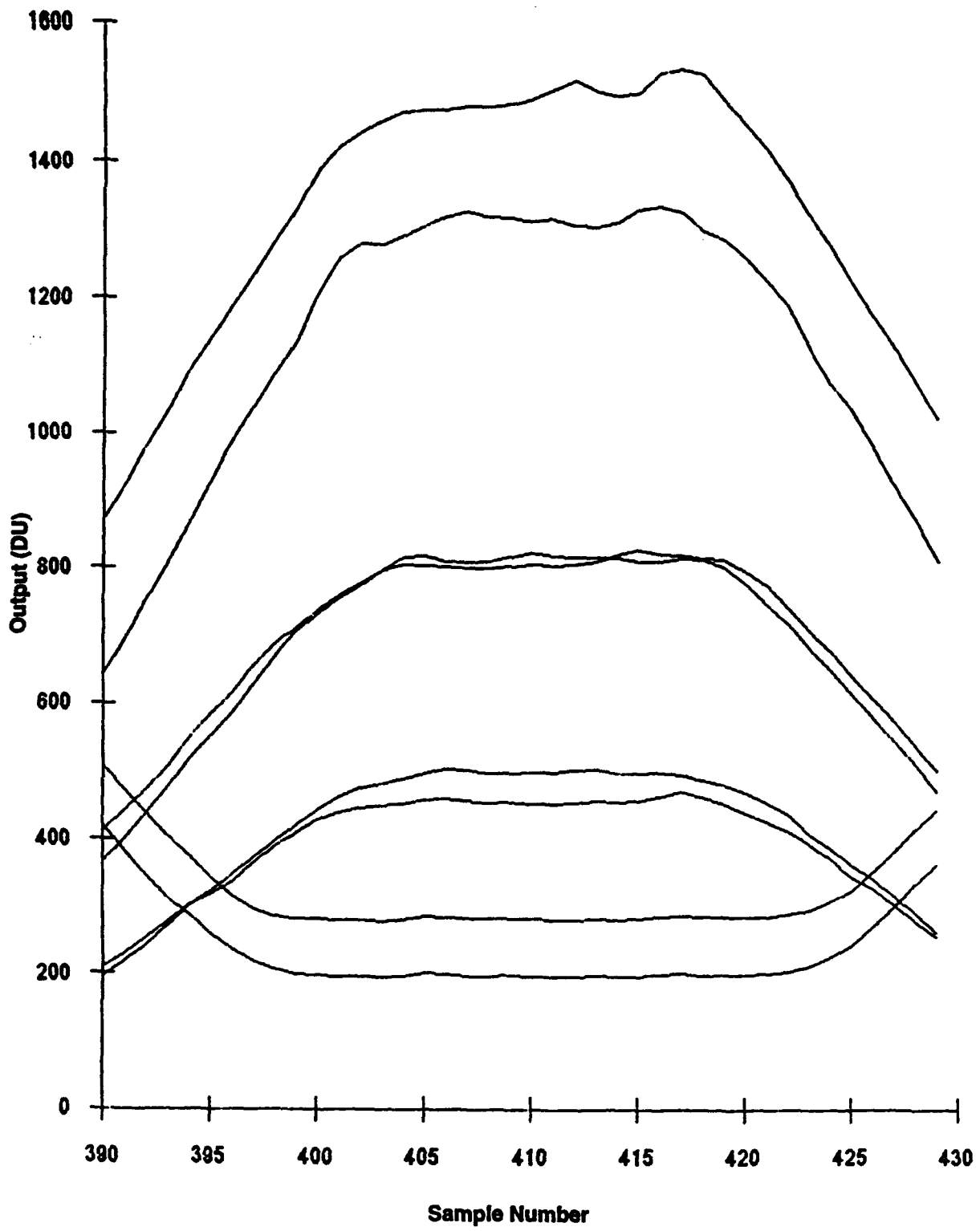
Figure 47. Similar to Figure 46 during a period of $E_{ztb} = -40$ kV/m somewhat later in the same flight

81
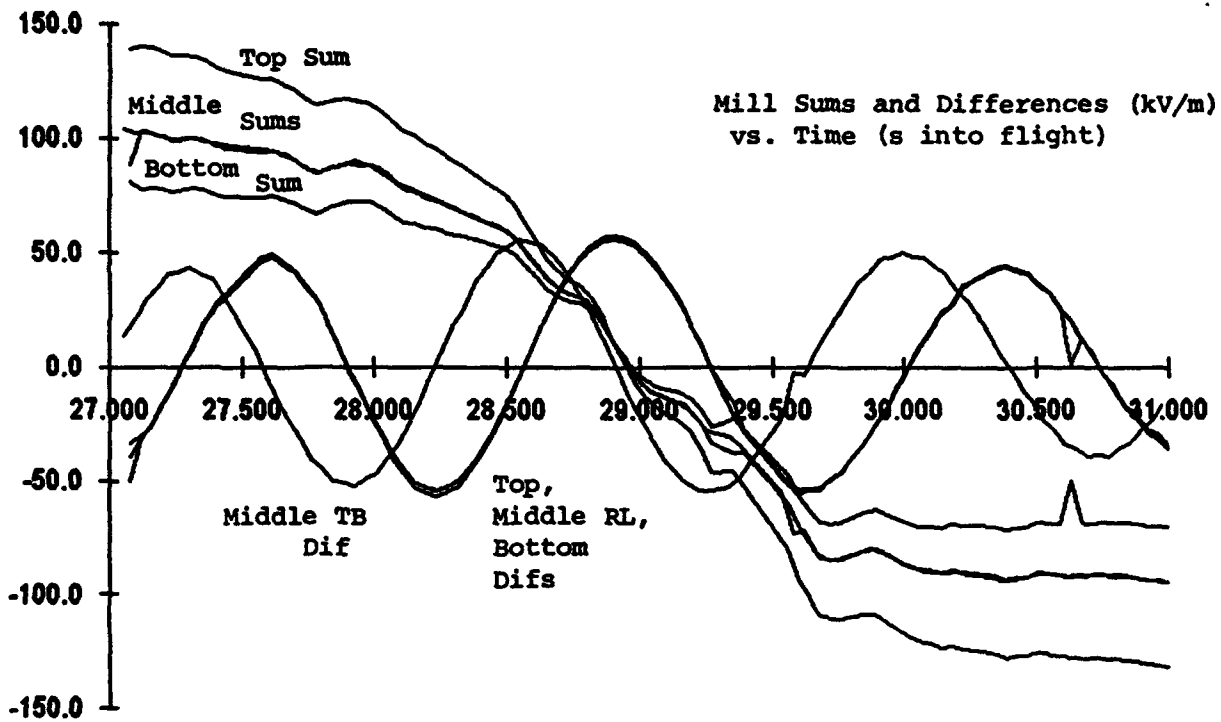
Figure 48. All eight raw differences and sums (F_{im}, F_{mn}, F_{ip}, and F_{mq} defined in Equation 18) are plotted in kV/m versus time for 4 s centered on the apogee of the 17 July 92 flight -- the same period shown in the upper panel of Figure 43

82

three independent measures of E_y are in excellent agreement. Not only are these differences uncontaminated by changes in longitudinal field and vehicle potential (as determined by the sums), but the sums also appear free of any contamination from the transverse fields that are expressed by these differences. Evidently, the symmetry of the vehicle assumed in Eq. (1) is nearly perfect.

The accuracy of the potential coefficients (a_{iv}) can be verified by examining the calculated longitudinal field during artificial charging cycles, since it is these coefficients that must be accurately known to remove the effect of potential variations from E_z (see Eqs. (18) and (19)). This has been done in Figure 49, which shows V_{tb} and E_{ztb} late in the flight of 8 July. This is a worst-case test, since it combines the largest potential changes produced by the on-board, high-voltage system with a period of relatively low ambient fields. Although there are noticeable perturbations in E_{ztb} associated with the charging events, they are seen to be smaller than 1 kV/m and, comparable to the noise level.

The accuracy of the longitudinal-field coefficients (a_{iz}) may be tested in a similar manner by examining the calculated vehicle potential during abrupt changes in the ambient longitudinal field, since these coefficients control the removal of E_z variations from V (again see Eqs. (18) and (19)). Natural lightning provided several sudden changes in ambient field during the rocket flights, as indicated by the ground-based field mills. Figures 50, 51, and 52 show simultaneous plots of surface field (Bill Winn, personal communication) and of E_{ztb} for the three flights. Unfortunately, only three of the lightning field changes shown in these plots were greater than 5 kV/m at the ground, and one of those occurred during a gap in the telemetry stream.

The only lightning signature that is unambiguously identifiable in the rocket data is that near the end of the 19 July flight. We know from video records that the flash producing this field change struck the ground SSW of the rocket launcher. Thus, this strike was probably not far from the location of the rocket on the descending leg of its trajectory. The video also shows at least five strokes in this flash, spanning half a second.

Examination of Figure 53 shows that a large change in longitudinal field (at least +40 kV/m, reversing its polarity) and a smaller change in transverse field magnitude (perhaps -10 kV/m) occurred near the time of this lightning flash. Although the rocket-field change preceded that at the surface by some 0.5 s and shows little evidence of multiple strokes, it is likely that the rocket change was a result of the flash. Were it assumed that the net charge on the rocket could not change abruptly due to the lightning, then any coincident change in computed vehicle potential would indicate errors in one or more of the a_{iz}. There was indeed a sudden change in V (nearly +10 kV) at this time, but the size of the ambient field change suggests that this might have been caused by a puff of corona charge from the tail of the rocket, so no conclusion can be reached.

The other large surface-field change for which rocket data are available occurred early in the flight on 17 July and is shown in Figure 54. In this case there was no abrupt field change at the rocket like that shown in Figure 53. Thus, it is not possible to clearly identify a lightning field change in this record. Similarly, the several smaller field changes registered by the ground-based mills during the flights showed no obvious lightning signatures in the rocket data.
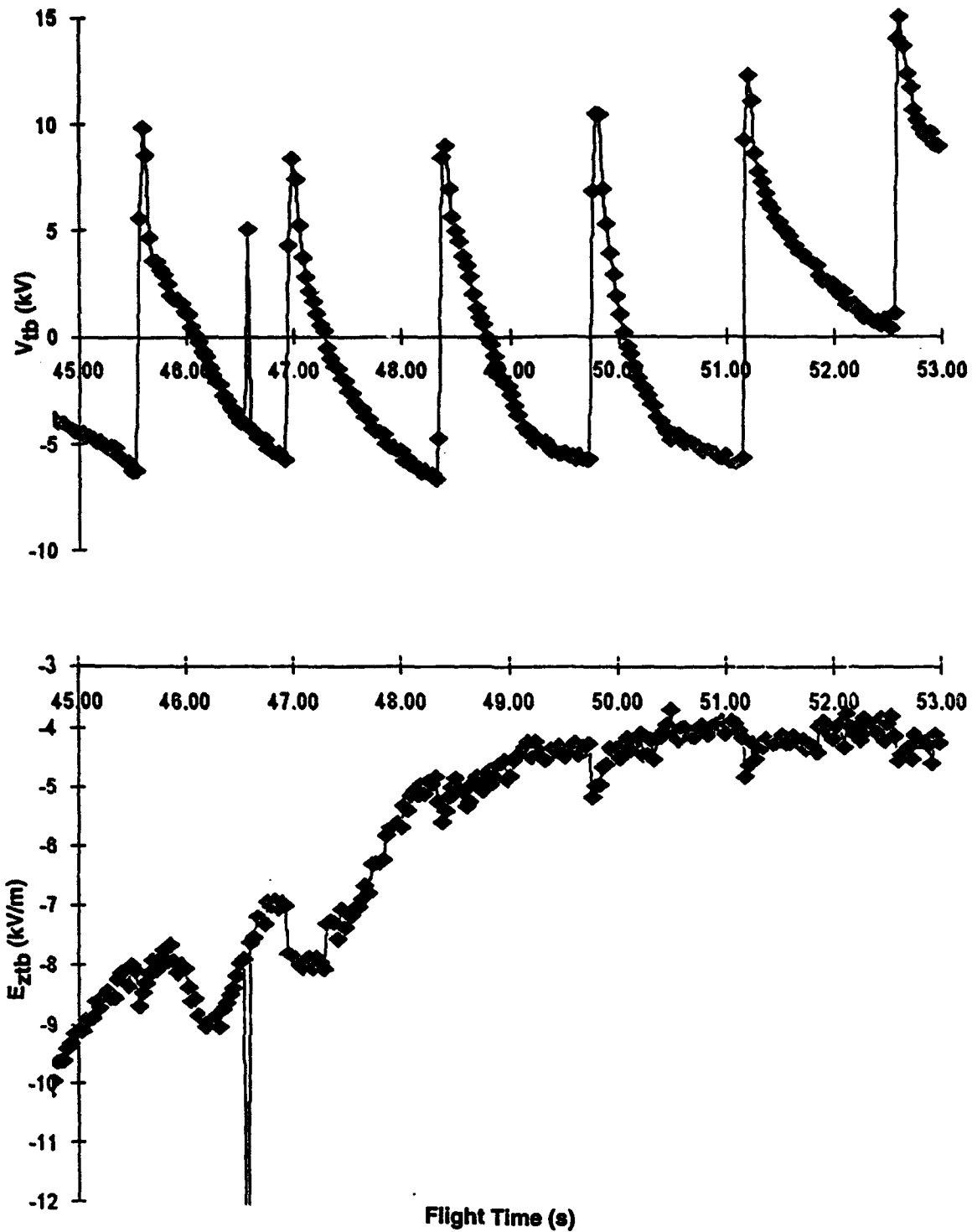
Figure 49. Raw V_{tb} (upper panel) and E_{ztb} (lower panel) versus time late in the flight on 8 July 92, showing the minimal effect of the charging cycle on the longitudinal field component
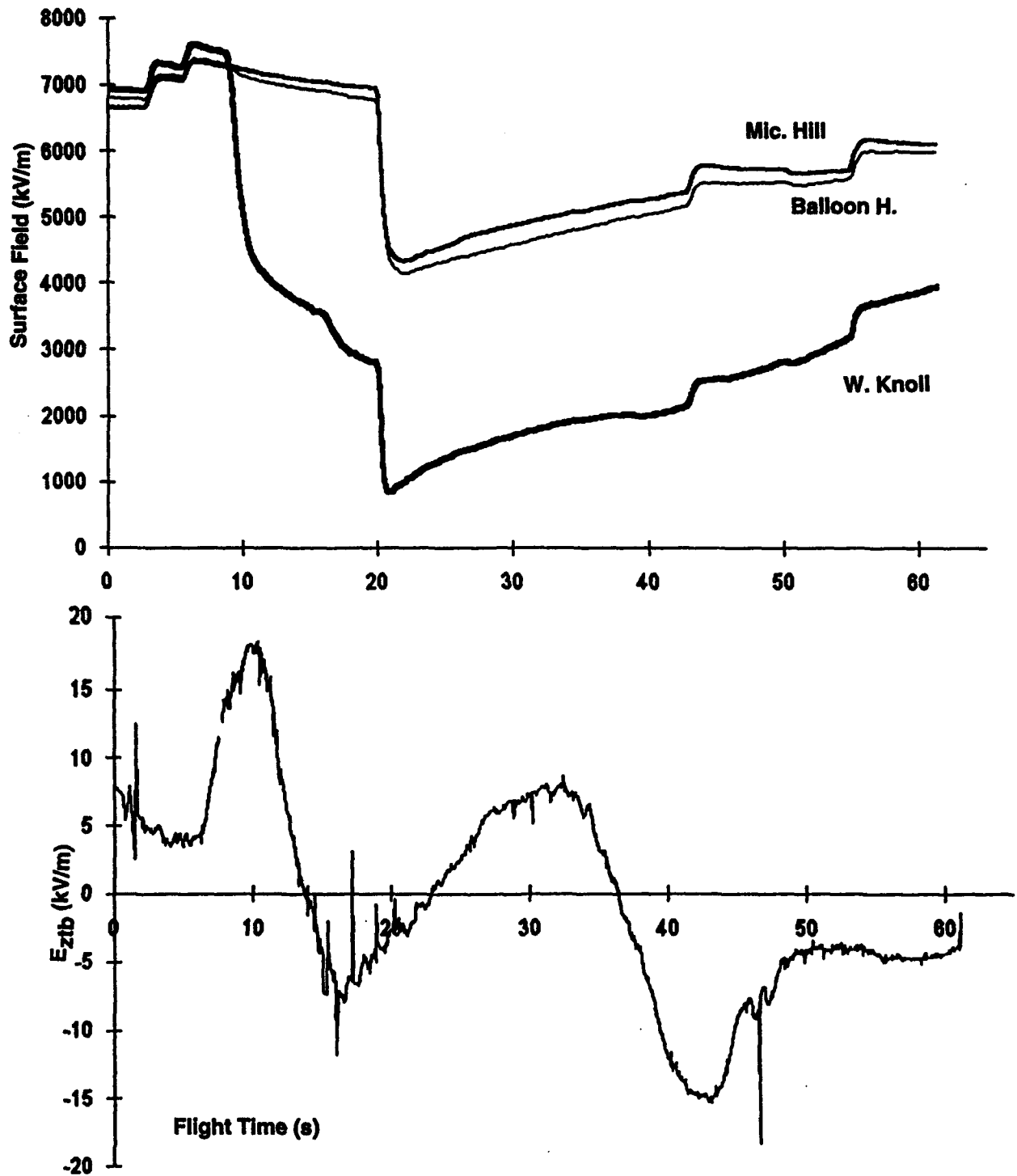
Figure 50. The upper panel shows surface-field records from three Langmuir-Laboratory field mills during the flight of 8 July 92. Note that the "physics" sign convention is used here -- a positive (foul-weather) vertical field is produced by negative charge aloft. The mill closet to the REFS launcher (West Knoll) is plotted with the heaviest line, the next closest (Microphone Hill) with the medium line, and the farthest (Balloon Hangar) with the fine line. The lower panel repeats the raw E_{ztb} record from the rocket (Figure 40) for comparison
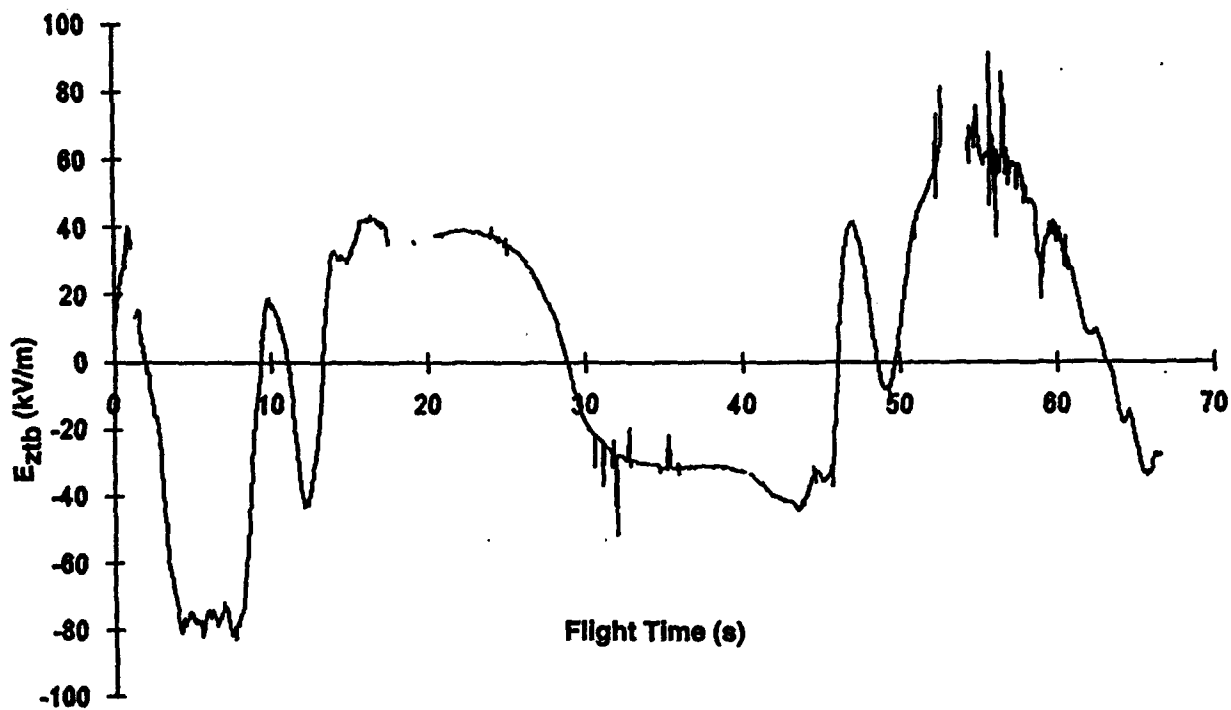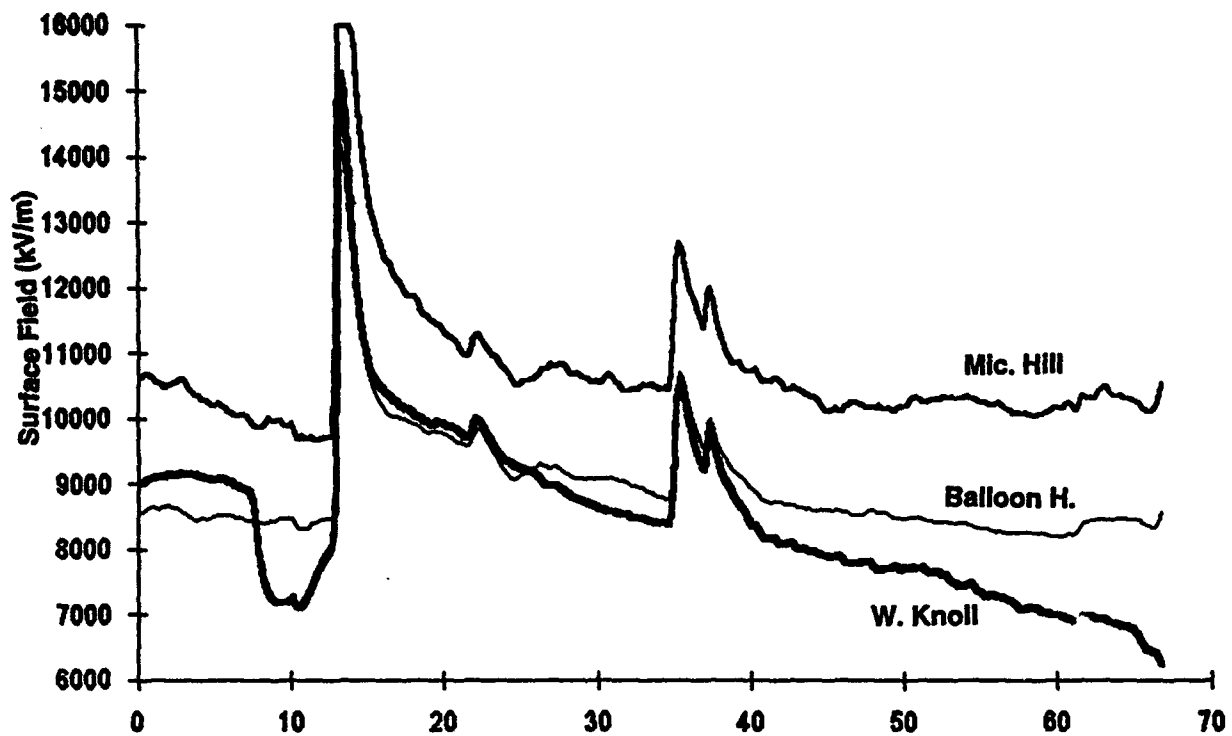
Figure 51. Same as Figure 50, but for the 17 July flight. Note the large surface-field change at t + 13 s, which is shown in more detail in Figure 54

86
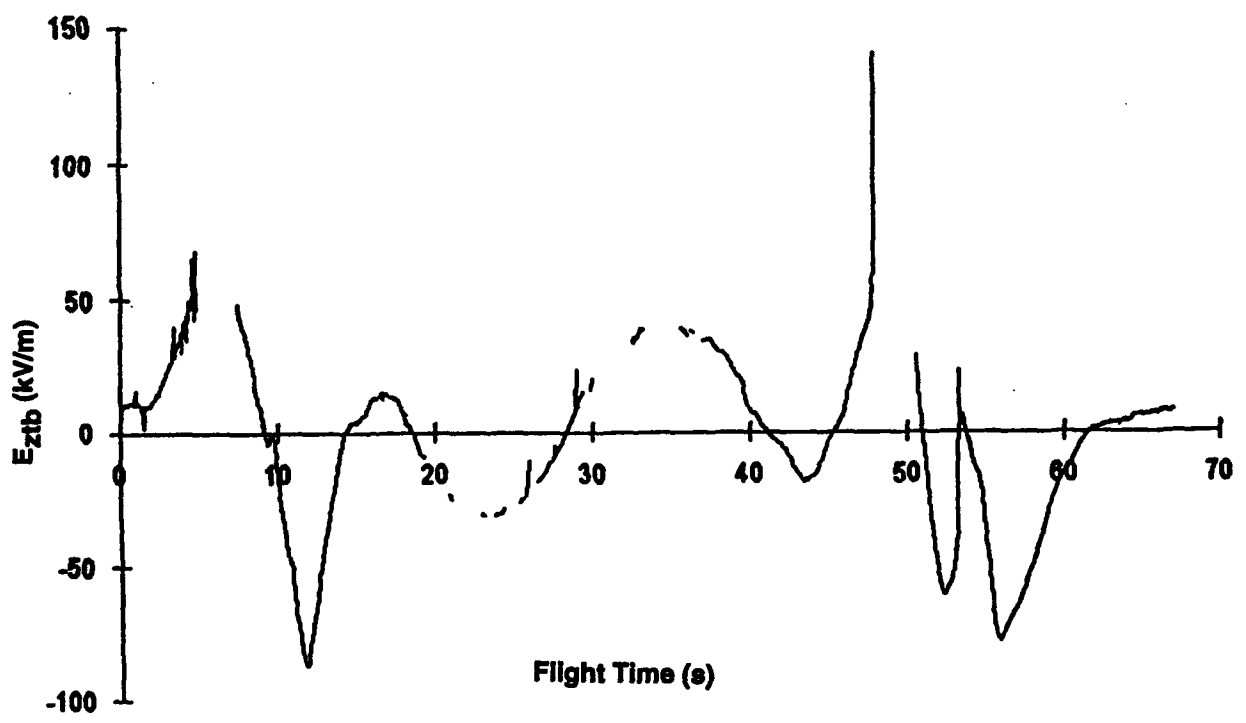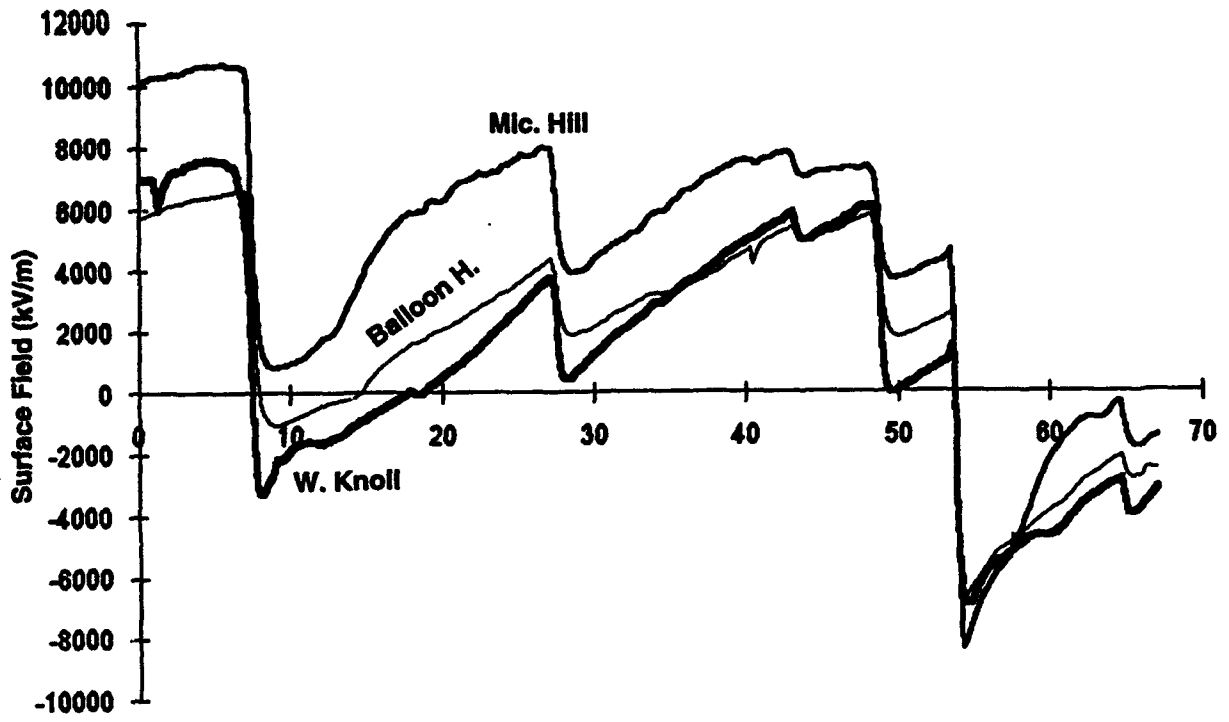
Figure 52. Same as Figure 50 for the 19 July flight. Note the large surface-field changes at t + 7.5 s and at t + 53.7 s. The former occurred during a telemetry drop-out, but the latter is clearly visible in the rocket E_{ztb} record and is examined in more detail in Figure 53
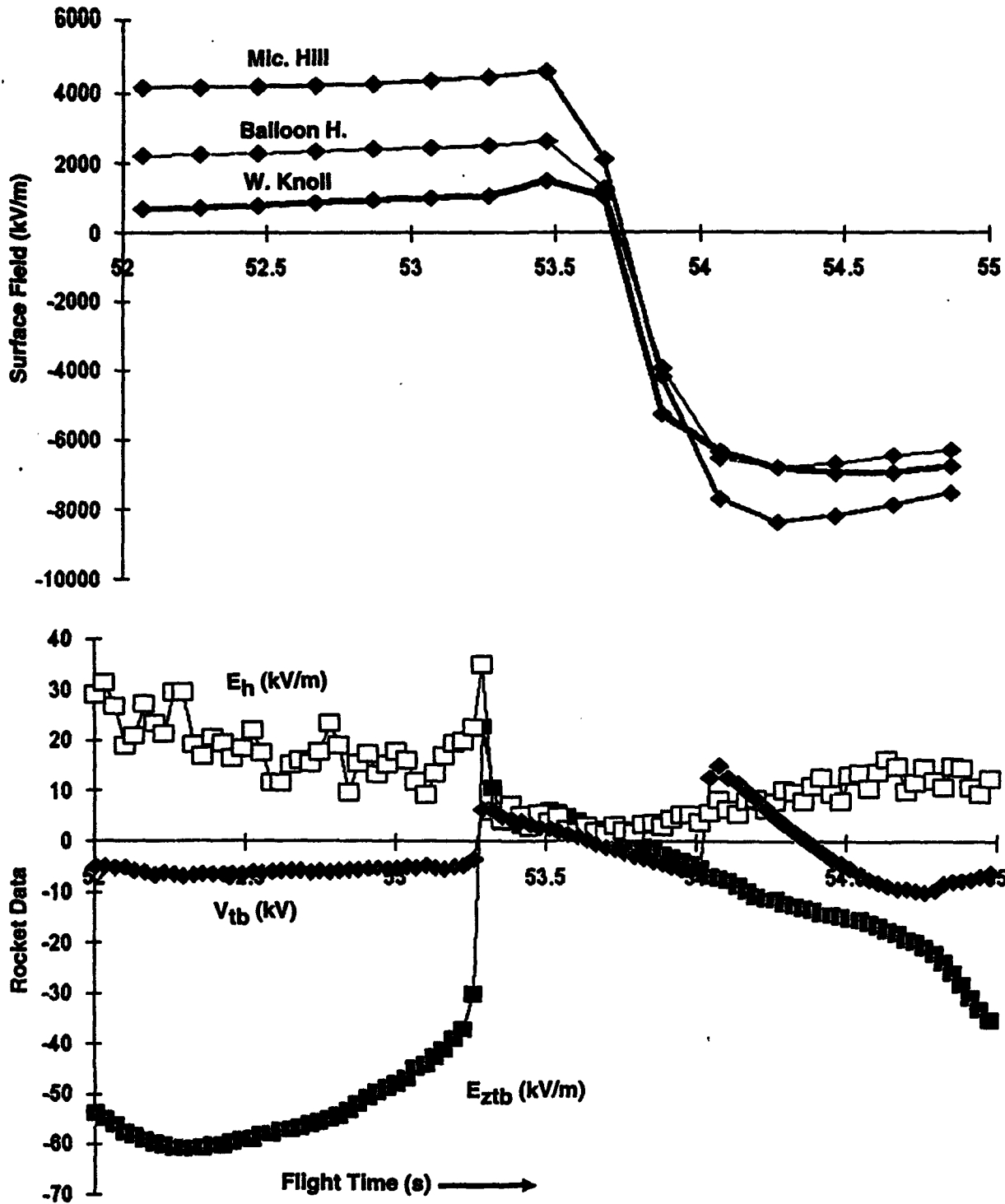
Figure 53. A magnification of the second large lightning event in Figure 52. The upper panel shows the surface-field records as before. The lower panel shows the raw rocket data for the same period. The solid squares are E_{ztb}, the open squares are E_h, and the solid diamonds are V_{tb}. Note that the lightning field change is clearly visible in the rocket data, where it appears at a slightly earlier time because of the slow response of the ground-based mills. (The abrupt change in potential about 0.7 s after the lightning is caused by the on-board charging system)
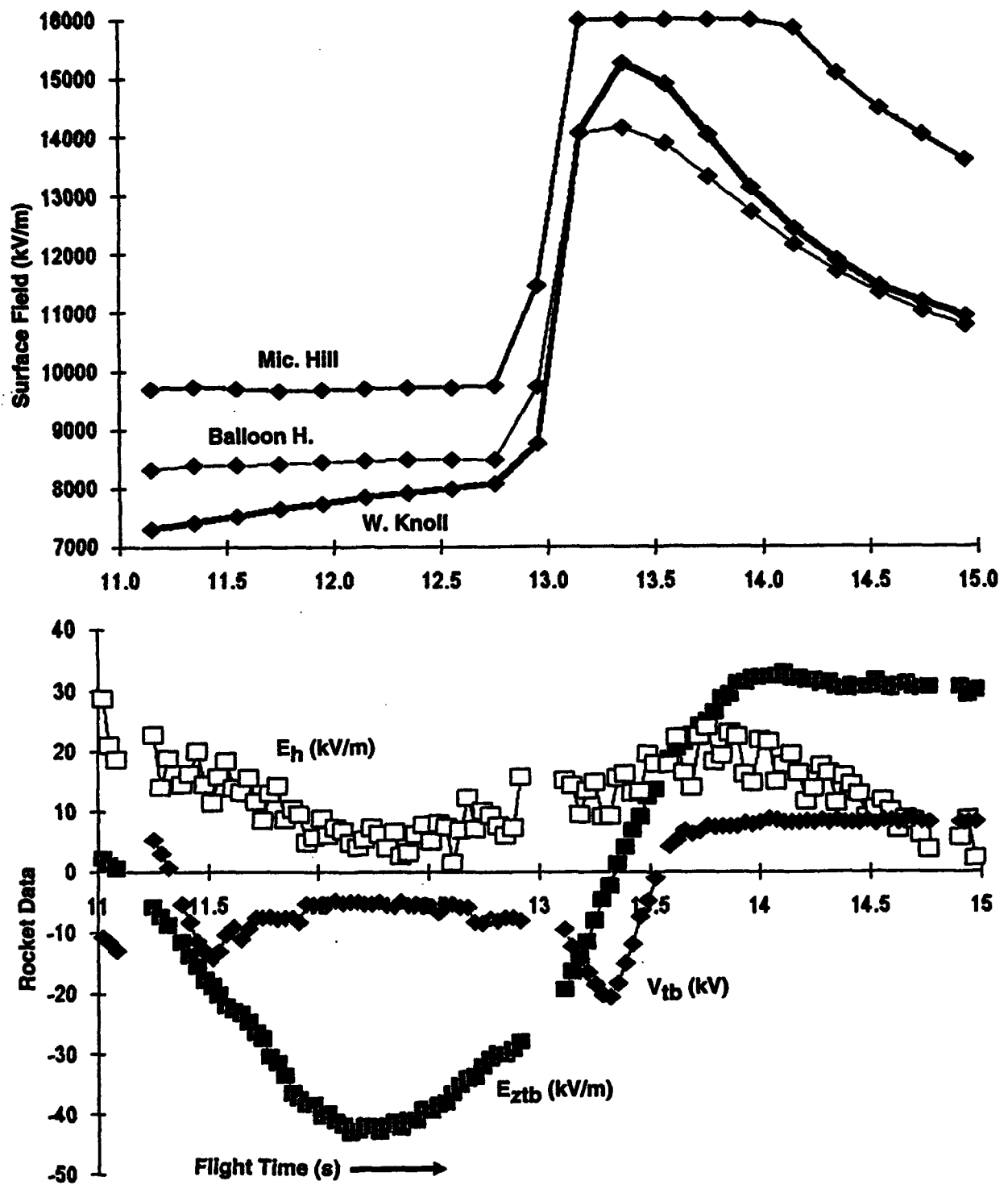
Figure 54. A magnification, similar to Figure 53, of the large lightning event shown in Figure 51. Note that the Microphone-Hill mill is saturated briefly after the lightning. The gaps in the rocket data are due to telemetry dropouts coincident with the high-voltage system's being energized

5.3.1 CONSISTENCY WITH LINEAR MODEL

Winn[5] has pointed out a clever means of checking the consistency between our rocket data and the model stated in Section 3. Basically, this model assumes that the fields measured at each of the eight mills depend linearly on only four independent quantities -- the three ambient-field components and the vehicle potential. In other words, it should be possible to construct only four linearly-independent variables from the eight mill readings. This assumption will be valid, for example, if the ambient field is uniform throughout a sufficiently large volume containing the rocket (that is, there are no substantial conductors or appreciable space charge close to the rocket) and if the rocket itself is a perfect conductor (that is, there is no significant charge deposited on any of its insulating surfaces). These conditions might easily be violated when the rocket is in corona, is being charged by impact with precipitation particles, or is penetrating a region of strong ambient space-charge density. The expected linear dependence among mill readings might also be destroyed by excessive noise on, or improper operation of, individual field mills.

Testing for linear dependence among a set of variables becomes straightforward if only one dependent variable is anticipated. Winn's method is simply to construct a linear formula that predicts the variable chosen to be dependent in terms of the others. It is easy to compute the coefficients of such a relationship by a linear least-squares fit to the data. Then the RMS deviation between the predicted and observed values of the dependent variable (that which has been minimized) can be computed as a measure of the validity of the model. The beauty of this method is that it does not depend on the stationarity of the ambient field in either time or space.

Because of symmetry, the variables naturally separate into two groups, as demonstrated in Section 5.1. Eq. (18) shows that each of the differences, F_{lm} and F_{mn}, between opposing mills is determined by only one of the transverse-field components, E_x or E_y, whereas the sums, F_{lp} and F_{mq}, depend only on the longitudinal field and vehicle potential, E_z and V. In particular, F_{tp}, F_{mp}, and F_{bp} form a set of three simultaneously measured variables of which only two should be independent. It is this set to which Winn's method has been applied.

We chose to take F_{mp} as the dependent variable and express it in the form

$$F_{mpk} = AF_{tpk} + BF_{bpk} + e_k, \quad k = [1,N] \tag{21}$$

where A and B are constants, e_k is the error between the predicted and observed values of F_{mpk}, and the subscript k refers to one set of measurements at a particular time. "Laboratory" values of A = 0.415 and B = 0.564 can be derived by substituting solutions for E_{ztb} and V_{tb} from Eq. (19) into the definition of F_{mp} in Eq. (18) and using the laboratory values of the a_{ij} from Eq. (5) or from Table 15.

The RMS error in Eq. (21) was minimized over a sample of N sets of measurements to determine separate values of A and B for each of the three rocket flights. This was done using reduced samples that included the apogee turn-over and some artificial-charging events in each case but excluded noisy or otherwise problematic data. The domain and results of these calculations are shown in Figure 55 and in Table 16. The figure shows the values of F_{mpk} and 10

90

x e_k as functions of time for the samples used to compute A and B during each flight. The table shows the resulting values of A and B, the RMS error over the sample, the sample size, N, the RMS error over the entire flight, and the number of measurement sets in the entire flight. Also shown for comparison are the RMS error produced by using the "laboratory" values of A and B, and the standard deviation of the predicted variable (F_{mp}), over the entire flight. (The last column in Table 16 will be explained below.)

Table 16. Results of Linear-Dependence Test on F_{lp}

| Case | A | B | Sample | | Entire Flight | | | | |
			RMS(e) (kV/m)	N	RMS(e) (kV/m)	N	Lab RMS (kV/m)	$\sigma (F_{mp})$ (kV/m)	$\sigma (E_y)$ (kV/m)
"Lab"	0.415	0.564							
08 July	0.422	0.565	0.269	708	0.505	1573	0.669	44.7	0.331
17 July	0.407	0.568	0.494	235	1.694	1473	1.922	129.8	0.930
19 July	0.433	0.542	0.794	767	1.544	1491	1.835	112.2	0.685

We find it reassuring that the constants A and B deduced from the laboratory calibrations and those computed from the three flights are very similar and that the RMS errors in each case are fairly small -- less than 2% of the standard deviation of the predicted variable, even when calculated over significantly larger data sets than the samples used to derive those constants. Clearly, the linear formula of Eq. (21) explains nearly all of the observed variability in F_{mp}, lending credibility to both the rocket data and its interpretation.

There is another obvious test that can be applied to the rocket data. As discussed in Section 5.1, at any particular time there are three independent ways to derive E_y, from the measured value of F_{tm}, F_{mm}, or F_{bm}. According to our linear model, these three results should be identical. We have therefore computed the average over the entire flight (k) of the standard deviation $\sigma (E_{yk})$ among E_{ytk}, E_{ymk}, and E_{ybk}, and tabulated this error estimate in the last column of Table 16. Again, the errors are rather small on all three flights. Furthermore, averages of the ratios E_{ytk}/E_{ymk} and E_{ybk}/E_{ymk} do not differ systematically from unity, providing indirect corroboration for the transverse-field coefficients summarized in Table 15, above.

The individual errors, e_k, and standard deviations, $\sigma (E_{yk})$, at particular times, t_k, can also be used to detect failures of the linear model due to measurement errors or breakdown of the model assumptions at those times. For example, Figure 56 shows time series of these errors and standard deviations, along with the raw longitudinal fields, during a short period in the middle of the 17 July flight. Notice that the spikes on the E_{ztb} record coincide with spikes in e_k, $\sigma (E_{yk})$, or both. A somewhat arbitrary data-selection criterion has been applied to discard field measurements for which [| e_k | > 1.8] or [$\sigma (E_{yk})$ > 2.0] or {[|e_k| > 1.0] and [$\sigma (E_{yk})$ > 1.4]}. Applying this criterion to the raw field data in the upper panel of Figure 56 results in the "filtered" field data shown in the lower panel of the same figure.
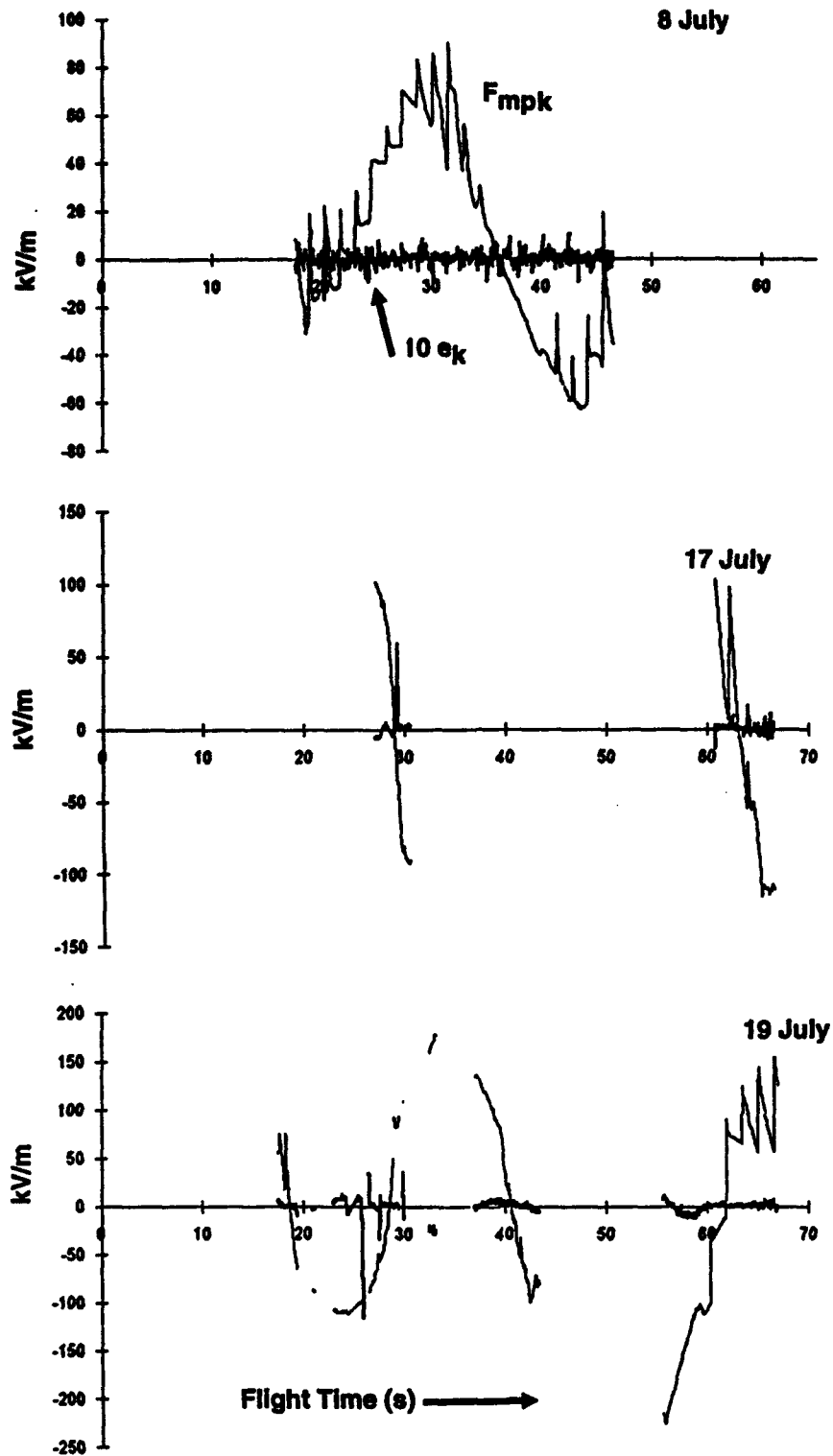
Figure 55. Plots of measured F_{mpk} (thin line) and 10 X e_k (thick line) versus time for the samples used in the least-squares minimizations on the flights of 8 July (top panel), 17 July (middle panel), and 19 July (bottom panel). These graphs may be compared to Figures 40, 41, and 42, which show the computed ambient fields during these flights on the same time scales
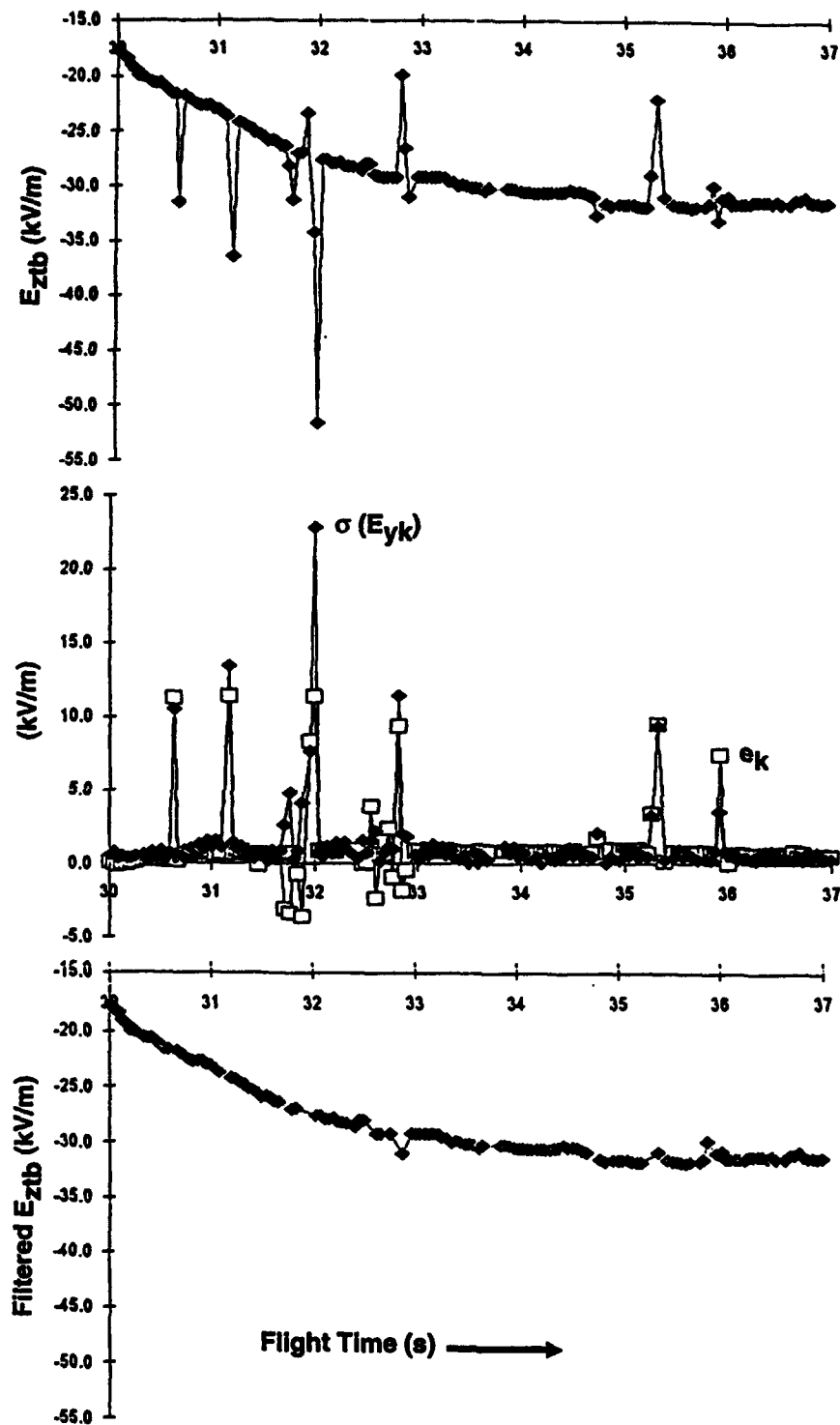
Figure 56. The upper panel shows the raw longitudinal component of the ambient field (a magnification of the top panel of Figure 41) for seven seconds just after apogee on 17 July. The middle panel shows the fit error from Equation 21 (open squares)and the standard deviation among the three estimates of E_y (solid diamonds) for the same period. The lower panel shows "filtered" E_z, after removal of data for which $|e_k|$ or $\sigma (E_{yk})$ exceed specified thresholds

This data-selection criterion has been applied to all three flights to produce the filtered-data plots in Figures 57, 58, and 59, which correspond to the raw-data plots presented earlier in Figures 40, 41, and 42. Notice that data selection has eliminated most of the noise evident in the earlier plots, especially that in E_z. In the process, 10/1573 (ten out of the total of 1573), 133/1473, and 113/1491 data points have been deleted from the flights of 8, 17, and 19 July, respectively. These new plots represent our current best estimate of the actual ambient field and rocket potential during the 1992 soundings. The filtered data will be used from here on throughout this report.

5.3.2 APOGEE TURN-OVER

Another opportunity to check the validity of the rocket-measured fields is afforded by the portion of the flights around apogee. As shown in Section 4.2, above, the 80-degree launch-elevation angle resulted in the rocket's arcing over in a fairly short time and small volume near the top of its trajectory. In the higher trajectory attained on 17 and 19 July, for example, the flight angle rotated from +45 degrees (upward) to zero (horizontal) in a period of 4.8 s, during which time the rocket traveled only 100 m upward and 200 m down range. Continued rotation through zero to -45 degrees was accomplished over similar intervals.

As discussed by Willett et al.[1] (Section 2.1), it was intended that this portion of the flights be used to transfer the transverse-field calibration to the longitudinal component as a check on the laboratory calibration of the longitudinal-field coefficients. This can be done only if the ambient-field vector is sufficiently constant and uniform over the time and volume required to execute the apogee turn-over. Although such stationarity of the field cannot be expected on every flight, it was hoped that the conditions for cross calibration would be satisfied on at least one occasion.

We have already seen in Figure 48 (Section 5.3) that the apogee turn-over on 17 July looks very regular, with the longitudinal field passing through zero at the top of the trajectory. The relevant portion of this flight is re-plotted in Figure 60, which shows the longitudinal-field component and the transverse-field magnitude as functions of flight angle, derived from the trajectory calculated in Section 4.2. Evidently, the transverse field maximizes at apogee, as expected. This figure suggests that the ambient field is directed vertically upward.

Unfortunately, closer examination of these data leads to inconsistencies. The stationary-field assumption implies that the magnitude and direction of the ambient field measured by the rocket should be constant when transformed into a coordinate system attached to Earth. The magnitude of the field can be directly calculated, of course, subject only to the caveats about the transverse-field magnitude, E_h, stated in Section 5.2, above:

$$|E| = (E_z{}^2 + E_h{}^2)^{1/2} \tag{22}$$

If we assume that the ambient field is vertically upward, then an apparent flight angle can also be calculated from the measured field components as follows:

$$\alpha = \tan^{-1}(E_z/E_h) \tag{23}$$

94
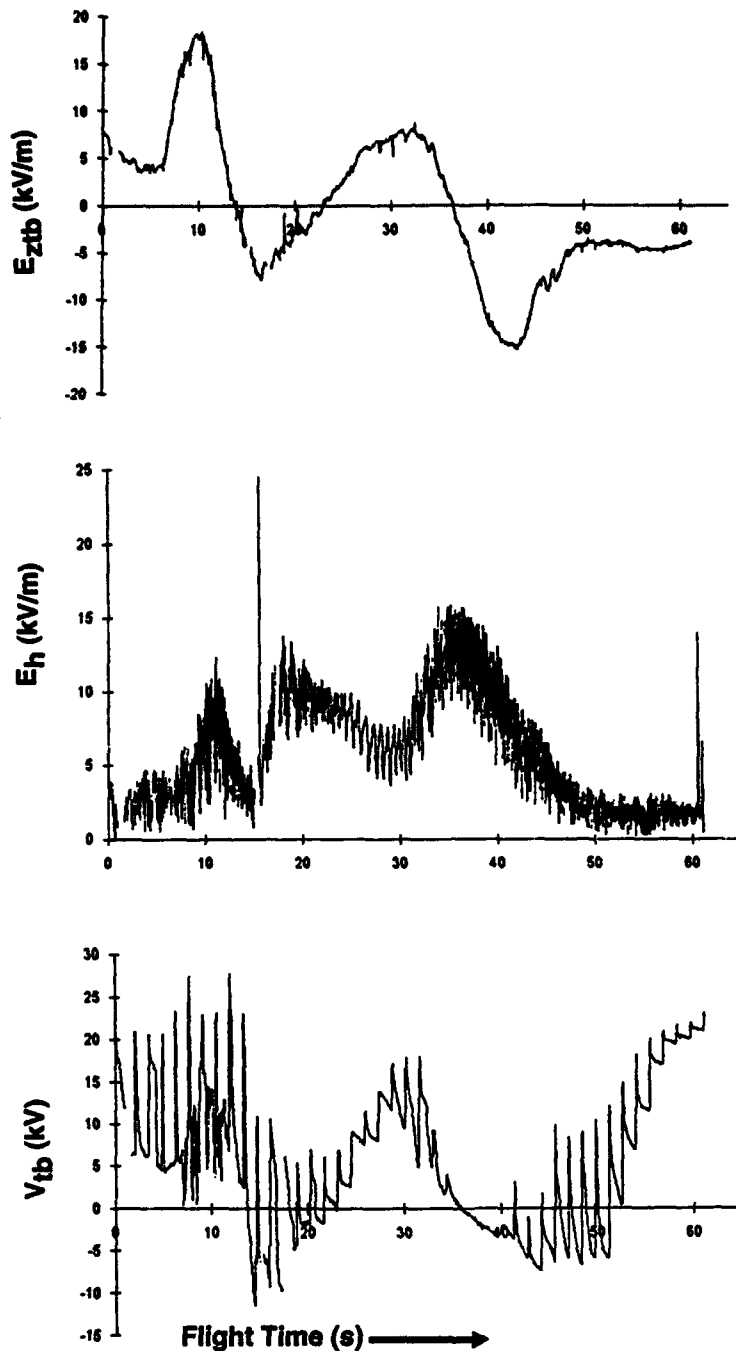
Figure 57. Filtered electrical time series for the flight on 8 July 92. A somewhat arbitrary data-selection criterion has been applied to the raw data to discard measurements for which [| e_k | > 1.8] or [σ (E_{yk}) > 2.0] or {[| e_k | > 1.0] and [σ (E_{yk}) > 1.4]}. Corresponds to Figure 40. The top panel shows the component of the ambient field along the rocket axis (E_{ztb}); the middle panel shows an estimate (E_h) of the magnitude of the field components perpendicular to the rocket axis and the bottom panel shows the vehicle potential (V_{tb}). Simultaneous gaps in all three records are caused by telemetry drop-outs, by the saturation of one or more field mills, by failure of the synchronous-rectification algorithm to correctly determine the rotational position of the shell, or by the data-selection process. Only gaps longer than 250 ms have been shown as breaks in the traces
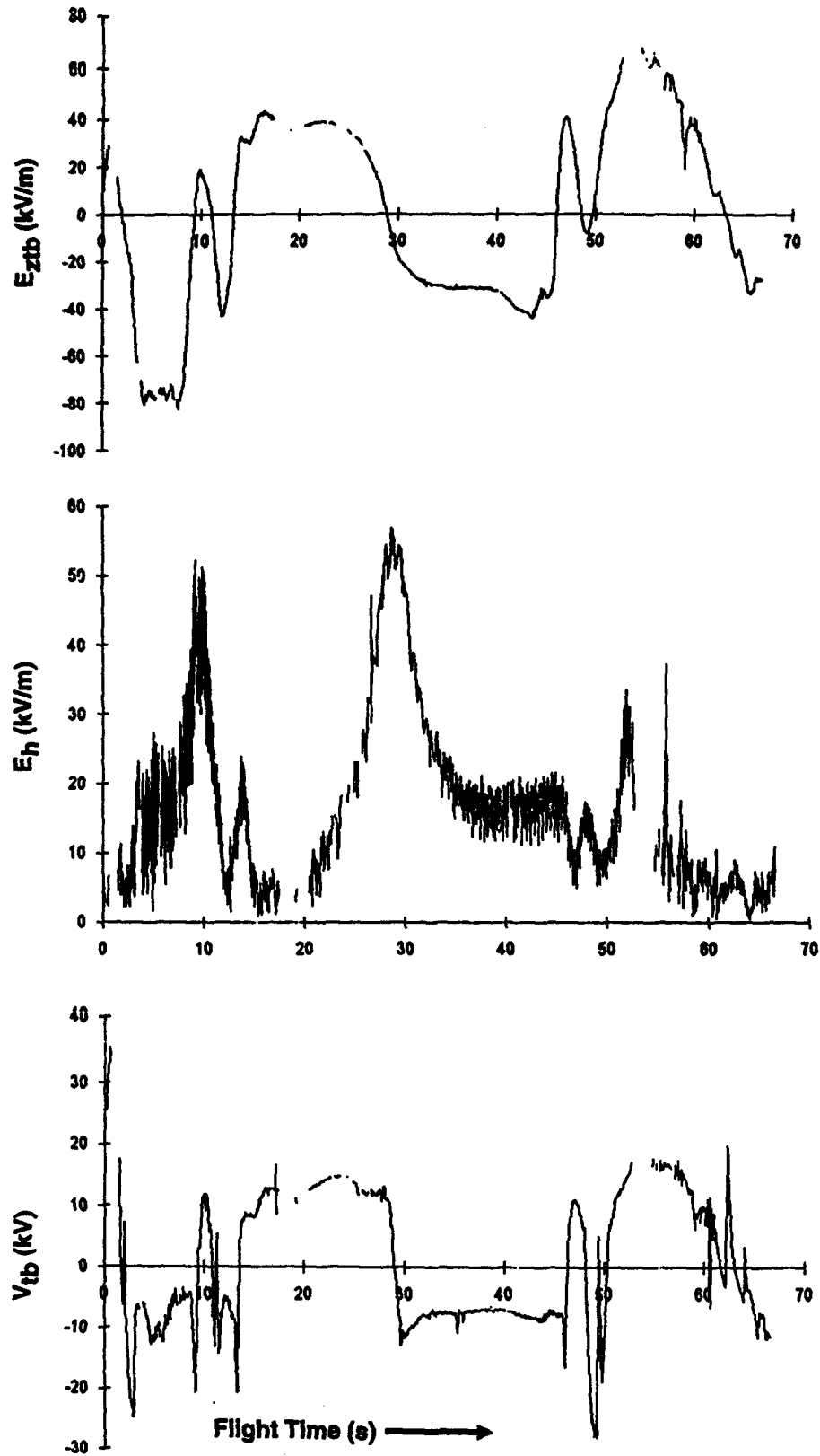
Figure 58. Filtered electrical time series for the flight on 17 July 92. Corresponds to Figure 41. See caption of Figure 57 for details
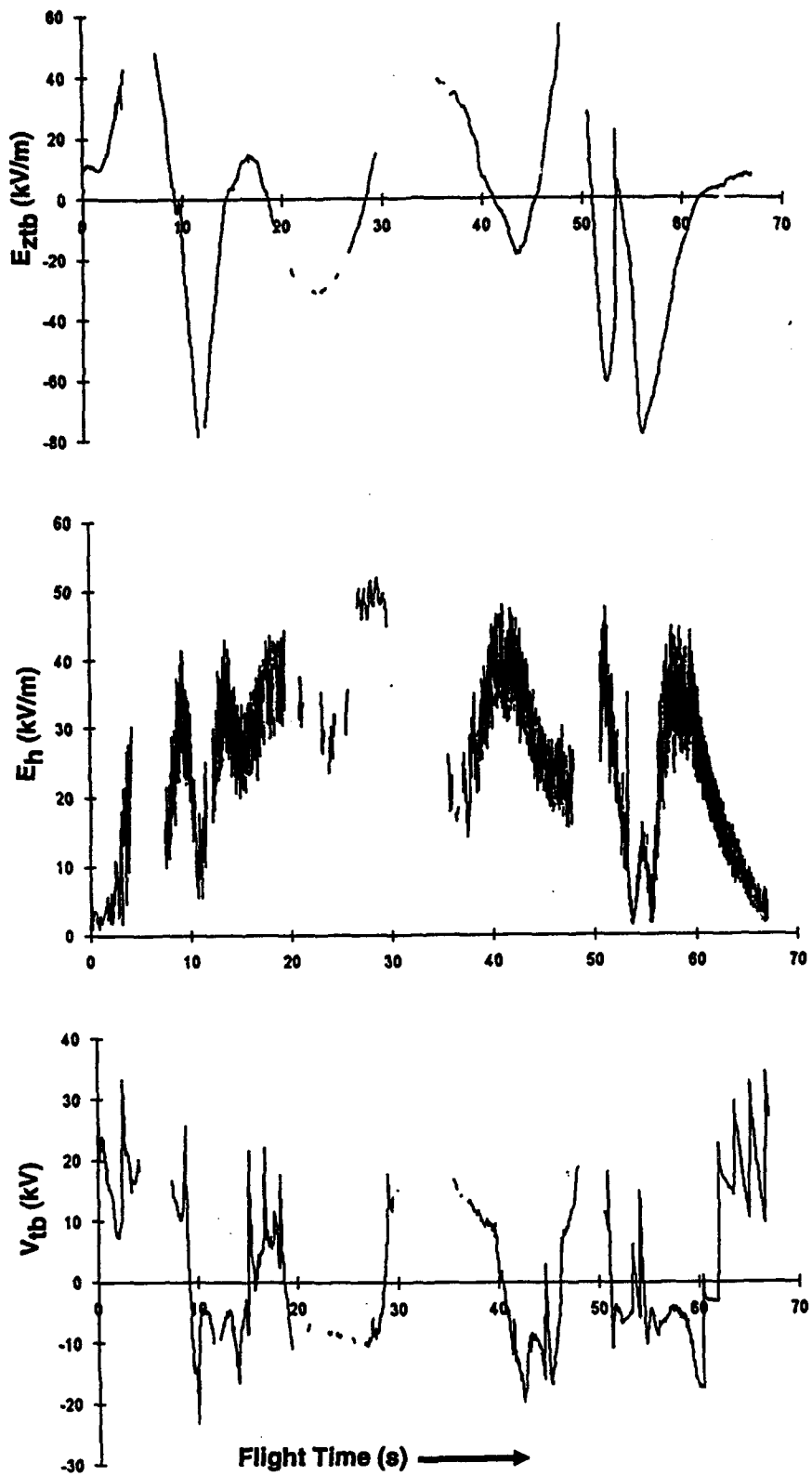
Figure 59. Filtered electrical time series for the flight on 19 July 92. Corresponds to Figure 42. See caption of Figure 57 for details
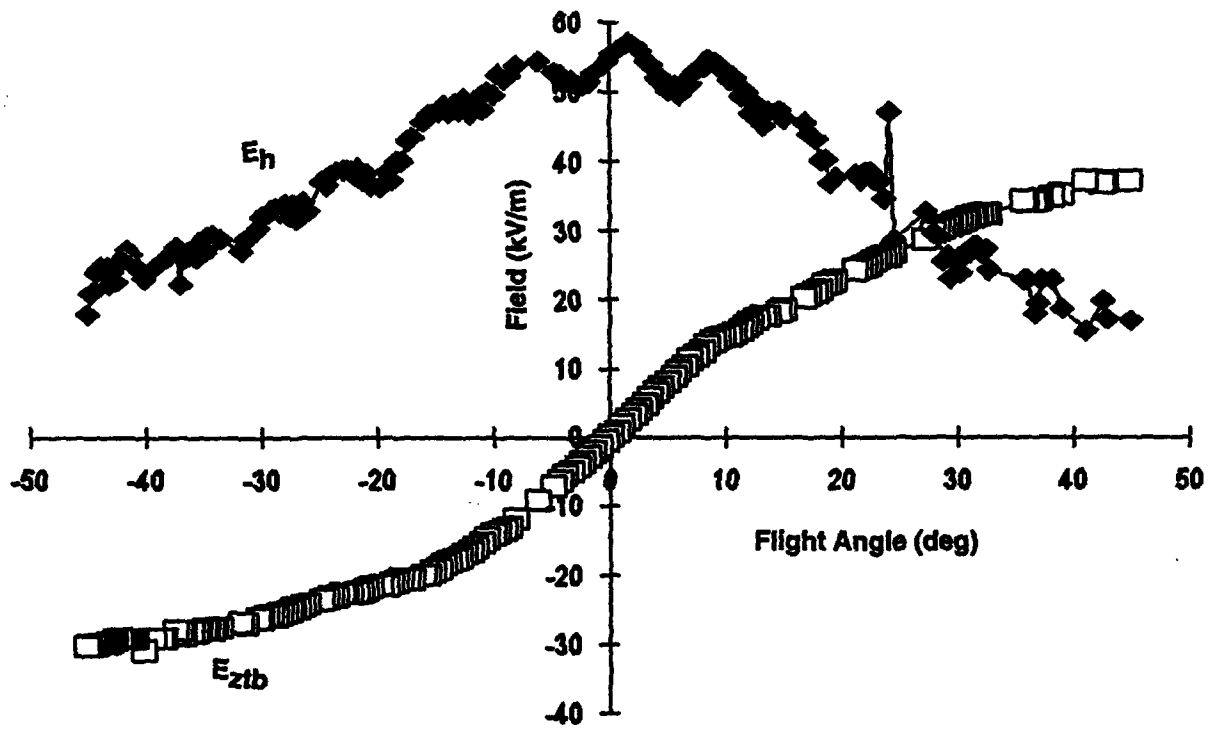
Figure 60. Filtered longitudinal field (open squares) and transverse-field magnitude (solid diamonds) versus flight angle (measured upward from the horizontal, from the computed trajectory) during the apogee turn-over on 17 July

98

(Vertically downward ambient fields require a negative sign.) These formulas have been applied to yield the graphs shown in Figure 61. Evidently neither the magnitude nor the direction of the ambient field has the expected behavior.

The field magnitude shown in the upper panel of the figure can be corrected if we allow a scale factor between the longitudinal- and transverse-field calibrations. If the magnitude of the longitudinal field is increased by a factor of 1.55, for example, the adjusted field magnitude becomes constant, as shown in the upper panel of Figure 62. Unfortunately, this causes the adjusted apparent flight angle to deviate even further from its expected behavior. The scale factor must be decreased to 0.6 to bring the apparent and actual angles into agreement, as illustrated in the lower panel of Figure 62. Apparently, the stationarity assumption is not justified in this case.

Better success is attained on 19 July. E_z and E_h near apogee on this flight are shown in Figure 63. In this case the longitudinal field crosses zero before apogee, suggesting that the ambient field is oriented downward but is not exactly vertical. Field magnitudes and apparent flight angles based on these data are shown in Figure 64. Although the magnitude is fairly constant, the larger-than-expected slope of the apparent angle again suggests a longitudinal-field scale factor somewhat less than unity. Assuming a scale factor of 0.8 and an ambient- field vector lying in the plane of the trajectory but skewed 10 degrees from nadir toward the down-range direction, we find adjusted field magnitudes and apparent flight angles shown in Figure 65. These results are consistent with the assumption of stationary ambient field.

The 8 July flight is somewhat more complicated, but also yields reasonably satisfactory results. Figure 66 shows the measured longitudinal and transverse fields. Again, E_z crosses zero before apogee, suggesting a downward ambient field deviating some 37.5 degrees from nadir in the down-range direction. The data in Figure 66 imply the field magnitudes and apparent flight angles shown in Figure 67. The magnitude is seen to be fairly constant, but the slope of the angle is less than 1:1. In this case, E_z cannot simply be scaled up to correct the apparent angle without destroying the constancy of the field magnitude.

It is possible to resolve this dilemma by allowing the ambient field vector to lie outside the plane of the rocket trajectory. Suppose that this trajectory lies in the x'-z' plane (where primes designate a right-handed coordinate system following the rocket's translation but with the z'-axis vertically upward and the x'-axis horizontal in the down-range direction. Let the direction of the ambient field be defined by the usual spherical polar angles, θ and ϕ, in the primed coordinate system. The ambient-field vector can then be projected onto the x'-z' plane to form an angle, γ, measured clockwise from the z'-axis, as illustrated in Figure 68:

$$\gamma = \tan^{-1}(\tan \theta \cos \phi) \tag{24}$$

The flight angle, α, is measured counter-clockwise from the horizontal x'-axis to the rocket's longitudinal z-axis in the x'-z' plane,' as shown in Figure 69. Equivalently, α is the counter-clockwise angle from the z'-axis to the negative x-axis. Thus we can write

$$\alpha + \gamma = \tan^{-1}(E_z/-E_x) \tag{25}$$
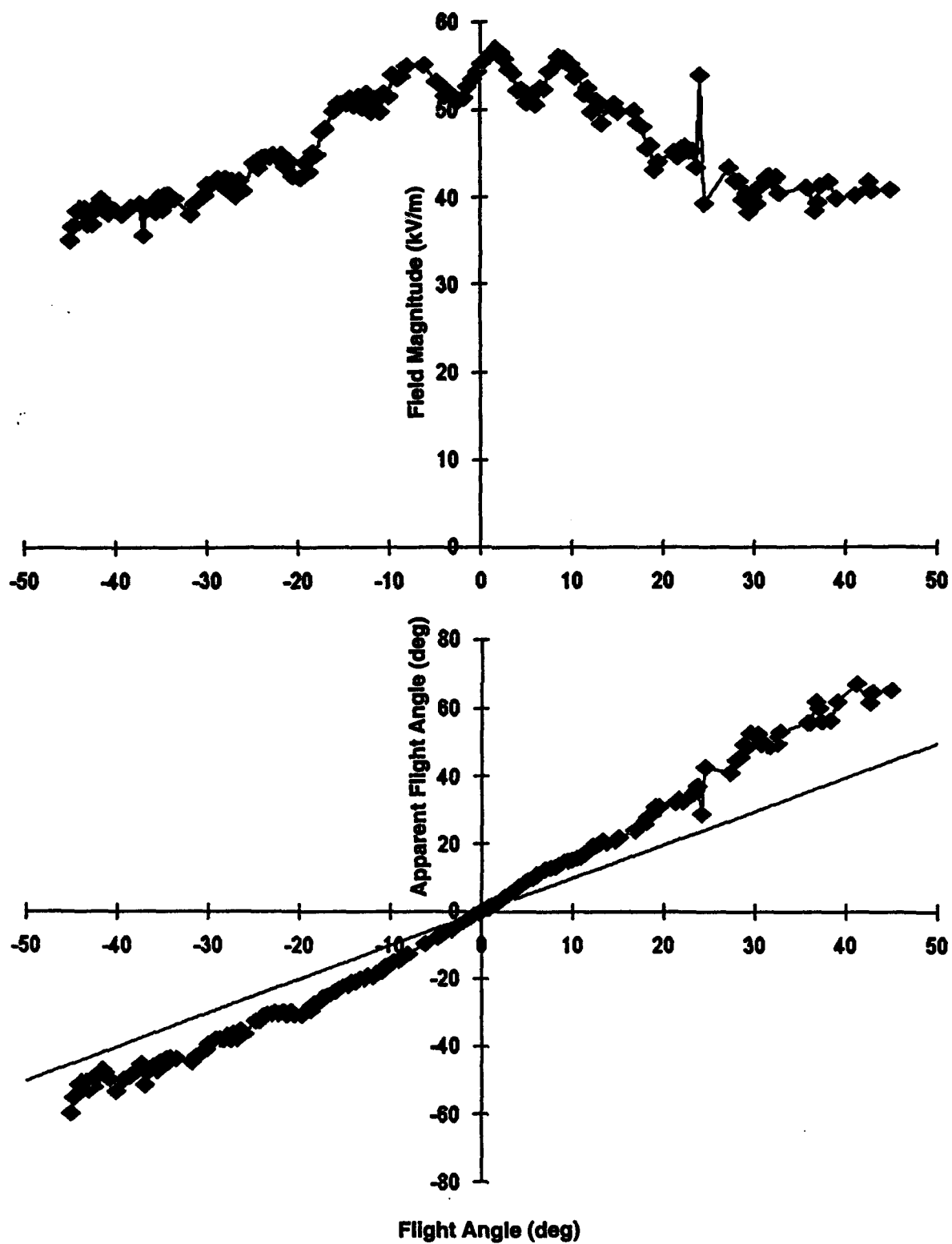
Figure 61. Total field magnitude (upper panel), from Equation 22, and apparent flight angle (lower panel), from Equation 23, versus actual flight angle for the same data shown in Figure 60. The straight line in the lower panel indicates the expected 1:1 relationship between apparent and actual flight angle
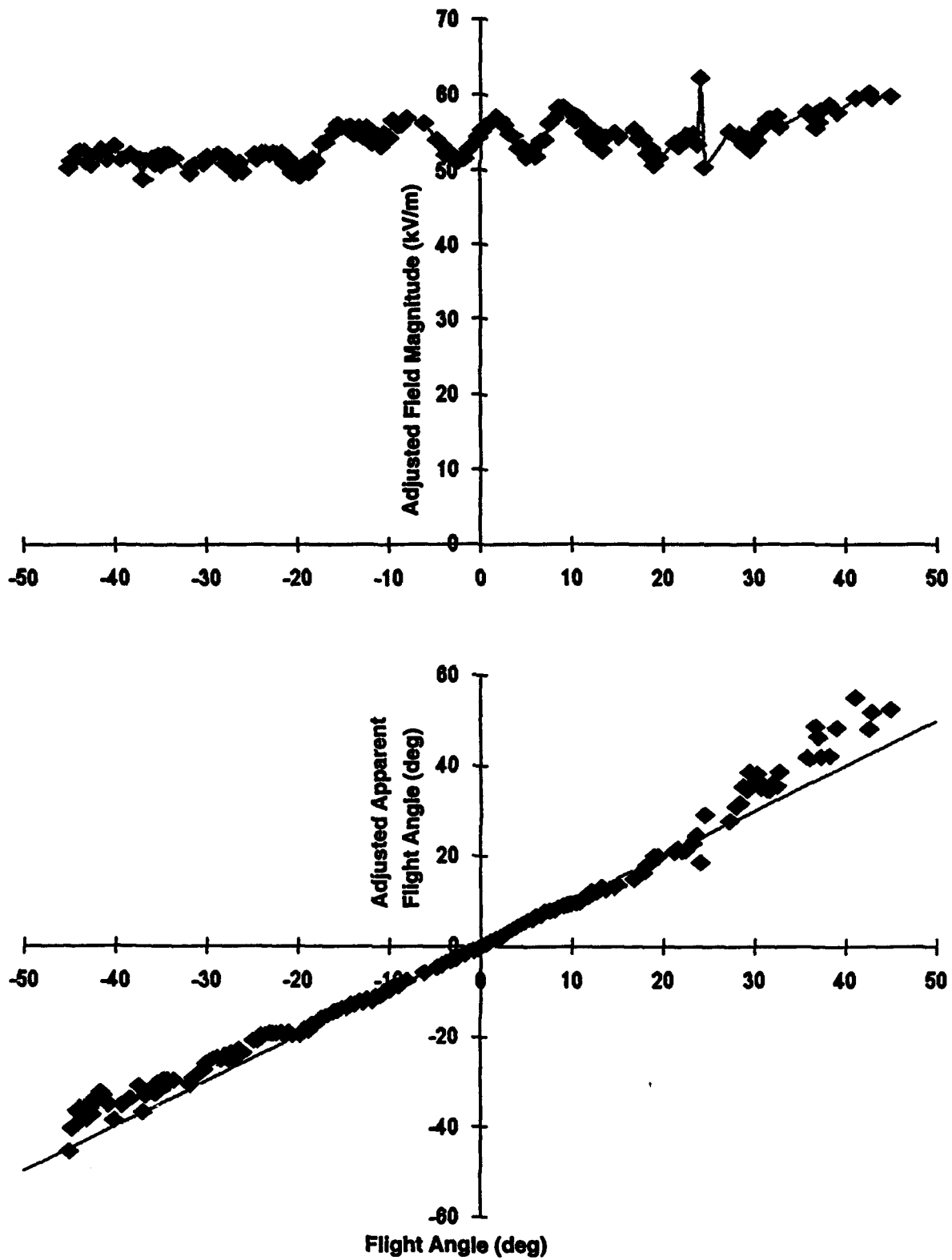
Figure 62. Similar to Figure 61, except that the adjusted field magnitude in the upper panel is computed after scaling E_z up by a factor of 1.55, whereas the adjusted apparent flight angle in the lower panel is computed after scaling E_z down by a factor of 0.6
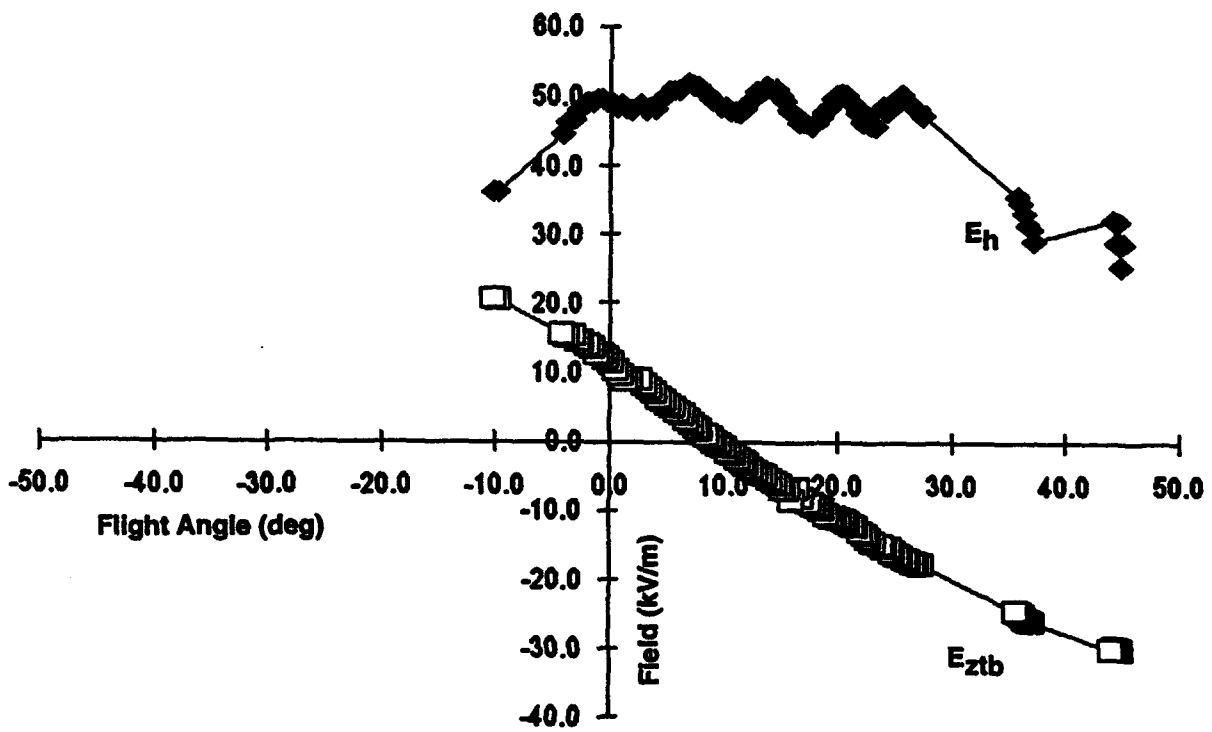
Figure 63. Similar to Figure 60 for the 19 July flight
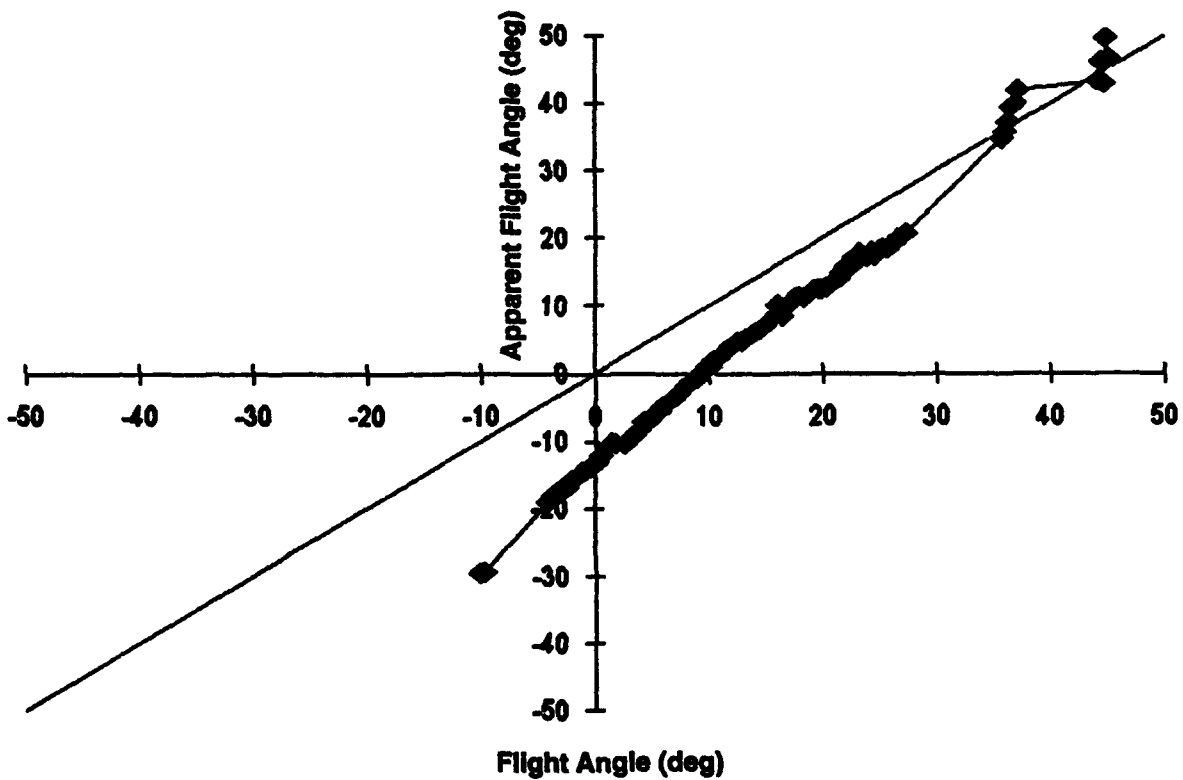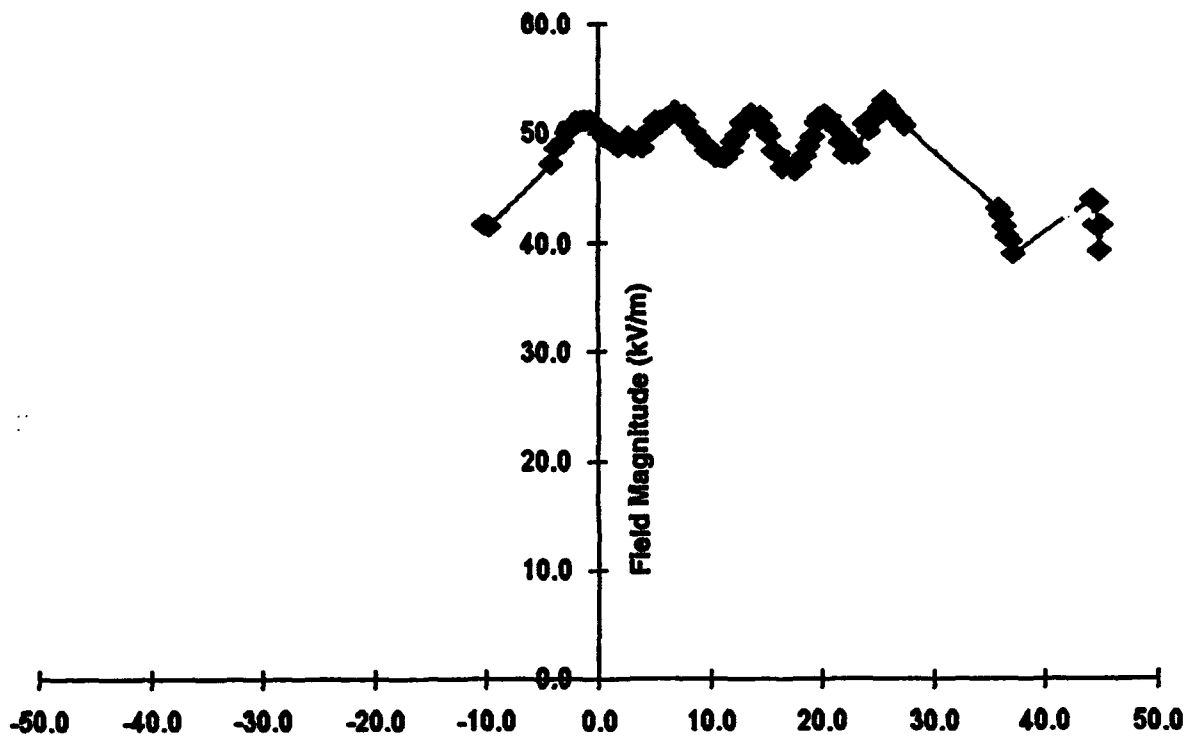
Figure 64. Similar to Figure 61 for the 19 July flight

103
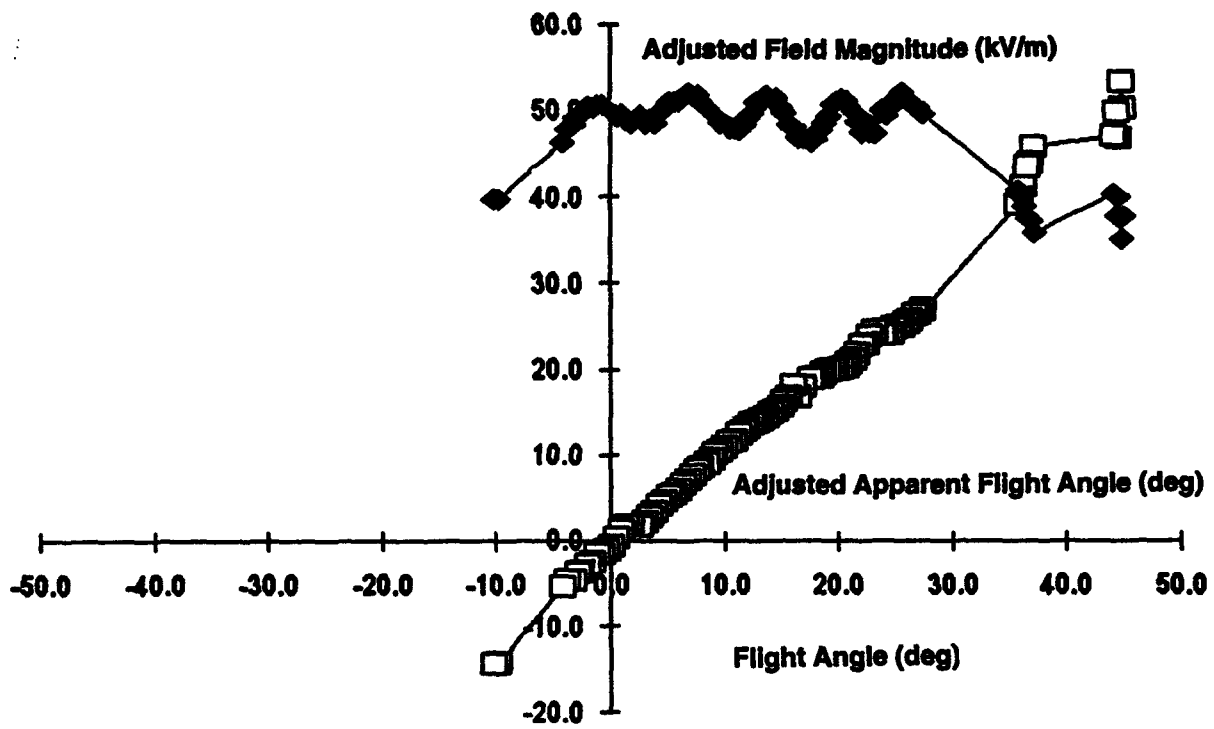
Figure 65. Adjusted field magnitude (solid diamonds) and adjusted apparent flight angle (open squares) versus actual flight angle for the same 19 July data shown in Figure 63. E_z has been scaled down by a factor of 0.8 and the ambient field vector has been assumed to point 10 degrees down range from vertically downward
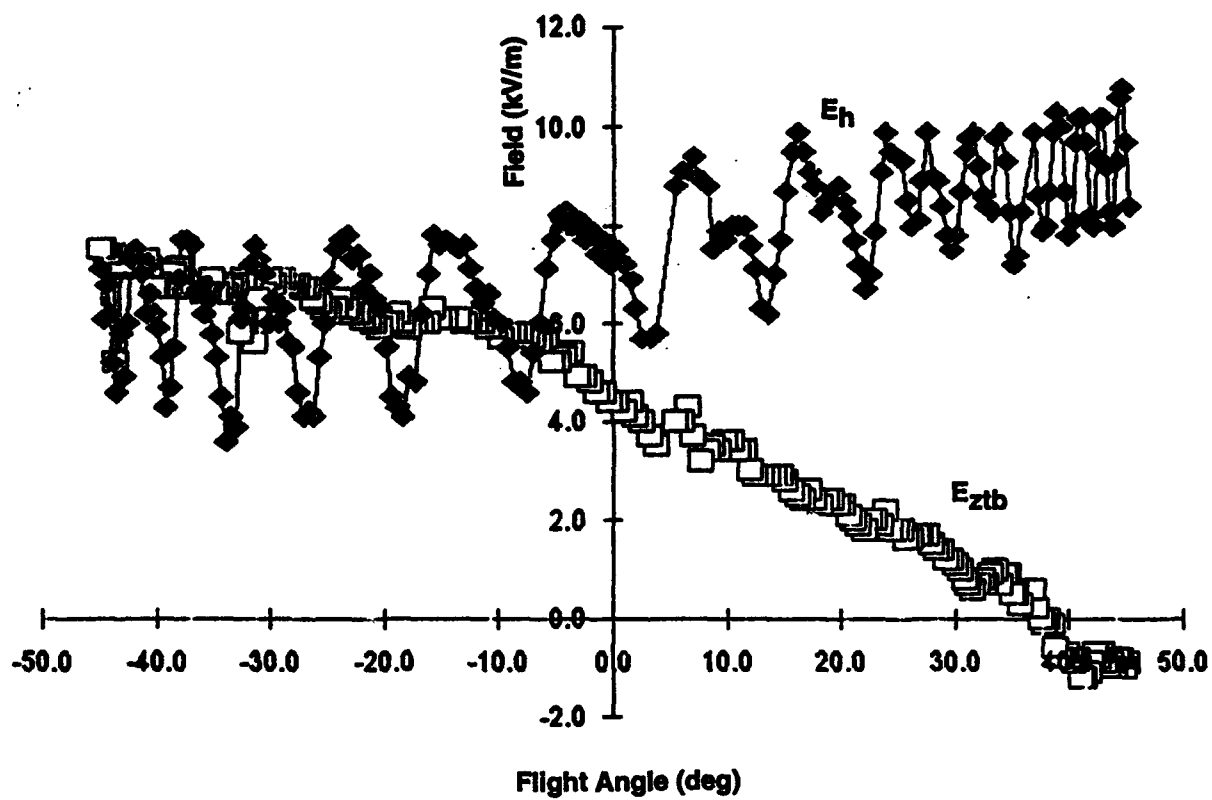
Figure 66. Similar to Figure 60 for the 8 July flight
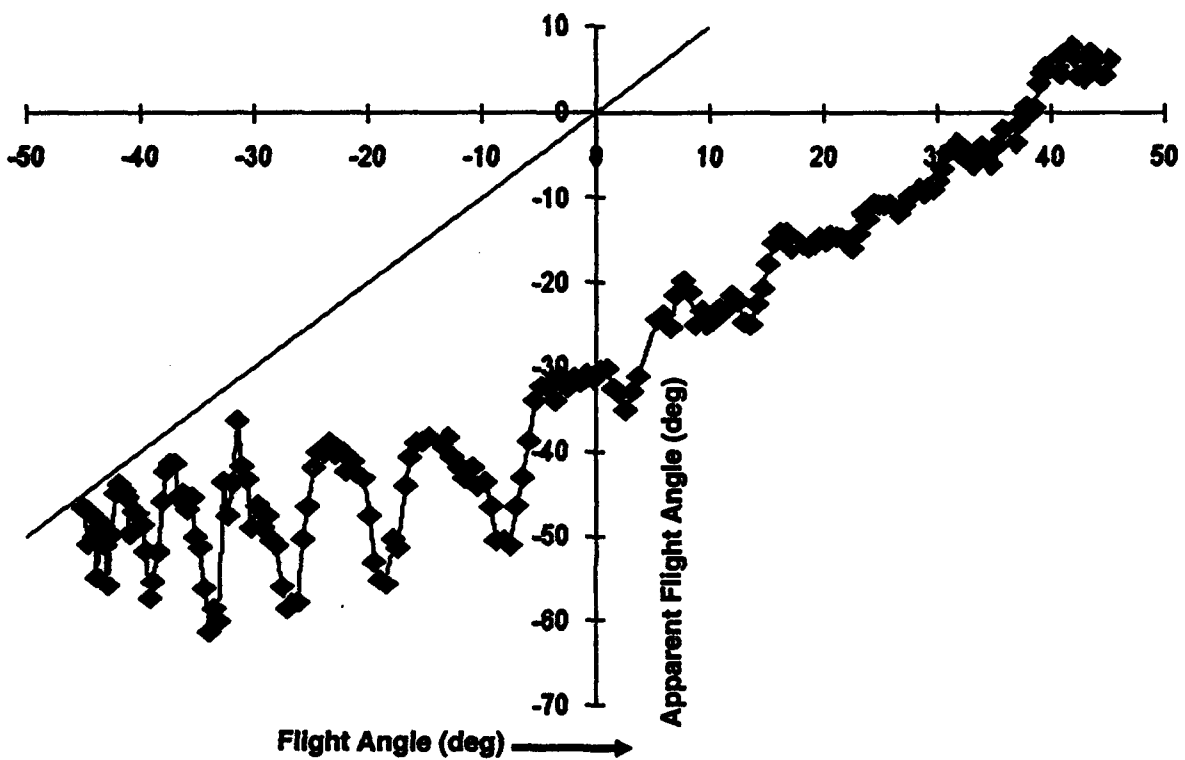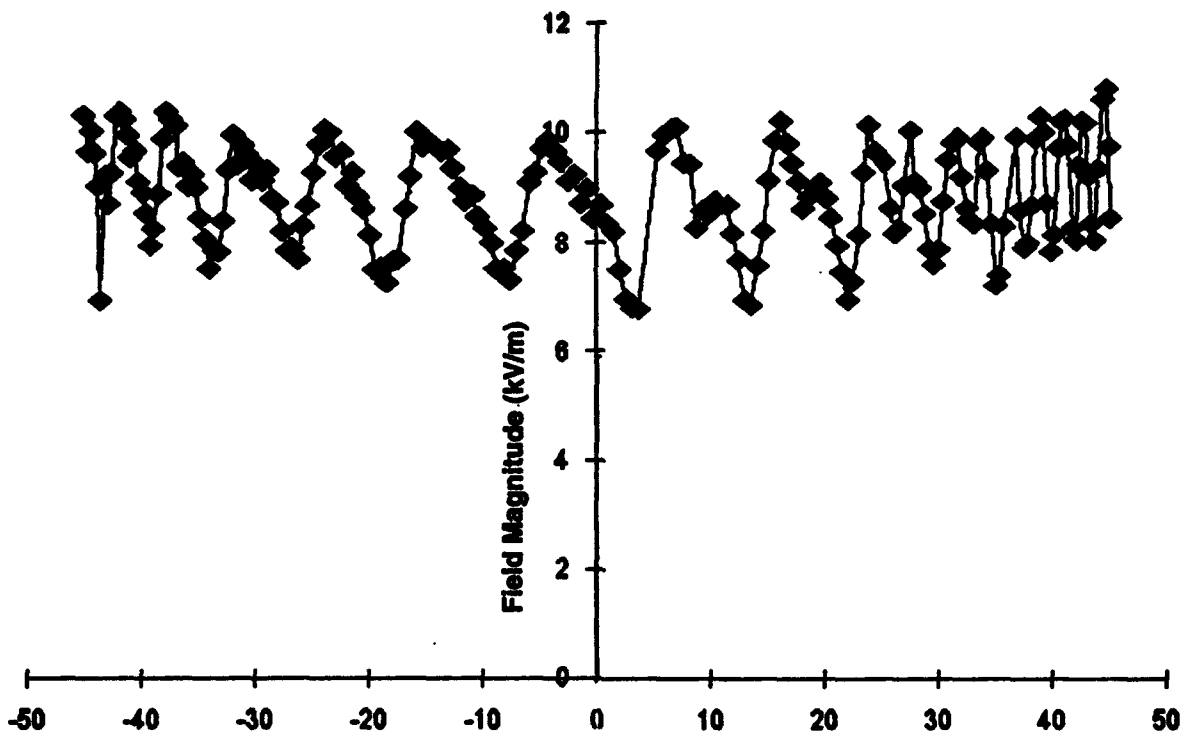
Figure 67. Similar to Figure 61 for the 8 July flight
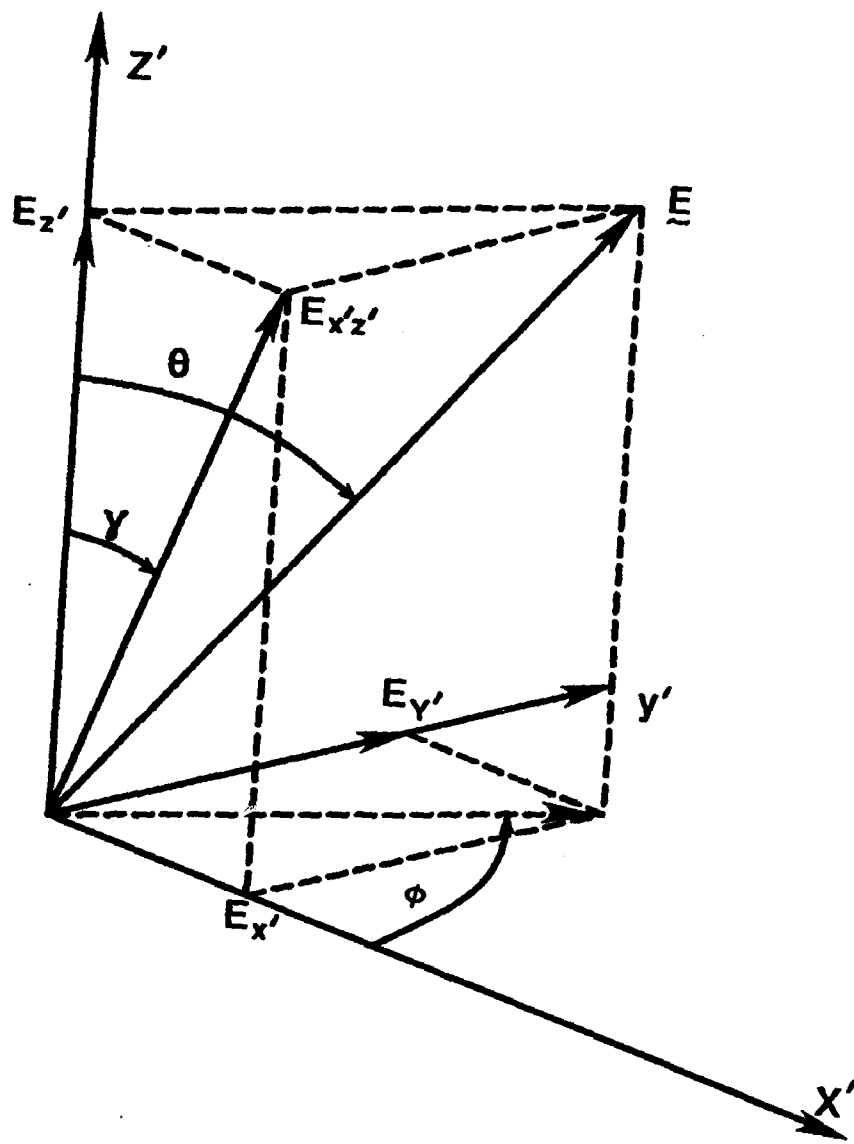
Figure 68. Definition of the ambient field direction in the primed coordinate system translating with the rocket but oriented so that z' is vertical and x' points horizontally down range. Angle γ defines the direction of the ambient field vector projected onto the plane of the trajectory
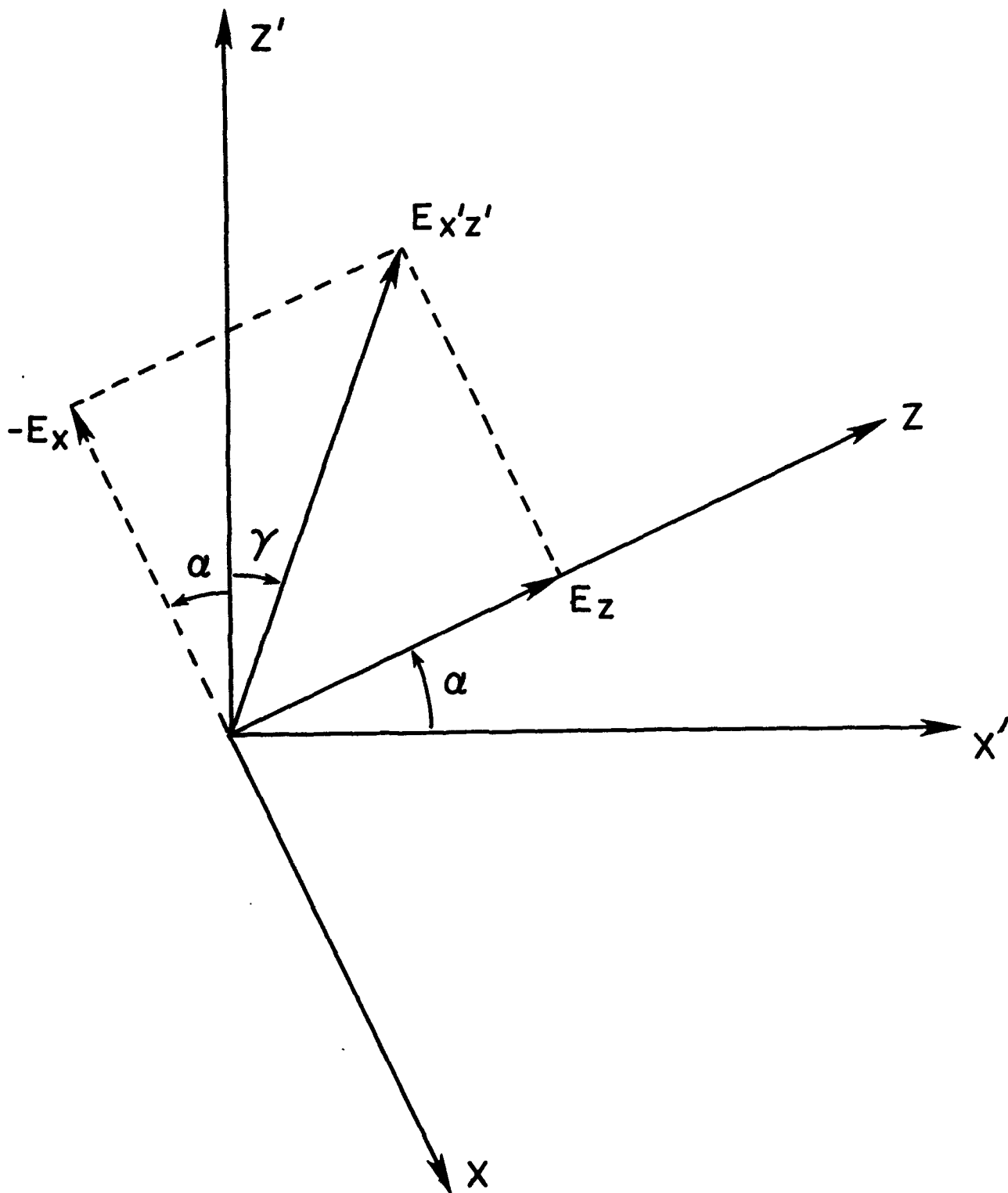
Figure 69. The relationship between the rocket and primed coordinate systems in the plane of the trajectory. Angle γ is the same as in Figure 68, and α is the flight angle

108

where E_z is the measured longitudinal field and E_x can be deduced from the measured transverse-field magnitude, E_h, as follows:

$$E_x = [E_h^2 - (|E| \sin \theta \sin \phi)^2]^{1/2} \qquad (26)$$

(Note that this last step would be obviated by knowing the rotational orientation of the rocket so that E_x could be measured directly.)

Equations (22), (24), (25), and (26) have been solved for the apparent flight angle, α, given an assumed direction (θ and ϕ) for the ambient field using the data from 8 July. The iterative process of finding the appropriate field direction was made easier by realizing that γ, defined in Eq. (24), must equal 142.5 degrees to match the zero-crossing of E_z in Figure 66. This exercise yielded satisfactory adjusted apparent flight angles, as shown in Figure 70, for θ = 130 degrees and ϕ = ±50 degrees without any scaling of E_z. The appreciable deviation of the ambient field vector from the trajectory plane allowed a sufficient reduction in E_x to yield the correct slope of the flight-angle plot without compromising the constancy of the field magnitude.

The maximum information cannot be retrieved from these apogee maneuvers without knowledge of the rotational orientation of the rockets. Nevertheless, in two out of the three flights we have been able to show that the data around apogee are reasonably consistent with the assumption of a stationary ambient field. In neither of these cases was there indication of a large error in the longitudinal-field calibration. These data will be studied further in a future publication, however.

5.3.3 COMPARISON WITH SURFACE MILL

Surface-field records during the rocket flights have already been reported in Section 5.3, as shown in Figures 50, 51, and 52. In Figure 71 we have plotted the filtered longitudinal-field profiles over the lowest 1000 m of the trajectories together with the range of surface-field measurements recorded on West Knoll during the same time intervals. Clearly, the agreement is as good as could be expected, given the horizontal and vertical separation of the measurements.

5.3.4 COMPARISON WITH BALLOON-BORNE MILLS

Also shown in the top panel of Figure 71 is a single measurement from a tethered balloon that was holding a field meter at a height of 305 m above the Balloon Hangar during the flight of 8 July (Tom Marshall, personal communication). Since the Balloon Hangar was about 55 m above (and some 600 m to the NE of) the rocket launcher, the field measured by the balloon was plotted at 360 m AGL in the figure. Again, agreement is as good as could be expected, given the large horizontal distance between the two instruments.

Similar field meters were carried aloft on free balloons near the times of the rocket flights on 17 and 19 July. On the former day, the free balloon was launched at 1406 MST, 22 minutes prior to the rocket, and drifted rapidly eastward, reaching 6900 m AGL before the rocket was launched on its southerly trajectory. Therefore, this flight cannot be used for validation. On 19 July, however, the free balloon was launched while the rocket was in the air. This balloon was observed
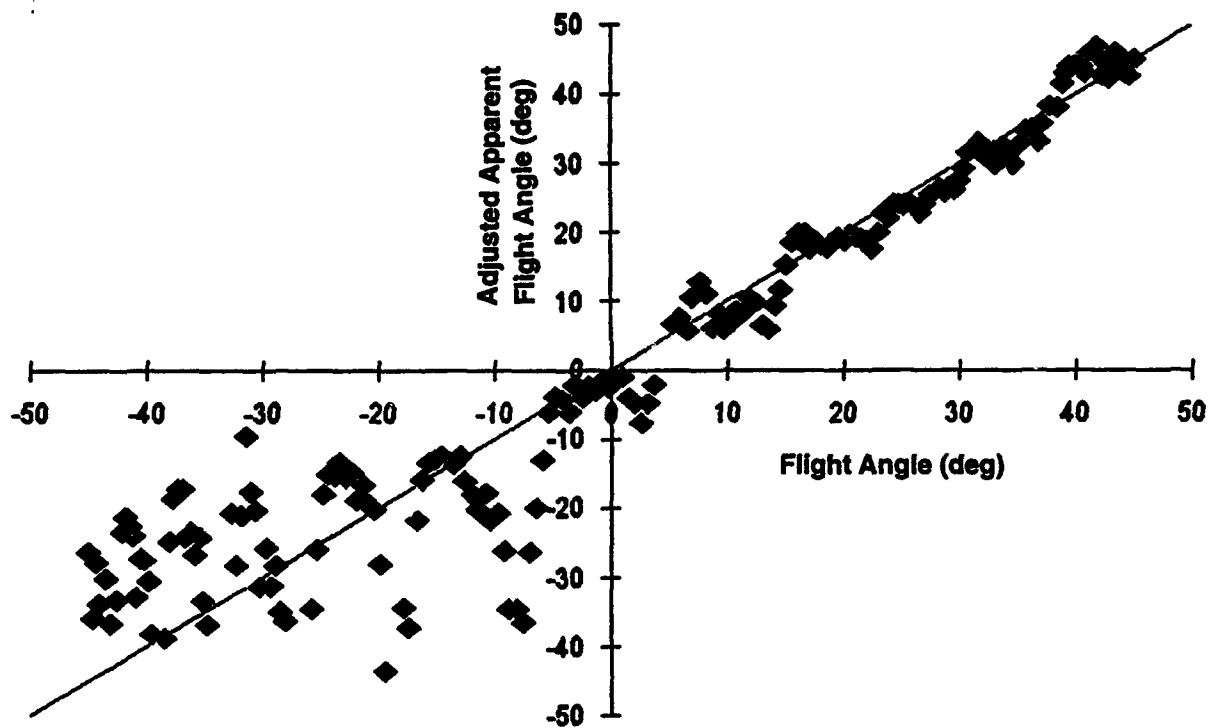
Figure 70. Adjusted apparent flight angle versus actual flight angle for the same 8 July data shown in Figure 66. The ambient vector field has been assumed to point in the direction defined by the spherical polar angles $\theta = 130$ degrees and $\phi = \pm 50$ degrees relative to the primed coordinate system illustrated in Figure 68. No scaling has been applied to E_z. Again the straight line indicates a 1:1 relationship

110
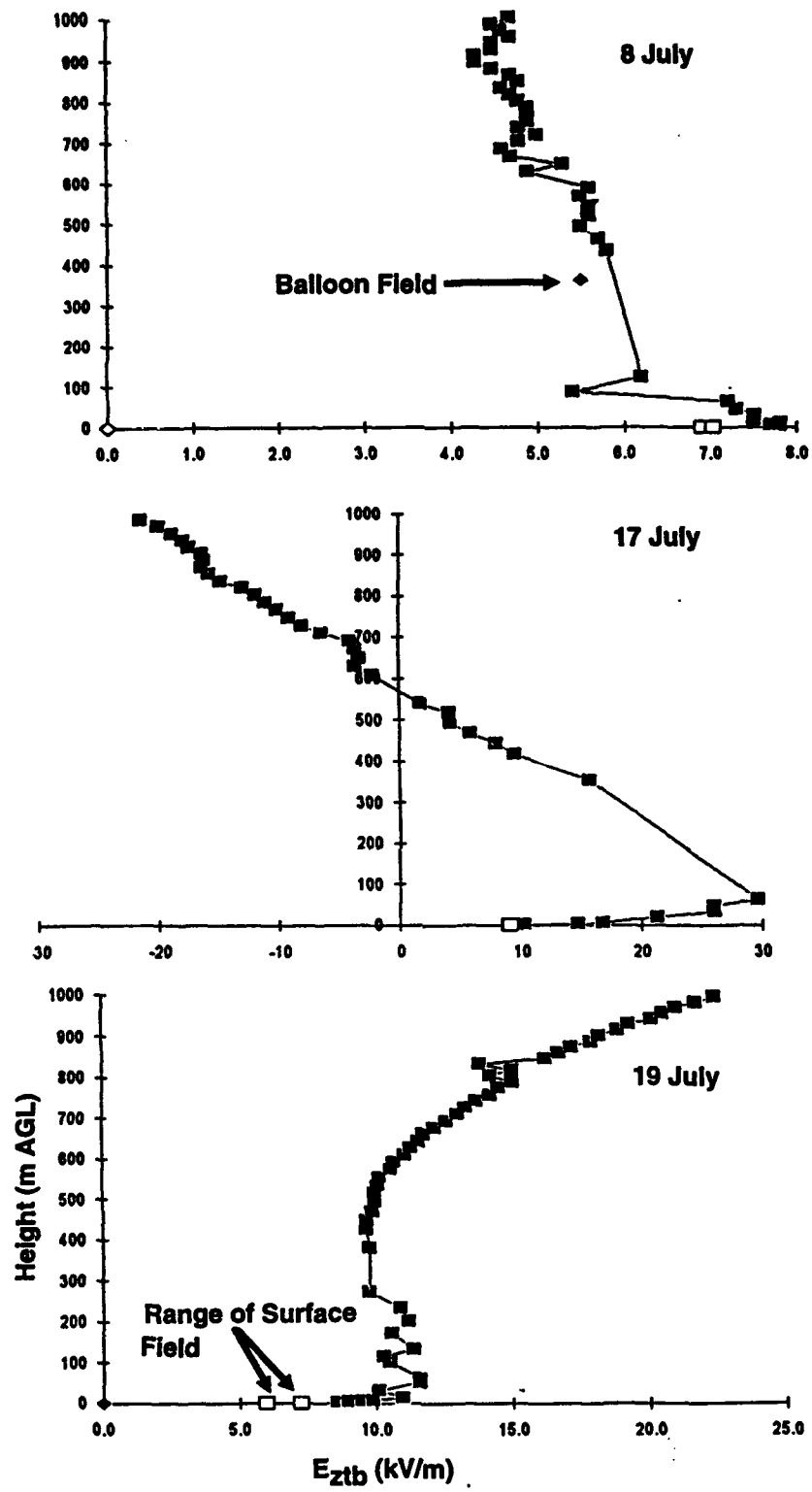
Figure 71. Filtered longitudinal-field profiles (solid squares) over the lowest 1000 m of the flights on 8 July (upper panel), 17 July (middle panel), and 19 July (lower panel). The open squares plotted at z = 0 in each panel indicate the maximum and minimum of the surface fields measured at West Knoll during the corresponding profile. The solid diamond plotted at z = 360 m in the upper panel indicates the vertical field measured by a tethered balloon at the beginning of the 8 July flight

111

to enter the cloud around 1504 MST, at an altitude of 1830 m AGL, only 7 minutes after the rocket landed. Figure 72 shows a plan view of the rocket and balloon trajectories, making it clear that the two instruments sampled roughly the same volume up to at least 2400 m AGL, although the time difference becomes increasingly important as altitude increases. The best comparison should be several hundred meters above ground.

Figures 73 and 74 compare the up and down soundings of the rocket on 19 July for estimated vertical field (E_z divided by the sine of the flight angle, on the assumption that the ambient field is predominantly vertical) and total field magnitude (as defined in Eq. (22), averaged over five consecutive samples to reduce the fluctuations due to E_h that were noted in Section 5.2). Evidently, the up and down soundings agree quite well in spite of horizontal separations up to 2.7 km, notwithstanding the effects of a close lightning flash that occurred as the rocket was descending through 2450 m AGL, toward the end of its flight (see Section 5.3). Unfortunately, this flash occurred immediately after the balloon was launched.

Similar comparisons of the balloon data (Tom Marshall, personal communication) and the rocket's up sounding in Figures 75 and 76 indicate excellent agreement below cloud base and good agreement overall. Interestingly, the numerous lightning flashes that occurred during the balloon flight did not appear to change the general shape of the field profile. These comparisons with a proven instrument lend further credibility to the rocket calibration, although they cannot confirm it in detail.

5.3.5 POTENTIAL PROFILES

One of the important advantages of the REFS payload over previous instruments is its potential to perform an accurate line integral of electrostatic field over a reasonably vertical path and, thereby, to measure electrostatic-potential differences between points at different altitudes beneath and inside thunderstorms. Instrumented aircraft have been shown capable of measuring the vector ambient field (for example, Winn,[5] Kositsky et al.,[6] and Bailey et al.,[7]), but the component along their direction of motion is usually fairly uncertain. In any case, their motion is primarily horizontal, making it hard to construct accurate, vertical, potential differences. Although the motion of free balloons is often predominantly vertical, it is slow enough that significant field changes may occur during the time required to traverse any interesting vertical path, invalidating the assumption of stationarity implicit in the line integral. Further, any significant horizontal motion requires accurate measurement of the horizontal-field components -- not always available from balloon sensors -- to construct the desired potential difference. The rocket, by contrast, appears capable of accurate measurement of the field component along its direction of motion, and it can traverse significant vertical distances in very short time intervals.

For this reason, it is of interest to examine line integrals of field along the rocket trajectories. Such integrals (calculated by the trapezoid rule using incremental path lengths derived from the computed trajectories) are presented versus altitude in Figure 77 for each of our three flights. The validity of interpreting these integrals as electrostatic-potential profiles is greatest on 8 July, when the lightning was fairly distant, and least on 19 July, when a large lightning field change caused an obvious kink in the line integral in the middle of the descending leg, and when a

92201
Plan View of Trajectories
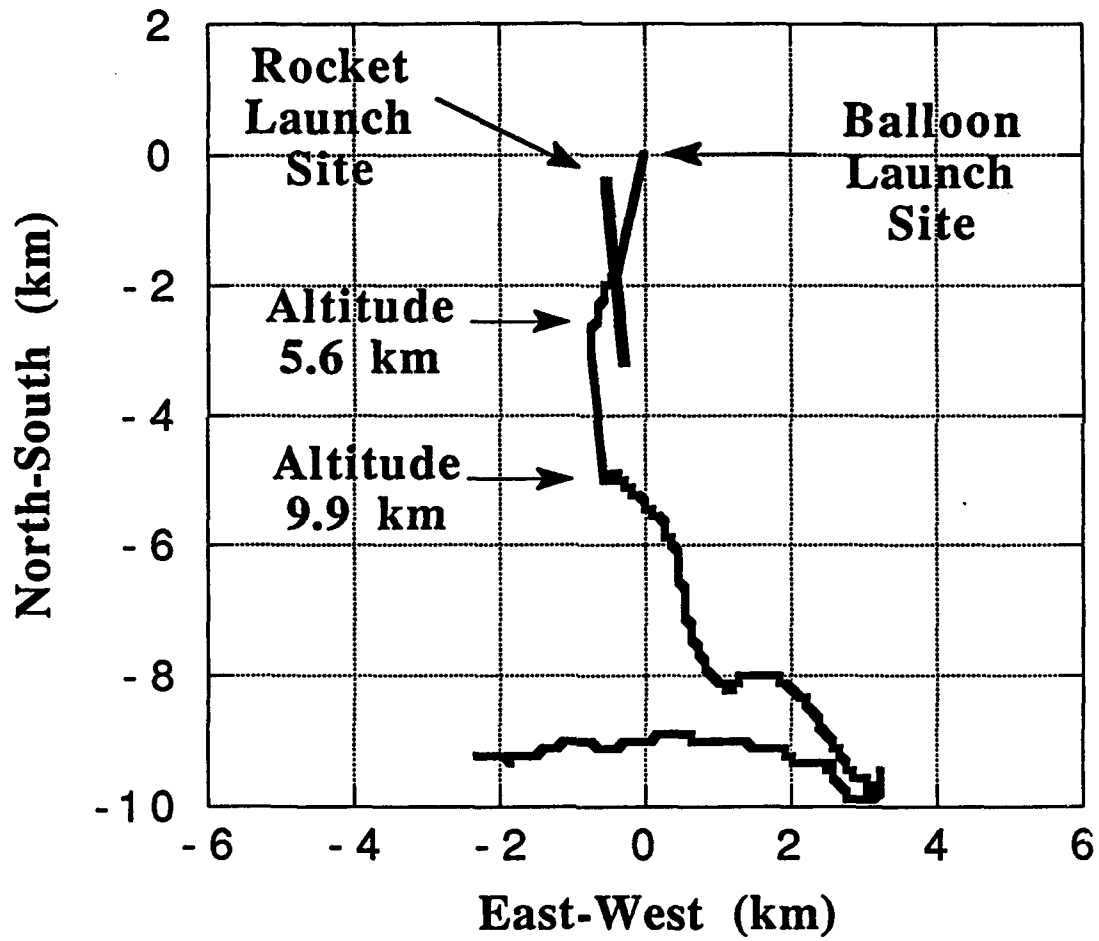
Figure 72. Plan view of balloon and rocket trajectories on 19 July 92

113
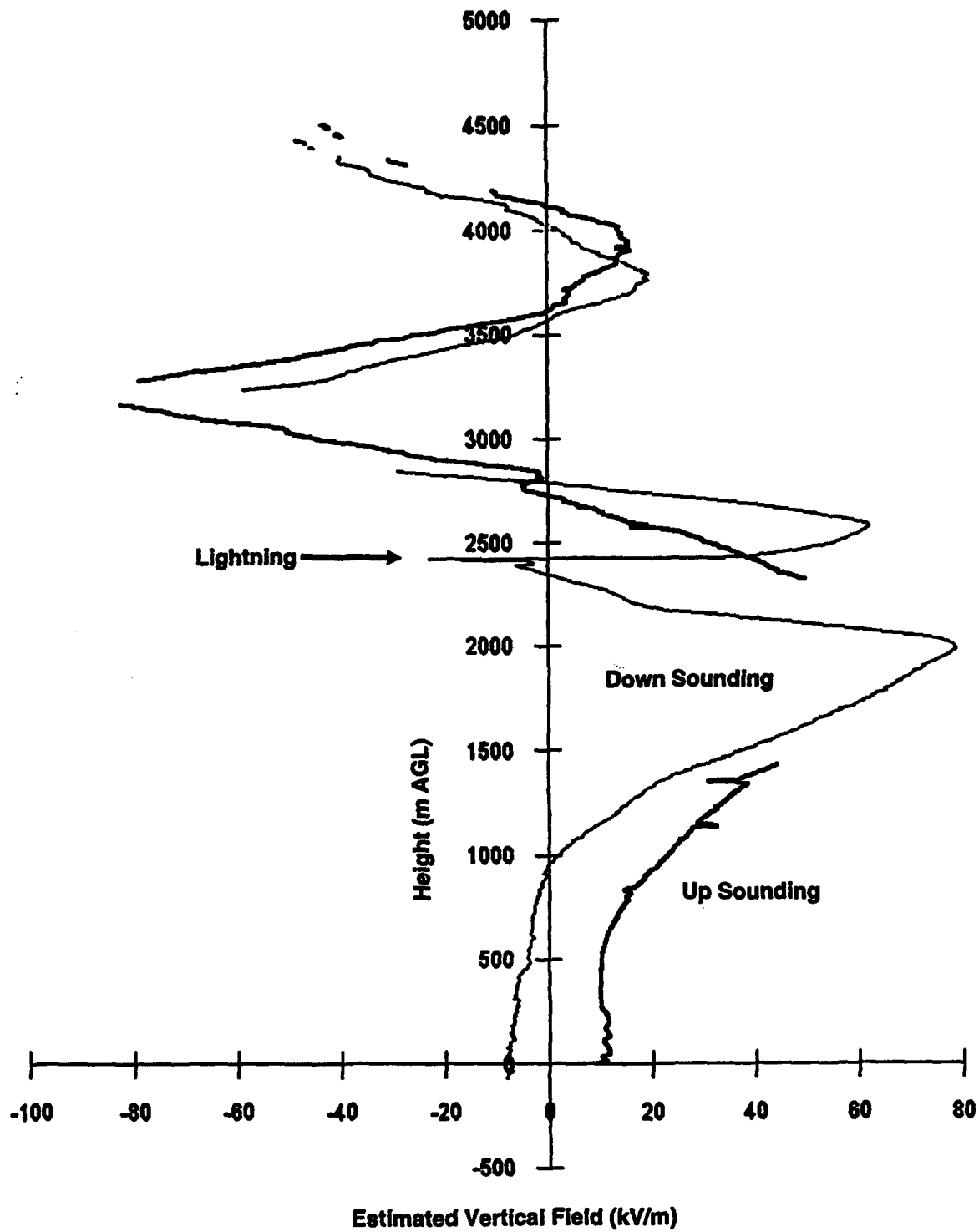
Figure 73. Rocket up-sounding (thick line) and down-sounding (thin line) of estimated vertical field component (E_z divided by the sine of the flight angle) versus height on 19 July. Data for flight angles less than 45 deg. have been omitted to minimize errors due to the conversion from longitudinal field

114
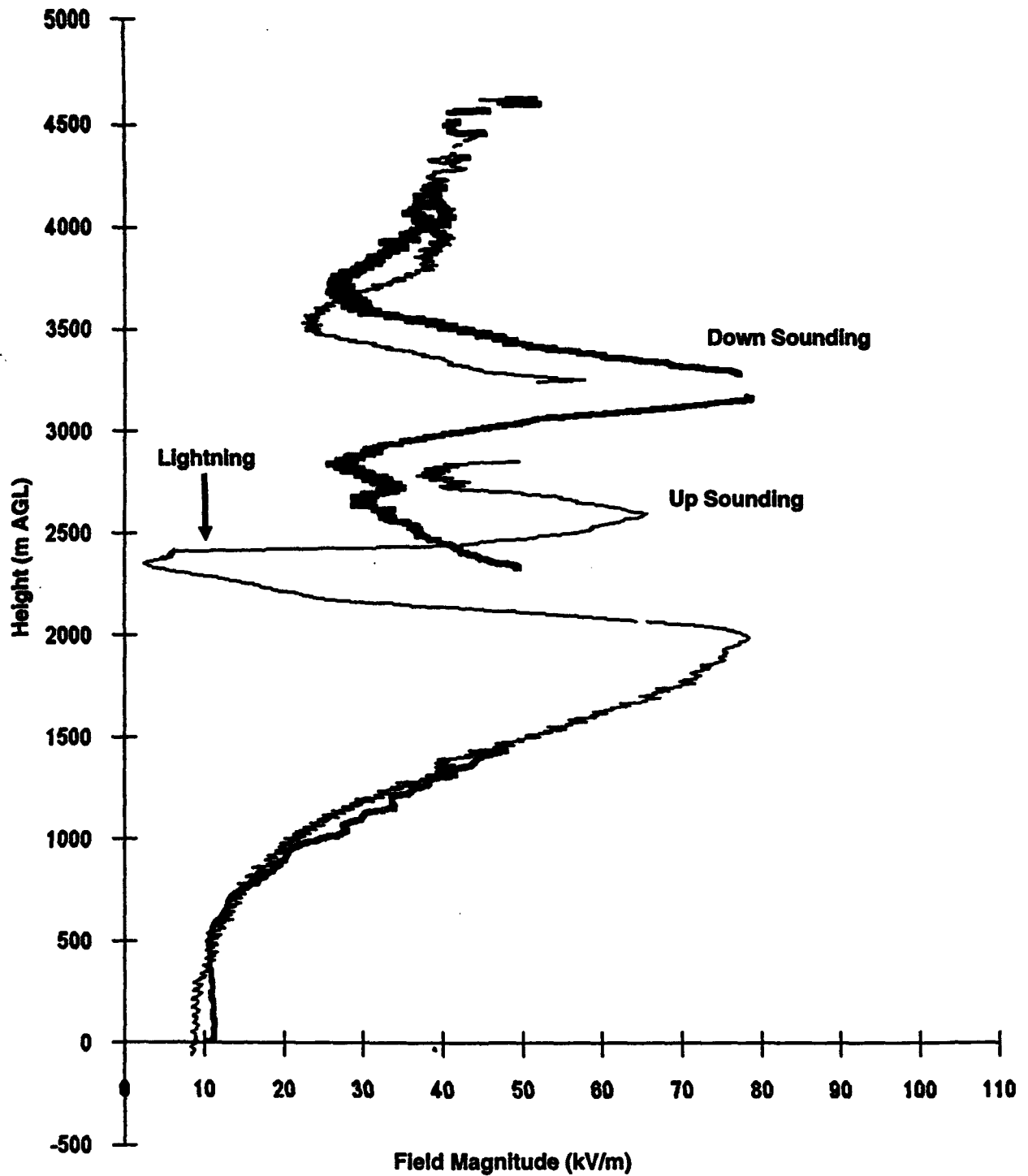
Figure 74. Rocket up-sounding (thick line) and down-sounding (thin line) of total field magnitude versus height on 19 July. The data have been smoothed by a five-point moving average to minimize the fluctuations due to E_h
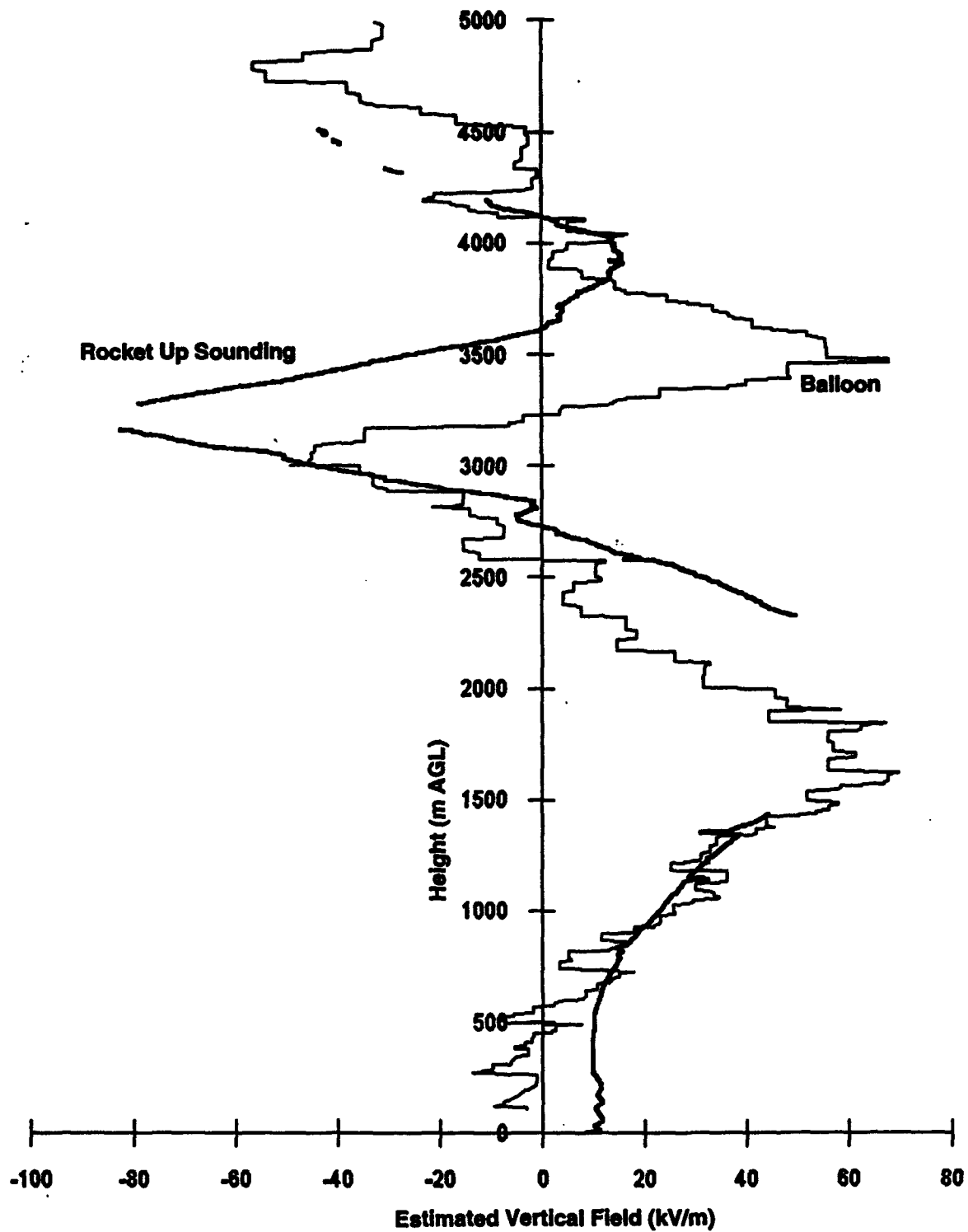
Figure 75. Rocket up-sounding of estimated vertical field component (from Figure 73 -- thick line) and balloon sounding of vertical field component (taken as the value of smallest magnitude in nine consecutive samples -- thin line) versus height on 19 July
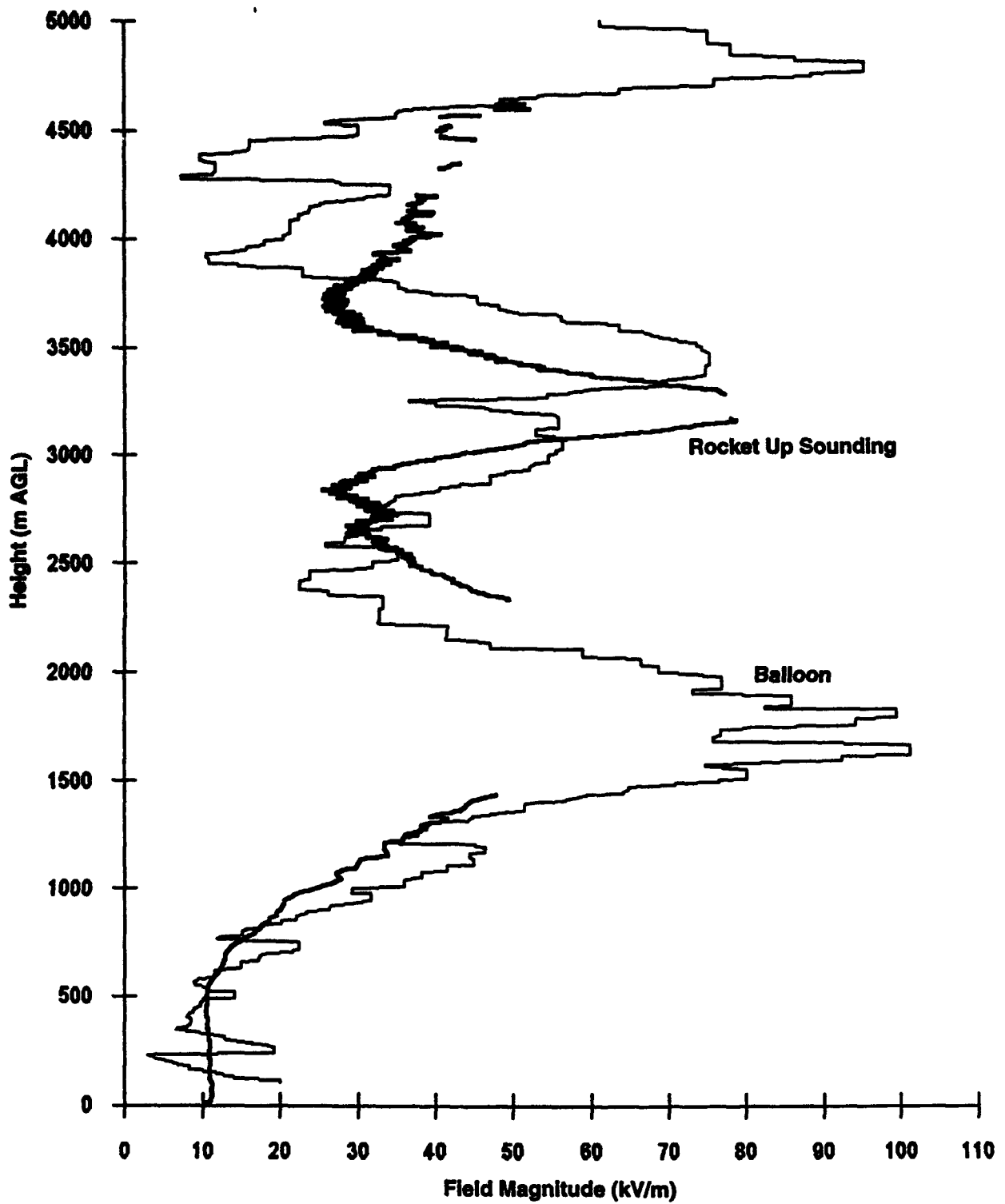
Figure 76. Rocket up-sounding of total field magnitude (from Figure 74 -- thick line) and balloon sounding of total field magnitude (taken as the largest magnitude in nine consecutive samples -- thin line) versus height on 19 July
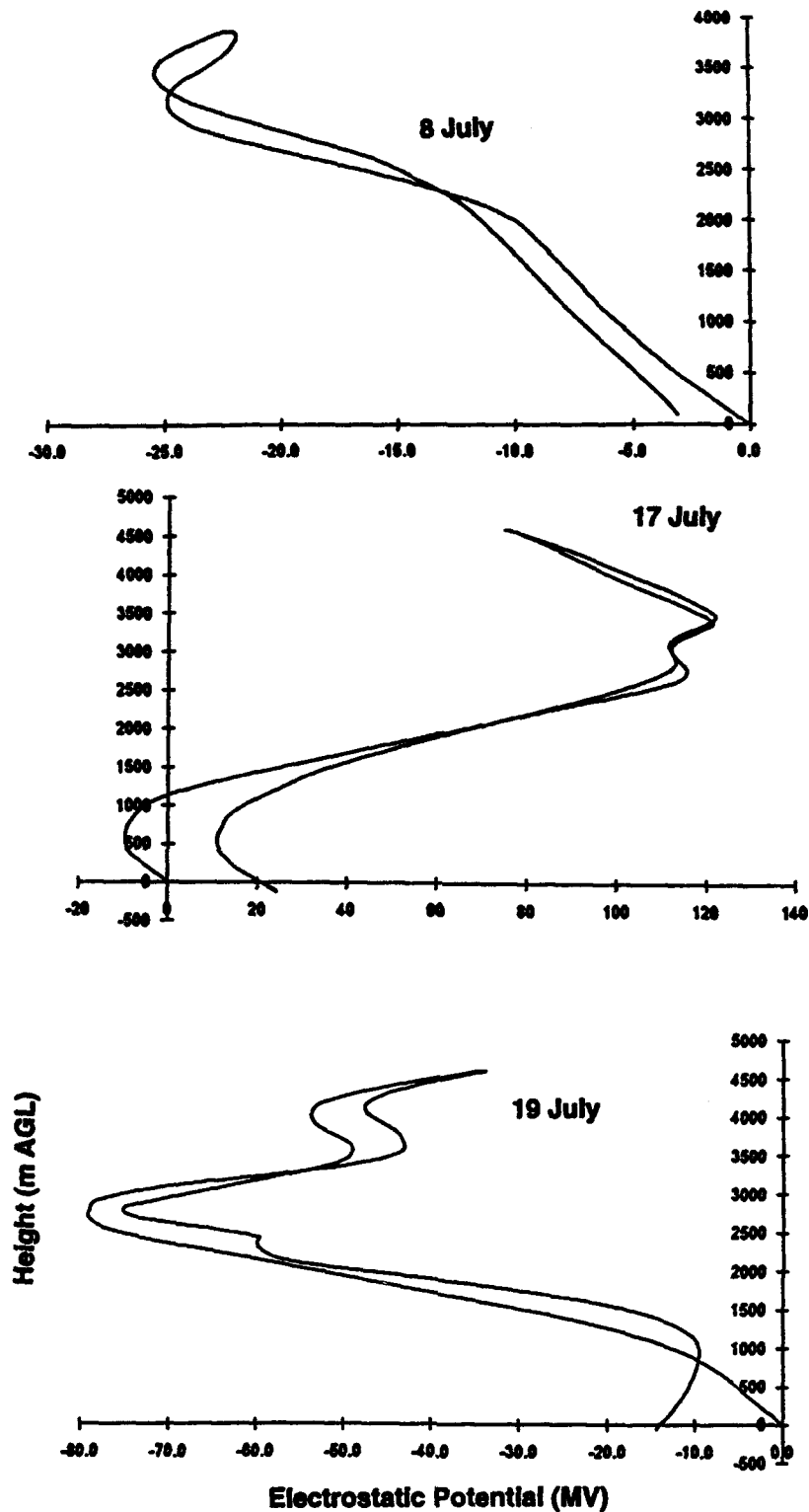
Figure 77. Negative line integral of electrostatic field versus altitude along the trajectories of the rocket flights on 8 July (upper panel), 17 July (middle panel), and 19 July (bottom panel). Note that the interpretation of these data as electrostatic potentials depends on the assumption that the field is stationary over the duration of the soundings

118

considerable amount of data is missing (see Figure 59). Nevertheless, it is interesting that the maximum potentials of about +125 and -80 MV, attained on 17 and 19 July, respectively, are comparable in magnitude to estimates in the literature (for example, Uman,[8] p.323).

The ascending and descending legs of these profiles are not expected to coincide, of course, because they are traversed at different horizontal positions. The values of potential at launch and impact must be identical, however, because the earth is a conductor. Unfortunately, we do not record the entire flight because the impact point is below the horizon from our telemetry antennas. Nevertheless, it is gratifying that each of the line integrals in Figure 77 returns relatively close to zero at the end of the flight -- especially on 8 July, when the stationarity assumption is likely to be well satisfied. This can be regarded as evidence for the relative accuracy of the measured longitudinal fields.

It is interesting to consider the potential profile of 19 July (lower panel of Figure 77) in more detail. Recall that a cloud-to-ground lightning flash, lowering negative charge, was observed near the rocket trajectory during the down sounding on this day. A minimum potential of -79 MV at a height of 2700 m was registered on the up sounding. The down sounding passed through a similar minimum about 42 s later, just before the lightning. The vertical field profile from the free balloon, which was launched about the time of the flash, was similar to that from the rocket (Figure 75) and placed the potential minimum at about the same altitude several minutes later. Thus we can conclude that there was a persistent, horizontally extensive, negative-charge layer in this storm. Assuming that the lightning flash extended from this negative charge to ground, we can estimate the average field driving this flash at about 30 kV/m. This can be compared with average fields for 50 percent breakdown of 7 m, negative, rod-to-plane gaps in long laboratory sparks of over 400 kV/m ("Les Renardieres Group",[10] Table 4.1).

5.3.6 SUMMARY OF PERFORMANCE CHARACTERISTICS

In this section we summarize what is known about the performance of our prototype payload for the measurement of electrostatic-field profiles in thunderstorms. The nominal full-scale range of each individual field mill was set at +/-923 kV/m (see Section 2.2). Since the raw field-mill signals were digitized with 12-bit accuracy, the nominal minimum detectable amplitude (1 DU) corresponds to a field of 225 V/m. Because of inherent system noise and other possible measurement errors, however, the minimum detectable field (after synchronous rectification) is best estimated from laboratory and in-flight data.

Our best indications of the actual noise level on the fields measured by the mills during normal operation are the standard deviations among individual readings (two per shell revolution -- nominally one every 33 ms) during potential calibration (see Table 5) and transverse-field calibration (see Table 7). Ignoring the large, unexplained standard deviations from the 17 July payload in the former table, we conclude that the noise level is normally between one and two digital units, or less than 450 V/m.

The relative accuracy of the mill readings, comparing one to another in flight, can be estimated from the linear-dependence tests reported in Table 16. The RMS magnitude of the fit error in Eq. (21), and the average standard deviation among independent estimates of the

transverse field component, E_y, are both seen to be less than 2 kV/m over the entire flights on all three days. If attention is restricted to data believed to be "good" (the reduced samples used to calculate the coefficients in Eq. (21)), then the these measures of relative error are less than 1 kV/m. These tests actually bear on the uncertainties of the sums, F_{ip}, and differences, F_{im}, of opposing mills, defined in Eq. (18). Thus, the relative accuracy of individual mill readings should be a factor of $2^{1/2}$ smaller.

Relative errors can also be estimated from the potential calibrations, both in the laboratory and in flight. From the laboratory data in Table 5, for example, we can compare one half the sum of the fields at the MT and MB mills with that at the MR and ML mills. These sums should be identical, since any transverse field is cancelled and any longitudinal field (like the vehicle charge) has the same effect on all four mills at the middle longitudinal position. The difference between these two sums has an RMS magnitude of only 540 V/m over the three payloads. A similar result can be obtained from the flight data leading to Table 13 (not shown).

Our conclusion is that the relative uncertainty due to all error sources of the individual sums and differences is normally less than 1 kV/m. It appears that we can detect and reject data whose relative accuracy is significantly worse than this by means of the data-selection criteria described in Section 5.3.1.

The relative and absolute accuracy of the ambient fields deduced from Eqs. 19 are somewhat more difficult to quantify. Based on the analysis in Sections 5.1 and 5.3, the transverse-field components are not influenced at all by either longitudinal field or charge on the rocket (as long as none of the field mills is saturated) and should have relative uncertainties comparable to the differences from which they are derived -- less than 1 kV/m. The longitudinal-field component is easily made insensitive to rocket charge as well, by adjusting the potential coefficients as described in Sections 4.3.4, and is independent of transverse field (Section 5.1). Because longitudinal field depends essentially on the difference between, two sums, its relative uncertainty should be about $2^{1/2}/(a_{iz} - a_{jz})$, or about 0.6, times that of the transverse field.

The relative accuracy of the total field magnitude, and the absolute accuracy of the individual field components, depend not only on the relative accuracy of the individual sums and differences discussed above, but also on the relative and absolute accuracies of the calibration coefficients, a_{ik}. The relative accuracy of these coefficients is best evaluated by a detailed study of the apogee turn-over maneuver, which will be the subject of a future publication. The transverse-field component has been absolutely calibrated to an accuracy of 10 percent or better, as described in Section 3.5. The absolute calibration of the longitudinal-field coefficients by Willett et al.[1] (Section 6.2.2) should be of comparable accuracy and has been checked against the transverse-field calibration in Section 5.3.2. That preliminary analysis gave no reason to doubt the absolute accuracy of our longitudinal calibration. Thus, the relative accuracy of the total field magnitude should also be better than 10 percent.

5.4 Further Remarks on Validation

It has been pointed out previously (for example, by Krider et al.,[9]) that a highly conductive exhaust plume from the motor can significantly distort the electrical geometry of a rocket during the boost phase, effectively adding a conducting extension to the aft end. High-speed photographs of the first (daytime) REFS launch at Wallops Island (Willett et al.,[1]) showed no visible incandescence in the exhaust plume. The temperature of this plume must be less than 2300 K (the "flame temperature" of the propellant) and greater than 1200 K (after adiabatic expansion of that flame temperature from combustion-chamber to atmospheric pressure). Since we expect the exhaust to be closer to the latter temperature and to rapidly cool further by mixing after leaving the nozzles, it probably is not highly conductive. Nevertheless, one of the stated reasons for including redundancy in the REFS field-mill system was to detect any such distortion of the electrical geometry (Willett et al.,[1] Section 2.1).

Here we consider the effect of a hypothetical conducting plume on the electrical measurements. The theoretical estimates of the longitudinal-field coefficients that agreed best with the laboratory measurements came from a formula due to Heckman and Williams (Willett et al.,[1] Equation (14)). This approximation says that the longitudinal-field coefficients are directly proportional to the longitudinal distance, z, from the electrical center of the rocket, with a proportionality factor, C m^{-1}, depending only weakly on rocket length. The corresponding approximation for the potential coefficients is that they are all equal to a_v, independent of z (in good agreement with measurements) and only weakly dependent on rocket length. Let z take on the values T + L, M + L, and B + L at the top, middle, and bottom longitudinal positions, respectively, where 2L is the length of the conducting plume. Then insertion of these two approximations into Eqs. (19) (for E_{ztb} and V_{tb}) and Eq. (21) (the presumed linear relation among the F_{ip}'s defined in Eq. (18)) yields

$$E_{ztb} = \frac{F_{tp} - F_{bp}}{C(T - B)} \tag{27}$$

$$V_{tb} = \frac{TF_{bp} - BF_{tp}}{a_v(T - B)} - \frac{CL}{a_v}E_{ztb} \tag{28}$$

$$F_{mp} = \frac{M - B}{T - B}F_{tp} + \frac{T - M}{T - B}F_{bp} \tag{29}$$

Notice that Eq. (29) is strictly independent of plume length. Thus, within the Heckman and Williams approximation, the existence of a conducting plume is not detectable by Winn's linear-dependence test! Fortunately, the calculation of E_{ztb} [Eq. (27)] is only slightly dependent on plume length, through the weak dependence of C on overall rocket length mentioned above, so any reasonable-sized plume will not significantly affect the measurement of longitudinal field. The principal effect of the plume should be to introduce contamination from E_z into the measurement of V [Eq. (28)] during motor burn, which is not of great concern.

Figures 78, 79, and 80 show the raw longitudinal field, E_{ztbk}, and the results of the two linear-model tests developed in Section 5.3.1, e_k and σ (E_{yk}), during the first 2 seconds of each flight. (Recall that the rocket motor burns for the first 1.55 s of each flight.) As indicated previously, thresholds on the fit error and transverse-field standard deviation do a good job of removing suspect data. The only other consistent feature of these three figures is the tendency toward large errors late in the burn phase. These errors are probably due to the slow shell rotation at these times, rather than to any effects of the exhaust plume.

Given the data-selection procedure developed in Section 5.3.1, it is of interest to re-examine the period early during the flight on 17 July, when the longitudinal field appeared to saturate at -80 kV/m. These data were discussed in Section 5.2 and plotted in Figure 45. If the plateau in E_z were actually due to severe corona from the nose of the rocket, the resulting cloud of space charge around the payload could invalidate the linear model and might therefore lead to large fit errors and/or transverse-field standard deviations. Figure 81 shows these errors and standard deviations and the longitudinal-field data filtered by two different selection criteria during this period. Even though there appear to be significant model violations, especially at the beginning and end of the plateau, there are still plenty of apparently valid field readings around -80 kV/m. It seems that we have no objective justification for rejecting these data.

5.5 Remarks on Triggering Conditions

"Classical" triggering rockets were fired by NMIMT, a few seconds after each of our soundings, from launchers located within a few tens of meters of the REFS launch site. These triggering rockets were not of the French design (Laroche et al.,[11]), but instead consisted of the most powerful readily-available model rocket (the "Mustang" made by AeroTech of Las Vegas, Nevada, and powered by their "G" motor) towing grounded wires pulled from spools salvaged from surplus TOE or ENTAC missiles. The velocity profile of the NMIMT triggering rockets is not known, but they were capable of reaching heights over 500 m (as determined by the lengths of wire pulled from the spools) and were demonstrated to trigger lightning discharges on six occasions during the summer at altitudes ranging from 170 to 270 m (as verified by video images of the discharges). None of the rockets fired during our REFS flights triggered discharges that were visible on the video recordings. Table 17 summarizes the times and wire lengths of these unsuccessful triggering attempts. Note that the effects of the grounded wire being pulled aloft by a triggering rocket can usually be seen on the West Knoll field-mill records in Figures 50, 51, and 52 (Section 5.3).
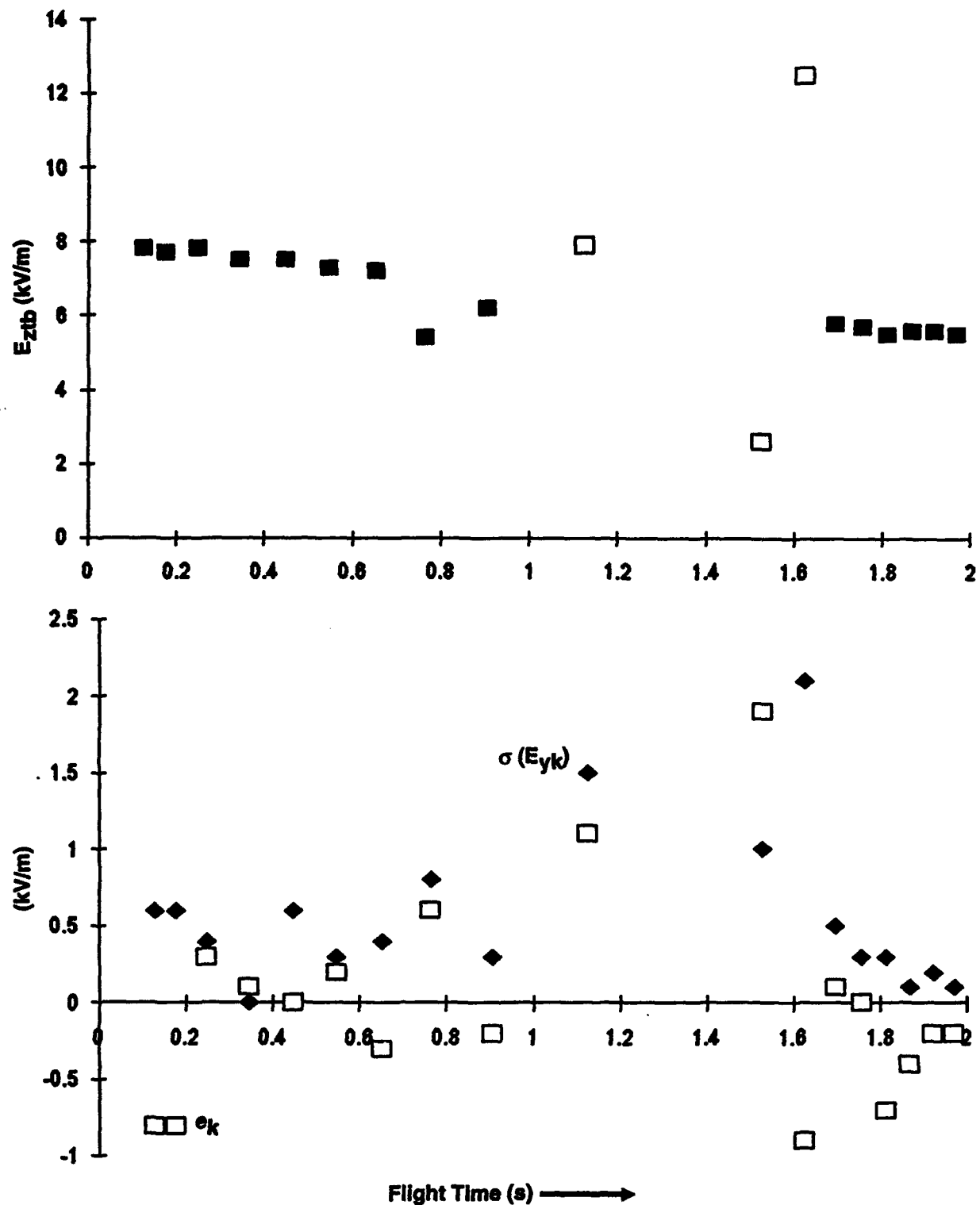
Figure 78. The upper panel shows raw longitudinal field versus time during the first two seconds of the flight on 8 July. Open squares indicate points rejected from the filtered data by the selection criteria discussed in Section 5.3.1. The lower panel shows the fit error from Equation 21 (open squares) and the standard deviation among the three estimates of E_y (solid diamonds) for the same period
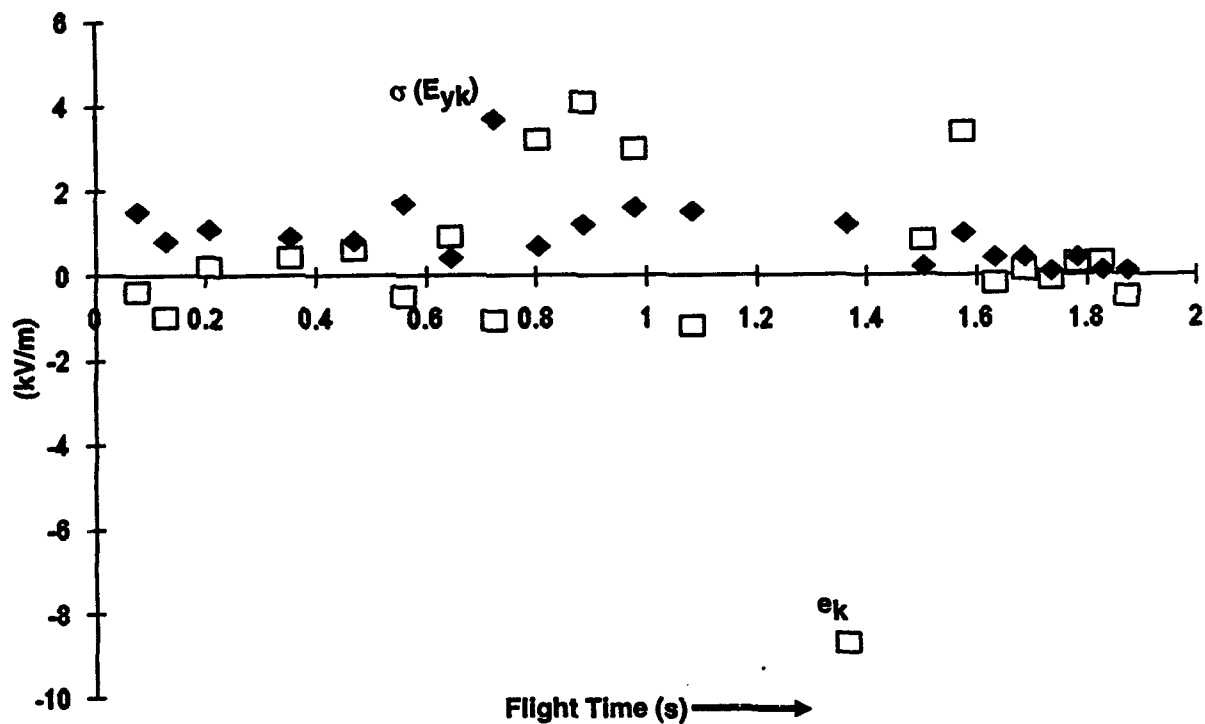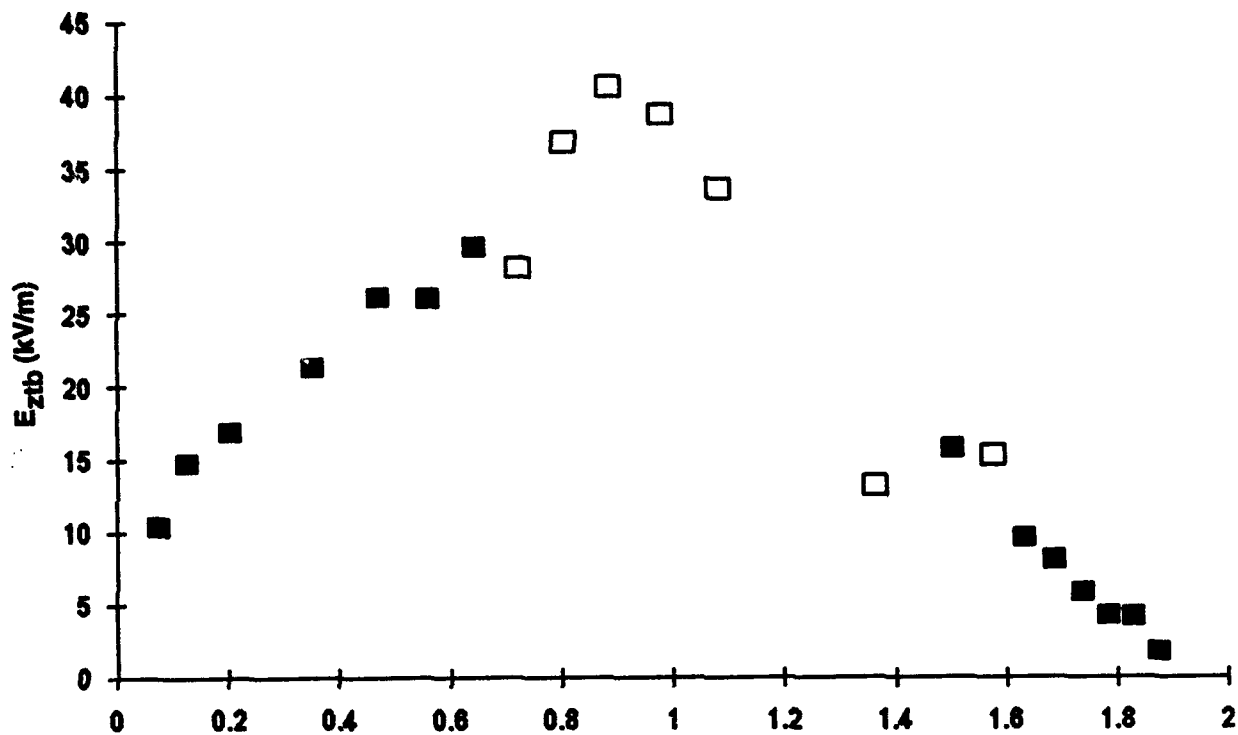
Figure 79. Similar to Figure 78, but for the 17 July flight

124
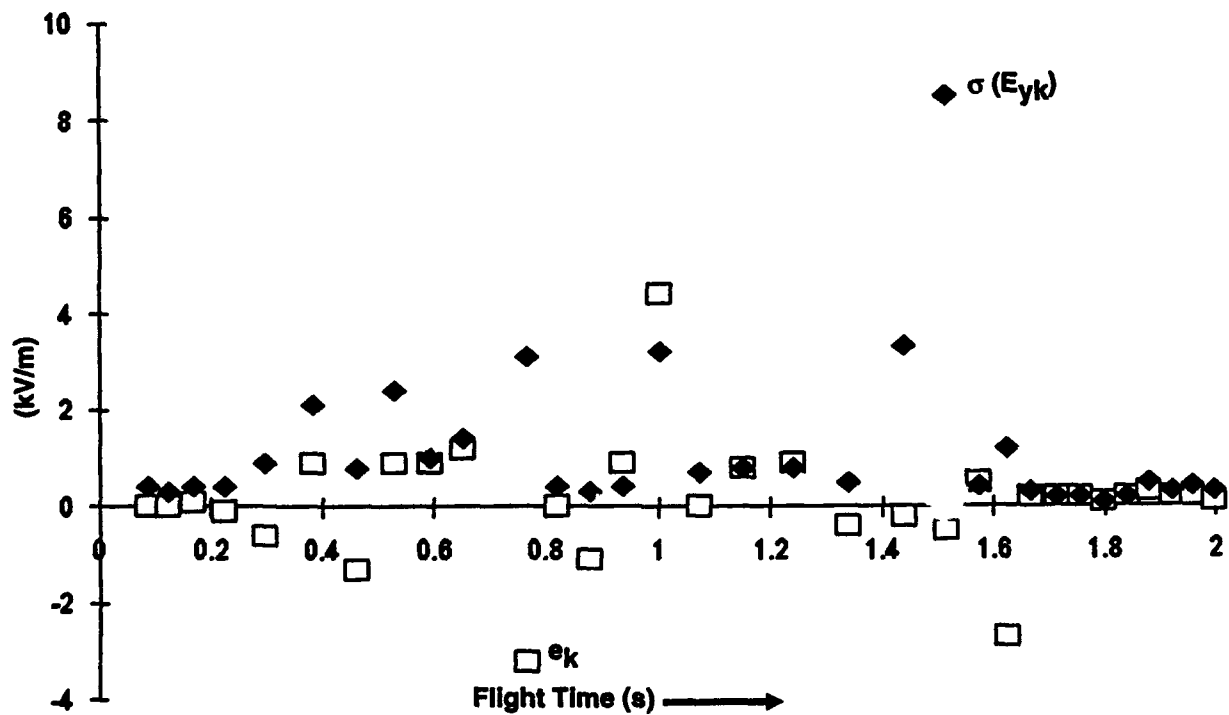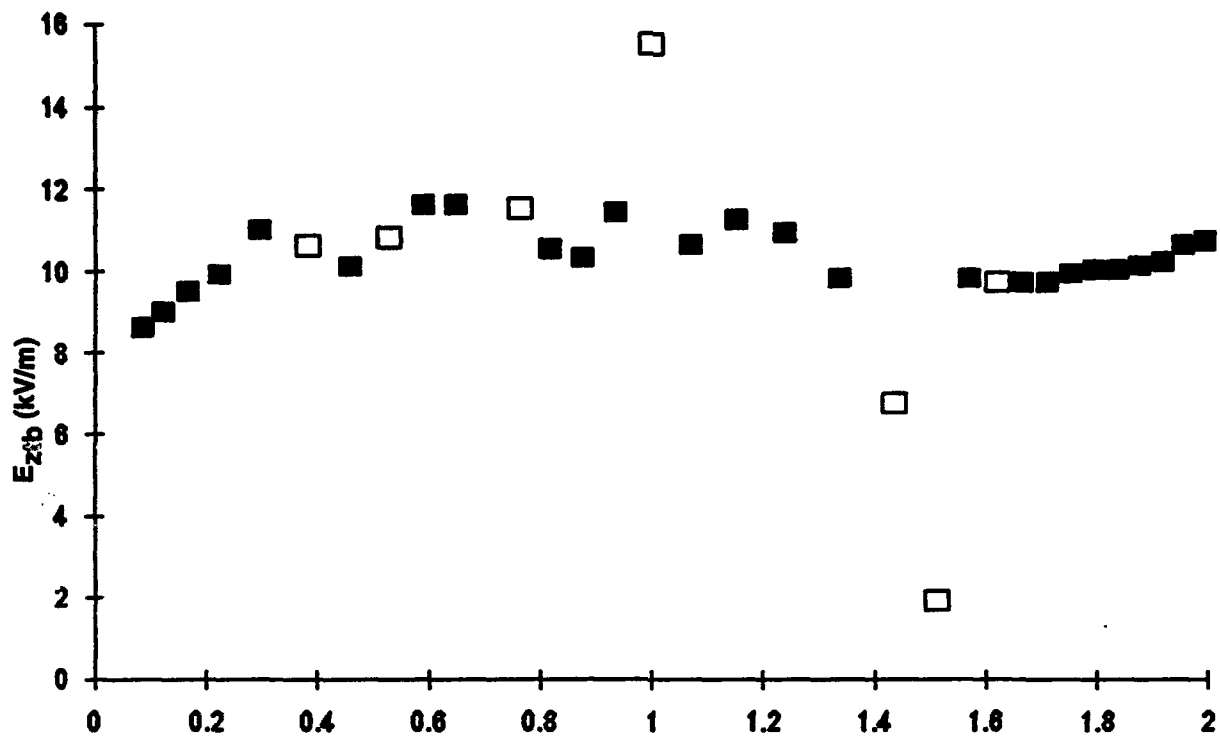
Figure 80. Similar to Figure 78, but for the 19 July flight

125
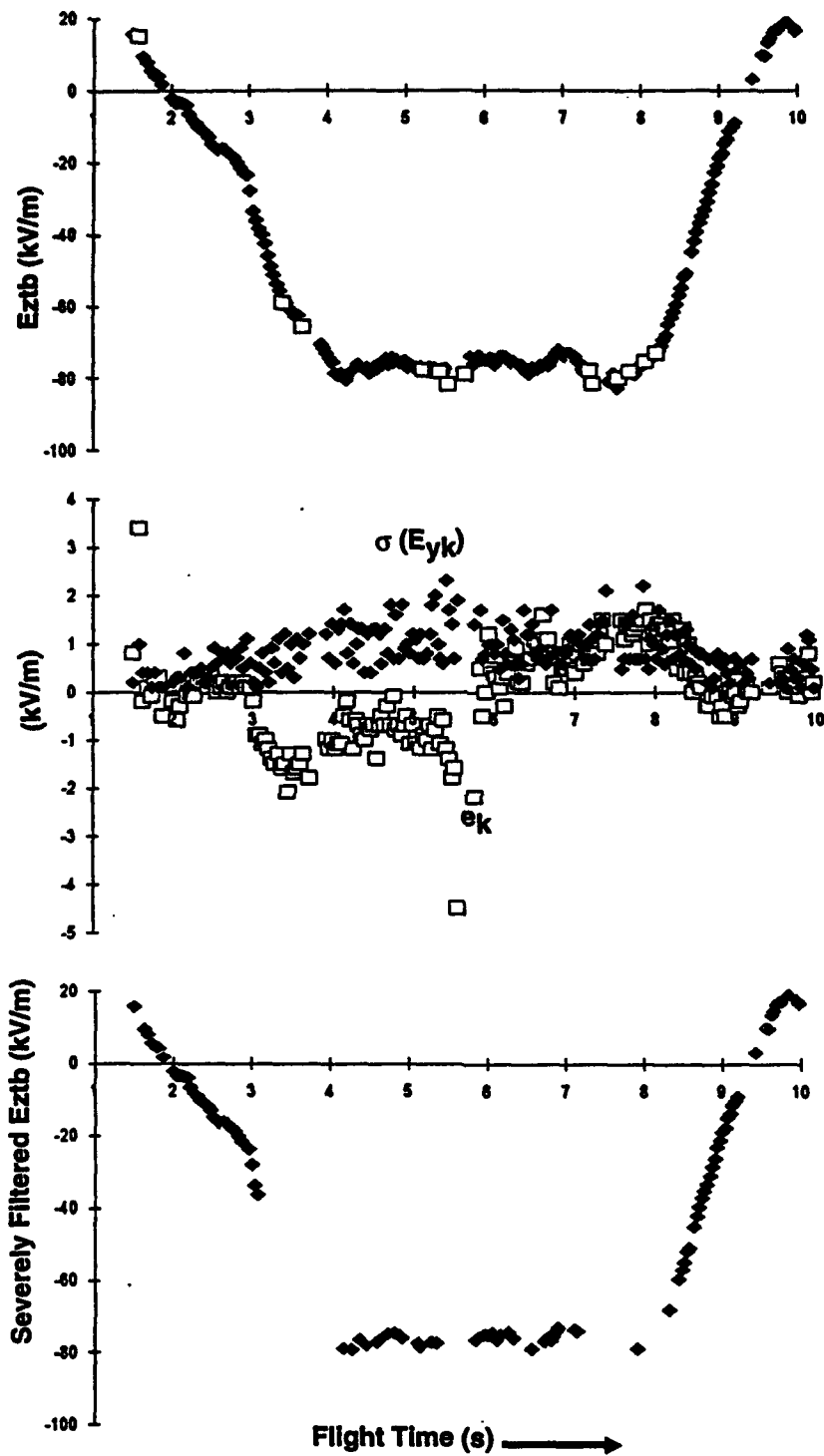
Figure 81. The upper panel shows raw E_{ztb} for nine seconds early in the flight on 17 July. The open squares are data rejected by the original selection criteria discussed in Section 5.3.1. The middle panel shows e_k (open squares) and $\sigma (E_y)$ (solid diamonds) for the same period. The lower panel shows E_{ztb} filtered more severely by rejecting all data for which $[| e_k | > 1]$ or $[\sigma (E_{yk}) > 1]$

Table 17. Triggering Rockets Fired During REFS Flights

Date	Time (s After REFS Ignition)	Height (m)	Potential (MV)
8 July	t+9	357	-2.3
	t+16	264	--
17 July	t+7	?	-9.6*
19 July	t+1(?)	wire broke	--
	t+6(?)	478	-5.1
* Assuming a height of 500 m.			

We have already seen in Figure 71 that the vertical-field magnitude did not exceed about 10 kV/m in the lowest 500 m of the profiles on either 8 or 19 July. In these cases no triggered lightning might have been expected. On 17 July, however, the vertical field reached or exceeded +30 kV/m. (Based on the rejected data shown in Figure 79, the field may have risen as high as +40 kV/m within 120 m of the ground.) This is approaching the levels at which triggering was observed by Soula and Chauzy[12] -- the only other observation of fields aloft during rocket-triggering attempts -- although the field reversal above 500 m should have prevented it in our case.

Figure 82 shows the first 1000 m of the potential profiles presented earlier in Figure 77. The ambient potentials corresponding to the wire heights have been interpolated from these profiles and entered in the last column of Table 17 -- nearly -10 MV at 500 m on 17 July! Notice that all of these potentials are comparable to, or larger than, those at which long positive leaders are produced with impulse voltages in the laboratory (for example, "Les Renardieres Group"[13]). In fact, piecewise-linear integration of the field profile of Soula and Chauzy[14] (Figure 3) at the time of their first triggered flash (2347 UT) yields a potential of only -10 MV at 436 m, although the field at that level is 45 kV/m and the potential decreases further to -18 MV at 603 m. We will now appeal to the literature on long laboratory discharges, admittedly in much less divergent field geometries, to explore what might be happening at the tips of our triggering rockets.

The field distribution above a grounded triggering rocket can be estimated by approximating it with a tall, thin, vertically-oriented spheroid embedded in a uniform vertical field -- a reasonable approximation except on 17 July. The formula for the vertical field on the axis of a prolate conducting spheroid under these circumstances is a generalization of that given by Willett et al.[1] (in their Eq. (8)) for the field at the spheroid's surface. We return to Moore[15] to obtain

$$E_z(\eta) = E_0 \left\{ 1 - \frac{\frac{1}{2}\ln\left(\frac{\eta+1}{\eta-1}\right) - \frac{1}{\eta}}{\frac{1}{2}\ln\left(\frac{\eta_0+1}{\eta_0-1}\right) - \frac{1}{\eta_0}} + \frac{1}{\eta(\eta^2-1)\left[\frac{1}{2}\ln\left(\frac{\eta_0+1}{\eta_0-1}\right) - \frac{1}{\eta_0}\right]} \right\} \tag{30}$$
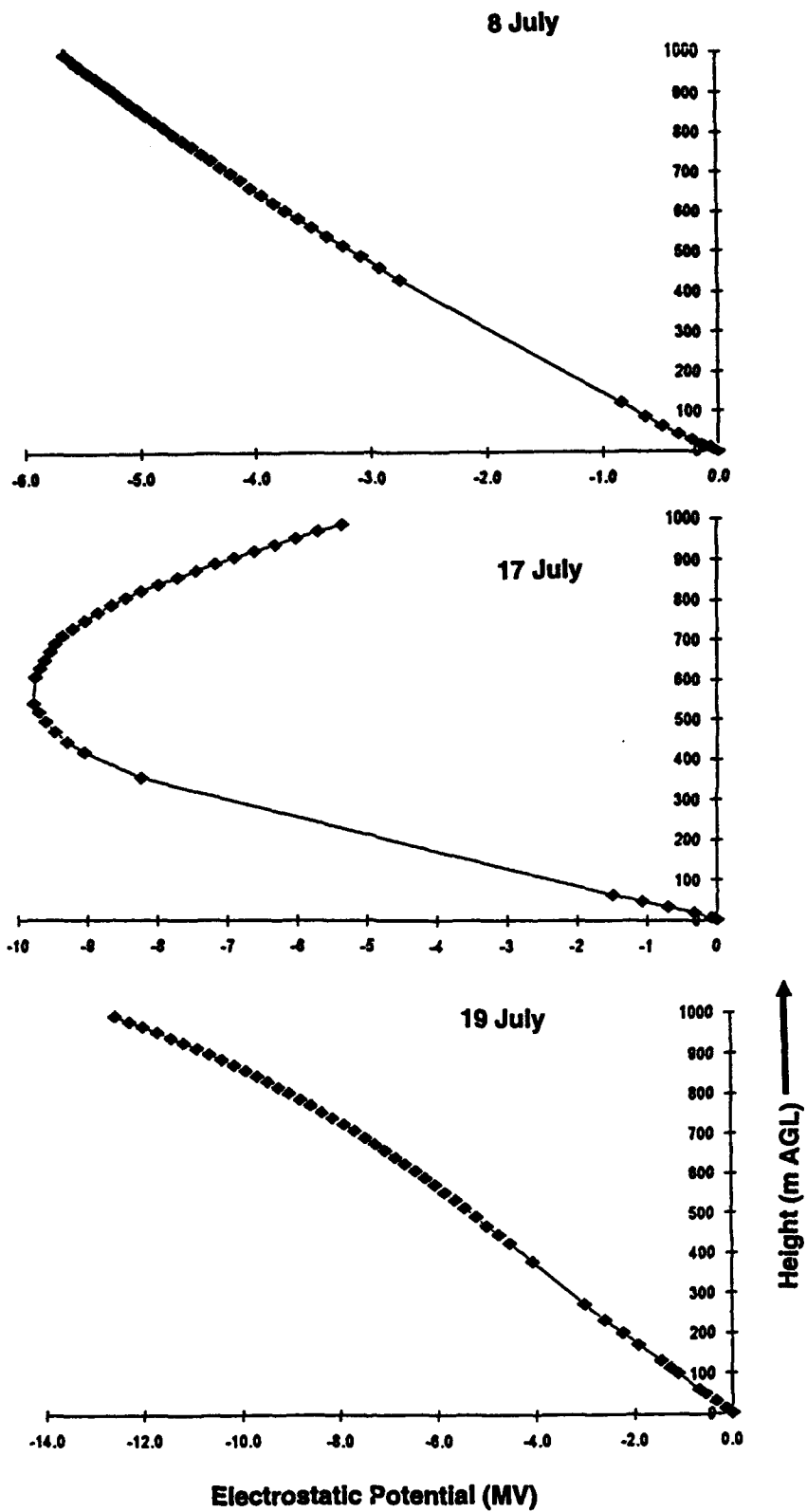
Figure 82. Profiles of ambient electrostatic potential for the lowest 1000 m of the ascents on 8 July (top panel), 17 July (middle panel), and 19 July (bottom panel) -- magnifications of Figure 77

where $\eta = (z/c) \, \eta_0$ applies on axis, and $\eta_0 = (1 - b^2/c^2)^{-1/2}$ is determined by the semi-axis ratio of the spheroid. The notation is the same as that used in Section 5.2 and in the previous report.

Consider 8 July, for example. To construct a suitable spheroid, we require that the radius of curvature of its tip equal the radius of the triggering wire, 0.125 mm. Since the ambient potential at c = 357 m was -2.3 MV, E_0 = +6.4 kV/m, and b = 0.211 m. Not surprisingly, the field at the tip of the spheroid turns out to be orders of magnitude above breakdown. In fact, breakdown fields (>2.7 MV/m) extend about 6 cm above the tip. (This result and those to follow from this model are remarkably insensitive to the value assumed for the semi-minor axis-length. If b is decreased more than three orders of magnitude to 1.25×10^{-4} m, for example, we still find breakdown fields more than 4 cm above the tip.)

Based on theoretical modeling and laboratory measurements of impulse coronas in long rod-to-plane gaps, Badaloni et al.[16] noticed that positive corona propagates until the average ambient field over its length falls below the "stability field," which is around 500 kV/m in atmospheric air. Using this criterion, the maximum extent of positive streamers above our triggering rockets can be computed by integrating Equation 21. On 8 July we find that corona should extend 3.6 m above the rocket! (This might be an over-estimate, since we have blindly integrated through the region of breakdown field, which contributes more than half of the integral in this case. Starting the integral at 6 cm, the average falls below 500 kV/m at 0.96 m -- undoubtedly an underestimate of the corona extent.)

Crude estimates of the distances that laboratory ("cold") positive leaders will propagate can be obtained from the 50 percent breakdown potentials measured for long, positive, rod-to-plane gaps. These potentials imply average fields in 13.5 m gaps on the order of 150 kV/m for 50 percent breakdown probability ("Les Renardieres Group",[13] Table 3.2.1). The average fields under these conditions decrease slowly with increasing gap length. Repeating the calculation in the previous paragraph for 150 kV/m, we find that positive leaders should have developed 13.6 m above the rocket on 8 July!

We have discussed our case with lowest ambient field near the ground and smallest (negative) ambient potential at the top of the triggering wire, finding that large impulse coronas and discharges comparable to the longest laboratory leaders (drawing currents up to several Amperes) would have developed if this potential had been applied rapidly enough. Since the upward velocity of our triggering rockets is unknown, and since no measurements of current at the base of the wire are available, we cannot say whether or not such leaders were prevented by space-charge effects. The laboratory data do not extend to much longer gaps, nor do we understand why long leaders stop, once they have begun to propagate, so we cannot guess how close our other two cases came to triggering a lightning flash. Nevertheless, it appears that (1) strong corona, and perhaps long discharges, occurred at the tips of all three triggering rockets but (2) the ambient fields were not sufficient to sustain the development of these discharges to become lightning.

The profile of 19 July (see Figure 71) is of some practical interest regarding triggering conditions. In this case the vertical field was constant near +10 kV/m from the surface to about 500 m altitude, above which the field intensity increased rapidly with height. If a viable leader

had been initiated by one of the triggering rockets, which ascended to at least 478 m, it surely would have continued to propagate into the much larger ambient fields aloft. Therefore, it appears that 10 kV/m is insufficient to trigger lightning by the rocket-and-wire technique. This is significant, since it is about a factor of three larger than the previously proposed safe field magnitude at the same altitude (Heritage,[17] Section 7).

6. CONCLUSIONS AND FUTURE PLANS

The performance of the revised REFS payloads during their first flights into thunderstorms was generally excellent. The most serious problems encountered were telemetry drop-outs (see Section 4.3.1), excessively slow shell-rotation rates during rocket-motor burn (see Section 4.3.3), uncertainty about the effects of corona from the nose of the vehicle (see Section 5.2), and occasional noise and/or saturation on the field mills (see Section 4.3.3). Reduction of the vibration-induced noise in the magnetometer signal (see Section 4.3.5) would also be desirable. These test flights served to confirm the basic design of the payload while identifying several areas where minor improvements should be made.

Further analysis of the existing data will include the use of magnetic-field measurements from the rockets to determine their rotational orientations as functions of time, so that the ambient-field data can be separated into three components and presented in the Earth coordinate system for more complete comparison with the free-balloon data (see Section 5.3.4). During the portions of the flights near apogee (see Section 5.3.2), the information on rocket orientation will be used for self-calibration, as described by Winn.[5] More work is also planned on the aerodynamics of the vehicle (see Section 4.2), especially to understand the interaction of the canted fins with vehicle rotation and to determine their joint effect on drag.

Meanwhile, a contract has been awarded to Harris Corp. of Melbourne, Florida, to re-design REFS for better performance and much lower unit cost and to build three manufacturing prototypes for field testing at Langmuir Laboratory. The paper design is now complete, and the construction and testing phase is beginning. Functional improvements of the Harris design over the system described in this report include the following:

1) Better torque driving the rotating shell to minimize slowing during motor burn.

2) A hemispherical nose "cone" to minimize corona from the nose of the vehicle in high longitudinal fields.

3) Reduced noise levels in the electronics.

4) Field-mill gains adjustable over a factor of 8 in three discrete steps.

5) Increased longitudinal separation of the field mills so that the forward pair is closer to the nose and the aft pair is closer to the electrical center of the vehicle.

6) Accurate laboratory calibration of the longitudinal-field coefficients by placing the entire vehicle inside a sufficiently large, static-field chamber.

7) AC coupling of the magnetic-field sensor to eliminate temperature drift while preserving adequate low-frequency response (see Section 4.3.5).

The July, 1992, experiment succeeded in its primary goal of verifying the REFS design in a thunderstorm environment and also indicated that vertical fields of 10 kV/m over the lowest 500 m were not sufficient to trigger lightning with the rocket-and-wire technique (see Section 5.5). Nevertheless, its scientific value was limited by the lack of detailed data on the meteorological environment penetrated by our sounding rockets and balloons and by poor knowledge of the performance of the triggering rockets and the nature of the electrical discharges at their tips. A second experiment is planned at Langmuir Laboratory during the summer of 1994 to test the three manufacturing prototypes. This experiment should include the following enhancements to make the best use of the resulting soundings:

1) Better telemetry reception. The use of two tracking antennas and the recording of their angular orientations is recommended both to minimize dropouts and to obtain a record of the actual trajectory of the vehicle. Arrangements to record the flight all the way to impact should also be made so that the line integral of field along the entire trajectory can be checked (see Section 5.3.5).

2) A meteorological radar should be operated both to aid in choosing launch opportunities and to document the storm structure during rocket flights. Radar data should also aid in the diagnosis of some of the anomalous behavior of the field mills (see Section 4.3.3) and charging system (see Section 4.3.4), some of which may have been due to collisions with precipitation.

3) Better reliability and a better understanding of the performance of the triggering rockets is needed, especially their velocity profile while towing grounded wires. This is important so that their triggering capability can be compared with that of other similar techniques and, ultimately, with that of flying aerospace vehicles.

4) Current measurements at the base of the triggering wires are required to determine the time evolution of the discharges from their tips during ascent and during the subsequent development of any upward leaders that may be triggered. This is only a minimum requirement, however. Since the planned experiment will be unique in giving detailed electrostatic-field profiles associated with triggered lightning, it is important to gather as much information as possible about the resulting discharges. Ideally this would include, in priority order, streak photography of the developing upward leaders, fast-antenna and/or VHF recordings of the electric fields they produce, and slow-antenna records of the charges deposited aloft.
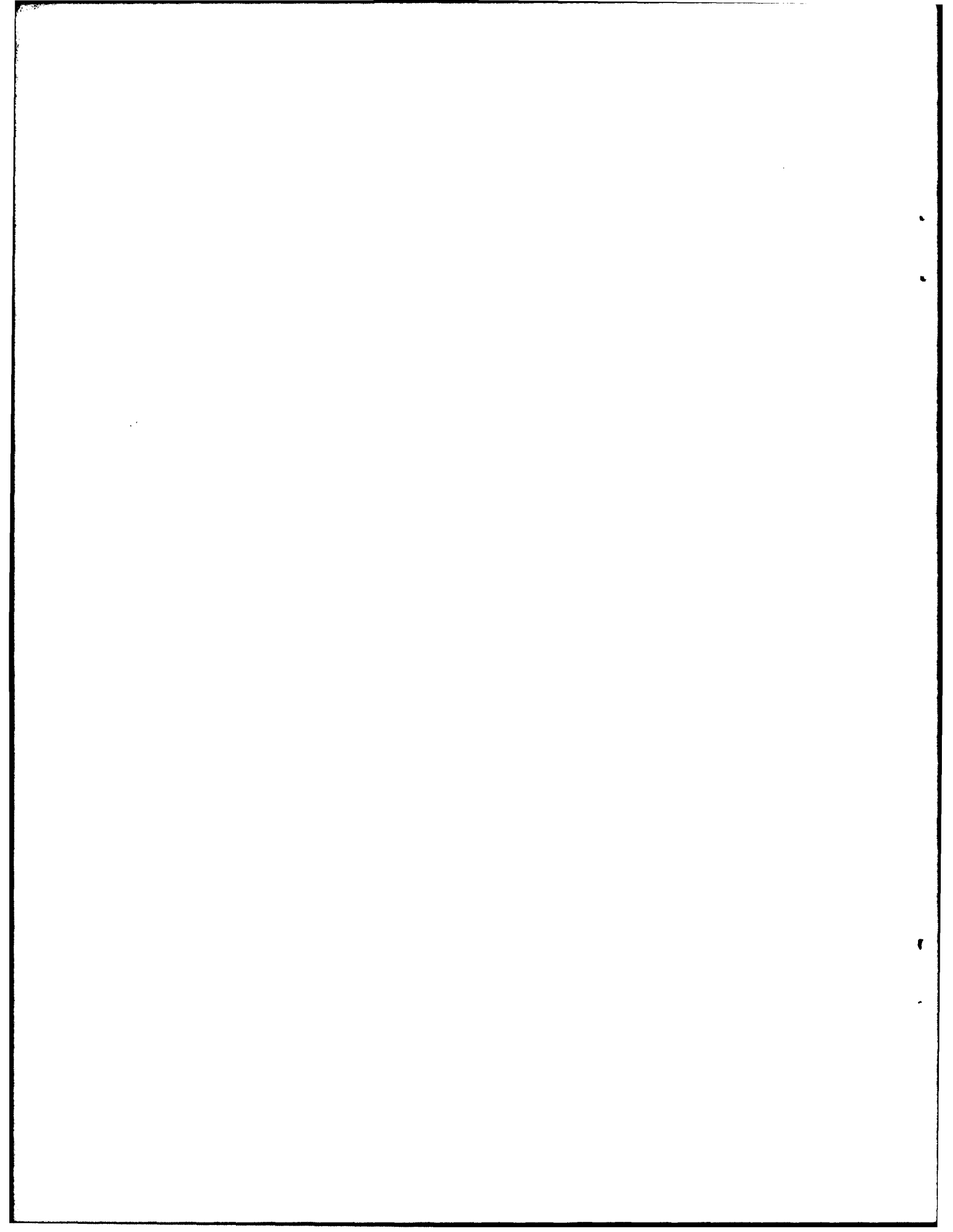
References

1. Willett, J.C., Curtis, D.C., Driesman, A.R., Longstreth, R.K., Rison, W., Winn, W.P., and Jones, J.J., (1992) *The rocket electric field sounding (REFS) program: prototype design and successful first launch*, PL-TR-92-2015, Phillips Laboratory, Directorate of Geophysics, Hanscom AFB, MA 01731-3010, 15 January 1992. **ADA257762**

2. Winn, W.P., Moore, C.B., Holmes, C.R., and Byerley, L.G. III, (1978) Thunderstorm on July 16, 1975, over Langmuir Laboratory: a case study, *J. Geophys Res.*, **83**, 3079-3092.

3. Hankey, W.L., (1988) *Re-Entry Aerodynamics*, AIAA Education Series, J. S. Przemieniecki, Editor-in-Chief, American Institute of Aeronautics and Astronautics, Inc., p. 23ff.

4. Jumper, G.Y., Jr., Frushon, C.J., Longstreth, R.K., Smith, J., Willett, J., and Curtis, D., (1991) *Effects of Magnus Moments on Missile Aerodynamic Performance.*, PL-TR-92-2168, 10 Dec 1991. ADA 268 975

5. Winn, W.P., (1993) Aircraft measurement of electric field: self- calibration, *J. Geophys. Res.*, **98**, 7351-7365.

6. Kositsky, J., Giori, K.L., Maffione, R.A., Cronin, D.H., Nanevicz, J.E., and Harris-Hobbs, R., (1991) Airborne field mill (ABFM) system calibration report, Project 1449, SRI International, Menlo Park, CA, Jan., 1991.

7. Bailey, J., Mach, D.M., and Christian, H.J., (1990) In flight vector calibration of shutter type field mills aboard a Lear 28/29 aircraft, presented at the Fall Annual Meeting of the American Geophysical Union, San Francisco, CA, Dec. 4, 1990.

8. Uman, M.A., (1987) *The Lightning Discharge*, Academic Press, Orlando, 377 pp., 1987.

9. Krider, E.P., Noggle, R.C., Uman, M.A., and Orville, R.E., (1974) Lightning and the Apollo 17/Saturn V exhaust plume, *J. Spacecraft and Rockets*, **11**, 72-75.

10. "Les Renardieres Group", (1981) Negative discharges in long air gaps at les Renardieres -- 1978 results, *Electra*, **74**, 72-216.

11. Laroche, P., Eybert-Berard, A., and Barret, L., (1985) Triggered lightning flash characterization, in *Tenth International Aerospace and Ground Conference on Lightning and Static Electricity (ICOLSE), Paris*, pp.231-239, Les Editions de Physique, Les Ulis, France.

12. Soula, S., and Chauzy, S., (1991) The detection of the electric field vertical distribution underneath thundercloud: principle and applications, paper presented at the 1991 International Aerospace and Ground Conference on Lightning and Static Electricity, Cocoa Beach, Florida, April 16-19, 1991.

13. "Les Renardieres Group", (1974) Research on long air gap discharges at les Renardieres -- 1973 results, *Electra*, **35**, 107-214.

14. Soula, S., and Chauzy, S., (1991) Multilevel measurement of the electric field underneath a thundercloud 2. dynamical evolution of a ground space charge layer, *J. Geophys. Res.*, **96**, 22,327-22,336.

15. Moore, C.B., (1983) Improved configurations of lightning rods and air terminals, *J. Franklin Inst.*, **315**, 61-65.

16. Badaloni, S., Gallimberti, I., and Marode, E., (1993) A simplified model of streamer formation in weakly electronegative gases, *J. Phys. D*, in press.

17. Heritage, H., *Launch Vehicle Lightning/Atmospheric Electrical Constraints Post-Atlas/Centaur 67 Incident*, Report No. TOR- 0088(3441-45)-2, The Aerospace Corporation, El Segundo, CA 09245.

ACSL Program of Trajectory Model
Developed in Section 4.2

Program REFS TRAJECTORY Rev: 19 Nov 92

"Program is a 2 Degree of Freedom model of the REFS trajectory"

"The two degrees of freedom are altitude and range."

"Mod of 19 Nov includes tracker elevation reading."

Initial

"Constants:"

Constant	lambda = 0.2325	$ "Reference Length - ft"
Constant	Sr = 0.042456	$ "Reference Area - ft^2"
Constant	mu = 1.40765E16	$ "Gravitational Par (ft3/sec2)"
Constant	Lift = 0.	$ "Lift (lb)"
Constant	PayWt = 14.60	$ "Payload Wt (Lb)"
Constant	Tbo = 1.620	$ "Time burn out (s)"

"-----------------------------Initial Condition Values "

Constant	Vel0 = 1.	$ "Initial Velocity (ft/s)"
Constant	Gamd0 = 80.	$ "Initial Flt Pth Angle (deg)"
Constant	radtod = 57.29578	$ "Convert radians to degrees(deg)"
Gamma0	Gamd0/RADtoD	$ "Initial Flt Pth Angle (rad)"
=		
Constant	Alt0 = 10400.	$ "Initial Altitude (ft)"
Constant	Rad0 = 20925670.	$ "Radius of the Earth(ft)"
Constant	Range0 = 0.	$ "Initial Range (ft)"
Constant	RefRe = 0.15	$ "Ref Length for Re - ft"
Constant	CdFac = 1.0	$ "Drag Multiplier"
Constant	Time0 = 0.0	$ "Adjustment from integ time"
Constant	DelR = - 2500.	$ "Tracker Coord Offset (ft)"
Constant	DelH = 200.	$ "Tracker Coord Offset (ft)"

```
"-----------------------Thrust - lb"
        Table        Th        1        4...
                     /0.       1.620    1.621    100.     734.     734.     0.       0./
"-----------------------Propellant Wt (Lb) vs. Time"
        Table        PropWt    1        3...
                     /0.       1.621    100.     6.4      0.       0./
"-----------------------Mass Flow Rate - slugs/s"
        Table        Mdot      1        4...
                     /0.       1.54     1.56     100.     0.1266   0.1266   0.       0./
"-----------------------Cx Thrusting vs mach"
        Table        Cxt       1        17 ...
                     /0.       0.1      0.2      0.3      0.4      0.5      0.6      ...
                     0.7       0.8      0.9      1.0      1.1      1.2      1.3      ...
                     1.4       1.5      2.0      ...
                     0.492     0.492    0.434    0.404    0.383    0.367    ...
                     0.354     0.342    0.247    0.384    0.483    0.576    ...
                     0.650     0.700    0.984    1.404    0.967/
"-----------------------Cx Coasting vs mach"
        Table        Cxc       1        17 ...
                     /0.       0.1      0.2      0.3      0.4      0.5      0.6      ...
                     0.7       0.8      0.9      1.0      1.1      1.2      1.3      ...
                     1.4       1.5      2.0      ...
                     0.624     0.629    0.571    0.541    0.520    0.504    ...
                     0.490     0.478    0.481    0.516    0.665    0.779    ...
                     0.843     0.797    1.168    1.583    1.114/
        "-----------------------Computed constants"
        Srlamb = Sr * lambda
Dynamic
        Cinterval Cint = .5
        Constant Tstp = 80.
        Constant altstp = 7000.
        Termt (Time .ge. Tstp .or. alt .lt. AltStp)
Derivative
     Algorithm Ialg = 1
     Nsteps Nstp = 1
     Maxterval Maxt = .5
        !-----------------------environment module
        !-----------------------log of atmospheric density
        TABLE    lro          1          10        &
                 / 0.0        1.0e4      2.0e4      3.0e4      4.0e4      &
                 5.0e4        6.0e4      7.0e4      8.0e4      9.0e4      &
                 -6.04191     -6.34502   -6.67084   -7.02346   -7.43995  &
                 -7.91851     -8.39664   -8.87953   -9.36448   -9.87239/
```

!----------------------calculate actual atmospheric density
ro = EXP(lro(alt))
!----------------------velocity of sound - function of altitude

	TABLE	vsf	1	10 &			
		/ 0.0	1.0e4	2.0e4	3.0e4	4.0e4	&
		5.0e4	6.0e4	7.0e4	8.0e4	9.0e4	&
		1186.5	1077.4	1036.4	994.8	968.1	&
		968.1	968.1	970.9	977.6	984.3 /	

vs = vsf(alt)

Time = T + Time0

Thrust = Th(Time)

Mach = vel/vs

q0 = 0.5 * ro * vel**2

Re = RefRe * vel / 0.000212

Weight = PayWt + PropWt(Time)

Mass = Weight / 32.17

"---------2D Trajectory Equations"

'Trajectory computes a simple 2d trajectory given initial'

'velocity and flight path angle. '

VelD = (Thrust - Drag)/Mass - mu*sin(Gamma)/Radius/Radius

Vel = Integ(VelD,Vel0)

GammaD = Lift/Mass/Vel - mu*cos(Gamma)/Vel/Radius/Radius...
            + Vel*cos(Gamma)/Radius

Gamma = Integ(GammaD,Gamma0)

AltD = Vel*sin(Gamma)

Alt = Integ(AltD,Alt0)

Radius = Alt + Rad0

AltT = Alt - DelH - alt0

RangeD = Vel*cos(Gamma)

Range = Integ(RangeD,RAnge0)

RangeT = Range - DelR - Range0

ElevT = Atan(AltT/RangeT)

Cdt = Cxt(Mach)

Cdc = Cxc(Mach)

If (Time.lt.Tbo) Then

  Cd = Cdt

Else

Cd = Cdc

EndIf

  Drag = Cd*Sr*q0*CdFac

"-------Conversions for output:"

      AltNmi = Alt*0.000164579
      RangeN = Range*0.000164579
      Gamdeg = Gamma*RadtoD
      ElevDT = ElevT*RadtoD

End $ "of Derivative"

End $ "of Dynamic"

Terminal

End $ "of Terminal"

End $ "of Program"